Technische Universität München
Physik Department E21 (Lehrstuhl für Experimentalphysik III)

Single crystal growth of intermetallic compounds with unusual low temperature properties

Dipl. Phys. (Univ.) Andreas Neubauer

Vollständiger Abdruck der von der Fakultät für Physik der Technischen Universität München zur Erlangung des akademischen Grades eines

Doktors der Naturwissenschaften (Dr. rer. nat.)

genehmigten Dissertation.

Vorsitzender:	Univ.-Prof. Dr. Roland Netz
Prüfer der Dissertation:	1. Univ.-Prof. Christian Pfleiderer, Ph.D.
	2. Univ.-Prof. Dr. Rudolf Gross

Die Dissertation wurde am 22.11.2010 an der Technischen Universität München eingereicht und durch die Fakultät für Physik am 02.03.2011 angenommen.

Contents

Chapter 1

Introduction

1.1 Motivation and Overview

High-quality single crystals are one of the most important prerequisites for major advances in fundamental and applied condensed matter physics. For instance, a tremendous variety of unexpected novel properties has been discovered in recent decades in materials with strong electron correlations. Examples include unconventional forms of superconductivity [1], complex forms of magnetic order [2] as well as exotic metallic and insulating states [3, 4]. Motivated by these findings it was the aim of this thesis to put into operation an ultra high vacuum (UHV) compatible image furnace as part of a new crystal growth laboratory and to prepare high purity single crystals of intermetallic compounds. In addition, it was the goal to investigate the low temperature properties of the crystals grown.

From a technical point of view this comprised the design and assembly of the necessary equipment for the preparation of starting rods for use in the image furnace and to develop a basic expertise in crystal growth using the vertical float-zoning method. It further included the use of diverse methods of metallurgical characterization.

For the investigation of the physical properties we applied various bulk methods and neutron scattering techniques at low temperatures both at ambient pressure and at high pressures. Neutron depolarization radiography was thereby found to be a very efficient and powerful new method for the investigation of the distribution of the (ferro)magnetic properties along the crystals.

Having put into operation a new crystal growth furnace we addressed the feasibility of the growth of various intermetallic compounds with different equilibrium phase diagrams; namely the congruently melting compounds MnSi and $NbFe_2$, the incongruently melting systems Mn_3Si and Ni_3Al, and systems with narrow (MnSi) and wide ($NbFe_2$) homogeneity ranges. Subsequent, we optimized the experimental equipment towards high purity conditions in order to grow highest purity crystals. This means that the whole processing chain necessary for crystal growth was changed to meet UHV purity standards.

In the course of this thesis thirty-eight crystal growth experiments of twelve different intermetallic compounds were carried out. For Cu_2MnAl, Mn_3Si, Fe_2VAl, and $NbFe_2$ we grew, to the best of our knowledge, for the first time single crystals by means of the optical heated floating zone technique and, in the case of Fe_2TiSn, we managed to grow the first single crystals at all. The float-zoned crystals generally showed very good structural properties and a high purity that allowed for detailed investigations of the physical properties. Six of those compounds were investigated in detail, namely the Heusler compounds Cu_2MnAl, Mn_3Si, and Fe_2TiSn, the B20 gradient crystals $Mn_{1-x}Fe_xSi$ and $Fe_{1-x}Co_xSi$, and the C14 Laves phase $NbFe_2$. Except for Cu_2MnAl, where the technical application as a monochromator for polarized neutrons was of main interest, the compounds can be summarized as materials that exhibit various forms of subtle magnetic order at low temperatures driven by strong electronic correlations. The emphasis of the investigation rests thereby on the role of defects and impurities, that promote or destroy these forms of order, as a common theme.

The outline of this thesis is as follows. In the remainder of this chapter a detailed account is given of the systems grown as part of this thesis and the underlying scientific issues that motivated this work. This is followed by a theoretical introduction to crystal growth given in section 1.3. An overview of the crystal growth equipment as well as the methods used for the metallurgical characterization is given in chapter 2. The experimental techniques are summarized in chapter 3. The results of the six compounds that were investigated in detail are presented in subsequent chapters following the same layout. A description of the crystal growth process is followed by a discussion of the metallurgical investigation and the single crystal properties. Next, the results of the investigations of the physical properties are presented and discussed. Each chapter is closed by short summary and outlook.

1.2 Reviews of the material systems

1.2.1 Heusler compounds

Heusler compounds are named after Friedrich Heusler, who reported in 1903 that non-magnetic Cu-Mn is turned into a ferromagnetic material by addition of non-magnetic sp-elements (Al, In, Sn, Sb or Bi) [5]. Nowadays Heusler compounds are generally referred to as ternary compounds with the full Heusler X_2YZ or the half Heusler XYZ composition, where X and Y are transition metal atoms and the Z atom has a sp-valence band configuration (see Fig. 1.1 (a)). The full and the half Heusler compounds crystallize in the $L2_1$ and $C1_b$ crystal structure, respectively, as shown in Fig. 1.1 (b). The unit cell consists of four interpenetrating fcc sublattices with the positions (0,0,0) and $(\frac{1}{2},\frac{1}{2},\frac{1}{2})$ for X, $(\frac{1}{4},\frac{1}{4},\frac{1}{4})$ for Y, and $(\frac{3}{4},\frac{3}{4},\frac{3}{4})$ for the Z atoms. In the half Heusler compound the $(\frac{1}{2},\frac{1}{2},\frac{1}{2})$ site is vacant. Consequently, the structure is no longer centro-symmetric.

A typical disorder phenomena observed in Heusler compounds is partial occupation of Y and Z atoms on each others sublattices. This leads to $L2_1$-B2 type disorder, resulting in a B2 type structure if half of the Y and Z atoms interchange their position. The ratio of $L2_1$/B2 depends on the synthesis and heat treatment of the alloys. Due to smaller interatomic distances in B2-type structures, antiferromagnetic ordering becomes energetically favorable [7]. In general, it is found that disorder effects occur quite frequently in Heusler compounds and can strongly influence their magnetic and electronic properties.

At low temperatures several Heusler alloys, e.g., Ni_2MnGa and Co_2NbSn, undergo a martensitic transition from a highly symmetric cubic austenitic to a low symmetry martensitic phase. Unlike atomic order-disorder transitions a martensitic transition is caused by non-diffusional cooperative movement of the atoms in the crystal [7].

Heusler compounds became first famous for having a high ferromagnetic transition temperature. Nowadays they generate interest in various fields like spintronics [8], magnetic shape memory alloys [9], superconductors, thermoelectric devices and metal-insulator

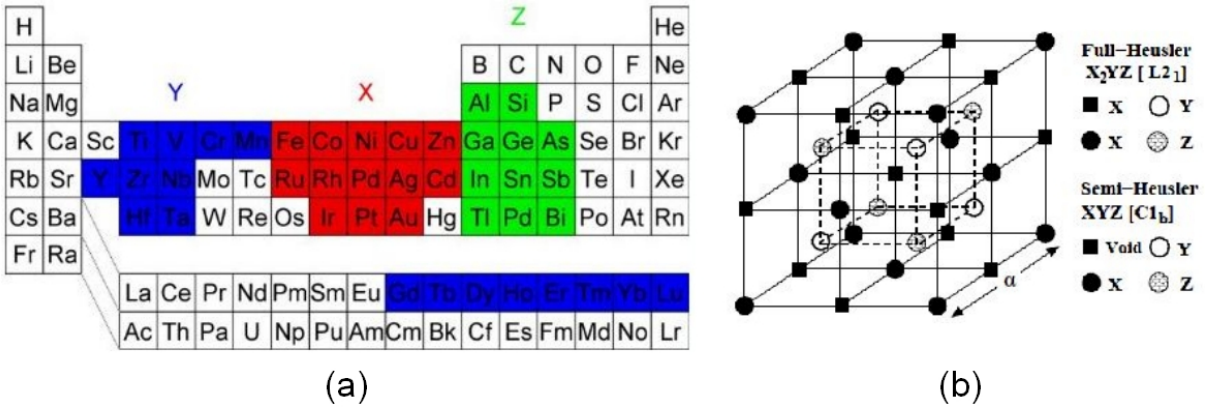

Figure 1.1: (a) Periodic table of elements highlighting typical elements for Heusler alloys [6]. (b) Cubic crystal structure of full ($L2_1$) and half ($C1_b$) Heusler compounds taken from Ref. [7].

transitions (for an overview see [10–12]). The abundance of stoichiometric full and half Heusler compounds as well as further compositional doping towards quaternary Heusler compounds makes this class of material an ideal playground for material scientists.

In Heusler alloys a series of interesting magnetic phenomena like itinerant and localized magnetism, antiferromagnetism, helimagnetism, Pauli paramagnetism or heavy fermion behavior can be found. Investigating the effect of pressure on a number of Mn based Heusler compounds, Castellitz [13] and later Kanomata [14] reported a positive ($\frac{dT_C}{dp} > 0$) pressure dependence of the ferromagnetic transition temperature.

In a recent study Şaşioglu [7] presented theoretical calculations of the pressure dependence of T_C in Ni_2MnSn. He proposed two competing trends resulting from a decreasing lattice constant. Firstly, the decreasing lattice constant leads to a broadening of the bands that stems from the increasing overlap of the atomic states. A consequence of band broadening is a decrease of the magnetic moments. In the spirit of the Heisenberg model of localized moments, decreasing atomic moments decrease the interatomic exchange interactions by a factor of m_p^2/m_0^2, where m_p is the atomic moment at pressure p and m_0 is the moment at ambient pressure. Correspondingly, one expects a decreasing Curie temperature associated with decreasing atomic moments. Secondly, decreasing interatomic distance leads to an increasing electron hopping and, hence, a more efficient mediation of the exchange interactions between magnetic moments. This would result in an increase of the Curie temperature with pressure. The competition of the two opposing trends opens the possibility for both increase and decrease of the Curie temperature with applied pressure.

A phase diagram of the transition temperature versus interatomic distance that contains both experimental and theoretical results is shown in Fig. 1.2 (a)(taken from Ref. [7]). The phase diagram presents the formation of a pressure-controlled magnetic dome. Note that the interatomic distance is inversely proportional to the applied pressure. These results,

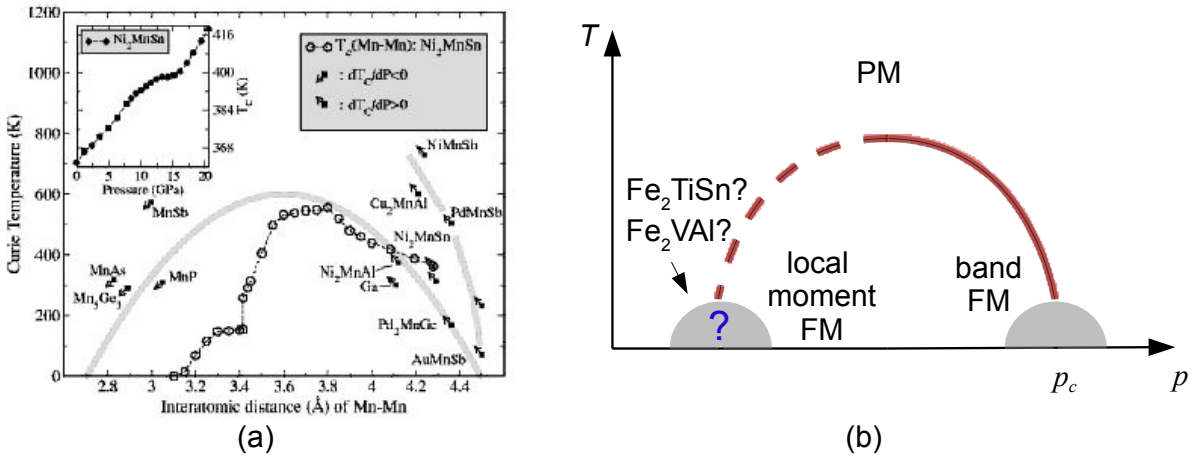

Figure 1.2: (a) Phase diagram of the Curie temperature vs. lattice spacing that contains both experimental and theoretical results for Heusler compounds (taken from Ref. [7]). The formation of a ferromagnetic dome depending on the interatomic Mn-Mn distance is shown. (b) Schematic image of a pressure dependent ferromagnetic dome. Fe_2TiSn and Fe_2VAl are candidates for a pressure induced quantum phase transition.

combined with preliminary work on the pressure dependence of CuMnSb and Mn_3Si [15–17] (see Fig. 1.3 for the pressure dependence of Mn_3Si), inspired us to search for Heusler compounds on the border of magnetism where applying pressure would generate long range magnetic interaction. This means, a pressure induced quantum phase transition from a non-magnetic to a magnetic ground state (see Fig. 1.2 (b)). As possible candidates the Heusler compounds Fe_2TiSn and Fe_2VAl were studied in this thesis.

Except for Mn_3Si no detailed equilibrium phase diagrams were available for the ternary Heusler compounds grown in this thesis. Hence, testing the feasibility of high purity single crystal growth of these Heusler alloys with the vertical floating zone technique is an important first step paving the grounds for future experiments.

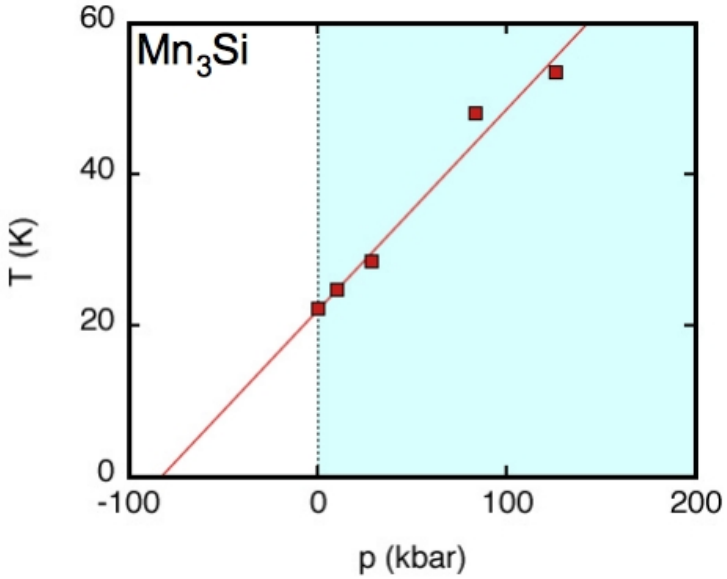

Figure 1.3: Pressure dependence of the antiferromagnetic transition temperature T_N in Mn_3Si taken from Ref. [15]. With increasing pressure an increase of T_N is observed, as inferred from resistivity measurements.

1.2.1.1 Cu_2MnAl

Cu_2MnAl was one of the alloys first investigated by Heusler in 1903 [5]. It orders ferromagnetically at $T_C = 622\,K$ with an ordered magnetic moment of $3.6\,\mu_B$ per formula unit. A detailed ternary phase diagram is not available, but a series of publications on crystal growth of Cu_2MnAl suggest that it is a congruently melting system that crystallizes in the cubic $L2_1$ Heusler phase, the so-called β - phase [18–23]. This β - phase is metastable and does not exist in the equilibrium phase diagram at room temperature. Below 650°C it decomposes via solid state reactions into Cu_9Al_4, Cu_3Mn_2Al, and β - Mn phases. However, since the transformation kinetics of the solid state reaction become very slow far below 650°C, sufficiently fast cooled Cu_2MnAl is found to be quasi-stable at room temperature.

Recent interest in Cu_2MnAl arose due to its technical potential as a polarizing neutron monochromator [23–25]. Bragg (111)-reflection from Cu_2MnAl Heusler crystals gives rise to a monochromatic beam of polarized neutrons [26]. Large crystals have been grown with the Bridgman method [19, 26]. With optimized growth parameters a high flipping ratio of 46 was obtained, which corresponds to a polarization efficiency better than 95% [23]. No information about single crystal growth using the floating zone technique was found in the literature. It was hence of great technical interest to investigate the polarizing properties of crystals grown with the floating zone technique.

1.2.1.2 Mn_3Si

The binary compound Mn_3Si is discussed in the context of the ternary Heusler compounds. It crystallizes in the $L2_1$ Heusler structure with two different Mn sites, Mn_I and Mn_{II}. Hence it can be written in the general Heusler form X_2YZ as $Mn_{II,2}Mn_ISi$. As shown in Fig. 1.4, Mn_3Si forms via a peritectic reaction ($L + Mn_5Si_3 \leftrightarrow Mn_3Si$) at a temperature of 1075.3°C [27]. So far, single crystals have been grown by the Czochralski technique [28]. All of the crystals were reported to contain a small amount of a secondary phase, presumably Mn_5Si_3, due to the peritectic reaction. Recently, single crystal growth using a traveling solvent zone method in a high frequency induction-heated vertical system was reported [29]. The contamination with the Mn_5Si_3 phase, which orders antiferromagnetically below 68 K, was thereby reduced to a minimum.

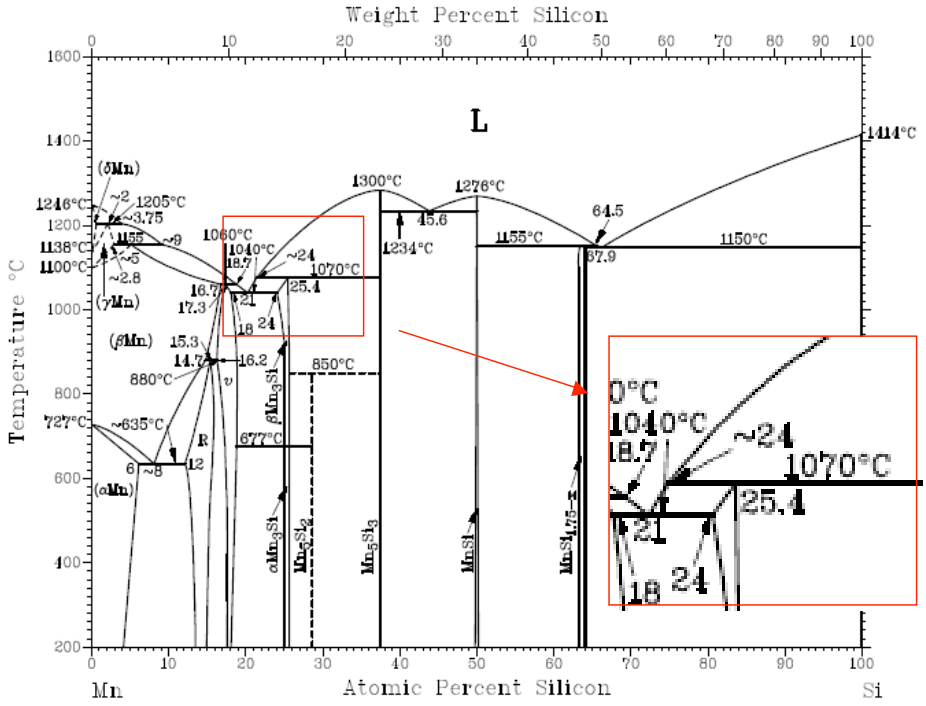

Figure 1.4: Temperature versus composition phase diagram of the binary manganese-silicide system [27]. The peritectic formation of Mn_3Si is shown in detail.

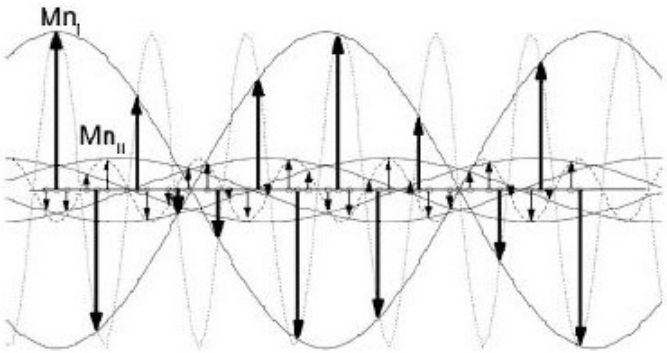

Figure 1.5: Proposed transverse sinusoidal spin structure of Mn_3Si with different magnetic moments of $\mu_{\mathrm{MnI}} = 2.4\,\mu_{\mathrm{B}}$ and $\mu_{\mathrm{MnII}} = 0.3\,\mu_{\mathrm{B}}$ for $\mathrm{Mn_I}$ and $\mathrm{Mn_{II}}$ atoms [29].

Mn_3Si orders antiferromagnetically below 23.5 K with an incommensurate spin structure along the $\langle 111 \rangle$ directions. The magnetic wave vector is $Q = 0.425 \cdot G_{111}$, where G_{111} is the reciprocal lattice vector of (111) [30]. Neutron scattering results suggest a transverse sinusoidal spin structure (see Fig. 1.5) of Mn_3Si with magnetic moments of $\mu_{\mathrm{MnI}} = 2.4\,\mu_{\mathrm{B}}$ and $\mu_{\mathrm{MnII}} = 0.3\,\mu_{\mathrm{B}}$ for $\mathrm{Mn_I}$ and $\mathrm{Mn_{II}}$ atoms, respectively [29]. The antiferromagnetic state in Mn_3Si exhibits an unusual stiffness against strong magnetic fields. Measurements of the magnetization in pulsed fields of up to 50 T do not reveal saturation or a metamagnetic transition [31]. Also the resistivity and specific heat do not show a field dependence up to magnetic fields of 14 T [32]. As an explanation for these unusual properties a strong asymmetry of the density of states of majority and minority charge carriers is proposed, so-called half metallic antiferromagnetism [15, 31, 33]. Furthermore, a strong increase of T_{N} with applied pressure was observed in poly-crystalline Mn_3Si, as shown in Fig. 1.3 [15].

1.2.1.3 Fe_2TiSn

The physical properties of polycrystals of Fe_2TiSn show a rich variety of unusual features [34–37]. The resistivity shows semi-metallic behavior above 50 K and semiconductor-like behavior below 50 K. Specific heat measurements reveal an unusual increase of C/T below 10 K and a broad maximum at 1.1 K, that may be assigned to a Schottky anomaly. The upturn was discussed in terms of heavy fermion behavior with a quasiparticle effective mass of $\sim 40\,m_e$. Although electronic structure calculations within the local muffin-tin orbital (LMTO) approximation suggest that Fe_2TiSn should be a non-magnetic semi-metal with a pseudogap in the density of states, weak ferromagnetic behavior was observed experimentally (see Fig. 1.6). The inverse susceptibility at high temperatures ($T > 350$ K) shows a linear Curie-Weiss behavior extrapolating to zero for $T \approx 0$ K, indicating an effective magnetic moment close to that of pure iron ($\mu_{\mathrm{eff}} \approx 2.2\,\mu_{\mathrm{B}}/\mathrm{Fe}$). A drop of the inverse susceptibility indicates a transition to a weak ferromagnetic state at 250 K and field dependent magnetization measurements show a weak hysteretic behavior at low temperatures. The occurrence of the ferromagnetic behavior has been assigned to atomic disorder. Theoretical calculations [38] supported by refinement of X-ray diffraction data were interpreted as evidence of anti-site disorder of the Fe and Ti atoms in every 5th unit cell.

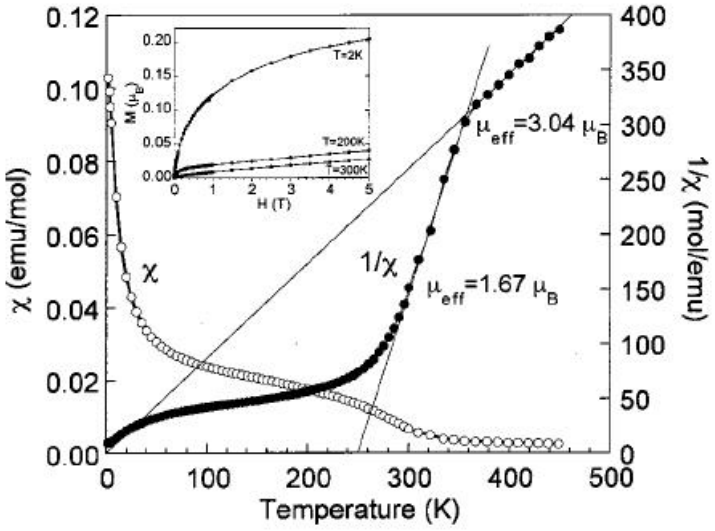

Figure 1.6: Temperature dependence of the susceptibility (open circles) and the inverse susceptibility (full circles), taken from Ref. [34]. The drop of the inverse susceptibility indicates a transition to a weak ferromagnetic state at 250 K. Magnetization measurements at low temperatures (see inset) show a weak hysteretic behavior. Note that the effective magnetic moments are given in μ_B per formula unit.

In general it is assumed that atomic disorder strongly influences the electronic and magnetic properties of Fe_2TiSn [37]. This agrees well with the findings that the properties of Fe_2TiSn show a strong sample dependence [34, 39, 40]. A paramagnetic ground state of Fe_2TiSn has even been reported [39, 41]. Up to now only arc-melted and annealed polycrystals were available. Hence high quality single crystal samples are desirable to isolate or address the origin of the sample dependent properties and to investigate the intrinsic properties.

1.2.2 $NbFe_2$

The intermetallic compound $NbFe_2$ melts congruently at 1627°C and crystallizes in the hexagonal C14 Laves structure. $NbFe_2$ has a wide solubility range as shown in Fig. 1.7, first derived by Goldschmitt [42] and Raman [43], and later revisited by Okamoto [44]. The solubility range of the $NbFe_2$ ϵ-phase was originally thought to be from 27 to 38 at.% Nb [45], but later confined to 32 - 37 at.% Nb [46]. For the non-stoichiometric compositions it was shown experimentally that the excess atoms occupy sites on the other sublattices [47], the so called anti-site substitution. At stoichiometric composition the atoms crystallize in the hexagonal C14 Laves structure with Nb at $4f$ (1/3,2/3,x) and Fe at $2a$ (0,0,0) and $6h$ (y, 2y, 3/4). The unit cell consists of four formula units and has a layered structure, as shown in the inset of Fig. 1.8.

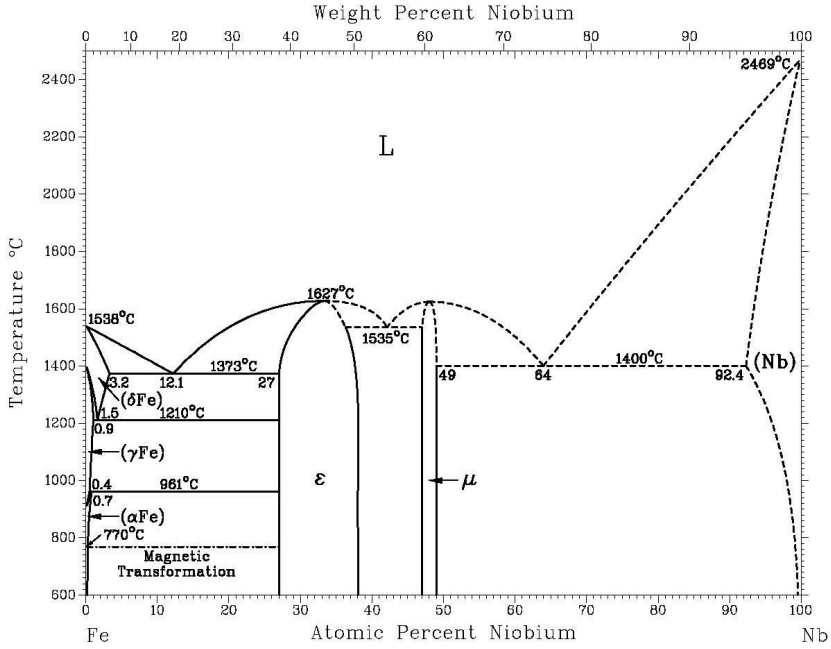

Figure 1.7: Binary phase diagram of the Nb-Fe system taken from Ref. [44]. $NbFe_2$ forms congruently in the C14 Laves structure at 1627°C and exists over a wide solubility range, the ϵ - phase.

Historically stoichiometric $NbFe_2$ was first thought to be paramagnetic on the edge to ferromagnetism [48–51]. In 1987 Yamada and Sakata indirectly found by NMR and magnetization measurements that $NbFe_2$ is a weak antiferromagnet with $T_N \sim 10\,K$ [52]. Further experimental [53–58] and theoretical [59] work on stoichiometric and off-stoichiometric $Nb_{1-y}Fe_{2+y}$ led to a magnetic phase diagram first derived by Yamada and Sakata in 1988 [52]. A revised phase diagram, given by Moroni-Klementowicz *et al.* [60], is shown in Fig. 1.8. The most prominent features of this phase diagram are summarized as follows: three magnetically ordered low temperature states can be accessed within a narrow composition range at ambient pressure. Slight excess of iron or niobium induces itinerant ferromagnetism. Stoichiometric $NbFe_2$ displays anomalies in the magnetic susceptibility, the magnetoresistance and the heat capacity, indicative of an antiferromagnetic phase transition at $T^* \simeq 10$ - $20\,K$. Further microscopic evidence for low temperature magnetic order in $NbFe_2$ is provided by longitudinal μSR measurements [55]. Nevertheless, the nature of this low temperature phase remains enigmatic: it is usually referred to as a spin density wave (SDW) state [54], but direct evidence from neutron scattering remains elusive. Slight enrichment with niobium suppresses T^* towards zero at a critical composition of $y = -0.015$. $Nb_{1-y}Fe_{2+y}$ samples in the vicinity of this quantum phase transition display non-Fermi liquid behavior of the electrical resistivity and the heat capacity [61].

Most of the previous studies of $Nb_{1-y}Fe_{2+y}$ have been performed on polycrystals. The difficulty of phase purity in arc-melted and annealed samples has been addressed in detail by Moroni-Klementowicz *et al.* [60]. They found a second phase in almost all investigated samples leading to additional signals in zero field susceptibility measurements at higher

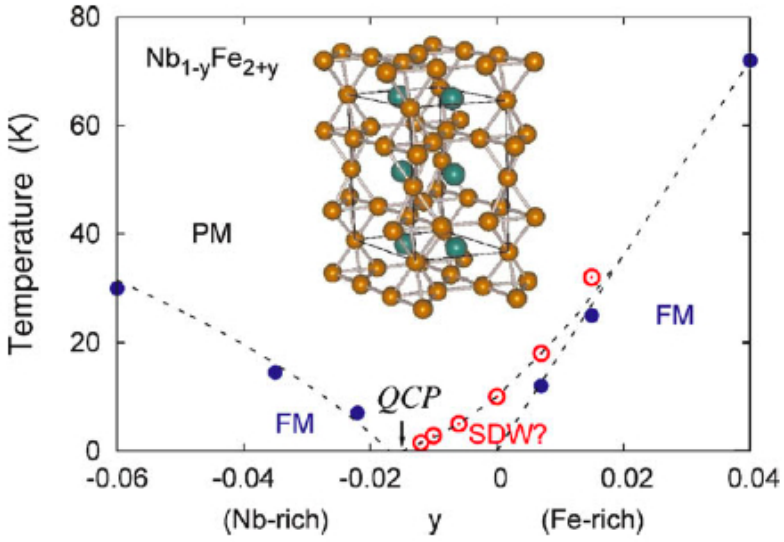

Figure 1.8: Composition dependent magnetic phase diagram of $Nb_{1-y}Fe_{2+y}$ taken from Ref. [60]. Both the excess of iron and niobium induce ferromagnetism (blue points indicate the first observation of ferromagnetic hysteresis). Near the stoichiometric composition, a so far unidentified low temperature phase is observed as evidenced by anomalies in the magnetic susceptibility (peak in χ, red points), in the magnetization and in the magnetoresistance. The phase is usually referred to as a spin density wave (SDW).

temperatures. Single crystals of $Nb_{1-y}Fe_{2+y}$ investigated so far [56, 60, 62] were grown by the Czochralski technique. The single crystals showed a good sample quality with residual resistivity ratios of 18 [60]. Attempts to directly resolve the magnetically ordered state via neutron scattering on the single crystals did, so far, not yield satisfying results.

In a cooperation with William Duncan[1] we attempted as part of this thesis the growth of large single crystals of $Nb_{1-y}Fe_{2+y}$ of several compositions near stoichiometry using the floating zone technique. The wide solubility range of $Nb_{1-y}Fe_{2+y}$ thereby poses a special challenge for the growth of homogeneous bulk samples, especially since small changes in the stoichiometry lead to distinct changes of the magnetic behavior. These crystals would allow a whole series of more detailed studies including thermal expansion, anisotropy of the magnetoresistance, and elastic as well as inelastic neutron scattering. Inelastic neutron scattering measurements of magnetic fluctuations were recently proposed by Subedi and Singh [63] as an important experimental tool to deliver information about the underlying magnetic interactions of the low temperature magnetic order in $Nb_{1-y}Fe_{2+y}$.

[1]Part of the Ph.D. thesis of William Duncan at Royal Holloway, University of London.

1.2.3 B20 compounds

The Strukturbericht designation "B20" accounts for all binary compounds that crystallize in the $P2_13$ space group symmetry, for which the lack of inversion symmetry is a prominent feature. In this thesis, we only consider silicon based compounds, which by themselves already offer a large variety of interesting physical properties. Binary CrSi is reported to be a Pauli paramagnet [64, 65], MnSi an itinerant helimagnet [66], FeSi a paramagnetic Kondo insulator [67, 68] and CoSi a diamagnetic metal [64]. In addition, substitutional doping of the metallic elements may change the physical properties, as shown in Fig. 1.9. For MnSi, doping with Fe or Co leads to a suppression of the helical order, while substitutional doping of FeSi with Co leads to an insulator-metal transition at $x_{\mathrm{Co}} = 0.02$ as well as to a helical magnetic order for $0.05 < x_{\mathrm{Co}} < 0.7$.

The investigation of compounds that show helical magnetic order, i.e., MnSi, $Mn_{1-x}Fe_xSi$, $Mn_{1-x}Co_xSi$ and $Fe_{1-x}Co_xSi$ (shown in blue in Fig. 1.9), has been of major interest to our group in the last couple of years. We will therefore give an extended introduction below to review the most important results we obtained. In the last section (1.2.3.3) we present the open questions concerning the chirality of the magnetic order that was examined in detail as part of this thesis.

1.2.3.1 MnSi

The intermetallic compound MnSi is a congruently melting binary system that crystallizes in the cubic B20 structure with a lattice constant of 4.58 Å. Its remarkable physical properties in combination with its relatively simple crystal structure have made it the subject of intense experimental and theoretical investigations over the last four decades. The main research activities on MnSi may be summarized, roughly speaking, in three parts.

First interest arose in the 1970's and 1980's, when it was found that MnSi is an ideal example for a weak itinerant-electron ferromagnet [66, 70–72]: MnSi orders magnetically at $T_{\mathrm{c}} = 29.5\,\mathrm{K}$, its magnetic susceptibility follows a Curie-Weiss behavior above T_{c}, where the effective Curie-Weiss moment $m_{\mathrm{eff}} = 2.2\,\mu_{\mathrm{B}}$/f.u. is much larger than its ordered magnetic moment $m_{\mathrm{s}} = 0.4\,\mu_{\mathrm{B}}$/f.u.. Well below T_{c} MnSi shows a highly unsaturated magnetization that is well described as $B/M \propto M^2$. It was thereby of great importance that the magnetic properties could be *quantitatively* described by a phenomenological theory that extended the Stoner model by taking into account thermal spin fluctuations [73–75], and that in MnSi the relevant thermal spin fluctuations could be measured by inelastic neutron scattering [76], for the first time in any material, over the entire Brillouin zone.

NMR [79] and neutron scattering experiments [80] established around the same time that MnSi orders below T_{c} in a helical structure along the $\langle 111 \rangle$ directions with a long pitch of the helix of $\lambda \approx 190\,\text{Å}$ (see Fig. 1.10 (b)). The formation of this helical order arises due to an interplay of three interactions at different energy scales [81–83]: (i) the strong ferromagnetic exchange interaction that tends to align the spins parallel, (ii) the Dzyaloshinskii-Moriya spin-orbit interaction ($\mathbf{D} \cdot (\mathbf{S}_1 \times \mathbf{S}_2)$) [84, 85] that results from the lack of inversion

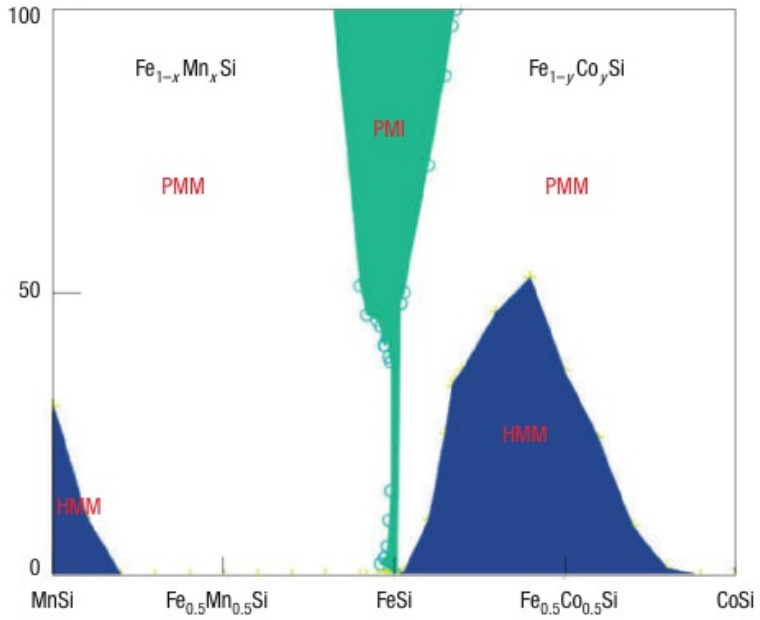

Figure 1.9: Composition dependent phase diagram of Si-based B20 compounds taken from Manyala *et al.* [69]. The composition changes from MnSi to FeSi to CoSi. Regions with different behavior are highlighted: blue denotes the helimagnetic metallic states (HMM), green the paramagnetic isolating state (PMI), and white the paramagnetic metallic states (PMM). In this thesis we investigated compounds that develop helimagnetic order, shown in blue.

symmetry of the crystal structure and tends to align neighboring spins perpendicular to each other, and (iii), as the weakest scale, higher order spin-orbit interaction induced by the cubic crystalline electric fields that pin the helix along the $\langle 111 \rangle$ directions. The interplay of these interactions leads to the magnetic phase diagram shown in Fig. 1.10 (a), which is composed of five different phases: (I) the paramagnetic phase above T_c and for small fields; (II) the helical phase below T_c and for fields $B \leq B_{c1} = 0.1\,\mathrm{T}$, in which the propagation of the helical order is parallel to $\langle 111 \rangle$; (III) the spin-flop or conical phase below T_c and for field $B_{c1} \leq B \leq B_{c2}$, in which the helix aligns parallel to the external field and the spins start canting into the field direction; (IV) the field induced ferromagnetic phase at low temperatures and for fields $B \geq B_{c2} = 0.6\,\mathrm{T}$; and (V) the so called A-phase or skyrmion lattice, a small phase pocket next to T_c for fields $0.1\,\mathrm{T} \leq B \leq 0.3\,\mathrm{T}$.

The interest in MnSi revived in the 1990's, when unconventional behavior was found in MnSi as driven towards a quantum phase transition by applying hydrostatic pressure. The pressure dependent phase diagram of MnSi, taken from Ref. [86], is shown in Fig. 1.11. The magnetic phase transition turns from second to first order for $p^* \leq p \leq p_c$ ($p^* \approx 12\,\mathrm{kbar}$, $p_c = 14.6\,\mathrm{kbar}$) [87]. Above p_c the low temperature resistivity deviates from standard Fermi liquid (FL) behavior ($\rho \propto T^2$) and shows an unconventional $\rho \propto T^{1.5}$ dependence [88]. In addition, neutron diffraction measurements revealed the existence of partial magnetic order for pressures above p^* [89]. The nature of this partial order is currently an open issue. Amongst other suggestions, topological non trivial structures were proposed theoretically to account for this unconventional magnetic behavior [90].

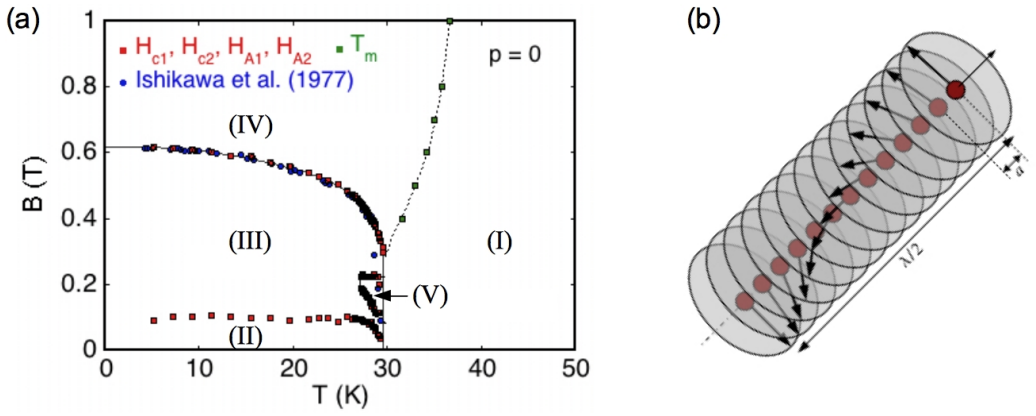

Figure 1.10: (a) Magnetic phase diagram of MnSi taken from Ref. [77]. The phase diagram is composed of five different phases: (I) paramagnetic phase, (II) helical phase, (III) conical phase, (IV) field induced ferromagnetic phase, and (V) A-phase. (b) Schematic drawing of a helical structure taken from Ref. [78]. For further details see text. The spins are arranged perpendicular to the propagation vector of the helix. In MnSi the helical structure is incommensurable.

Most recently MnSi attracted interest when we identified the A-phase of MnSi as a topologically stable skyrmion lattice, a new form of magnetic order [2, 92]. This line of work started with the discovery of a sixfold scattering pattern in small angle neutron scattering (SANS) measurements in the A-phase of MnSi, which aligns always perpendicular to the applied magnetic field (see Fig. 1.12 (a)). Theoretical calculations in the framework of a Ginzburg-Landau theory taking into account thermal fluctuations identified a fluctuation stabilized multi-**Q** ground state in a plane perpendicular to the applied field. It consists of three helices with a relative angle of 120° between them. A characterization of the topology of the spin structure established a winding number $\Phi = -1$ per magnetic unit cell. This is the characteristic of so-called anti-skyrmions. A schematic real space depiction of this skyrmion lattice is shown in Fig. 1.12 (c).

Since neutron scattering cannot distinguish between a multi-**Q** single domain and a single-**Q** multi-domain structure, measurements of the Hall effect were used to proof the skyrmionic nature of the A-phase. The additional contribution in the Hall resistivity ρ_{xy} (see Fig. 1.12 (b)), the so-called topological Hall effect, clearly identifies the A-phase as a single domain multi-**Q** structure [91]. The Hall resistivity was measured during my diploma thesis [93] and the final interpretation in the framework of the topological Hall effect was carried out in the course of this thesis. Further measurements to confirm the data recorded as part of my diploma thesis were also carried out.

These recent findings highlight the need for high quality single crystals of MnSi for further investigations. In fact, using small angle neutron scattering we recently observed directly the influence of an electric current on the magnetic skyrmion state in MnSi crystals grown in our group [94]. The six-fold diffraction pattern rotates by an angle when the currents exceed an ultra-low threshold of only $10^6\,\mathrm{Am}^{-2}$. This is an extraordinary finding given the fact that the currents needed to see spin transfer torques are over five orders of magnitude smaller than those typically applied in experimental studies on current-driven magnetization dynamics in ferromagnetic metals and semiconductors.

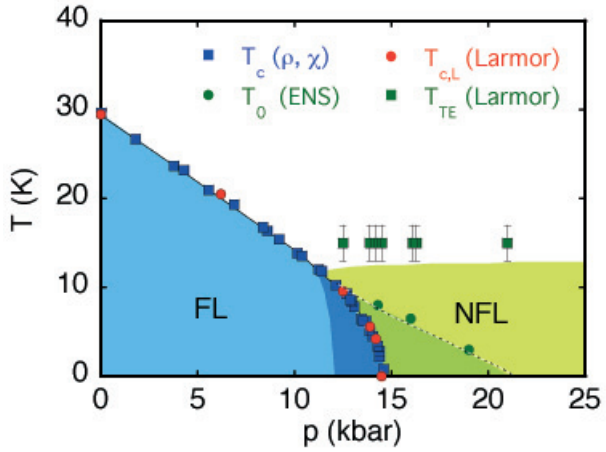

Figure 1.11: Pressure dependent phase diagram of MnSi, taken from Ref. [86]. The blue and green areas distinguish the regimes where MnSi shows Fermi liquid (FL) and non Fermi liquid (NFL) behavior, respectively. For the dark blue area the magnetic transition changed from second to first order. In the dark blue and dark green area the partial magnetic order was found [89].

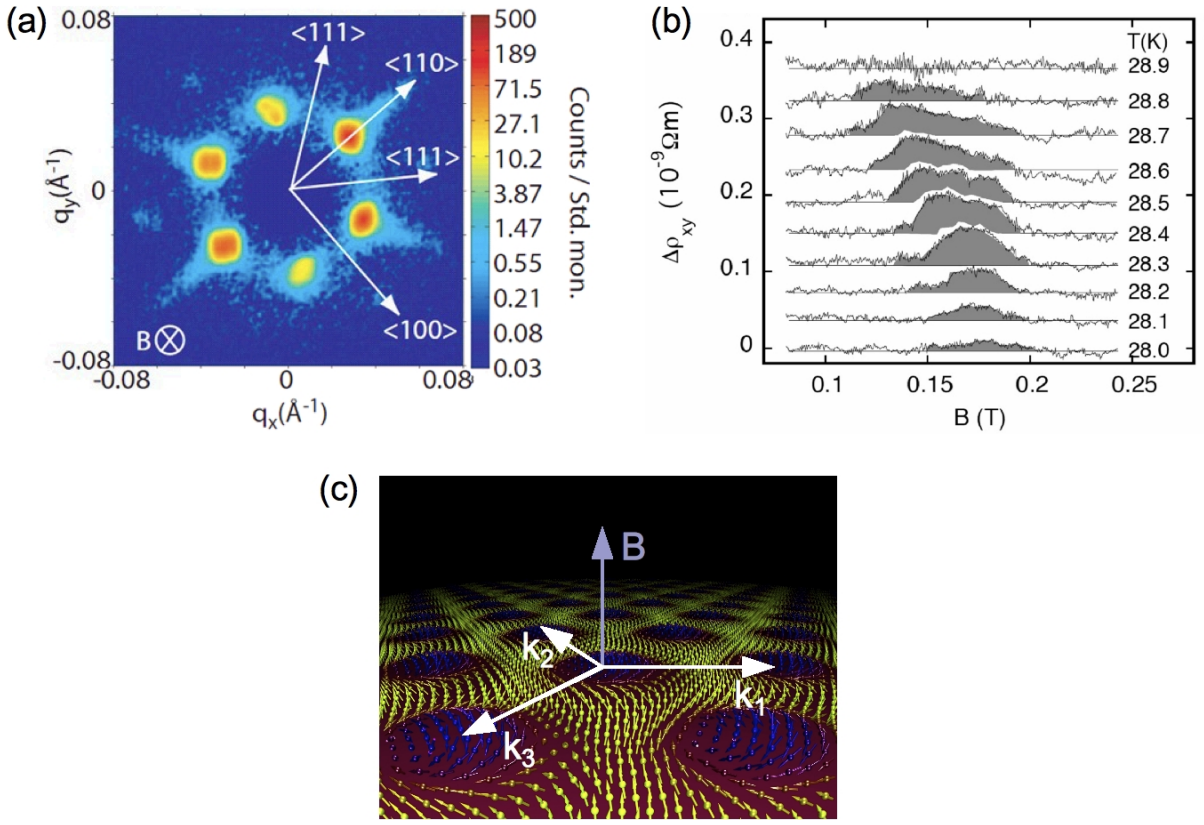

Figure 1.12: (a) Hexagonal neutron diffraction pattern of the skyrmionic phase in the A-phase of MnSi [2]. (b) Topological contribution to the Hall resistivity for fields and temperatures in the A-phase [91]. (c) Schematic real space depiction of one layer of the skyrmion spin structure perpendicular to an applied field. At the center of the vortexes the spins are aligned anti-parallel to the applied field [2].

1.2.3.2 $Mn_{1-x}Fe_xSi$, $Mn_{1-x}Co_xSi$ and $Fe_{1-x}Co_xSi$

Motivated by the discovery of the skyrmion phase in MnSi we extended our investigations to the substitutionally doped B20 compounds $Mn_{1-x}Fe_xSi$, $Mn_{1-x}Co_xSi$ and $Fe_{1-x}Co_xSi$ [78, 92, 95–99]. As for MnSi, the binary silicides FeSi and CoSi are congruently melting compounds that crystallize in the B20 structure. Due to their isomorphic structure, the d-metal atoms Mn, Fe and Co can be substituted by each other in the entire concentration range, allowing to tune the physical properties of the quasi-binary compounds (see Fig. 1.9).

$Fe_{1-x}Co_xSi$ single crystals ($x = 0.2$, 0.25) were grown and investigated by Wolfgang Münzer in the course of his diploma thesis [95]. As shown in Fig. 1.13 (a), these crystals show a helical order at low temperatures, with the transition temperature depending strongly on the Co concentration. The wavelength of the helix is generally longer than for MnSi and depends on the Co concentration, e.g., $\lambda_{x=0.2} = 390$ Å. Münzer showed that the magnetic phase diagram of $Fe_{1-x}Co_xSi$ is qualitatively similar to that of MnSi and he identified, in collaboration with Tim Adams, a skyrmion lattice in the A-phase of semiconducting $Fe_{1-x}Co_xSi$ [95–97, 99]. As reported recently, even individual skyrmions have been observed by means of Lorentz force microscopy in $Fe_{1-x}Co_xSi$ for $x = 0.5$ [102, 103].

Subsequently, several $Mn_{1-x}Fe_xSi$ and $Mn_{1-x}Co_xSi$ single crystals ($x = 0$ - 0.22) were grown and investigated by Andreas Bauer in the course of his diploma thesis [78]. As shown in Fig. 1.13 (b), these crystals also exhibit helical magnetic order at low temperatures, with the transition temperature being strongly doping dependent. The wavelengths of the magnetic helices decrease linearly with increasing concentration $x_{\mathrm{Mn,Fe}}$. Bauer established further, that the magnetic phase diagrams of $Mn_{1-x}Fe_xSi$ and $Mn_{1-x}Co_xSi$ are qualitatively similar to that of MnSi [78, 98]. The magnetic phase diagrams of $Mn_{1-x}Fe_xSi$ and $Mn_{1-x}Co_xSi$ were studied extensively with small angle neutron scattering by Tim Adams, who established the existence of skyrmion lattices in the A-phase of Fe and Co doped MnSi [96].

1.2.3.3 Crystalline and magnetic chirality

A key feature of the B20 compounds is the lack of inversion symmetry in their crystal structure. The atomic coordinates of the $P2_13$ structure are $(u, u, u), (1/2 + u, 1/2 - u, -u), (1/2 - u, -u, 1/2 + u)$ and $(-u, 1/2 + u, 1/2 - u)$. A view of the crystal structure along the (111) axis of (a) left-handed MnSi with $u_{\mathrm{Mn}} = 0.135$ and $u_{\mathrm{Si}} = 0.845$ and (b) right-handed MnSi with $u_{\mathrm{Mn}} = 0.865$ and $u_{\mathrm{Si}} = 0.155$ is shown in Fig. 1.14 (taken from Ref. [101]). Since misleading interpretations of the crystal structure have been given in literature we note the following. The Mn and Si sublattices have opposite chirality. In the left-handed case, Fig. 1.14 (a), the Mn atoms are skewed right-handed while the Si atoms are skewed left-handed. Consistent with Ref. [101, 104], we denote the $P2_13$ structure with $u_{\mathrm{Mn}} = 0.135$ and $u_{\mathrm{Si}} = 0.845$ as crystallographic left-handed, referring to the left-handed skew of the Si atoms.

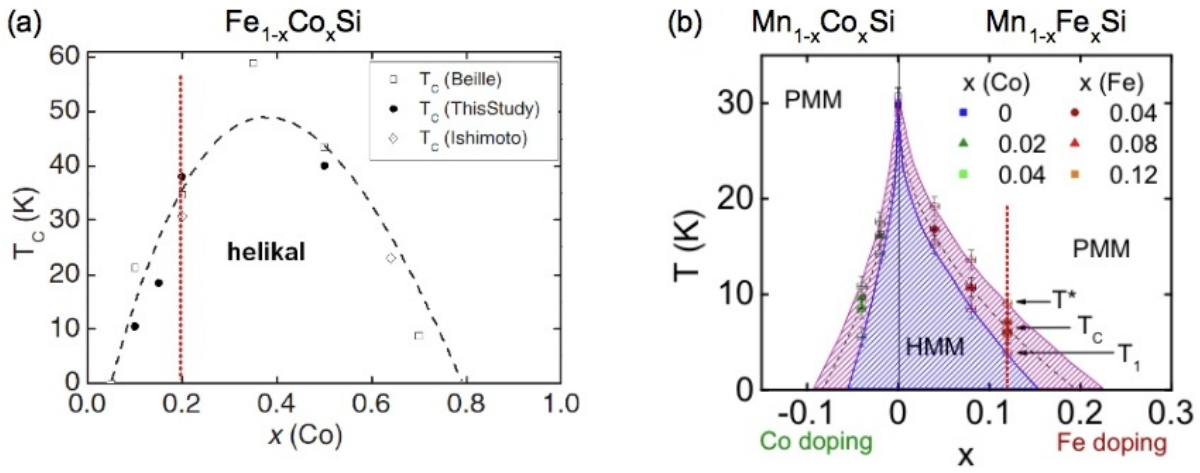

Figure 1.13: Concentration dependence of the helical magnetic state in (a) $Fe_{1-x}Co_xSi$ and in (b) $Mn_{1-x}Fe_xSi$ and $Mn_{1-x}Co_xSi$. Images were taken from Ref. [2] and Ref. [78]. The red lines mark the doping dependent change of the chirality handedness as proposed by Grigoriev [100, 101].

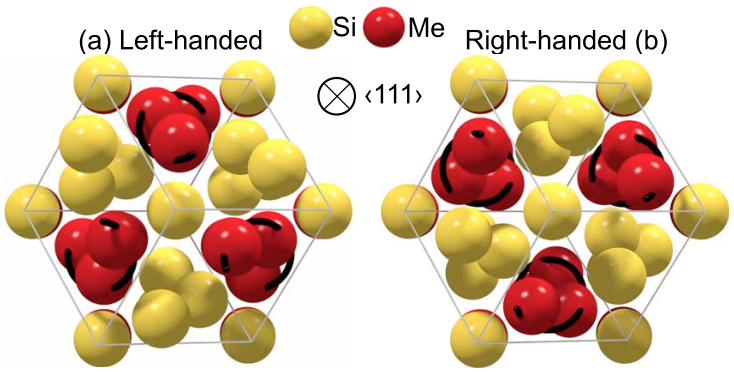

Figure 1.14: Depiction of the crystal structure of MnSi along the (111) axis taken from Ref. [101]. The atomic coordinates are (u,u,u), $(1/2+u, 1/2-u, -u)$, $(1/2-u, -u, 1/2+u)$ and $(-u, 1/2+u, 1/2-u)$. The chirality of the Si sublattice shown in panel (a) is left-handed for the left-handed crystal structure ($u_{\mathrm{Mn}} = 0.135$ and $u_{\mathrm{Si}} = 0.845$). It is right-handed in panel (b) for the right-handed crystal structure ($u_{\mathrm{Mn}} = 0.865$ and $u_{\mathrm{Si}} = 0.155$. Note that the Mn sublattice shows opposite chirality as indicated by the black lines.

The handedness of the crystal structure cannot be identified by neutron scattering techniques [105] and is generally determined by means of X-ray diffraction. The corresponding technique is based on the Flack parameter. Since measurements of the crystal chirality were not carried out in the course of this thesis, we refer to literature for a description [100, 101, 104].

As explained above (see section 1.2.3.1), the chiral magnetic order in the B20 compounds can be explained in terms of the interplay of the ferromagnetic exchange interaction and the Dzyaloshinskii-Moriya (DM) interaction [84, 85], $\hat{H}_{\mathrm{DM}} = \mathbf{D} \cdot (\mathbf{S}_1 \times \mathbf{S}_2)$, that arises due to the missing inversion symmetry of the crystal structure. $\mathbf{D}$ denotes the Dzyaloshinskii-

Moriya vector, that determines the strength of the antisymmetric exchange interaction between two spins $\mathbf{S}_1$ and $\mathbf{S}_2$. A theoretical description of the helical magnetic order in MnSi and FeGe was given by Bak and Jensen [82]. According to their model, the chirality of the helix is determined by the sign of the Dzyaloshinskii-Moriya vector. For $|\mathbf{D}| < 0$ they claim a left-handed spiral and for $|\mathbf{D}| > 0$ a right-handed spiral. Furthermore, they point out that both spirals are energetically equivalent, since $\mathbf{D}$ has full rotational symmetry.

The chirality of the magnetic helix may be determined by means of polarized neutron diffraction. The scattering cross section for polarized neutrons was originally discussed by Blume [106] and revised by Ishida *et al.* [104]. In the following we summarize the results that are important for this study. For a helical spin structure

$$\mathbf{S}(\mathbf{r}) = \mathbf{S}_1 \cos(\mathbf{Q} \cdot \mathbf{r}) + \mathbf{S}_2 \sin(\mathbf{Q} \cdot \mathbf{r}), \tag{1.1}$$

where $\mathbf{S}_1 \perp \mathbf{S}_2$ and $S_1 = S_2 \equiv S_0$, the polarized neutron scattering cross section is given as

$$\frac{\mathrm{d}\sigma}{\mathrm{d}\Omega} = \frac{1}{4} N \frac{(2\pi)^3}{v_0} \left(\frac{\gamma e^2}{m_e c^2} \right)^2 S_0^2 |f(\mathbf{q})|^2 [F_+(\mathbf{p}) \delta(\mathbf{q} + \mathbf{Q} - \boldsymbol{\tau}) + F_-(\mathbf{p}) \delta(\mathbf{q} - \mathbf{Q} - \boldsymbol{\tau})]. \tag{1.2}$$

$\mathbf{Q}$ represents the propagation vector of the helix, which is parallel (antiparallel) to $[\mathbf{S}_1 \times \mathbf{S}_2]$ for the clockwise (anticlockwise) helix, $\mathbf{q}$ the scattering vector, $\boldsymbol{\tau}$ the reciprocal lattice vector, which is (000) in the case of small angle scattering, and $f(\mathbf{q})$ the magnetic form factor. The other symbols are the same as used commonly except the factors $F_\pm(\mathbf{p})$:

$$F_\pm(\mathbf{p}) = 1 + (\mathbf{e}_q \cdot \mathbf{e}_\mathrm{z})^2 \pm 2(\mathbf{p} \cdot \mathbf{e}_q)(\mathbf{e}_q \cdot \mathbf{e}_\mathrm{z}). \tag{1.3}$$

In the above expression $\mathbf{e}_q$ and $\mathbf{e}_\mathrm{z}$ represent the unit vectors in the directions of $\mathbf{q}$ and $\mathbf{Q}$, respectively, and $\mathbf{p}$ is the neutron polarization vector ($|\mathbf{p}|$=1 for fully polarized neutrons). The direction of $\mathbf{e}_\mathrm{z}$ is defined so that the vectors $\mathbf{S}_1$, $\mathbf{S}_2$ and $\mathbf{e}_\mathrm{z}$ in this order form a right-handed coordinate system, and hence, according to Eq. (1.1), the vector $\mathbf{Q}$ is parallel to $\mathbf{e}_\mathrm{z}$ in the case of the clockwise helix, while $\mathbf{Q}$ is antiparallel to $\mathbf{e}_\mathrm{z}$ in the case of the anticlockwise helix.

From the above expressions it follows that the helical structure with a single $\mathbf{Q}$ for either clockwise or anticlockwise rotation only scatters either spin-up or spin-down neutrons under the experimental conditions that the scattering vector is parallel to the propagation vector of the helix, $\mathbf{e}_q || \mathbf{e}_\mathrm{z}$, and that the neutron polarization direction is either parallel or antiparallel to the scattering vector, $\mathbf{p} || \pm\mathbf{e}_\mathrm{z}$. This result may be formulated as the following selection rules for fully polarized neutrons, which gives the helicity of the magnetic structure:
(i) scattering from a clockwise helix is allowed when $\mathbf{p} \| \text{-}\mathbf{q}$ (forbidden when $\mathbf{p} \| \mathbf{q}$).
(ii) scattering from an anticlockwise helix is allowed when $\mathbf{p} \| \mathbf{q}$ (forbidden when $\mathbf{p} \| \text{-}\mathbf{q}$).

An open question in the non-centrosymetric B20 compounds is the lack of inversion symmetry of the crystal structure and, hence, of the chirality of the magnetic structure. Until recently only left-handed crystallographic handedness has been reported for all MnSi and $Fe_{1-x}Co_xSi$ samples studied in the literature [104, 107]. This was a very unusual observation, since two enantiomers, i.e., stereoisomers that are mirror images of each other,

should exist with equal probability. In addition, it has been reported for $Fe_{1-x}Co_xSi$ that the left-handed atomic configuration is associated to a right-handed magnetic helix in contrast to MnSi, where a left-handed atomic configuration is associated to a left-handed magnetic helix.

Very recently, Grigoriev *et al.* have reported the existence of both atomic chiralities in $Mn_{1-x}Fe_xSi$ $(x = 0 - 0.29)$ [101] and $Fe_{1-x}Co_xSi$ $(x = 0.1 - 0.5)$ [100]. In the latter case they investigated five $Fe_{1-x}Co_xSi$ crystals ($x = 0.1, 0.15, 0.2, 0.3, 0.5$) grown by the Czochralski technique. They claimed, using X-ray diffraction, that the structural chirality changed from right-handed for $x < 0.2$ to left-handed for $x > 0.2$. In addition, they confirmed by neutron diffraction that the magnetic chirality is antisymmetric to the atomic structure and switches from left- to right-handedness for $x > 0.2$, preserving the relationship of crystal to magnetic chirality. The observation of the absence of stereoisomers would be of great general importance for many disciplines in the natural sciences.

Further, for $Mn_{1-x}Fe_xSi$ they grew a total of 12 single crystals $(x = 0 - 0.29)$ with the Bridgman or Czochralski technique. They identified both left- and right-handed structural chiralities and found that the structural chirality symmetrically determines the magnetic chirality of these compounds: left-(right-)handed crystalline chirality establishes left (right) handedness of the magnetic helix. Nevertheless, they found that for $x \leq 0.12$ the crystals seem to prefer left-handedness, while the right-handedness is predominant for the crystals with a higher degree of substitution. This would then support their earlier observation in $Fe_{1-x}Co_xSi$ that chiral symmetry is spontaneously broken.

In order to investigate the substitution dependence of the handedness of the crystal chirality and magnetic helicity in $Mn_{1-x}Fe_xSi$ and $Fe_{1-x}Co_xSi$ we decided to grow single crystals with a concentration gradient by means of optical float-zoning. The idea was to start with a single crystal of a given concentration and cross the critical substitution value for which Grigoriev *et al.* claimed the change of chirality [100, 101]. This critical composition is $x = 0.12$ for $Mn_{1-x}Fe_xSi$ and $x = 0.2$ for $Fe_{1-x}Co_xSi$ (see the dashed red lines in Fig. 1.13). This would allow us to investigate if a predefined chirality exists in the crystals as a function of composition and, thus, a spontaneous symmetry breaking, that explains the absence of stereoisomers.

We did not carry out an investigation of the structural chirality as part of this thesis. It is therefore important to note that we assumed a fixed correlation between the atomic and magnetic chirality in $Mn_{1-x}Fe_xSi$ and $Fe_{1-x}Co_xSi$. A fixed correlation has been observed in all experimental investigations reported so far [100, 101, 104, 107]. In $Mn_{1-x}Fe_xSi$ the structural chirality is symmetric to the magnetic chirality, while in $Fe_{1-x}Co_xSi$ the structural chirality is antisymmetric to the magnetic chirality.

1.3 Basics of crystal growth

The aim of single crystal growth is the synthesis of macroscopic samples with a 3-dimensional periodicity, i.e., a defined crystallographic arrangement, of the atoms. The crystalline state emerges via a phase transition from a liquid, gaseous or morphous state. Investigating and controlling the parameters, that lead to or accompany the phase transition, in such a way as to achieve a reproducible and undisturbed crystallization is a main goal in crystal growth. This comprises a detailed knowledge of the equilibrium phase diagrams, of growth processes at the phase boundaries and of the involved (mass) transport phenomena. Moreover, optical and element sensitive investigations of the morphology and composition of the crystallized solids are important tools that provide additional information.

This section provides basic information necessary for a comprehension of the processes during crystallization and of the parameters chosen for crystal growth. It will first give an introduction to the thermodynamical origin of equilibrium phase diagrams and describe the basic and most common types. Second it will introduce theoretical considerations of the crystallization and segregation processes with an emphasis on zone melting. In the last part the vertical floating zone method, which was used as the growth method in this work, will be discussed in more detail.

1.3.1 Phase diagrams

Phase diagrams are an extremely important tool in describing alloy constitutional phase stability and for materials processing. In general, phase diagrams show which phases within a given system are in equilibrium with each other, depending on the variables of states pressure p, temperature T and molar fraction n_i of each compound. A precise knowledge of the phase diagram allows to choose the growth method and parameters for a stable crystal growth of the desired compound. Here it will be shown how binary phase diagrams can in principle be deduced from thermodynamic considerations and the basic types of phase diagrams that arise from those considerations will be described. Ternary phase diagrams will not be discussed, since no ternary phase diagrams for the compounds grown as part of this thesis were available. The introduction follows the books of Wilke/Bohm [108] and Rosenberger [109].

Gibbs free energy & Gibbs phase rule

Thermodynamically the derivation of the phase diagrams is based on considerations of the Gibbs free energy G, defined as

$$G(T, p, n_i) = U(S, V, n_i) + pV - TS = \sum_i \mu_i n_i. \tag{1.4}$$

In the differential form the Gibbs free energy is given as

$$\mathrm{d}G(T,p,n_i) = -S\mathrm{d}T + V\mathrm{d}P + \sum_i \mu_i \mathrm{d}n_i, \tag{1.5}$$

with μ_i being the chemical potential of the i component. The phase with the lowest content of Gibbs free energy is expected to exist. The principle course of the Gibbs free energy curves of a solid and its melt for a one component system is shown in Fig. 1.15. The phase having the lower Gibbs free energy is stable (indicated by the bold line) and a phase transition from liquid to solid occurs at the transition temperature T_m. At T_m the free energy G and therefore the chemical potential of both phases is equal, $\mu^s = \mu^l$. This is the condition for phase equilibrium and can be written in a more general form for a multicomponent system:

$$\mu_i^\alpha = \mu_i^\beta = \mu_i^\gamma = ..., \tag{1.6}$$

where i counts the components and α, β and γ denote the different phases. The number of different phases that can be in equilibrium with each other depends on the degrees of freedom. It is given by the Gibbs phase rule:

$$f = k - \pi + 2. \tag{1.7}$$

Eq. (1.7) states that for a system with k components and π phases only f intensive variables of state can be varied independently. For example, for a one-component ($k = 1$) system at the triple point, where three phases are in equilibrium ($\pi = 3$, gas - liquid - solid), f equals to zero. Since in most growth processes the pressure is not changed, from now on it will be regarded as a constant ($p = const.$) and the Gibbs phase rule is reduced to $f = k - \pi + 1$.

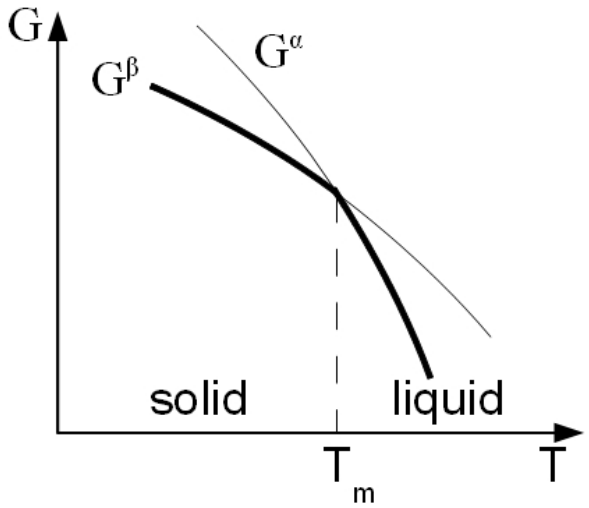

Figure 1.15: Gibbs free energy for a solid (G^β) and liquid (G^α) phase in a 1-component system. The phase with the lowest content of Gibbs free energy is expected to exist (indicated here by the bold line). A phase transition from liquid to solid occurs at the transition temperature T_m.

Binary systems

Looking at binary systems, the composition of each compound (x_1 and x_2) can be given by the molar fractions $x_1 = n_1/(n_1+n_2)$ and $x_2 = n_2/(n_1+n_2) = 1-x_1$. For a discussion of the equilibrium state it is useful to consider the molar free energy $g = G/n = \sum_i \mu_i n_i/n = \sum_i \mu_i x_i$ rather than G. This leads to

$$g = \mu_1 x_1 + \mu_2 x_2 = (\mu_1 - \mu_2)x + \mu_2, \tag{1.8}$$

with $x = x_1$ and $x_2 = 1-x$. Mixing of the pure components with chemical potentials μ_1^0 and μ_2^0 and neglecting any further interaction leads to a linear relation of the free energy $\bar{g}(x)$ (see Fig. 1.16):

$$\bar{g} = \mu_1^0 x + \mu_2^0(1-x) = (\mu_1^0 - \mu_2^0)x + \mu_2^0. \tag{1.9}$$

Ideal solutions

In comparison to Eq. (1.9) the solubility of two components leads to additional terms. Assuming an *ideal solution*, only the *configuration entropy of mixing* $T\Delta s^{id}$ has to be considered, which describes the enhancement of the entropy by intermixing of the atoms. This entropy always reduces g. The free energy g^{id} of an ideal solution can then be written as

$$g^{id} = \bar{g} - T\Delta s^{id} \tag{1.10}$$

with

$$\Delta s^{id} = -R[x\ln x + (1-x)\ln(1-x)]. \tag{1.11}$$

Since $T\Delta s^{id}$ is linear in temperature, its effect becomes more pronounced with higher temperatures as sketched in Fig. 1.16.

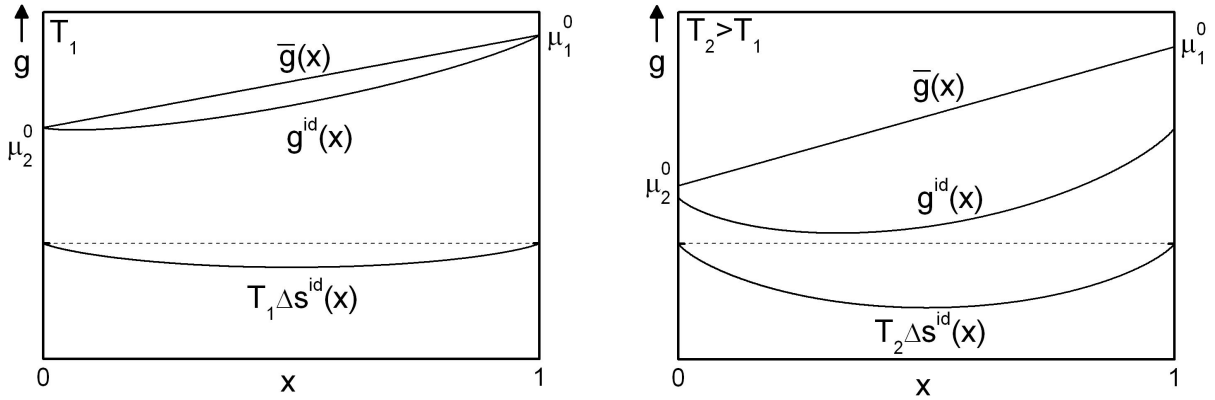

Figure 1.16: The molar Gibbs free energy of a binary system shows a linear relation $\bar{g}(x)$ if all interactions are neglected. For an *ideal solution* g^{id} the *configuration entropy of mixing* $T\Delta s^{id}$ always reduces g. $T\Delta s^{id}$ is linear in temperature and becomes more pronounced with higher temperatures ($T_2 > T_1$).

Comparing the Gibbs free energy of an ideal solution of two phases α (liquid) and β (solid) at different temperatures (Fig. 1.17 (a-e)) leads to the lens shaped phase diagram shown in Fig. 1.17 (f). At the lowest temperature T_1 the free energy $g^\beta(x)$ is always lowest, i.e., the solid β - phase is stable in the entire range of composition x. The same is true for the liquid phase α at the highest temperature T_5. For temperatures T_2 and T_4 the molar free enthalpies start to intersect at sites of the pure elements, the melting points of each element. The most interesting behavior relating to the equilibrium state between the two phases is sketched in Fig. 1.17 (c) for temperature T_3 and an intermediate composition x.

According to the so called tangent rule, a minimum of the free energy is obtained for a mixture of the solid and liquid phase between composition x_A and x_B, the points given by the common tangent to $g^\alpha(x)$ and $g^\beta(x)$. Applying this tangent rule to all temperatures between T_2 and T_4 and all compositions x, the binary phase diagram sketched in Fig1.17 (f) is obtained. The liquid α - phase is separated from the solid β - phase by a lens shaped liquid - solid region where a mixture of solid and liquid phase with different compositions exists.
The amount of the liquid and solid phases within this liquid - solid region follows from mass conservation considerations and is given as:

$$\frac{x^\alpha}{x^\beta} = \frac{x_B - x}{x - x_A}. \tag{1.12}$$

It states that the closer the overall composition x is to the composition x_A of the liquid phase, the larger is the amount of the liquid phase with composition x_A within the liquid - solid region, and vice versa.

The line separating the pure liquid from the mixed liquid - solid phase is called *liquidus* and the line separating the mixed phase from the pure solid phase is called *solidus*. For an ideal solid solution system equalizing the chemical potentials $\mu_i^\alpha = \mu_i^\beta$ leads to the van Laar equation for a two component system

$$\ln\frac{x_1^\beta}{x_1^\alpha} - \ln\frac{x_2^\beta}{x_2^\alpha} = \frac{\Delta h_1'^m}{RT}\left(1 - \frac{T}{T_1^m}\right) - \frac{\Delta h_2'^m}{RT}\left(1 - \frac{T}{T_2^m}\right), \tag{1.13}$$

from which solidus and liquidus curves can be calculated.

A typical crystallization process can now be described with the help of Fig. 1.17 (f). Starting from a liquid phase α with the composition x_A and lowering the temperature, crystallization of phase β with composition x_B will start when the liquidus curve is crossed at point A. Further lowering the temperature will shift the composition of the liquid phase (in a closed system) along the liquidus curve towards point C. At the same time the equilibrium state of phase β also shifts along the solidus curve towards A'. To retain equilibrium the crystalline phase β has to change its composition along the solidus curve, i.e., a constant mass transfer between the already solidified crystal phase and the liquid phase is necessary. The crystallization process will end with the last drops of the liquid phase at composition x_C crystallizing into the solid phase with composition x_A (at point A') and the whole crystalline phase will have the original composition x_A. In reality the mass transfer in the solid phase is often too slow or does not exist, therefore resulting in compositional gradients and segregation (non-equilibrium processes).

Regular solutions

In real solutions the interactions between the components lead to a finite heat of mixing Δh^M and an additional contribution to the entropy of mixing $\Delta s^M \neq \Delta s^{id}$. The molar Gibbs free energy can therefore be written (see Eq. (1.10)) as

$$g^r = g^{id} + \text{correction term} = \bar{g} - T\Delta s^{id} + \Delta g^{xs}, \tag{1.14}$$

where the correction term

$$\Delta g^{xs} = \Delta h^M - T(\Delta s^M - \Delta s^{id}) \tag{1.15}$$

is commonly known as the *excess free energy of mixing*.

For many real solutions, so called *regular solutions*, the deviation of the entropy of mixing from the ideal case is negligible small, $\Delta s^M \approx \Delta s^{id}$, since they satisfy the condition of a statistical distribution of the components in the mixture.
The heat of mixing Δh^M results from the interaction of the components and is therefore proportional to their concentration, leading to

$$\Delta h^M(x) = Ax_{(1)}x_2 = Ax(1-x) = A(x - x^2), \tag{1.16}$$

which is a parabolic function of x with its extremum at $x = 0.5$. The constant A results from the interaction of the components and can be positive or negative. A negative heat

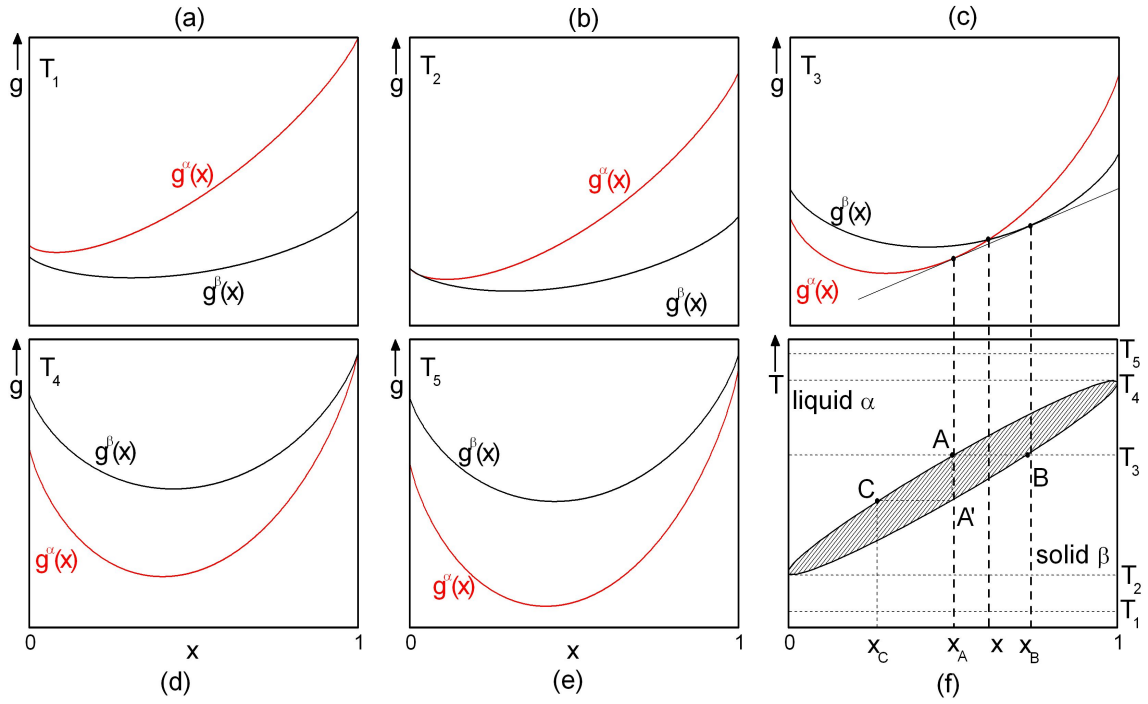

Figure 1.17: (a - e) Comparison of the molar free energies of a solid ($g^\beta(x)$) and liquid ($g^\alpha(x)$) phase for an *ideal* binary system at different temperatures. (f) The lens shaped region in the T - x - phase diagram consists of both a solid and a liquid phase with different composition. It is derived via the tangent common to the free energy curves as shown for temperature T_3 in (c).

of mixing defines an exothermic process, indicative of an attractive interaction between the components and, hence, of a tendency to compound formation. A positive $\Delta h^M(x)$, on the other hand, defines an endothermic process, indicative of a tendency for demixing and a miscibility gap of the components.
The Gibbs free energy g^{rg} for a *regular solution* can be written with Eq. (1.14) and Eq. (1.16) as:

$$g^{rg}(x) = g^{id}(x) + \Delta h^M(x) = g^{id}(x) + A(x - x^2). \tag{1.17}$$

The correction term for real solutions introduced above can decisively change the form of the phase diagrams. In general, one can distinguish between compounds with a positive and negative $\Delta h^M(x)$ term.

Examples of a negative heat of mixing are shown in Fig. 1.18. The Gibbs free energy curves are convex downwards for all temperatures, but differences of the heat of mixing terms $\Delta h^M(x)$ in each phase can lead to distinct curvatures of $g^\alpha(x)$ and $g^\beta(x)$. In those cases two common tangents can be constructed leading to double lens shaped phase diagrams.

The influence of a positive $\Delta h^M(x)$ term is sketched in Fig. 1.19. Here the $\Delta h^M(x)$ term competes with the entropy of mixing $T\Delta s^M$. At high temperatures $T\Delta s^M$ will be large,

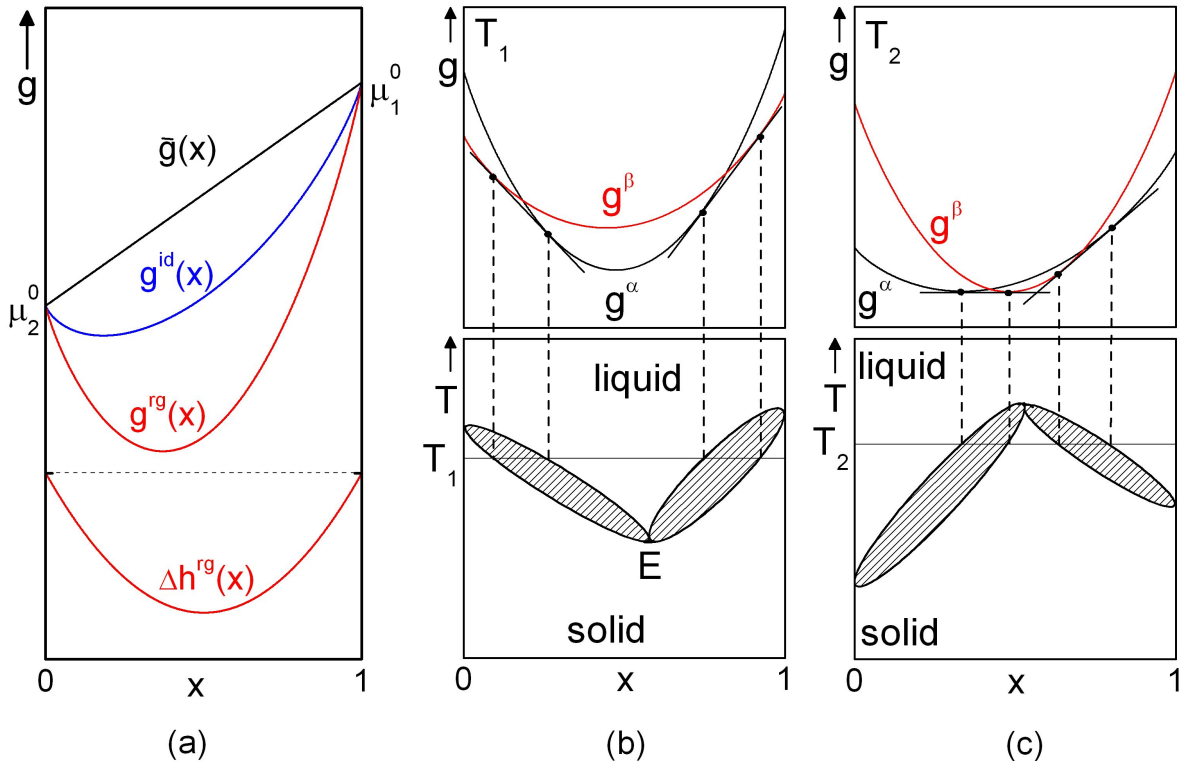

Figure 1.18: (a) The Gibbs free energy $g^{rg}(x)$ for a *regular solution* (red curve) with a negative heat of mixing $\Delta h^M(x)$ as derived from Eq. (1.17). The curve is convex downwards. Differences in the heat of mixing, $\Delta h^M(x)$, in the liquid α- and solid β-phases lead to distinct curvatures of $g^\alpha(x)$ and $g^\beta(x)$ and two common tangents can be constructed. This leads to the double lens shaped phase diagrams shown in (b) and (c).

resulting in a convex downward shape of the free energy. At lower temperatures the two terms can become comparable, leading to a point of inflection of $g^{rg}(x)$. Here the solid β - phase is chosen since this effect is usually found at low temperatures in the solid state. A common tangent can be constructed to the inflected line, stating that a mixture of two solid solutions with composition x_A and x_B has a lower Gibbs energy g^{β} than one solution with composition x_0. Scanning through all temperatures leads to a *solvus* line separating the two solid solutions β' and β'' within one phase as shown in Fig. 1.19 (b). The shaded region can be thought of as an instability range for single solid solutions and is generally referred to as *miscibility gap*. In combination with the previously discussed liquid - solid transition this leads to a phase diagram shown in Fig. 1.19 (c), which resembles the real phase diagram given for the NaCl - KCl solution. Here the double lens shaped liquid - solid transition is followed by a miscibility gap in the solid state.

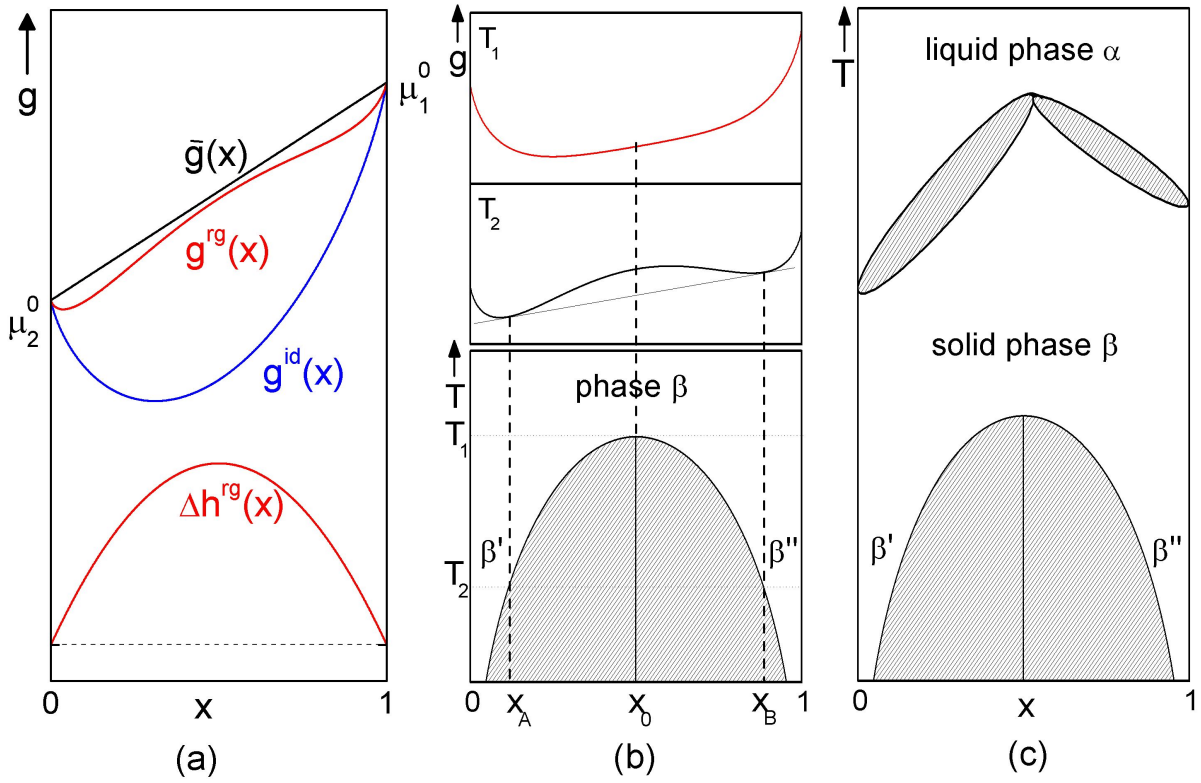

Figure 1.19: (a) The Gibbs free energy $g^{rg}(x)$ for a *regular solution* (red curve) with a positive heat of mixing $\Delta h^M(x)$ as derived from Eq. (1.17). A large $\Delta h^M(x)$ compared to the entropy of mixing term $T\Delta s^M$ leads to an inflection of $g^{rg}(x)$. This usually happens at lower temperatures in the solid phase and leads to an miscibility gap as derived from the common tangent to the inflected free energy curve of the solid phase as shown in (b). The solid β - phase demixes with decreasing temperature into the β' and β'' solid solutions with different compositions x_A and x_B. (c) Resulting phase diagram if the previously described effects are combined. A similar phase diagram is found, for example, for a solution of NaCl and KCl.

Invariant reactions

Up to now monovariant binary systems have been discussed, that is, systems with a continuous change of composition during liquid - solid transitions. The temperature, as the only degree of freedom, had to be lowered continuously to complete the solidification. Adding an additional solid phase γ reduces the degrees of freedom to zero according to the Gibbs phase rule. These reactions are called invariant.

The most common invariant reaction in binary solution systems is the *eutectic* reaction:

$$\text{liquid}\,(\alpha) \underset{\text{cooling}}{\overset{\text{heating}}{\rightleftharpoons}} \text{solid}(\beta) + \text{solid}(\gamma). \tag{1.18}$$

It consists of two solid solution phases (β and γ) and one liquid phase α. It generally appears if the two components are not isomorphic, i.e., they do not have the same crystal structure, and therefore a miscibility gap exists up to the melting equilibrium, while they are completely miscible in the liquid state. The shape of the phase diagram can be deduced from the free enthalpies $g^\alpha(x)$, $g^\beta(x)$ and $g^\gamma(x)$ as shown in Fig. 1.20 (a). For higher temperatures $T_2 > T_E$ a melting diagram similar to Fig. 1.18 can be derived for both phase pairs α/β and α/γ. At a certain temperature T_E, the eutectic temperature, a common tangent to $g^\alpha(x)$, $g^\beta(x)$ and $g^\gamma(x)$ exists. Here all the three phases are in equilibrium. This is the so called "eutectic point". On lowering the temperature an eutectic reaction occurs. A mixture of both solid phases (β and γ) is formed, often with a characteristic structure, the eutectic mixture. On further lowering the temperature (T_1) the free enthalpy of the liquid phase lies always above the common tangent to $g^\beta(x)$ and $g^\gamma(x)$. The eutectic composition therefore determines the lowest possible solidification temperature of the system. This is also expressed by the name eutectic, which has its root in the Greek word *eutectos*, meaning "easy to melt".

The other important type of a three-phase invariant reaction is the *peritectic* reaction

$$\text{liquid}\,(\alpha) + \text{solid}(\gamma) \underset{cooling}{\overset{heating}{\rightleftharpoons}} \text{solid}(\beta). \tag{1.19}$$

An example of a phase diagram for a peritectic system is shown in Fig. 1.20 (b). At higher temperatures, $T > T_P$, only one solid phase is in equilibrium with the liquid phase, (α+γ). At the peritectic temperature T_P, again given by a common tangent to $g^\alpha(x)$, $g^\beta(x)$ and $g^\gamma(x)$, all three phases are in equilibrium. Yet, the sequence of the Gibbs free energy curves is changed. In a peritectic system the minimum of the free enthalpy of the liquid phase $g^\alpha(x)$ does not lie between the solid phases (as in the case for the eutectic system), but outside. This leads to the typical form of the peritectic phase diagram. At the peritectic point P a solid phase (β) forms out of a solid - liquid mixture (α+γ). Generally the occurrence of peritectic reactions is favored by components with large differences in their melting temperatures.

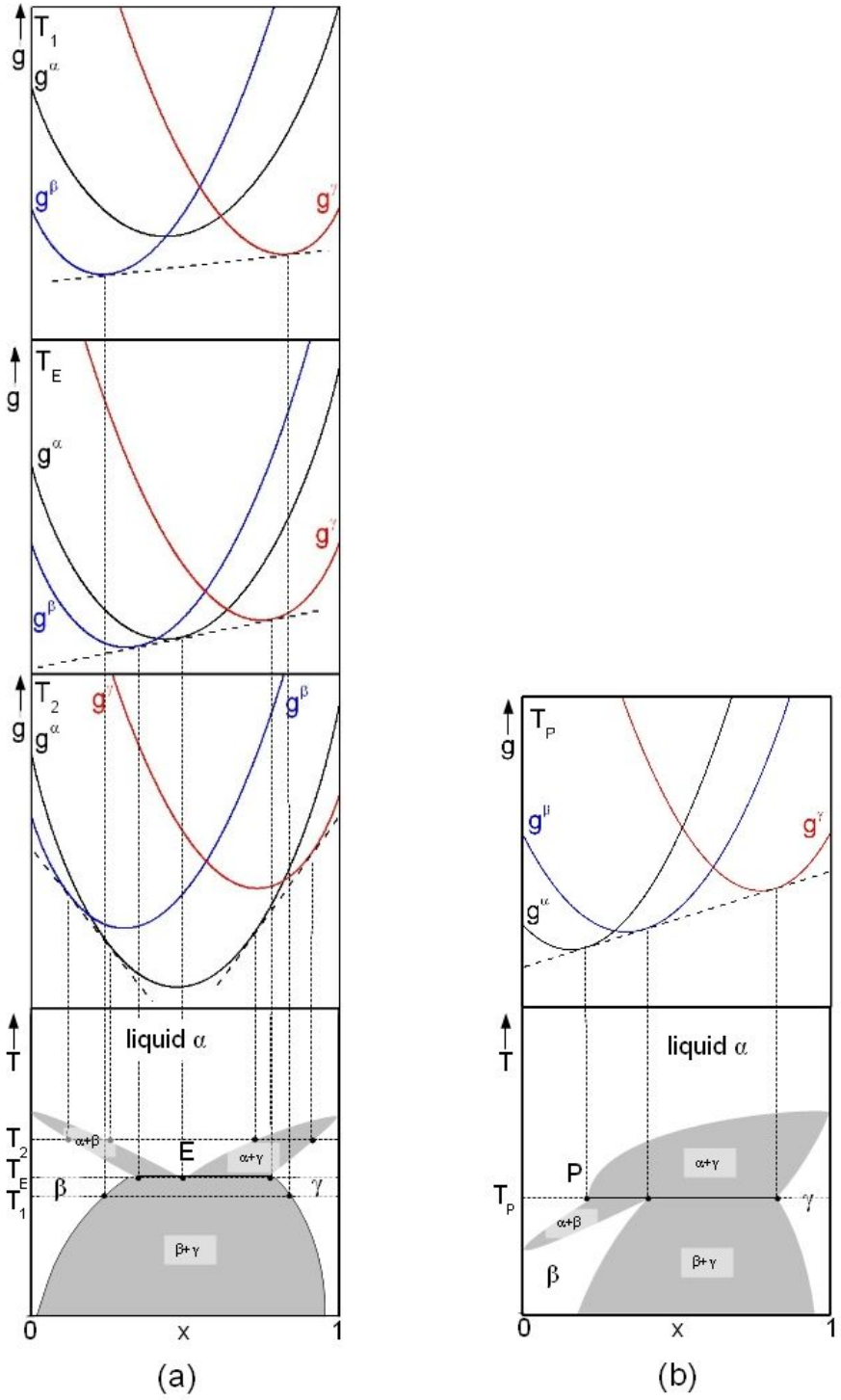

Figure 1.20: The most common invariant reactions, eutectic (a) and peritectic (b), of a binary system. (a) The phase diagram for the eutectic reaction $\alpha \rightarrow \beta + \gamma$ is derived from the free energy curves for different temperatures. At the eutectic temperature T_E a common tangent to $g^\alpha(x)$, $g^\beta(x)$ and $g^\gamma(x)$ can be constructed. (b) Phase diagram for the peritectic reaction $\alpha + \gamma \rightarrow \beta$. At the peritectic temperature T_P again a common tangent exists for the free energy curves, but the sequence is changed. Hence, in a peritectic reaction one solid phase (β) forms from a solid (α) and liquid (γ) phase, while in an eutectic reaction two solid phases (β and γ) form from one liquid phase (α).

Intermediate phases

In addition to substitutional solid solutions, where the solute atoms occupy regular host lattice sites at random, intermediate phases with different crystal structures can form. For a discussion of the phase diagram the free energy $g^{\delta}(x)$ of the intermediate phase δ has to be considered. Typical behavior is shown in Fig. 1.21 (a,b). Generally one can distinguish between an intermediate phase with a broad minimum of $g^{\delta}(x)$ leading to a broad homogeneity range of the intermediate phase and that with a narrow and steep form of $g^{\delta}(x)$, leading to a narrow homogeneity range. The former is typical for intermediate phases of intermetallic compounds where the bonding of the atoms in the intermediate phase is comparable to the bonding of the atoms of the pure compounds. The latter is typical for compounds with strong attractive forces between unlike atoms resulting in strong directional bonding. The difference between those two cases is gradual and all transitions exist. A typical phase diagram resulting from the interference of the free energies curves of the liquid and three solid phases is shown in Fig. 1.21 (c).

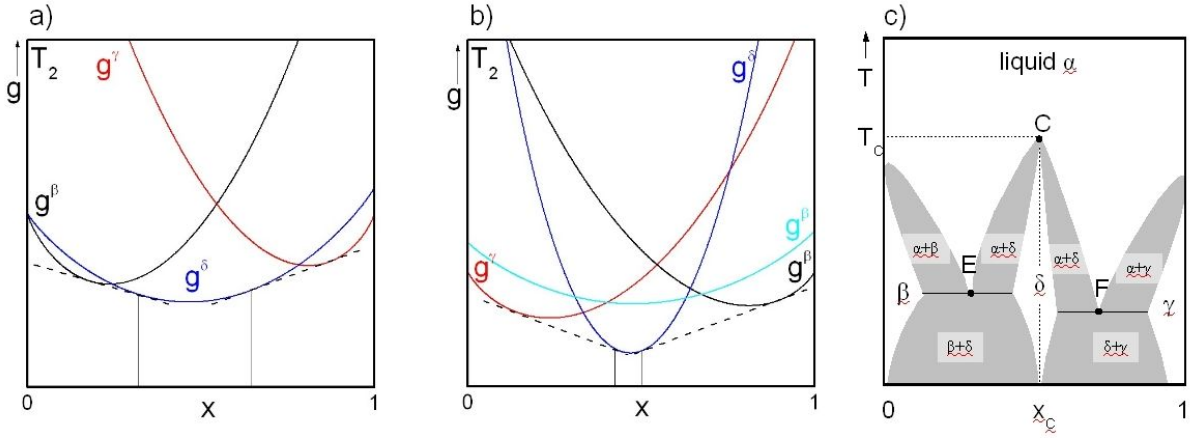

Figure 1.21: (c) Phase diagram for a binary system with an intermediate phase δ. For a derivation of the phase diagram the free energy $g^{\delta}(x)$ has to be considered. Depending on the form of $g^{\delta}(x)$ one can distinguish between an intermediate phase with a broad homogeneity range (a) and that with a narrow (b) homogeneity range of the intermediate phase.

Summary: congruent & incongruent melting

Combining the previous discussions of phase diagrams, two basic types of phase diagrams for binary systems with an intermediate phase can be given: one for *congruently* and one for *incongruently* melting compounds, respectively.

Fig. 1.22 (a) shows the phase diagram for a congruently melting compound. Here the solid and liquid phases of the same composition $x_{C,\gamma}$ are in equilibrium at a certain temperature T_C and transform without a change of composition. They are hence said to be congruently melting. In many cases the homogeneity range for both the intermediate phase and also the pure components are narrow and thus depicted as straight lines in phase diagrams

as for the γ - phase in this example. However, it is important to keep in mind that there is always a small homogeneity range. For crystal growth a congruently melting system is the most favorable since a melt with composition x_m directly crystallizes at T_C (the distectic point) into the solid γ - phase with the same composition. Transport problems due to different composition of melt and solid are avoided and usually fast growth rates can be applied. In reality deviations of the congruently melting composition and the stoichiometric composition can occur. Therefore even for congruently melting systems a detailed knowledge of the phase diagram is essential.

A compound that decomposes into a melt and another solid phase upon heating before its "intrinsic melting point" is reached, is said to melt incongruently. An example is shown in Fig. 1.22 (b). Here the γ - phase decomposes at the peritectic temperature T_P into a melt with composition x_P and the solid solution β. For crystal growth incongruently melting systems pose a major challenge. Theoretically the γ - phase can be grown from the stoichiometric melt with composition x_γ. In real compounds, though, the γ - phase forms at the interface between the solid β - phase and the liquid L. This leads to β - phase particles surrounded by the γ - phase. Diffusion in the solid γ - phase limits the compositional readjustment and extremely slow growth rates would be necessary. In metallurgical investigations the typical image resulting from peritectic melting shows island-like β - phase particles in a γ - phase matrix.

On the other hand, any melt with composition between x_E and x_P can be partly converted into the γ - phase without another solid phase. Following this approach is one of the main advantages of the vertical float-zoning technique. Positioning a pill with intermediate composition in the initial molten zone and feeding a stoichiometric rod theoretically allows a constant crystal growth of an incongruently melting system. This approach is known as the traveling solvent floating zone technique. Generally a reduced growth rate has to be applied for the growth of incongruently melting systems.

1.3.2 Crystallization

Following the introduction to phase diagrams, where thermodynamic relations between different phases and their stability were given, the following section provides an overview of the crystallization processes at the phase boundaries. This is the basis for the selection of the ideal process parameters and to an understanding and interpretation of the microstructure of the crystals grown as part of this thesis.

Except for perfectly congruent melting systems, there always exist concentration differences of the liquid and solid state ($c_L \neq c_S$) at the liquid - solid phase boundary of multicomponent systems. In equilibrium phase diagrams the concentrations of the liquid and solid phase are given by the horizontal isothermal crossing the liquidus and solidus line. The relation in thermodynamic equilibrium is given by the segregation coefficient:

$$k_0 = \frac{c_S}{c_L}. \tag{1.20}$$

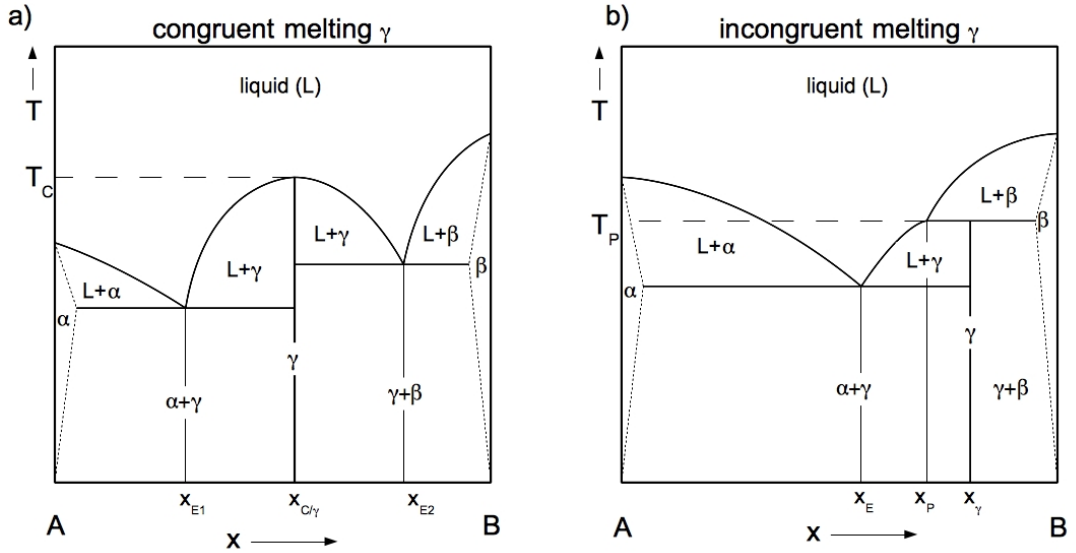

Figure 1.22: Basic types of phase diagrams for binary systems with an intermediate phase: (a) congruently melting and (b) incongruently melting. (a) In a congruently melting system the solid and liquid phases of the same composition $x_{C,\gamma}$ are in equilibrium at T_C and transform without a change of composition. They are hence called congruently melting. (b) In a incongruently melting system a compound (γ) decomposes into a melt (L) and another solid phase (β) upon heating before its "intrinsic melting point" is reached. The γ - phase is formed via a peritectic reaction.

During the growth process, which is a non-equilibrium process, the solid - liquid interface moves with a velocity v. Depending on k_0 being lower or larger than unity, a positive or negative concentration gradient in front of the interface builds up. For $k_0 < 1$ only a part of the components of the melt can be incorporated into the solid phase and an accumulation of the components in the melt next to the phase boundary is expected, depending on the rate of the interface movement. Assuming that diffusion is the only stirring mechanism in the vicinity of the phase boundary, a steady state concentration profile parallel to the growth direction is given by the diffusion coefficient D, the growth rate v and the concentration of the melt c_0 far from the interface [110]:

$$c_L(z) = c_0 \left[1 + \frac{1 - k_0}{k_0} \exp\left(-\frac{v}{D} z \right) \right]. \tag{1.21}$$

The characteristic profile is shown in Fig. 1.23 (a) for $k_0 < 1$. To anticipate the segregation within a growth process it is hence more reasonable to define an effective segregation coefficient k_{eff}. Here the melt composition far away from the phase boundary is regarded instead of the composition at the phase boundary where equilibrium conditions are assumed. Due to an incomplete mixing of the melt a diffusion boundary layer δ [111] is found at the liquid solid interface. Within this boundary layer, with a typical thickness $\delta = 100\mu\text{m}$, transport of matter is realized only by diffusion. In this case k_{eff} is given as [112]:

$$k_{\text{eff}} = \frac{c_S}{c_0} = \frac{k_0}{k_0 + (1 - k_0) \exp\left(-\frac{v\delta}{D} \right)}. \tag{1.22}$$

The effective segregation coefficient takes values $k_0 < k_{\text{eff}} < 1$ depending on the growth rate v, the diffusion coefficient D and the diffusion boundary layer δ. δ is a measure of the transition between dominant diffusive or convective transport. It can be influenced by different parameters like geometry, crystal rotation or electromagnetic fields.

The description of compounds with more than 2 components is more complicated since several segregation coefficients have to be considered for every component. Generally they also show an enhancement or depletion of the alloying elements in the melt next to the phase boundary which will lead to segregation within the crystal.

For the growth of single-phase single crystals from a melt or solution via directional solidification a morphologically stable solid - liquid phase boundary is essential. Morphologically stable means that the phase boundary, following disturbances, returns to its initial state. Supercooling of the melt in front of the phase boundary can lead to an unstable interface with cellular solidification, lateral concentration gradients and formation of second phases. The problem originates in the concentration distribution in the melt in front of the solid - liquid interface (see Eq. (1.21) and Fig. 1.23 (a)). Each position dependent concentration has its own liquidus temperature T_L which can be approximated by:

$$T_L(z) = T_m + m_L c_L(z). \tag{1.23}$$

T_m is the melting temperature of the pure component and $m_L = \mathrm{d}T_L/\mathrm{d}c_L$ the slope of the liquidus curve which is approximately linear in a narrow concentration range. Since the liquidus temperature is the lower limit of the single-phase melt stability, the local liquidus temperature $T_L(z)$ has to be compared with the temperature profile $T_{\text{exp}}(z)$ given by the experimental set-up. If $T_{\text{exp}}(z)$ falls below $T_L(z)$ other than at the phase boundary a constitutional supercooling of the melt occurs (see Fig. 1.23 (b)). Since the gradient of

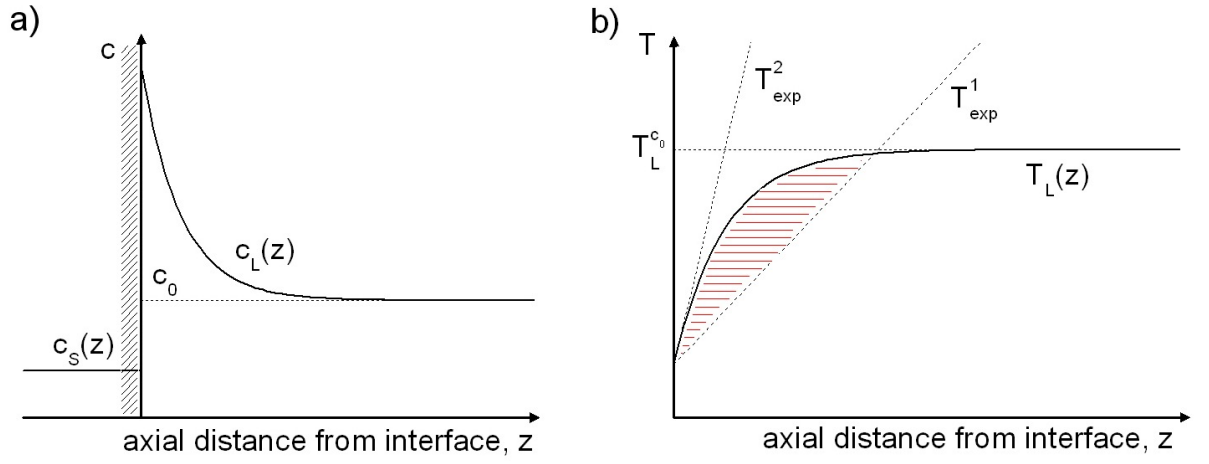

Figure 1.23: (a) A concentration gradient builds up in front of the solid - liquid interface for a segregation coefficient $k_0 < 1$ (see Eq. (1.21)). (b) Reduced liquidus temperature $T_L(z)$ in front of the interface due to the concentration gradient. If the temperature $T_{\text{exp}}(z)$, which is preset by the experimental set-up, lies below $T_L(z)$, the criterion of Tiller (see Eq. (1.24)), that prohibits constitutional supercooling, is violated.

the liquidus temperature is highest at the phase boundary, $z = 0$, the stability criterion that inhibits supercooling may be given as [113]:

$$\operatorname{grad} T_{\text{exp}} \geq \frac{\mathrm{d}T_L}{\mathrm{d}z} = m_L \frac{v c_0 (k_0 - 1)}{D k_0}. \tag{1.24}$$

The criterion for constitutional supercooling serves as a rough limit for the highest possible growth rate v that may be applied. Although the expression was derived from a diffusion controlled regime, the problem of constitutional supercooling even persists with intensive mixing by convection. In the vicinity of a solid phase convective motion is reduced to zero and diffusion is the only remaining process of matter transport. This is also the limiting reason for the low growth velocities in solutions compared to pure elements.

In the presence of constitutional supercooling some interface fluctuations may grow into the melt and cellular or even dendritic structures of secondary phases may form. An example is shown in Fig. 1.24 for rapidly cooled (as-cast) CoVSb. In the left picture the cellular structure can be seen macroscopically while with higher magnification in the right picture the dendritic structure is clearly visible. To avoid constitutional supercooling, following the criterion of Tiller (cf. Eq. (1.24)), a steep temperature gradient in the liquid near the solid - liquid interface together with an appropriate low growth rate have to be realized experimentally since the distribution coefficient k_0 and the diffusion coefficient D are fixed by the system.

A segregation coefficient $k_0 \neq 1$ generally leads to changes of the composition in the remaining melt. It shifts the equilibrium conditions at the phase boundaries and, hence, yields macroscopic compositional gradients in the solidified crystal. The zone melting technique, in comparison to normal freezing where the whole material is molten, reduces the problem of macroscopic component segregation. As sketched in Fig. 1.25 (a), in zone melting only a narrow zone c_L is liquid and made to pass along the ingot. Since only a small amount of the ingot is molten the compositional redistribution in the melt due to $k_0 \neq 1$ can be fast and steady state conditions can be reached after a few zone lengths

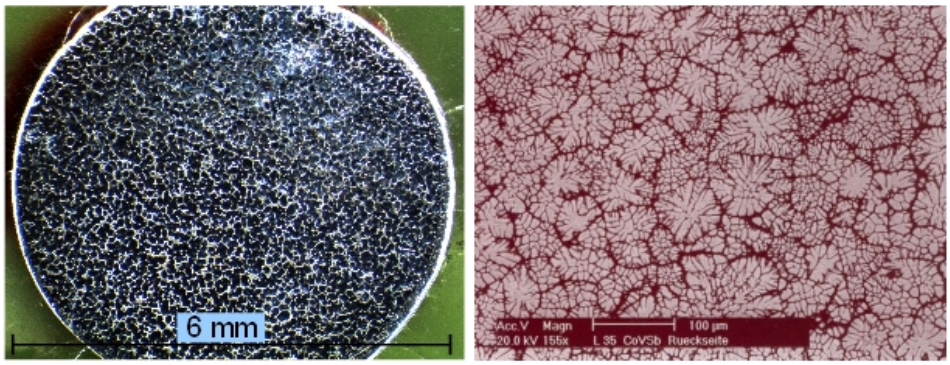

Figure 1.24: Dendritic structures of secondary phases in as-cast CoVSb due to constitutional supercooling as prepared in the context of this thesis. The left picture shows the macroscopic cellular structure while with higher magnification in the right picture the dendritic structure is clearly visible.

for k-values close to unity. The concentration distribution during (b) and after (c) the solidification process both for zone melting (c_{ZM}) and normal freezing (c_{NF}) are sketched in Fig. 1.25. The macroscopic distribution function for the solid phase concentration for zone melting can be calculated assuming a fixed volume of the molten zone with zone length l [114]:

$$c_S(z) = c_0 \left[1 - (1-k)\exp\left(-k\frac{z}{l}\right)\right]. \tag{1.25}$$

Depending on the growth rate and material transport conditions, either the effective segregation coefficient k_{eff} or k_0 from the equilibrium phase diagram may be taken for k.

Zone melting is hence an advantageous method for the growth of peritectic systems since a steady state condition with stable concentrations of the zone can be reached. Initially adding a zone with a different concentration (e.g. c_z in Fig. 1.25 (b)) between seed and feed material can result in crystal growth without the segregation process described above and thus to single crystals without concentration gradients. The method is generally referred to as the *traveling solvent* floating zone technique.

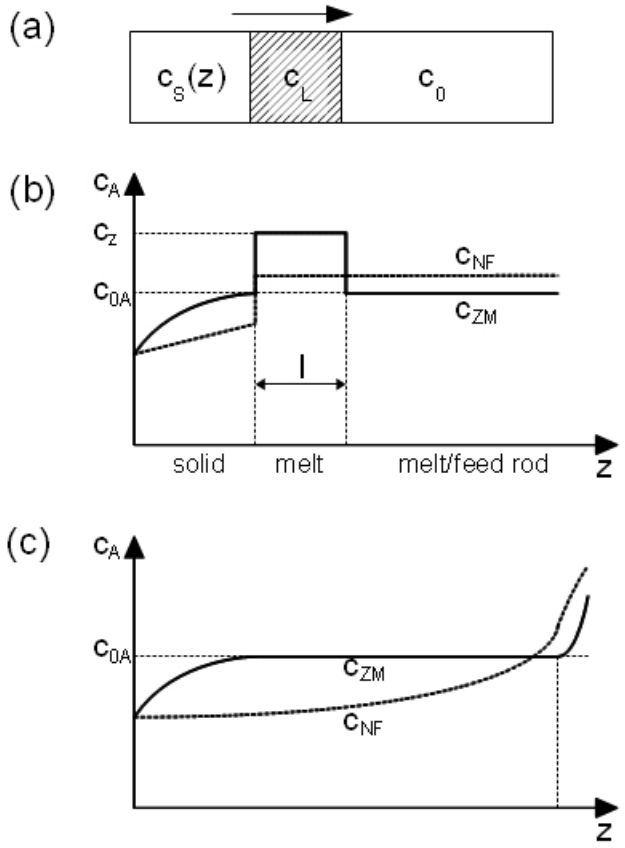

Figure 1.25: (a) In zone melting only a narrow zone with concentration c_L is molten and passed along the ingot. The concentration distribution along the growth direction z during (b) and after (c) the solidification process both for zone melting (c_{ZM}) and normal freezing (c_{NF}). Compared to normal freezing (with assumed ideal miscibility), the compositional redistribution in the melt is fast in zone melting, allowing to reach steady state growth conditions after a few zone lengths.

Zone melting is also used as a method to purify material, generally referred to as *zone refining*. It makes use of the fact that components with a segregation coefficient far from unity, $k \gg 1$, which is true for many impurities, accumulate in the molten zone and are passed towards the end of the ingot and therefore removed from the material. Several repetitions of the zone melting can lead to an enormous purification of the sample [115].

1.3.3 Vertical float-zoning

The vertical floating zone method was first introduced by Kec and Golay [116] in 1953 for the crystallization of high purity silicon. In this growth technique, as indicated by its name, a narrow molten zone is generated via local heating, optical or inductive, between two vertically mounted, free standing rods. Growth proceeds by moving the liquid zone along the rod, either by moving the rod or the heater unit. Single crystal growth either results from grain selection or from the use of a seed crystal. The diameter of the grown crystal can be varied by moving the two rods together or apart. A reduction of the diameter at the beginning of the growth (necking) supports the grain selection. Generally growth is performed from bottom to top and for good mixing of the melt the rods are counter-rotated. An image of the molten zone of Mn_3Si taken during growth in an image furnace is shown in Fig. 1.26 (a).

An advantage of this method is that it does not require any crucible. It inhibits the contamination through crucible material and eliminates any disturbances of crystal growth through nucleation at the crucible walls. In addition, zone refining occurs during growth with every passing of the zone through the rod. It furthermore offers the possibility to approach peritectic systems via the vertical traveling solvent floating zone method as described in the previous section. A drawback of the vertical floating zone method is that it is fairly elaborate, since appropriate starting rods with a homogeneous shape have to be prepared prior to growth. In general, the vertical floating zone crystal growth method is used for the growth of high purity single crystals.

An important factor for the float-zoning technique is the stability and shape of the molten zone. The liquid is only held in position by surface tension and the stability of the zone depends on the energy of the liquid-vapor interface and the density of the melt. The length and diameter of the molten zone is therefore stable up to an upper limit. Since experimental set-up, mechanical stability of the rotation of the rods, the rotation speed itself and material specific parameters play an important role for the stability, an exact calculation is very challenging. A rule of thumb states that the zone looses its stability if the zone length is larger than its perimeter [117]. Concerning the shape of the molten zone, a meniscus-like shape appears due to gravity (see Fig. 1.26 (a)). The swelling on the lower side is found to be less pronounced with the growth direction from bottom to top resulting in a more stable zone. For rod diameters of 6 mm, as used in this thesis, following the general rules to achieve a stable zone as mentioned above are sufficient, since mechanical instabilities due to vibrations, growth rate changes and misalignment of the rods interfere the stability far more.

For the growth of large single crystals the shape of the solid - liquid interface plays a decisive role. A concave shape of the solid - liquid interface allows parasitic (disoriented) grains to grow towards the middle of the crystal and prevents the growth of large single crystals. With a convex shape of the interface parasitic grains grow outwards and grain selection in the center allows for large single crystals throughout the cross section of the rod. An image of the preferred convex shape of the solid - liquid interface is shown for a quenched zone of Mn_3Si in Fig. 1.26 (b). However, this is not an ideal example as there is a step-like feature superimposed on the convex shape on the lower interface.

The shape of the interface depends mainly on the method of heating and the heat transfer within the molten zone. Inductive radio-frequency (r.f.) heating can lead to a slightly concave interface curvature in the outer part of the growing crystal [118]. This is caused by the finite penetration depth of the r.f. electromagnetic field which acts as a heat source in the melt. Furthermore the electromagnetic convection, which transports the hot melt from the surface to the inner part, can support this effect. In optical heating the radiation generates the heat immediately at the surface, favoring a convex shape of the interface. This is supported by the so called Marangoni convection that drives the hot melt along the surface towards the outer part of the crystal-melt interface [118].

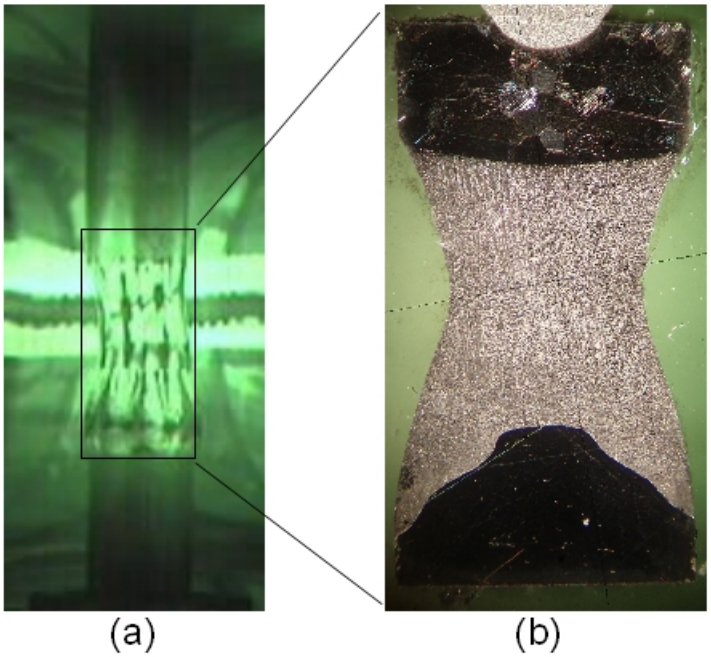

Figure 1.26: (a) Image of a molten zone of Mn_3Si taken during growth in our optical image furnace. The diameter of the molten zone is reduced in comparison to the rods. The horizontal bright lines on the back are reflections of the filaments of the lamps. (b) Polished cut through the quenched zone (as indicated by the rectangle) of Mn_3Si. Optical investigation of the quenched zone provides important information on the growth conditions. The lower interface (single crystal - molten zone) shows the desired convex shape (although a smoother shape would be ideal). At the top end (in the feed rod) a poly-crystalline grain structure is visible.

For metallic compounds, as studied in this thesis, the heat transfer is dominated by thermal diffusion. This may be deduced from the small Prandtl[2] number typical for metallic melts. Calculations [119] for diffusion dominated optically heated systems show a convex profile of the solid - liquid interface for temperatures slightly above the melting temperature. With further increasing temperature of the melt the profile of the interface changes to a concave form.

To sum up, the basic rules for crystal growth with the vertical floating zone method in an image furnace may be given as follows:

- It is advantageous to grow from bottom to top with a temperature slightly higher than necessary to melt up a zone throughout the rod diameter.
- It is important to have a mechanically stable system with well aligned rods.
- The heat transfer should be focused to a small area, leading to a steep temperature gradient necessary to avoid constitutional supercooling.
- The growth parameters should be changed as little as possible throughout the growth process once equilibrium has been reached.

[2]The Prandtl number k_{Pr} is a material specific measure of the relation between convection driven and diffusion driven heat transport.

Chapter 2

Single crystal growth

A central part of this thesis concerned setting up a laboratory for crystal growth of large, high-purity single crystals with an image furnace. The experimental equipment developed for both the preparation of starting rods and single crystal growth is described in the first part of this chapter. The different methods used for the metallurgical characterization of the samples grown are described in the second part. In the last part of this chapter an overview is given of the crystals grown as part of this thesis.

2.1 Crystal growth set-up

When this thesis started a four mirror image furnace from CSI (Crystal Systems Incorporate, Japan) was available for crystal growth with the vertical floating zone technique. Prior to setting this image furnace up in our laboratory it was modified to be UHV-compatible by Christian Pfleiderer and collaborators at the University of Karlsruhe, where preliminary tests were carried out. The modified image furnace will be described in detail in the second part of this section. For crystal growth with the image furnace the preparation of appropriate starting rods is necessary. For this purpose a rod casting furnace (RCF) based on a Hukin crucible [120] was developed as part of this thesis and the diploma theses of Wolfgang Münzer and Andreas Bauer. The rod casting furnace will be described in the first part of this section. A second furnace for the purification of the starting elements and the preparation of starting rods for the image furnace was set up in the form of a horizontal cold finger system (HCF), as presented in the third part of this section.

An overview of the individual steps necessary for crystal growth with the image furnace is given in Fig. 2.1 and may be summarized as follows:

(i) Preparation of correct weight of clean starting material. This includes chemical etching both for purification and mass adjustment, casting of pure starting elements (e.g. Mn or Fe) with the RCF and, for mass adjustment, simple mechanical breaking of the material (e.g. Si).

(ii) Casting of homogeneous rods with the RCF or the HCF.

(iii) Assembling of the rods in the image furnace and float-zoning.

(iv) Metallurgical characterization of the crystals.

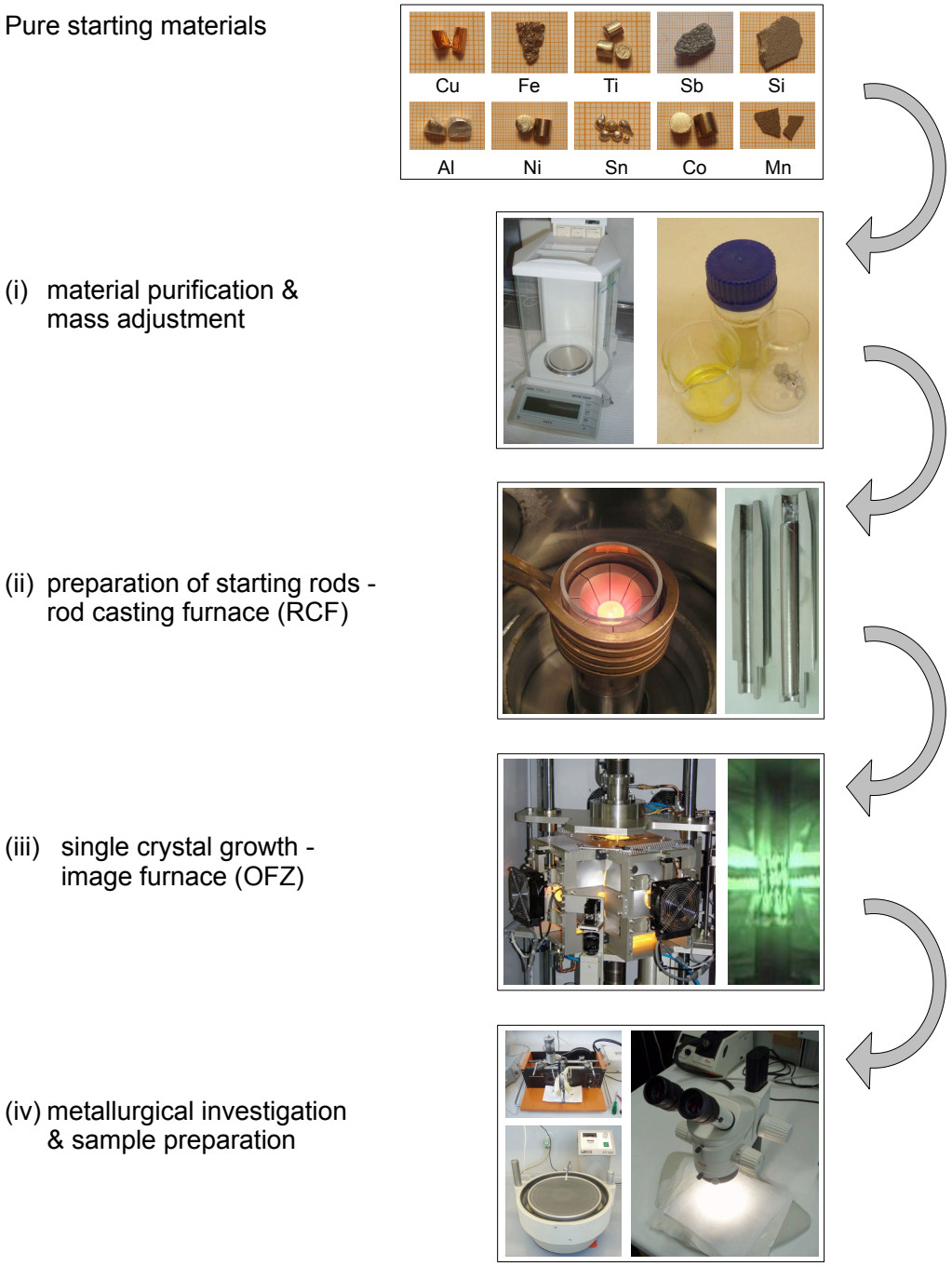

Figure 2.1: Summary of the various steps involved in crystal growth of intermetallic compounds with vertical float-zoning.

2.1.1 Rod casting furnace (RCF)

The aim of the rod casting furnace is the preparation of homogeneous metallic rods of a given composition using a water-cooled and mold. For this purpose a so-called Hukin crucible was used [120]. A cross section of the crucible is shown in Fig. 2.2 (a). The material is molten in the upper part of the crucible (see Fig. 2.2 (b)) and cast into the mold centered in the crucible by pulling down a water-cooled rod. An example of a Mn_3Si ingot cast with the RCF is shown in Fig. 2.2 (c). The advantage of this method is that cooling with water keeps the temperatures of the copper crucible, the casting mold and the pulling rod low. Hence a reaction of the crucible with the melt is suppressed and very pure, homogeneously formed rods may be cast. In addition, radio frequency (RF) inductive heating with an adjusted copper coil leads to an almost levitating melt, as shown in Fig. 2.2 (b), which reduces the contact of the melt with the crucible. Since inductive heating is a fairly soft way of melting and since all casting processes are conducted in an overpressure (∼1.5 bar) inert gas atmosphere, evaporation of material during the melting process is kept to a minimum.

To ensure good heat conduction, the Hukin crucible and the pulling rod are made of copper. The Hukin crucible is composed of eight sections to promote the coupling of the RF to the sample and to reduce eddy current heating of the crucible. Each section is water cooled. Excellent water circulation exists in each section. The crucible is bolted to a stainless steel counterpart (providing the water supply) via a fine pitch thread and sealed with two Viton O-rings as indicated by the black dots in Fig. 2.2 (a).

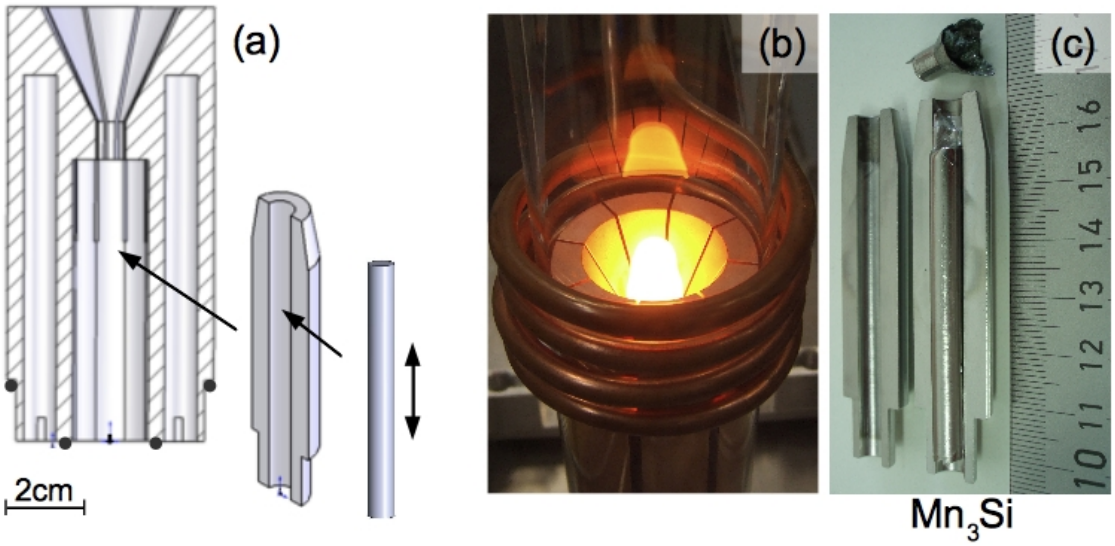

Figure 2.2: (a) Cross section of the water-cooled Hukin crucible. The mold (⌀ 6 mm, length 70 mm) is centered within the crucible and the melt is cast by pulling down the water-cooled pulling rod. The crucible is composed of eight sections, each with a borehole for water-cooling, to reduce eddy current heating of the crucible. The black dots indicate the two O-rings that seal the water-cooling. (b) Image of a levitating melt. (c) Image of a Mn_3Si ingot in a stainless steel casting mold. Shown in the upper part is "dirty" material that remained in the crucible.

The casting mold with a length of 70 mm and an inner diameter of 6 mm is made from two halves and hold together by a ring at the lower end. In later models the stability of the molds was enhanced by positioning additional sticks through the sides of both halves. Both copper and stainless steel were used as material for the casting molds.

RCF - initial design

For the preparation of starting rods with the Hukin crucible a rod casting furnace was set-up. To start with, the Hukin crucible, the support providing the water connection and the water-cooled pulling rod were purchased from Cyberstar S.A.. In addition, the support (made from stainless steel) was equipped with a O-ring seal to connect the quartz tube (⌀ 50 mm) effectively providing the sample chamber. This set-up was inspired by a similar apparatus used by the group of Günter Behr at the IFW in Dresden. For our system two additional requirements had to be fulfilled: (i) The RCF had to be movable, since in the beginning the RF-generator (Hüttinger TIG, 40 kW, 300 kHz) of the crystal laboratory of the Physics Department of TUM was used. (ii) To achieve the highest purity possible, the set-up should allow a conversion to an UHV-compatible system at a later point of time.

A sketch of the central components of the casting furnace is shown in Fig. 2.3. A photograph of the initial version of the rod casting furnace is shown in Fig. 2.4. The frame of the RCF is built of ITEM elements and set on wheels. The total width and height are 85 cm and 195 cm, respectively. For the sake of clarity the set-up of the RCF is discussed in two parts: the *gas handling stage*, that consists of fixed components providing the pure inert gas atmosphere, and the *rod casting stage*, that holds linear moveable parts participating in the actual casting process.

The components of the gas handling stage are mounted to the top of the frame and connected via metal sealed stainless steel crosses. Shown in the top part of Fig. 2.4 are from left to right: (a) a turbo pump (Leybold Turbovac 50), (b) an all-metal sealed edge valve (VAT), (c) an electronic pressure gauge (Leybold Ionivac), and (d) an overpressure manometer. The inert gas atmosphere may be provided via the gas purification system (e). An oil free scroll pump (Varian SH110) (m) is used as a roughing pump. The gas purification system is composed of all-metal valves (Swagelok) and a titanium getter furnace (Omni40, NuPure). It permits either a purification of the Ar-gas with the titanium getter or direct filling of the system with the gas as is. At its operating temperature of 400° C the getter furnace improves the purity of the Argon gas ($\sim$6N) as supplied by the gas cylinder to $\sim$9N. The whole gas handling stage is all-metal sealed and bakeable. The sample chamber made of a quartz tube connects the gas handling stage with the rod casting stage. The quartz tube is sealed via two Viton O-rings (f).

The rod casting stage (see Fig. 2.3) consists of the crucible support (h), which provides the cooling-water for the Hukin crucible, and a linear sledge (RK Rose+Krieger) (k), which includes the pulling rod (i). The pulling rod is water-cooled and consists of a steel tube (⌀ 12 mm) with a copper tube (⌀ 6 mm) hard-soldered to the top. Its steel part is guided and sealed by means of a Viton O-ring (j), which is mounted to the bottom of the crucible

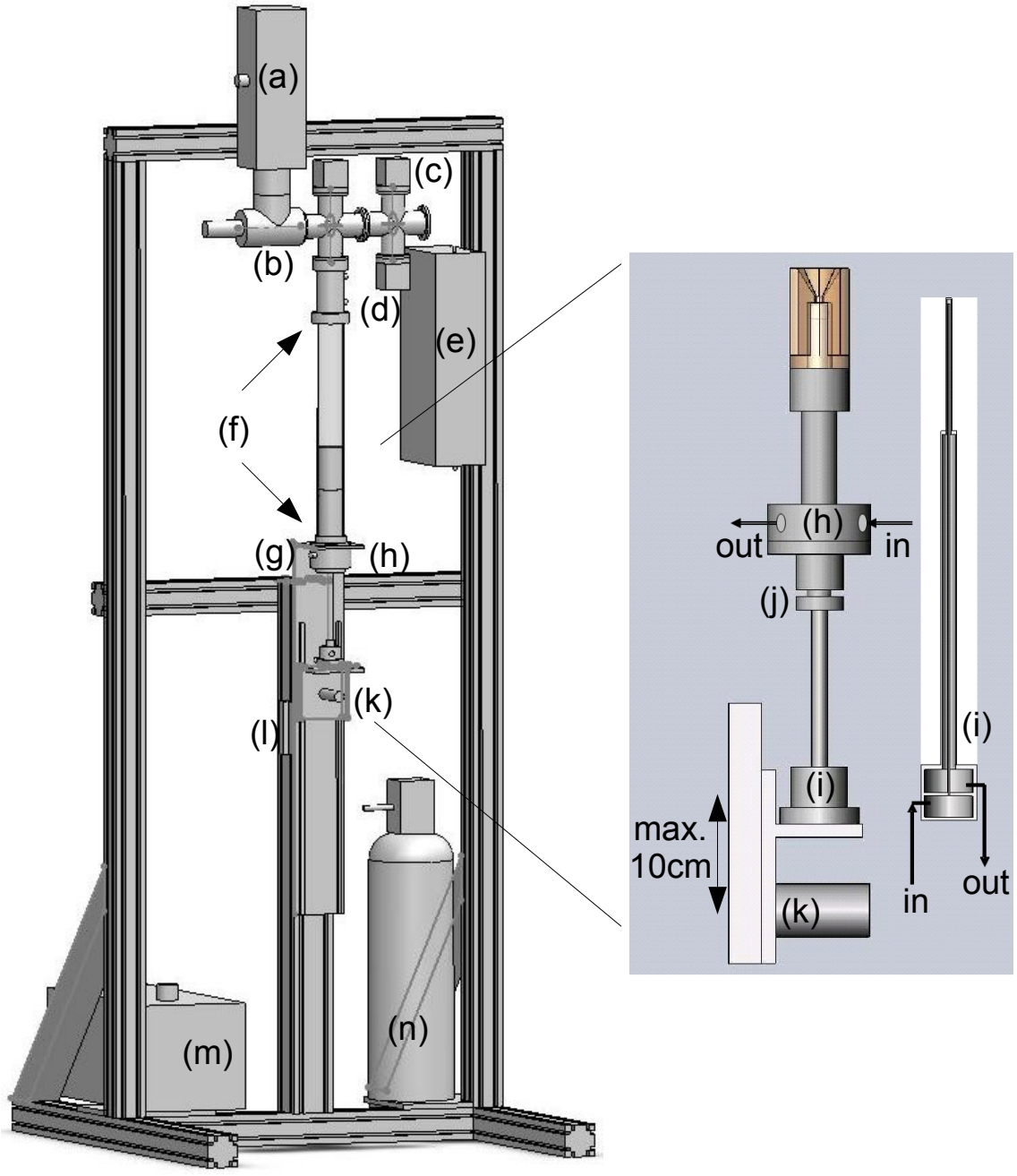

Figure 2.3: Initial set-up of the rod casting furnace (RCF). Components of the gas handling stage: (a) turbo pump; (b) UHV edge valve; (c) over-pressure manometer; (d) pressure gauge; (e) gas purification system; (f) Viton O-rings; (m) roughing pump; (n) Argon gas cylinder with pressure reducing valve. Components of the rod casting stage (see also inset on the right): (g) center plate retaining the crucible support (h); (j) O-ring seal; (k) linear sledge with water-cooled pulling rod (i); (l) electrically driven linear spindle drive. The direction of the cooling water of both the crucible support and the pulling rod are indicated by *in* and *out*.

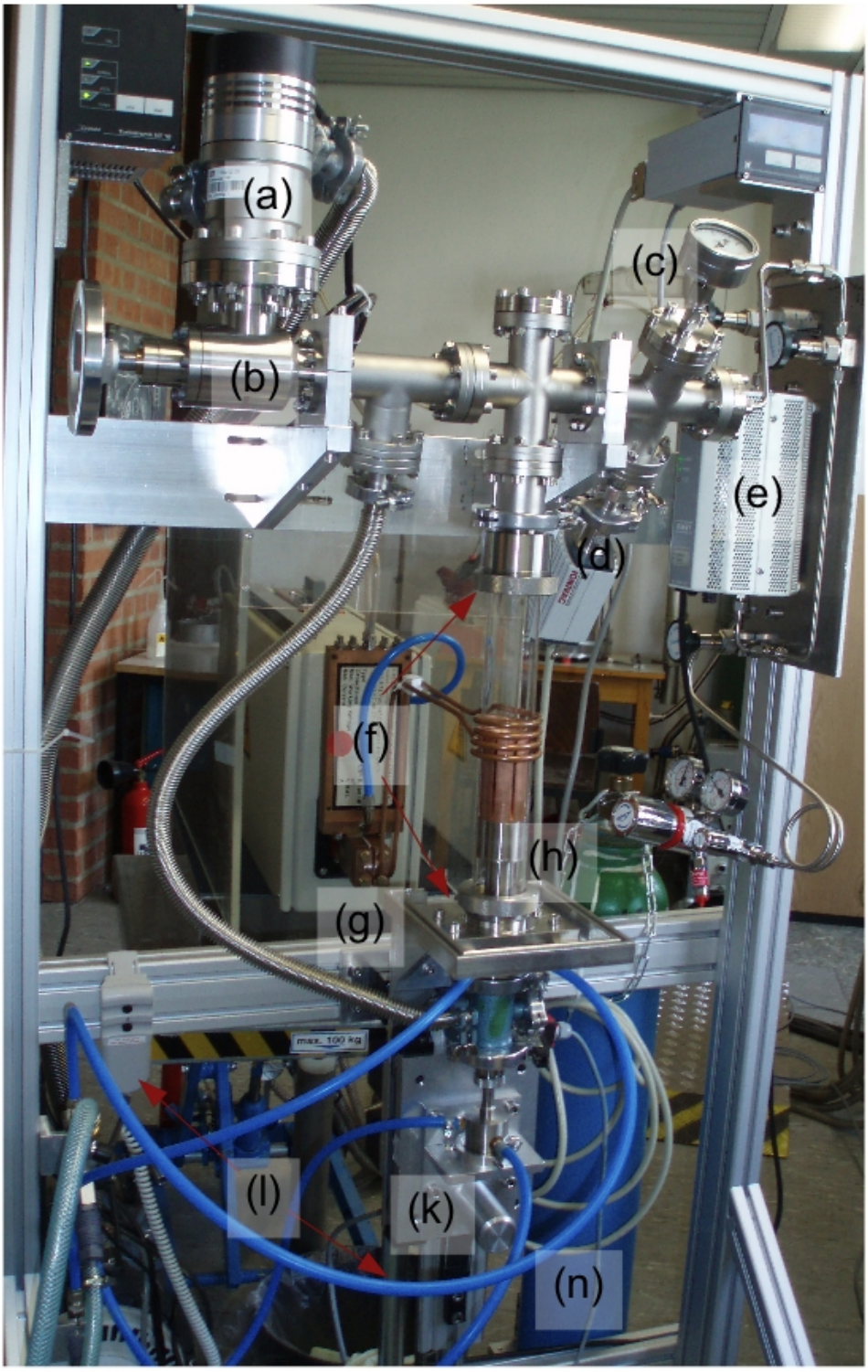

Figure 2.4: Photograph of the initial version of the RCF. Components are labeled consistent with Fig. 2.3. gas handling stage: (a) turbo pump; (b) UHV edge valve; (c) over-pressure manometer; (d) pressure gauge; (e) gas purification system; (f) O-ring seal; (n) Argon gas cylinder with pressure reducing valve. rod casting stage: (g) center plate; (h) crucible support; (k) linear sledge; (l) electrically driven linear spindle drive with remote control. Cooling-water is supplied by the blue hoses.

support. The linear sledge with the pulling rod may be translated vertically by 10 cm and lowered manually during the casting process. The linear sledge and the crucible support (via the center plate (g)) are mounted to an aluminum plate, which is connected to an electric spindle drive (RK Rose+Krieger) (l). The entire rod casting stage may be lowered by 30 cm, necessary for mounting and unmounting of the crucible and casting material.

The cooling water of the Hukin crucible and the pulling rod may be shut off and the circulation emptied with compressed air prior to unmounting the Hukin crucible. The gas handling stage is attached with an adjustable aluminum holder to the ITEM frame in order to allow a precise alignment of the gas handling stage. This is necessary in order to avoid mechanical stress on the sealed quartz tube. For inductive heating a coil with 4 turns fitting tightly around the quartz tube was made from a copper tube and connected to the RF oscillating circuit. For security reasons a removable plexiglass shielding may be positioned on the center plate surrounding the quartz tube and the RF coil.

The casting process of a rod may now be summarized as follows. The Hukin crucible with the mold is bolted to the steel support. The sledge with the pulling rod is locked in a position ensuring that the top of the pulling rod seals the trough of the Hukin crucible. The O-ring seal that guides the pulling rod is fastened. Sample material is put into the crucible. The quartz tube is inserted and the rod casting stage moved up until both ends of the quartz tube may be sealed. The system is vacuum pumped and filled with purified Argon gas up to a pressure of ~ 1.5 bar. The RF generator is switched on with the water-cooling circuit open. The power is controlled manually and raised slowly until the material melts. By further raising the power the shape of the melt may be changed from ball-like to an ellipsoid form in vertical direction. Prior to casting a rod, the material is remelted several times for proper homogenization, where the pill may be flipped over with the pulling rod. Having ensured a homogeneous melt, the O-ring at the pulling rod is loosened and the sledge with the pulling rod quickly lowered manually by $\sim$7 cm, allowing the melt to flow into the mold. After several minutes the water-cooling is stopped and cleared with compressed air. The sealing of the quartz tube is unlocked, the rod casting stage lowered, and the Hukin crucible unfastened. Now the rod may be taken from the mold.

During the casting process usually not all material flows into the mold, but parts of it remain in the crucible (see Fig. 2.2 (c)). This may be advantageous, since islands of oxidized material tend to float on the melt and hence "dirty" material remains in the crucible. We found, for example, that pure manganese, which oxidizes rapidly at normal atmosphere, stays shining and clean if it is cast to a rod.

With the RCF so far rods for more than 50 float-zoning growths were prepared. Prior to filling the system with inert Argon gas a vacuum of $\sim 10^{-6}$ mbar was reached. In order to optimize the system to be UHV-compatible, the Viton O-ring seals had to be replaced to be all-metal sealed.

RCF - first modification

In a first modification to turn the system all-metal sealed the Viton O-rings of the quartz tube and the pulling rod were replaced. An overview over the changes is given in Fig. 2.5. The quartz tube was replaced by a stainless steel recipient. At the top of the recipient a metal bellows serves to retain flexibility. At the bottom, the recipient is metal sealed directly onto a large center stage. The induction coil is connected to an UHV-tight RF feed-through (Hositrad). To improve the homogeneity of the magnetic field distribution the induction coil is made of copper tube with a square cross section. Three windows provide optical access. Due to its weight ($\sim 30\,\mathrm{kg}$), the recipient is attached with two spindles to the top of the ITEM frame. The crucible can be accessed in the usual way by lowering the center stage via the electric spindle drive. In addition, the center stage and the bottom end of the crucible contain a slot, that allows to mount a glove bag for loading of the starting materials under an inert gas atmosphere.

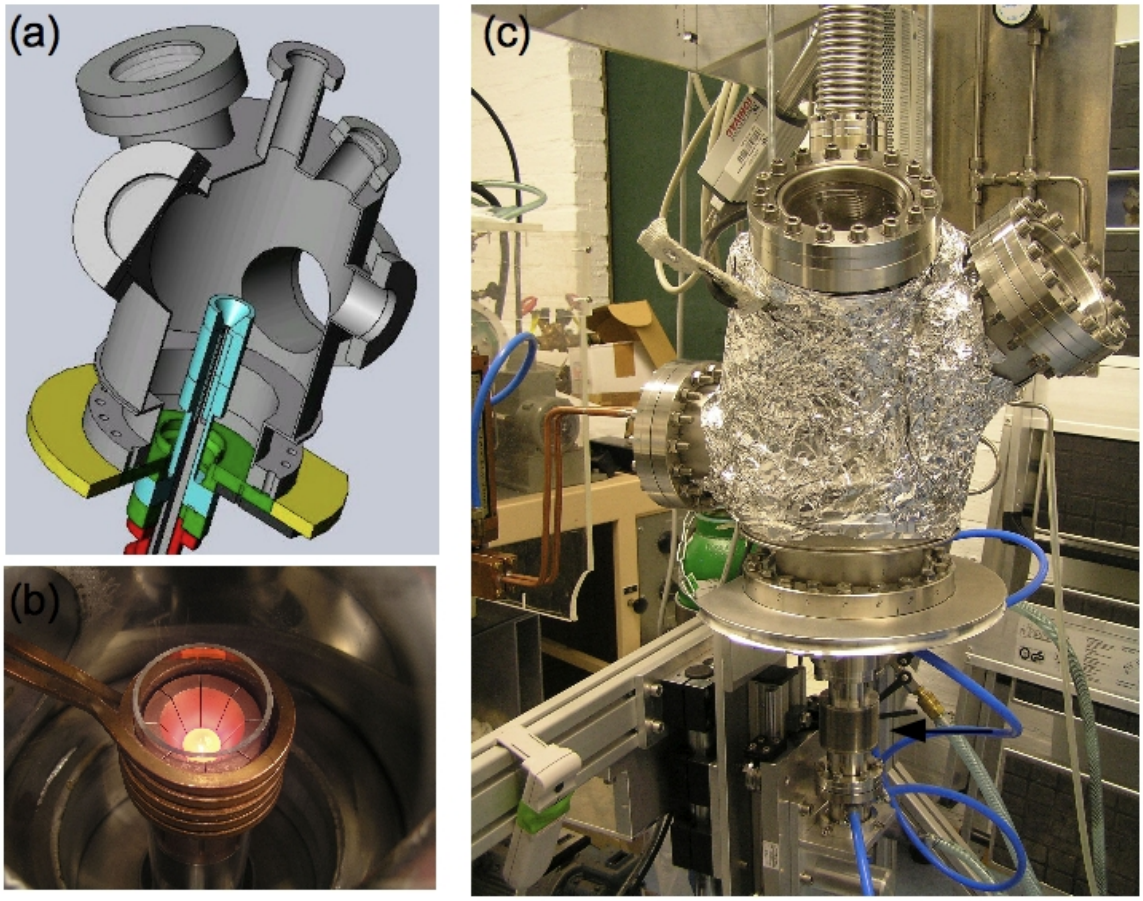

Figure 2.5: First modification of the RCF to be all-metal sealed. (a) Schematic drawing of the stainless steel recipient and the modified center stage (taken from Ref. [95]). (b) Photograph of the Hukin crucible during a casting process. The induction coil is fixed inside the recipient. The quartz cylinder electrically separates the coil from the crucible. (c) Photograph of the modified RCF with a heat tape wrapped around it covered by the aluminum foil. The flexible diaphragm bellows that replaced the O-ring seal of the pulling rod is marked by the black arrow.

The squeeze-type sealing of the pulling rod was replaced by a flexible diaphragm bellows (COMVAT, Switzerland; indicated by the arrow in Fig. 2.5 (c)). The diaphragm bellows is all-metal sealed with two adapters both at the bottom of the pulling rod and the crucible support on top. It allows a motion of 100 mm, which is sufficient for the vertical movement of the pulling rod during the casting process.

The changes incurred allow to bake the system, which leads to an improved vacuum of $\sim 10^{-7}$ mbar. The modified set-up of the RCF was used successfully for casting of the rods until now. A detailed technical description of the changes are given in the diploma thesis of Wolfgang Münzer [95].

RCF - final set-up

In a final effort to turn the RCF into an all-metal sealed system, the Viton O-rings of the water-cooling of the Hukin crucible had to be changed. To seal the cooling water against the inside and the outside, a stainless steel base plate was constructed, which is permanently connected to the copper crucible. Bolting this component from the outside to a modified crucible support allows to use two standard copper gaskets simultaneously. The main technical difficulty thereby turned out to be the connection between the copper crucible and the base plate, due to the limited space available. Several attempts to weld or hard solder this section failed due to a thermal deformation of the components. As final solution a UHV-leaktight connection was accomplished by Josef Remmel at the Forschungszentrum Jülich (Zentralabteilung Technologie) by means of high temperature vacuum soldering. A detailed technical description of the changes is given in the diploma thesis of Andreas Bauer [78]. The final modifications are currently implemented.

RCF - additional equipment

A fine blasting unit (Renfert - basic classic) was purchased in order to clean the crucible and the casting molds after each casting process. The small size of the sandblasting material (70-250 µm) allows to remove gently the remainders of the casting process even of parts that are not easily accessible.

Recently, a RF-generator (CELES MP 50kW) was purchased for the use with both the RCF and the horizontal cold finger. The generator operates at frequencies in the range 100 to 400 kHz at a maximum power of 50 kW. The oscillator was positioned on a movable table. It may be easily transferred from the RCF to the horizontal cold finger (HCF). An image of the oscillator and the induction coil as used with the HCF is shown in Fig. 2.11.

A pyrometer (Infratherm IGA 140-L) with an indium-gallium-arsenide detector allows a contact-free temperature measurement in the range 350 to 2500°C. Mounted to the small window of the metal recipient of the RCF it permits the measurement of the temperature of the ingot. Furthermore the pyrometer is used for a temperature control of annealing processes in the horizontal cold finger.

2.1.2 Optical float-zoning furnace (OFZ)

Single crystal growth was carried out with an image furnace for vertical float-zoning as described in the introduction [1.3.3]. The 4-mirror image furnace from CSI (model FZ-T-10000-H-III-VPS, Crystal Systems Incorporate, Japan) had been modified to be UHV-compatible by Christian Pfleiderer and collaborators at the University of Karlsruhe. In combination with an ultra-pure gas atmosphere this served to grow intermetallic single crystals under the conditions of highest purity possible.

In fact, a reduction of oxygen impurities in the system had a vital influence on the growth conditions of many intermetallic compounds. Oxidation during the growth process leads to oxide islands floating on the molten zone. Interaction of these oxide islands leads to disturbances of the molten zone and, in the worst case, to a dripping-off of the zone. With optical heating, the formation of oxide layers on the zone may furthermore reduce the heat transfer to the rod causing an inhomogeneous temperature distribution.

In the following sections the basic properties of the image furnace will be introduced and the modifications of the OFZ towards UHV-compatibility will be described.

Basic properties

A photograph of the modified furnace as used for crystal growth in this thesis is shown in Fig. 2.6 (a). Four horizontally arranged elliptical mirrors focus the light of halogen lamps onto a single spot on the sample. The use of four lamps and mirrors reduces the temperature gradient along the periphery of the zone. Halogen lamps of different power (150 W - 1000 W) may be mounted for melting temperatures up to 2200°C. Lamps with higher power have a larger focus due to their larger filaments. This leads to smaller temperature gradients at the rods. It is hence preferable to mount the smallest lamps possible that allow to melt the material. The power of the lamps is controlled via an Eurotherm control unit mounted in a control rack next to the furnace.

The molten zone is passed through the rods by a vertical movement of the mirror stage. A growth rate of 0.1 - 18.76 mm/h may be used. In addition, the upper rod may be moved independently by the same velocity, allowing to control the material supply and, hence, to modify the diameter of the molten zone. Both the upper and lower rod may be rotated individually with a rotational speed of up to 56 rpm in both directions. The rotational and translational velocities are controlled manually and displayed at the control rack, as well as the positions of both the mirror stage and the upper rod. During the growth process the molten zone is monitored via a CCD camera, which is connected to a small monitor in the control rack and to a computer. This allows to optically control and record the shape of the zone (see Fig. 2.7 (c)).

The seed and feed rod are mounted and aligned in the sample holders by means of four grub screws, as shown in Fig. 2.7 (a). The lower sample holder, surrounded by a drip-off protection, is directly bolted to the rotating spindle. The upper holder is attached by a hook, which is bolted to the upper spindle. This offers the necessary flexibility of the upper

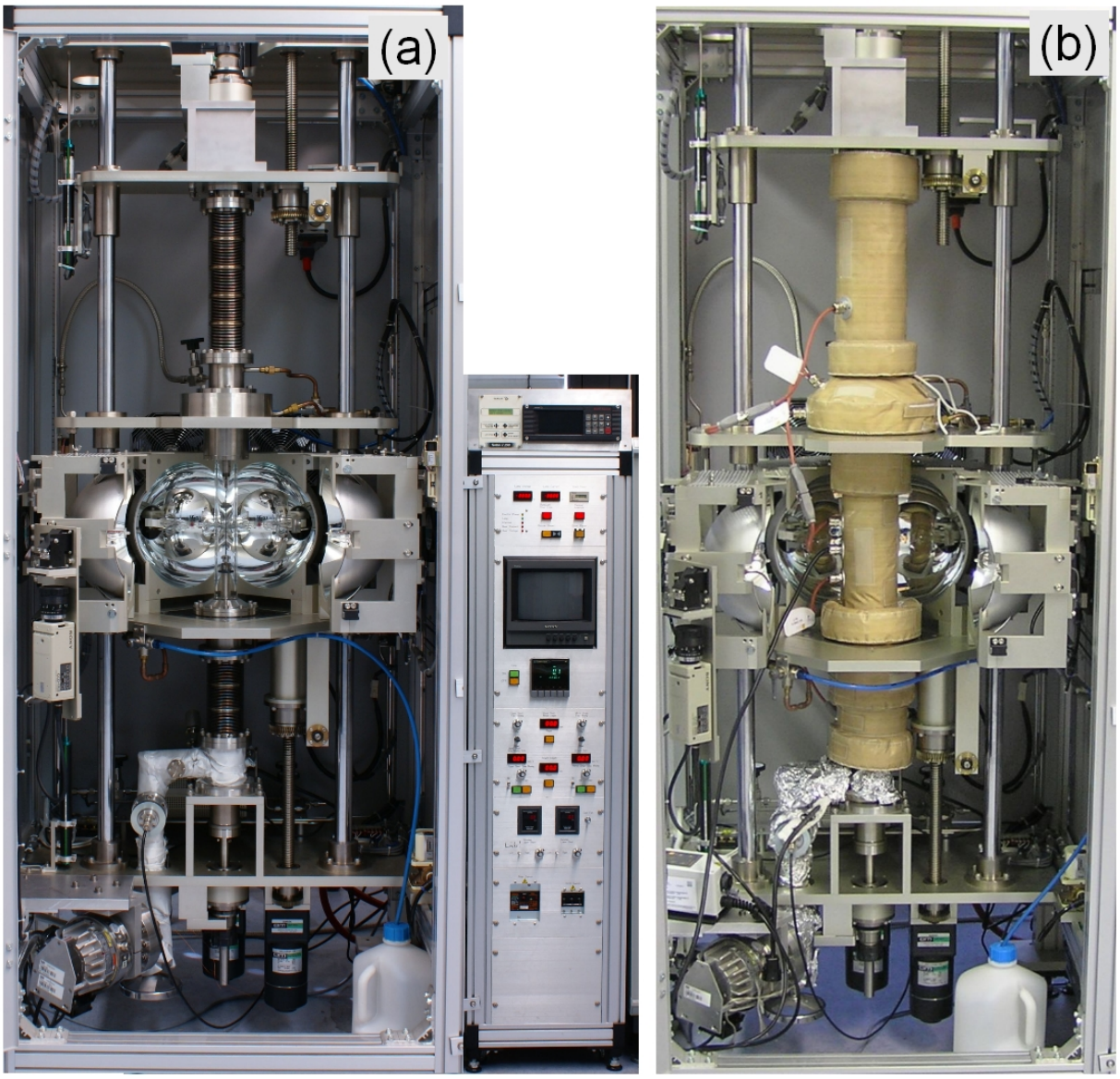

Figure 2.6: (a) Modified UHV-compatible image furnace with control board and (b) while baking out with heating jackets.

rod. Furthermore, the hook may be disconnected, which is necessary when unmounting crystals with a quenched last zone. The grub screws allow a precise alignment of the rods. A good vertical alignment of the rods is important for a homogeneous temperature distribution around the zone and high stability.

Prior to the growth process, the system is evacuated with a turbo pump (Varian, TV301 NAV), which is connected to the system with an all-metal valve (VAT). A scroll pump (Varian) serves as a roughing pump. Evaporation during growth may be reduced by means of an inert Argon gas atmosphere (up to 10 bar). A reduction of evaporation is essential since any material covering the quartz tube reduces the amount of heating.

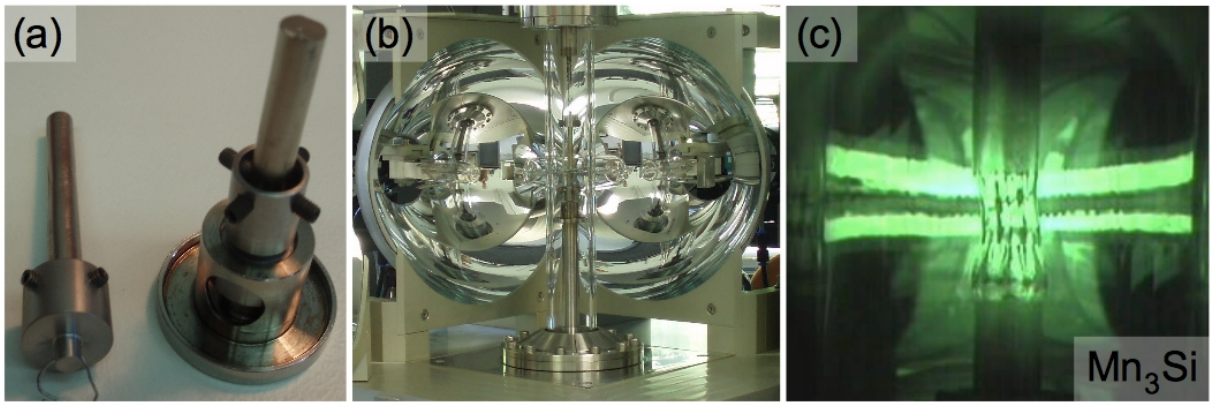

Figure 2.7: (a) Molybdenum sample holders for feed (left) and seed rod (right). (b) Mirror stage of the OFZ. Feed and seed rod sample holders are mounted to the spindles within the quartz tube. (c) The growth process is recorded by a CCD camera. The molten zone is kept by the surface tension in between the solid seed and feed rod. The green color is due to a strong filter placed in front of the camera. The horizontal striped lines are an image of the filaments of the lamps. Their horizontal position allows an alignment control of the lamps.

Conversion to UHV-compatibility

In the following the modifications of the image furnace will be described in further detail. In the last part of this section additional equipment, which is necessary to obtain a high purity inert gas atmosphere, will be summarized. In order to provide a better understanding of the modifications an overview of the original (I) and modified (II, III) version of the image furnace is shown in Fig. 2.8.

Zone melting of the image furnace takes place in a quartz tube. In the original set-up the quartz tube was connected to the image furnace with two Viton O-rings. These O-rings were replaced by glass-metal seals using a "helicoflex" (Garlock, Helicoflex HLV240) metal O-ring. The associated modifications are denoted as (a) in Fig. 2.8. The straight quartz tube was replaced by one with broadened, cone-like endings. A cross section and an image of the adapted quartz tube is shown in Fig. 2.9.

The lower part of the quartz tube is pressed onto the "helicoflex" seal with a metal ring. This metal ring is composed of two components that are kept in position by stainless steel pins and kept together with a metal support ring. Between the metal jacket and the quartz tube a teflon washer is used to reduce local strains. The sealing is attached with 16 screws directly to a stainless steel plate mounted to the bottom of the mirror stage.

The upper glass-metal seal follows the same design principle. Here the quartz flange is surrounded by a 2-component metal jacket which is kept together with two metal rings. The upper quartz-metal seal is connected permanently; only the metal bellows is detached from the image furnace for sample changes. The short bellows of the adapter serves as strain relief between the main frame of the furnace and the quartz tube under changes of pressure or temperature.

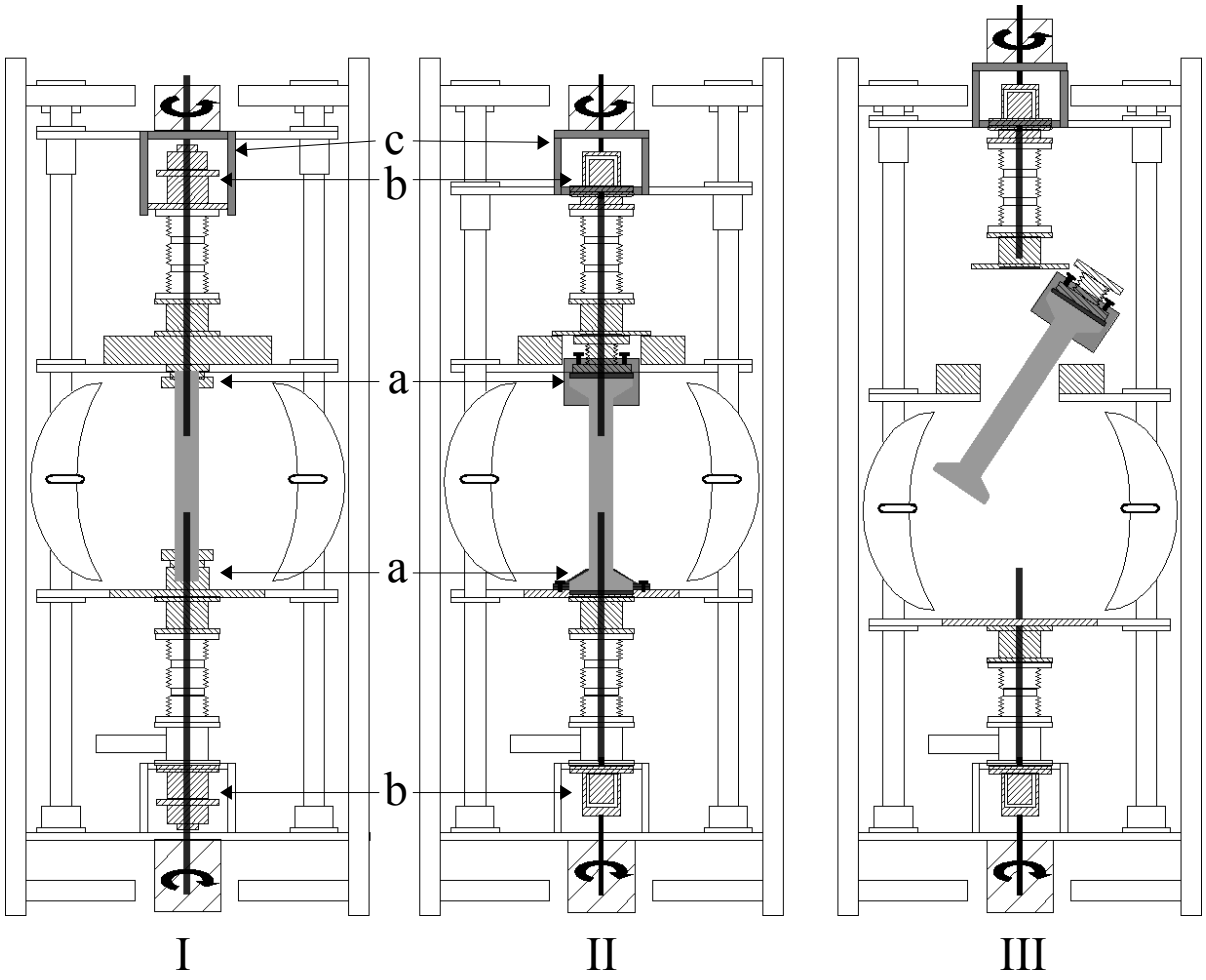

Figure 2.8: Overview of the original (I) and refurbished (II) image furnace. Mounting of the quartz tube with the modified OFZ is illustrated in (III). Components that have been modified are hatched: (a) the quartz-to-metal seals, (b) the rotary feedthroughs and (c) the components for sample mounting. Detailed descriptions are given in the text.

Rotation of the poly-crystalline starting rods was accomplished in the original OFZ by two electric motors mounted on top and bottom. This permits an individual (counter-) rotation of the seed and the feed rod. The rotation of the rods was conducted directly from each motor via one long spindle. The sample chamber was thereby sealed by means of Viton-sealed transmission feedthroughs (see Fig. 2.8 (I), b). These feedthroughs were replaced with commercially available UHV-compatible magnetic rotary feedthroughs (MagiDrive MD35X000, UHV Design Ltd). For those feedthroughs the rotation of the outside spindle is coupled magnetically to a second spindle inside the system. This permits an all-metal sealed transmission of the rotation. In return, it prohibits a vertical movement of the spindle through the feedthrough. The translational movement of the spindles is now limited to the flexibility of the two metal bellows. To guide the upper and lower spindles, slide bearings were constructed and inserted into the lower and upper end of the metal bellows. The slide bearings were made from TECASINT 2391 (Ensinger), a material with good gliding properties up to elevated temperatures of 370°C.

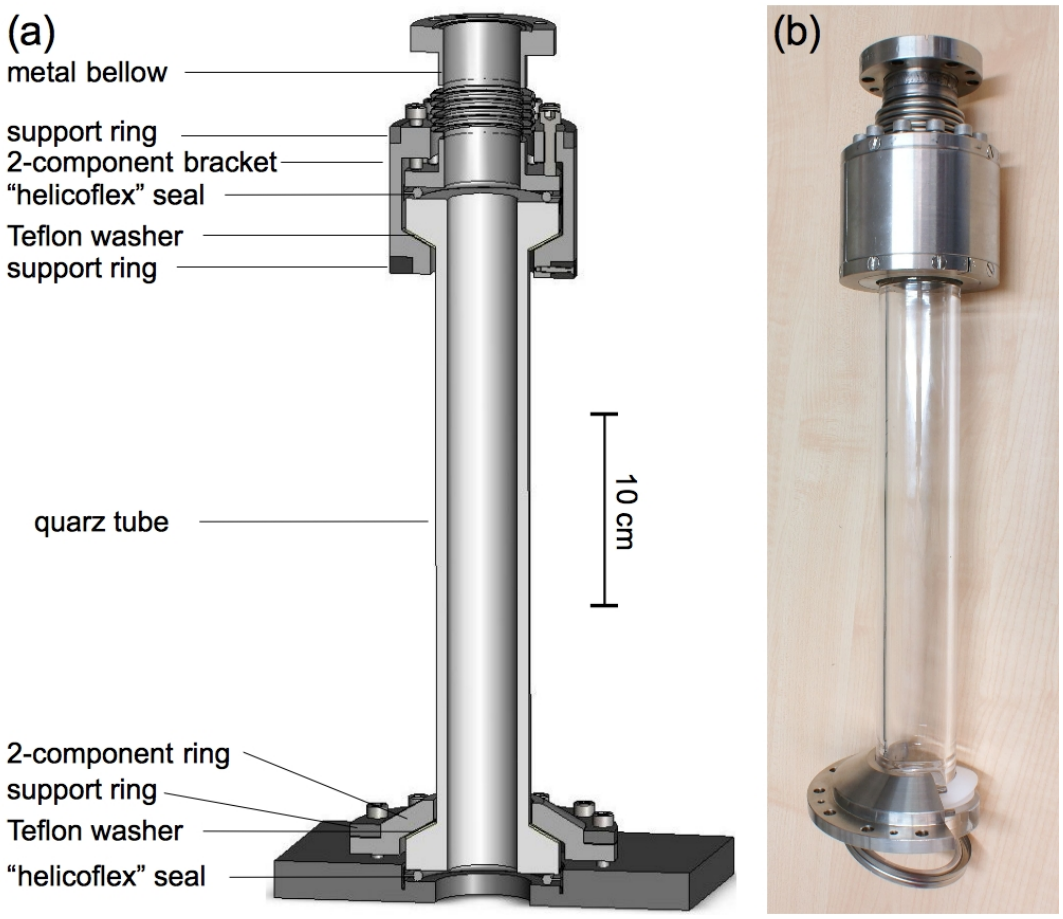

Figure 2.9: (a) Cross-section and (b) photograph of the quartz tube and quartz-to-metal seals. The "helicoflex" gaskets are placed between the quartz and steel surface. A teflon washer protects the quartz flange from damage. The short bellows serves as strain relief under changes of pressure between the main frame of the furnace and the quartz tube.

In the original set-up the quartz tube was mounted and unmounted from the front of the mirror stage, since the upper and lower spindles could be vertically translated through the Viton-sealed feedthroughs. Since the UHV-compatible rotary feedthroughs prohibit translation of the spindles, mounting of the quartz tube from the front was no longer possible in the modified OFZ. Instead, the samples and the quartz tube are mounted as sketched schematically in Fig. 2.8 (III). To gain vertical space, the rotary feedthrough was mounted on top of the upper stage. This change allows to open the system between the upper metal bellows and the top of the mirror stage in order to mount the quartz tube from the top. Furthermore, the water-cooling on top of the mirror stage was changed to permit the quartz-to-metal seals to fit through.

These changes lead to the following order for sample changes:

(i) Mounting of the lower sample (seed rod).

(ii) Inserting the quartz tube from the top.

(iii) Mounting of the top sample (feed rod).

(iv) Sealing the metal bellows at the top of the quartz tube with the upper metal bellows.

(v) Lowering the upper part and sealing both the upper water-cooling and the quartz-to-metal seal at the bottom.

To bake the all-metal sealed furnace bespoke heating jackets were purchased from Horst GmbH [121], as shown in Fig. 2.6 (b). The vacuum after baking is as good as 10^{-9} mbar after several days. Crystal growth of the intermetallic compounds is conducted in a high purity Argon gas atmosphere. A schematic drawing of the Argon supply is shown in Fig. 2.10. To improve the purity of the inert Argon gas (initially 6N), a titanium purifier system (Omni40, NuPure) was installed. This lead to a reduction of the oxygen content to around 0.1 ppm (7N). After filling the furnace with the desired Argon pressure (up to 10 bar), the system was closed. The growth process always took place in a static inert gas atmosphere in order to prevent accidental contamination.

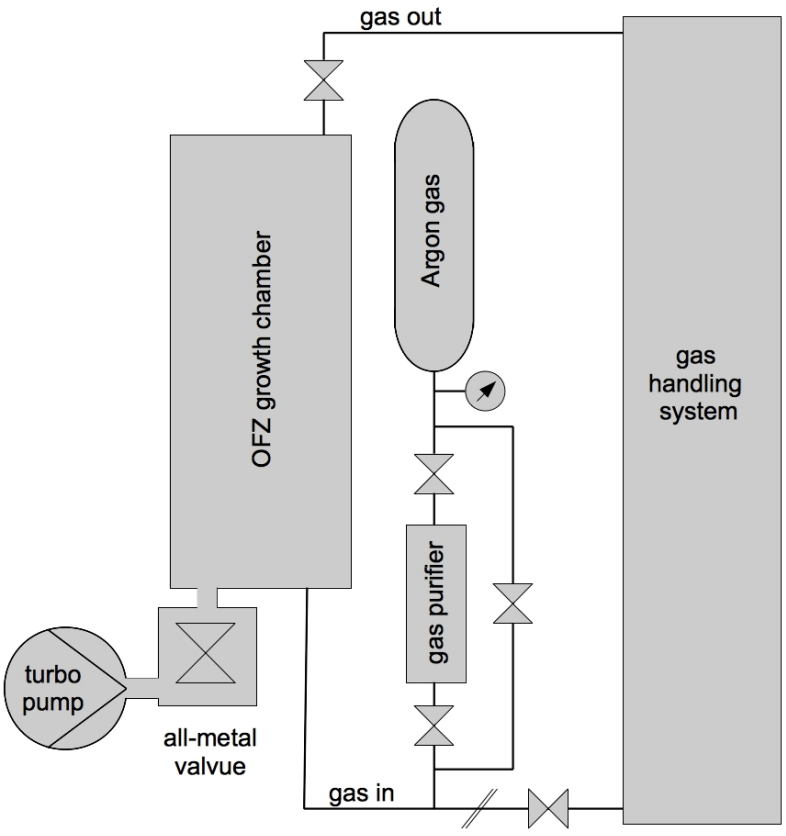

Figure 2.10: (a) Schematic of the inert-gas service connection.

2.1.3 Horizontal cold finger (HCF)

The horizontal cold finger (HCF) is a high-purity UHV system, which was used for the preparation of rods and annealing of samples. It was set-up by Andreas Bauer as part of an internship in our group. The entire system, shown in Fig. 2.11, is all-metal sealed and bakeable. The recipient is mounted on top of an ion getter pump (Varian Star Cell 919-0105). By means of the ion getter pump, a final vacuum better than 10^{-10} mbar can be reached in the HCF. After evacuation, the system may be filled with high purity Argon gas via the gas handling system of the RCF. In addition, the entire system is mounted on an electric linear drive for translation.

The "cold finger" (or copper boat) consists of a thin-walled copper tube with four troughs (see Fig. 2.12 (a)). The copper tube is hard-soldered into a standard CF40 flange and connected from the back side to the recipient. On the front side it is surrounded by a quartz tube with a glass-to-metal seal to a standard CF40 flange. The water circulation is provided by a second, thin capillary tube inside the copper tube serving as water inlet. The troughs are cold-pressed into the copper boat. The polished surfaces of the troughs

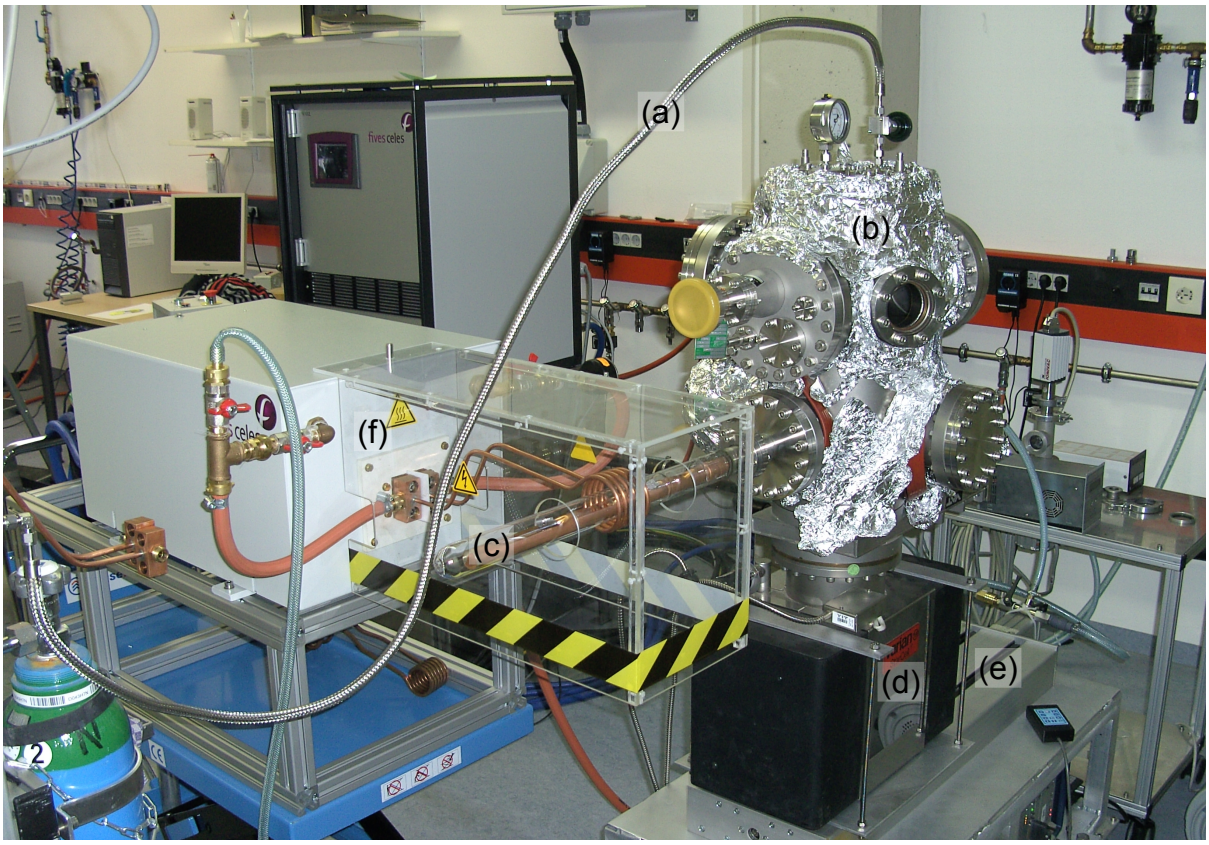

Figure 2.11: Horizontal cold finger system as used for sample annealing with the new RF generator. (a) Argon gas is supplied from the gas handling system of the RCF. The stainless steel recipient (b) holds the copper cold finger (c) and is mounted on top of the ion getter pump (d). The whole system is positioned on a linear drive (e) and can be moved through the induction coil mounted to the oscillating circuit(f). For security reasons the coil is shielded.

combined with the water-cooling prohibits a reaction of the heated sample material with the copper. The sample material is RF-heated by an induction coil. The linear drive allows to move the cold finger with the sample material through the induction coil.

In combination with the RF generator (Hüttinger TIG) of the crystal laboratory of the Physics department the horizontal cold finger was used for rod preparation as shown in Fig. 2.12. Parts of a broken Fe_2TiSn rod, that was cast with the rod casting furnace, were connected. First, the inert Argon atmosphere was purified with a titanium sponge in the second through (Fig. 2.12 (a)). The starting materials were molten from one end and slowly moved through the coil. Images (b - e) display the rod material before, while and after melting.

In combination with a new RF generator (CELES MP 50kW), installed in late 2009, the HCF was used for annealing of Fe_2TiSn and Ni_3Al. The set-up is shown in Fig. 2.11. Again, purified Argon gas was used as inert atmosphere to suppress evaporative losses. Annealing temperatures were chosen to be 850°C and 1050°C, respectively. Annealing times were 60 and 80 hours, respectively. The annealing temperatures were recorded with a pyrometer (Infratherm IGA 140-L) during the annealing process. The temperature was adjusted manually by regulating the power of the RF generator. For future annealing processes a direct feedback loop between pyrometer and RF generator may be installed. This would allow to use a defined temperature profile for the annealing process.

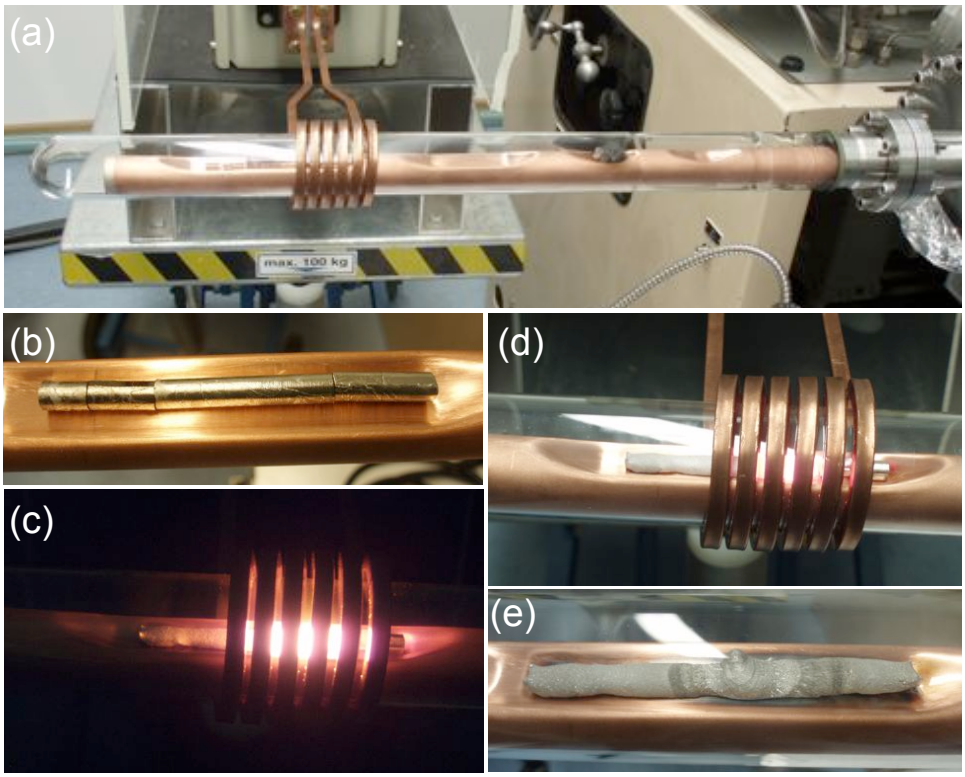

Figure 2.12: (a) Quadratic copper coil surrounding the cold finger as used in the earlier set-up for the preparation of starting rods. (b-d) A broken Fe_2TiSn rod is connected by moving the rod through the coil. The final rod (e) deviates from the ideal homogeneous shape.

2.2 Metallurgical characterization

The metallurgical characterization of the crystals grown served as first evidence of the "success" of the single crystal growth. It provided information in order to adjust the growth parameters. Furthermore it is necessary for the preparation of single crystal samples for further measurements. In this section the various methods employed for the metallurgical characterization are summarized.

The metallurgical preparation of the crystals was conducted in the crystal laboratory of the Department of Physics at TUM. The crystals were cut either with a diamond wire saw or with spark erosion. Where necessary surfaces were polished with sandpaper (grade 4000). To improve the surface smoothness further, the samples were additionally polished either with diamond paste (1 µm or 0.25 µm grain size) or a polishing suspension (Logitech Type SF1).

Prior to the preparation for the metallurgical characterization a photograph of each crystal was taken (see tables in section 2.3). The metallurgical cuts as marked in the pictures were labeled numerically in the growth direction. In the case of subsequent trenching of a part at a later point in time, the new pieces are labeled in the same way by an additional number. In combination with the crystal identification, i.e., OFZ (optical float-zoning) plus the growth number, this leads, for example, to OFZ19-3-3 as the label for the longitudinal cut sample from the last zone in Fig. 2.13.

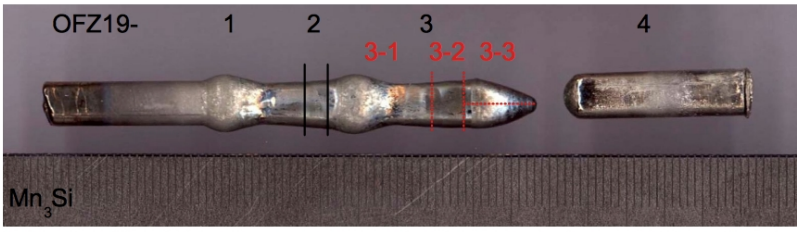

Figure 2.13: Image of OFZ19 (Mn_3Si) with the positions marked and labeled to illustrate the method of numbering explained in the text. The black lines mark the first cuts and the red lines mark cuts at a later point in time. For example, the longitudinal cut pieces of the final zone are labeled OFZ19-3-3.

2.2.1 Optical appearance

For the investigation of the appearance of metallurgical cuts of the crystals grown a light microscope (Leica MS5), a polarization microscope (Leitz, Metallux), and three scanning electron microscopes (SEM) (Akashi, WMI, Garching; Philips XL30, IFW, Dresden; Zeiss EVO MA25, Radiochemie, Garching) were used. With their different magnification the entire spectrum from milli- to nanometers is accessible. Depending on the compound, grain boundaries indicating poly-crystalline growth can be visible from the outside. On the other hand, the appearance of symmetrically aligned facets is a strong indicator for single crystal growth throughout the rod.

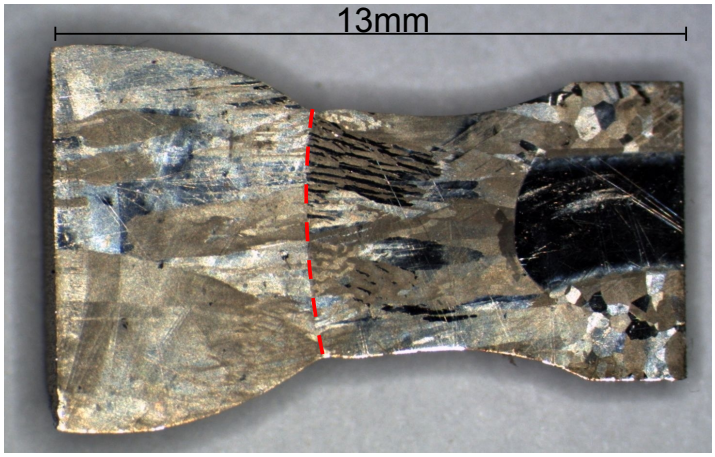

Figure 2.14: Image of the polished and etched last zone of a Ni_3Al sample as recorded with an optical light microscope. Growth direction is from the left to the right. The liquid-solid phase boundary (marked by the dashed red line) has a concave form. The crystal exhibits large grains spontaneously nucleating from the inside. The feed rod on the right shows a small polycrystalline grain structure surrounding a cone of pure Ni. The pure Ni results from insufficient melting during the preparation of the starting rods.

The magnification of the optical microscope was 6.3 - 40. The quality of the photograph depends strongly on the preparation of the sample (grinding, polishing, and/or etching). The best way of surface preparation was optimized for each compound. An image of the polished and etched last zone of a Ni_3Al sample taken with the light microscope is shown in Fig. 2.14. The etchant used was Marple reagent ($2.5\,\mathrm{g}\ CuSo_4 + 30\,\mathrm{cm}^3\ HCl + 25\,\mathrm{cm}^3\ H_2O$).

The magnification of the polarization microscope was 50 - 1000. For non-cubic systems the use of the polarizator color-codes different orientations of the same phases and, hence, offers the advantage of being able to easily identify different grains. For cubic systems it still allows to visualize grain boundaries and secondary phases similar to a normal light microscope.

The scanning electron microscopes offered a magnification of up to 3×10^6. Since the sample is scanned with an electron beam, a conducting surface is necessary[1]. The sample surface is visualized by optical imaging of either the back scattered electrons (BSE) or the secondary electrons (SE). The BSE allow a penetration depth of 0.1 - 6 µm and the SE of 5 - 50 nm, respectively. The images are taken in a high vacuum atmosphere to reduce scattering at air molecules. An image taken with the Zeiss SEM detecting secondary electrons is shown in Fig. 2.15 (a).

All three SEMs are equipped with an energy dispersive X-ray (EDX) analysis set-up, i.e., the characteristic X-rays emitted by the sample are analyzed by an energy dispersive spectrometer. It detects the characteristic X-rays that emerge when an outer shell electron fills an empty inner shell. The energy of the emitted X-rays are characteristic of the

[1]For samples imbedded in a plastic surrounding (Technovit) the conduction was assured by a connection with conductive silver.

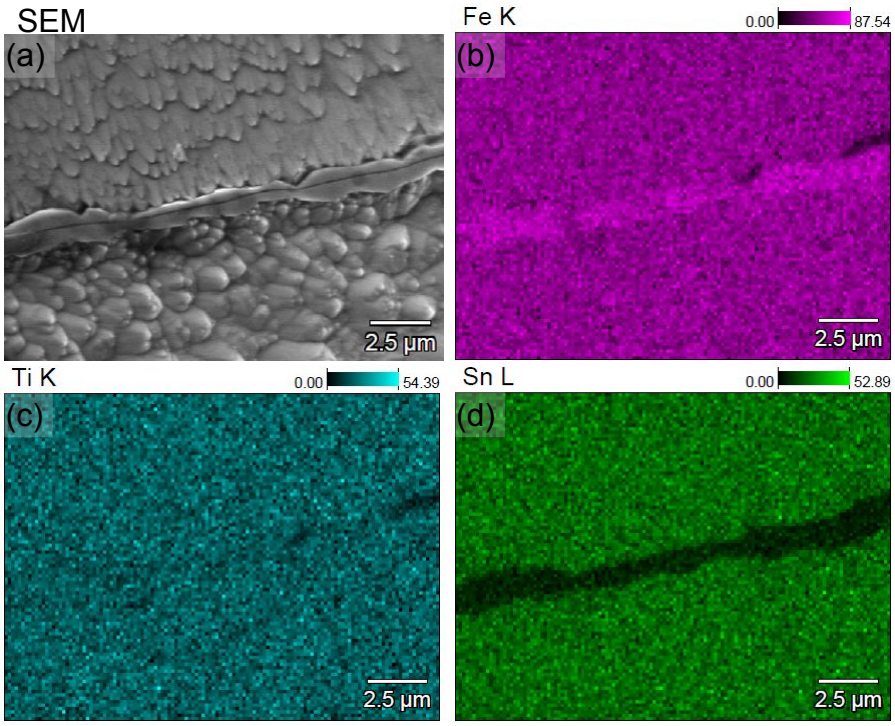

Figure 2.15: (a) SEM image of a grain boundary in Fe_2TiSn with a magnification of 6148. (b- d) The color-coded images show an element map of the sample. The off-stoichiometric grain boundary ($Fe_{67}Ti_{25}Sn_8$) is nicely illustrated.

energy difference of the two shells and of the atomic structure of the element. This allows to measure the element specific composition of the sample. An example is shown in Fig. 2.15 (b- d), where an element map of an Fe_2TiSn sample with an Fe-rich grain boundary ($Fe_{67}Ti_{25}Sn_8$) is illustrated.

All EDX measurements were carried out without use of a standard. It was found that the EDX measurements taken with the Akashi instrument show an absolute element specific error of up to 10%. Therefore only the absolute composition values measured with the Philips and Zeiss system with an instrument specific error of $\sim 1\%$ are presented in this thesis.

2.2.2 Laue X-ray scattering

X-ray Laue diffraction was carried out at the crystal laboratory of the Department of Physics at TUM. The white X-ray beam was generated by a copper X-ray tube (Seifert, Iso-Debyeflex 3000). The diffraction patterns were first recorded with polaroid film. In the course of this thesis a real-time back-reflection Laue camera system (Multiwire Laboratories, Ltd.) was installed. This system allows real-time orientation of the crystals and computer-aided identification of the crystal orientation. The Laue technique was both employed for a first examination of the single-crystallinity of the rods grown and for the preparation of the oriented single crystal samples for further investigations.

For a first check of a successful single crystal growth, diffraction patterns were recorded at several positions along the crystal grown. Since the Laue patterns are invariant to translational movement along a single crystal, the diffraction patterns recorded along a single crystal should be identical. If different diffraction patterns appear, this clearly indicates grains with different crystallographic orientations. Since X-ray diffraction is a surface sensitive method, no information about the crystal structure in the bulk can be inferred. Nevertheless, comparison of diffraction patterns taken on both sides of a rod (turned 180°) yield a first check of the bulk crystal structure of the rod. As an example the diffraction patterns of a Fe_2TiSn rod are shown in Fig. 2.16. Similar diffraction patterns showed up along each side. However, both sides - 0° and 180° - compared to each other showed a different pattern. This indicated the presence of at least two large grains, which was confirmed by optical investigation of the polished cross sections.

For the preparation of oriented single crystal samples the crystals were attached to a goniometer and oriented to the desired crystallographic orientation. Subsequently, the goniometer was mounted to the wire saw and the oriented plane was cut. This way an accuracy of better than 2° could be achieved. To improve the accuracy further, the as-oriented crystals were mounted to a sample holder that may be tilted for 2° and again oriented by X-ray Laue diffraction. Mounting this sample holder to the grinding rig and polishing the sample resulted in an accuracy better than 1°.

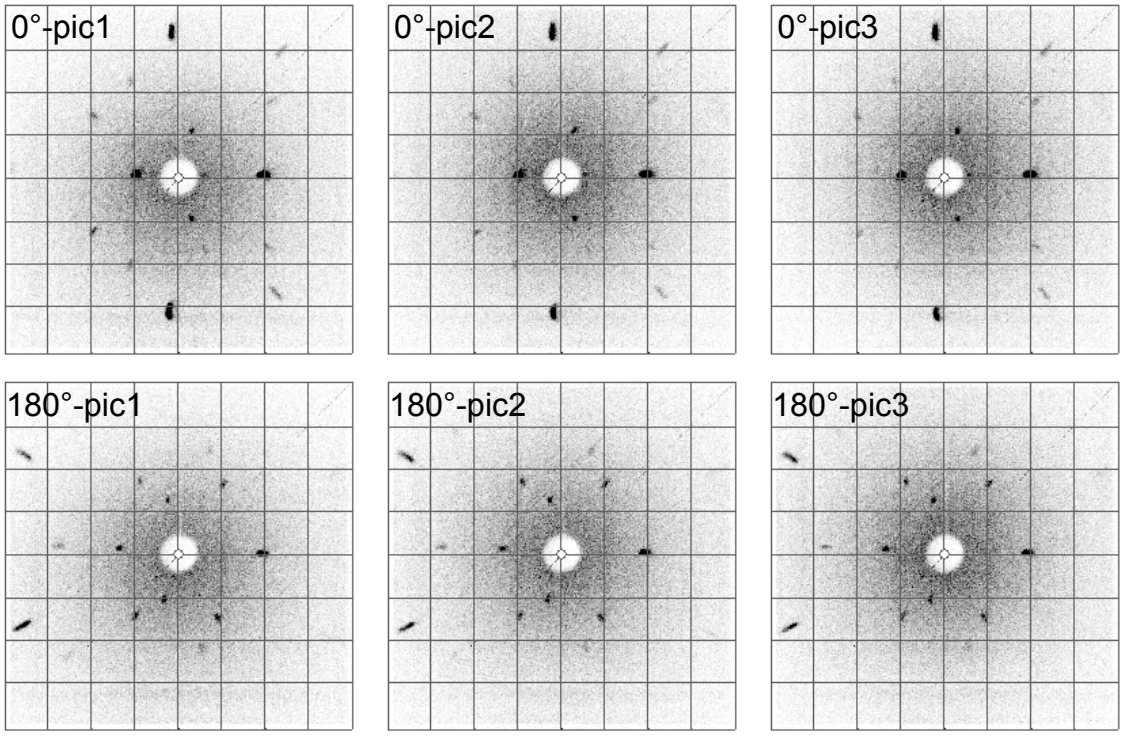

Figure 2.16: *top row:* Laue X-ray diffraction pattern recorded at three positions along a Fe_2TiSn crystal (OFZ41, step width $\sim 5\,\mathrm{mm}$). *bottom row:* Diffraction pattern taken at the same height with the crystal turned around by 180°. The diffraction pattern is similar within each row, but different for each side. This implies the presence of at least two large grains.

2.2.3 Neutron single crystal diffraction

Single crystal diffraction with neutrons provides non-destructive information of the bulk crystal structure. Measurements were carried out in collaboration with Björn Pedersen at the thermal single crystal diffractometer RESI [122] and with Martin Meven at the hot single crystal diffractometer HEIDI [123] at FRM II in Garching.

At HEIDI an eulerian cradle was used for the measurements. The diffracted neutron beam with a wavelength $\lambda = 0.87\,\text{Å}$ was detected by a ^{3}He counter. At RESI a monochromatic neutron beam ($\lambda = 1\,\text{Å}$, monochromator: Cu-422) was diffracted at the single crystal and the diffraction patterns were recorded by an area detector.

For measurements at RESI the crystal structure was scanned with a fixed set-up by turning the crystal. The diffraction intensity was typically integrated over a rotation angle of 0.5° and the crystals were typically rotated for 30°. This permitted to scan the crystals fast, while providing sufficient information on the crystal structure. The scanned area was $10 \times 7\,\text{mm}^2$ and the measurements were recorded at room temperature. A typical set of diffraction spots for the gradient crystal $Fe_{1-x}Co_xSi$ (OFZ48) is shown in Fig. 2.17 (a). The diffraction data was analyzed by Björn Pedersen, the instrument responsible at RESI. The measurements provide information about the single-crystallinity, i.e., if one or more grains exist within the crystal, about the orientation of the crystalline structure within the crystal and the lattice constants. As an example, Fig. 2.17 (b) shows the relative orientation of two large grains at the beginning of the $Fe_{1-x}Co_xSi$ gradient crystal (OFZ48). The two grids represent cubic crystal structures and illustrate the relative orientation of the grains in respect to each other. In addition, the volume fraction of the secondary grain can be estimated from the measured intensity. Analysis of the measured Bragg reflections furthermore contains information about crystal growth anomalies like twinning.

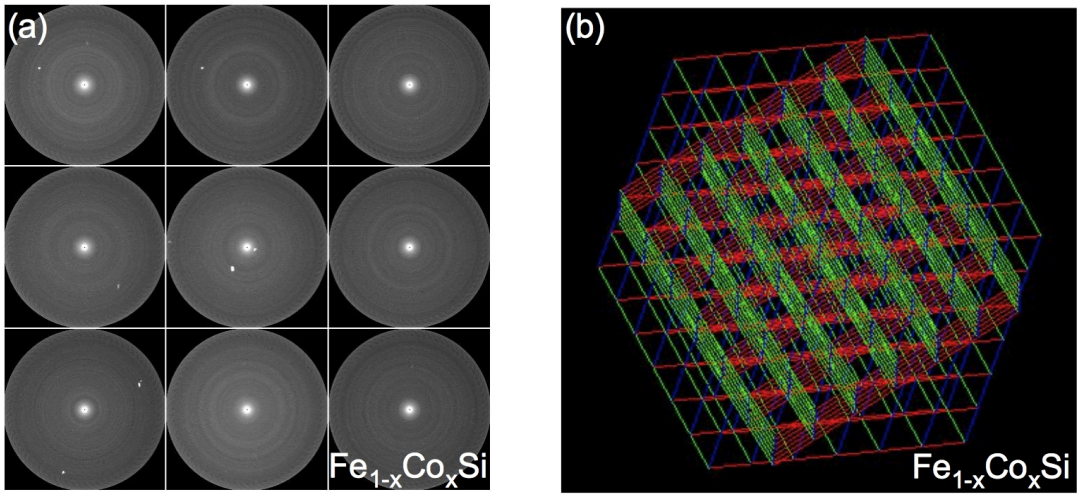

Figure 2.17: (a) A typical set of images as recorded with the neutron single crystal diffractometer RESI at FRM II [122]. (b) Relative growth orientation of two grains in the beginning of the crystal OFZ48, as calculated from the diffraction data. The grids resemble the cubic B20 crystal structure.

2.3 Summary of crystals grown

In the course of this thesis altogether 38 crystal growth experiments of 12 different intermetallic compounds were carried out. The tables in this section summarize the crystals grown. They show the composition of the compound, the identification of the crystal, the growth rate as the crucial process parameter, the result of the single crystal growth and a one to one image of each crystal. Further details are described in the chapters below.

The expression "yes" in the SINGLE CRYSTAL column states the successful growth of a mono-crystalline structure across the entire cross section of the rod, for the length stated. This usually implies the appearance of large grains prior to the single-crystalline zone. The expression "Large grains" refers to single-crystalline grains with a diameter larger than 3 mm. For those compounds a mono-crystalline structure across the entire cross section of the rod seems feasible by means of minor changes of the growth parameters or optimization of the grain selection (e.g. "necking" or the use of a single-crystalline seed). The expression "small grains" (< 2 mm) refers to situations where single crystal growth of large grains with the floating zone technique is not clear. Major changes of the growth parameters (as in the case of Fe_2TiSn) and possibly of the starting composition might result in single crystal growth, but a more systematic investigation is necessary to clear this question. For CoVSb and $CeCoSi_3$ a dendritic structure containing at least two phases was found, implying that for further growth attempts a much reduced growth rate should be applied.

2.3.1 Heusler compounds

Table 2.1 summarizes the Heusler compound Cu_2MnAl, the first crystals grown as part of this thesis. The first two crystals, HKZ 361 and HKZ 363, were grown in collaboration with Günter Behr at the IFW in Dresden. For the first growth experiments bars with a rectangular cross section ($4 \times 4\,mm^2$) cut from large poly-crystalline discs were used as starting rods, since the RCF was not set-up at that time.

In Table 2.2 the crystals grown of the full Heusler compounds Mn_3Si and Ni_2MnAl, the half Heusler compound CoVSb and the quaternary Heusler compound MnCoVAl are presented. For OFZ56 (Mn_3Si), an incongruently melting compound, growth was attempted with an off-stoichiometric $Mn_{79}Si_{21}$ pill sandwiched between the stoichiometric seed and feed rod.

In Table 2.3 crystals grown of the full Heusler compounds Fe_2TiSn and Fe_2VAl are shown. A drastic reduction of the growth rate in Fe_2TiSn for OFZ31 and OFZ41 resulted, to the best of our knowledge, in the first growth of large single crystal grains of this compound.

2.3.2 Weakly ferromagnetic Ni_3Al and $NbFe_2$

Table 2.4 and Table 2.5 summarize the crystals grown of the weak ferromagnets $Ni_{3+x}Al_{1-x}$ and $Nb_{1+x}Fe_{2-x}$, respectively. Even though various compositions and growth rates were tested, no successful growth of large single crystals of $Ni_{3+x}Al_{1-x}$ could be accomplished. Starting rods for $Nb_{1+x}Fe_{2-x}$ were prepared by William Duncan [124] with a horizontal copper boat system at Royal Holloway, University of London. Despite their irregular shape, stable growth conditions and the growth of large single crystal grains were achieved for every composition of $Nb_{1+x}Fe_{2-x}$. In future studies a more pronounced necking process promises to reduce secondary grains.

2.3.3 B20 compounds

Table 2.6 summarizes the B20 compounds grown in this thesis. Besides stoichiometric MnSi, we grew four gradient crystals, two with composition $Mn_{1-x}Fe_xSi$ ($x = 0 - 0.15$) and two with composition $Fe_{1-x}Co_xSi$ ($x = 0.1 - 0.3$). As gradient crystals we denote crystals with a predetermined doping gradient. The gradients were generated using seed and feed rods of differing composition. Single crystal growth across the entire rod diameter was accomplished for every B20 compound.

2.3.4 Heavy fermion compound $CeCoSi_3$

Shown in Table 2.4 are the results for the only heavy fermion compound $CeCoSi_3$ grown as part of this thesis. In the beginning an unstable and asymmetrically shaped zone resulted in dripping-off of the zone. Towards the end of the growth stable conditions were accomplished. The crystal shows a dendritic texture. In addition one single crystal grain could be prepared from the necking position. The starting material for this compound was prepared during a visiting research fellowship of DAAD at the Centro Brasileiro de Pesquisas Fisicas in Rio de Janeiro, Brasil.

Material	Growth Number	Growth rate	Single crystal?	Image
Cu_2MnAl	HKZ361	15 mm/h	large grains	
Cu_2MnAl	HKZ363	15 mm/h	large grains	
Cu_2MnAl	OFZ1	10 mm/h	yes, 0.5 cm	
Cu_2MnAl	OFZ3	10 mm/h	yes, 3 cm	
Cu_2MnAl	OFZ4	10 mm/h	yes, 1 cm	
Cu_2MnAl	OFZ5	12 mm/h	yes, 2.5 cm	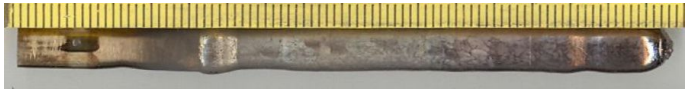
Cu_2MnAl	OFZ6	10.5 mm/h	yes, 1.5 cm	
Cu_2MnAl	OFZ10	5 & 10 mm/h	yes, 2 cm	

Table 2.1: Cu_2MnAl crystals grown in this work.

Compound	Growth Number	Growth rate	Single crystal?	Image
Mn_3Si	OFZ7	2 mm/h	yes, 1 cm	
Mn_3Si	OFZ8	2 mm/h	yes, 0.8 cm	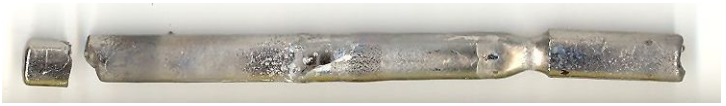
Mn_3Si	OFZ19	3 mm/h	yes, 0.5 cm	
Mn_3Si ($Mn_{79}Si_{21}$ pill)	OFZ56	2 mm/h	small grains	
Ni_2MnAl	OFZ18	5 & 8 mm/h	small grains	
MnCoVAl	OFZ25	10 & 4 mm/h	small grains	
CoVSb	OFZ22	5 & 18 mm/h	dendritic structure	

Table 2.2: Mn_3Si (binary), Ni_2MnAl (full), CoVSb (half) and MnCoVAl (quaternary) Heusler crystals grown in this work.

Compound	Growth Number	Growth rate	Single crystal?	Image
Fe_2TiSn	OFZ13	10 mm/h	small grains ($\sim$ 1 mm)	
Fe_2TiSn	OFZ14	10 & 5 mm/h	small grains ($\sim$ 1 mm)	
Fe_2TiSn	OFZ31	1 & 0.7 mm/h	large grains ($>$ 4 mm)	
Fe_2TiSn	OFZ41	0.8 mm/h	1 large grain	
Fe_2VAl	OFZ49	1.5 - 4 mm/h	yes, 1.5 cm	
Fe_2VAl	OFZ50	5 & 8 mm/h	yes, 2.5 cm	

Table 2.3: Fe_2TiSn and Fe_2VAl Heusler crystals grown in this work.

Compound	Growth Number	Growth rate	Single crystal?	Image
Ni_3Al	OFZ15	8 mm/h	small grains	
Ni_3Al	OFZ17	3 mm/h	small grains	
$Ni_{75.5}Al_{24.5}$	OFZ20	10 & 5 mm/h	small grains	
$Ni_{76}Al_{24}$	OFZ23	10 mm/h	small grains	
$Ni_{75.5}Al_{24.5}$	OFZ38	0.16 mm/h	small grains	
$CeCoSi_3$	OFZ39	1-6 mm/h	dentritic structure + 1 large grain	

Table 2.4: Ni_3Al crystals with varying composition. The last row shows the only 4f-electron compound $CeCoSi_3$ grown in this thesis.

Compound	Growth Number	Growth rate	Single crystal?	Image
$Nb_{1-x}Fe_{2+x}$ $x = 0$	OFZ11	5 mm/h	1 large grain	
$Nb_{1-x}Fe_{2+x}$ $x = 0$	OFZ12	8 mm/h	2 large grains	
$Nb_{1-x}Fe_{2+x}$ $x = 0.01$	OFZ27	5 mm/h	1 main grain	
$Nb_{1-x}Fe_{2+x}$ $x = 0.006$	OFZ28	$6-8$ mm/h	yes, 2.5 cm	
$Nb_{1-x}Fe_{2+x}$ $x = -0.007$	OFZ29	6 mm/h	1 main grain	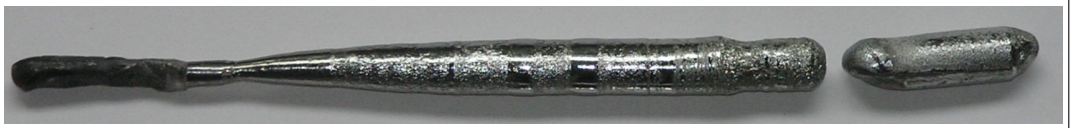
$Nb_{1-x}Fe_{2+x}$ $x = 0.018$	OFZ30	10 mm/h	2 large grains	

Table 2.5: $NbFe_2$ crystals grown in this work.

Compound	Growth Number	Growth rate	Single crystal?	Image
MnSi	OFZ9	10 mm/h	yes, 2 cm	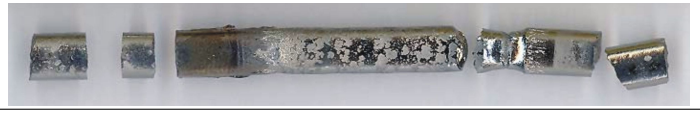
MnSi → $Mn_{0.85}Fe_{0.15}Si$	OFZ45	5 mm/h	yes, 3 cm	
$Mn_{0.85}Fe_{0.15}Si$ → MnSi	OFZ46	5.2 mm/h	yes, 2.5 cm	
$Fe_{0.7}Co_{0.3}Si$ → $Fe_{0.9}Co_{0.1}Si$	OFZ47	5 mm/h	yes, 1.8 cm	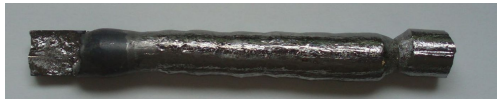
$Fe_{0.9}Co_{0.1}Si$ → $Fe_{0.7}Co_{0.3}Si$	OFZ48	5 mm/h	yes, 2.5 cm	

Table 2.6: MnSi, $Mn_{1-x}Fe_xSi$ & $Fe_{1-x}Co_xSi$ gradient crystals grown in this work.

Chapter 3

Experimental methods at low temperatures

For the investigation of the low temperature physical properties of the crystals grown in this thesis a number of methods were applied. The bulk properties magnetization, AC-susceptibility, specific heat and magnetotransport were measured in three different cryogenic systems, covering a large magnetic field and temperature range. An overview over the cryogenic systems and their parameters is given in Table 3.1. Neutron depolarization radiography (NDR), as a new technique, measured at the ANTARES [125] beamline at FRM II, was used to investigate the distribution of magnetic properties in the float-zoned crystals. Small angle neutron scattering (SANS) experiments with polarized neutrons were carried out at MIRA [126] at FRM II. In addition, high pressure techniques were applied to investigate the development of the magnetic and transport properties under pressure.

3.1 Cryogenic systems

The physical properties measurement system (*PPMS*, Quantum Design) is an apparatus providing an all-in-one package for the end-user. It provides all the hardware, software, electrical connections and sample holders for measurements of magnetization, susceptibility, specific heat, as well as electrical and thermal transport. It consists of a helium cryostat and a superconducting magnet providing a temperature range from 1.8 - 400 K and magnetic fields up to 9 T. A detailed description of the system is found on the Quantum Design homepage [127].

The *VSM* (vibrating sample magnetometer) system was bought second hand from Phillips (Eindhoven) and set-up during the author's diploma thesis [93]. It consists of a superconducting magnet providing fields up to 9 T and a continuous flow cryostat reaching temperatures of 2.4 - 300 K, which is mounted in a room temperature bore-hole of the magnetic system. The continuous flow cryostat is connected to a helium dewar via a transfer

tube (GFS-600, Oxford Instruments). The experimental parameters are controlled via electronic panels from Oxford Industries (ILM, IPS120, ITC503, SMC4, VCU) and measurements may be controlled by means of the Object Bench measurement software. Data is recorded with a Lock-In amplifier (SR830, Scientific Instruments). The set-up was used in this thesis for measurements of the magnetization and electrical transport. A detailed description of the system is given in the author's diploma thesis [93].

The *Sweet16* system is a magnet-cryostat commercially obtained from Oxford Instruments. It consists of a 16 T superconducting magnet and a variable temperature insert (VTI), which provides temperatures in the range of 1.4 - 300 K via helium cooling. The system is controlled via LabVIEW programs from Oxford Industries (ILM, IPS120, ITC503, Lambda Controller) and the measurements are controlled via a LabVIEW program written by Robert Ritz. The set-up was used for transport and torque magnetization measurements. A detailed description of the cryostat and the LabVIEW program is given in the diploma theses of Robert Ritz [128] and Christian Franz [129].

System	Temperature	Field	Measurement	Mode
PPMS	1.8 - 400 K	9 T	Magnetization AC - susceptibility Specific Heat	Step
VSM	2.4 - 300 K	9 T	Magnetization M under pressure Magnetotransport	Continuous
Sweet16	1.4 - 300 K	16 T	Magnetotransport ρ under pressure Torque magnetization	Continuous & Step

Table 3.1: Summary of the cryostat systems used in this thesis.

3.2 Magnetization

Magnetization measurements in this thesis were performed both at the *PPMS* and the *VSM* system (see Table 3.1).

The *PPMS* system measures the magnetization by means of an extraction method. The sample, glued with GE varnish to a non-magnetic sample holder, is thereby extracted with a servomotor from pick up coils within ~ 0.05 seconds. The voltage induced in the pick-up coils is recorded and numerically integrated as a measure of the magnetic moment. During the extraction, temperature and magnetic field are kept constant. For better accuracy the extraction process is repeated several times. For measurements in this thesis generally a repetition rate of 3 was used.

In contrast to the *PPMS*, the *VSM* system uses the vibrating sample method for the magnetization measurements. The sample, glued to a non-magnetic sample holder and

mounted to a long Kevlar-Epoxy-sample rod, continuously vibrates within the pick-up coils. The vibration is generated by a velocity transducer positioned on top of the cryostat. In principle, the transducer operates like a loud-speaker. Due to heating problems the driving coils burnt through several times. The driving-coil set-up within the velocity transducer was therefore redesigned as part of this thesis in cooperation with Udo Klein[1]. The material of the coil body was changed from Pertinax to Makrolon and the coil was glued to the coil body with a different silicone resin (Cramolin Isotemp).

The oscillation frequency and amplitude of the VSM drive are regulated with a VCU (Vibrator Transducer Control Unit, Oxford Instruments) and adjusted via the oscillator of a SR830 Lock-In amplifier. In general, frequencies around 40 Hz and an amplitude of $\sim$ 0.1 mm were used. For the detection of the induced voltage two sets of pick-up coil configurations (flat and peak) are available. The flat coil configuration has a larger distance between its two coils, hence measuring homogeneously a larger sample space. For the measurements of the large samples (>1 mm^3) in this thesis the flat configuration was used. The induced voltages are amplified by a Dual Input Preamplifier from Oxford Instruments and detected by the SR830 Lock-In amplifier. Data is recorded in continuous mode, i.e., during slow temperature and field sweeps.

Prior to each measurement the voltage induced by a nickel standard in a magnetic field of 0.6 T was measured. This provided a calibration of the measured voltages into magnetic units through comparison with the known value for the Ni sample:

$$M_{\text{sample}} = \frac{U_{\text{sample}}}{U_{\text{Ni}}} M_{\text{Ni}}. \tag{3.1}$$

For exact measurements of the sample temperature a thermometer was additionally mounted between the pick-up coils of the coil insert.

For measurements at a fixed temperature and changing field (field sweeps - FS) data was generally recorded in a 5-point-loop ($0 \rightarrow +B \rightarrow -B \rightarrow +B$). Temperature sweep (TS) measurements were, unless noted differently, generally taken in a zero field cooled - field heated (ZFC-FH) configuration with increasing temperatures.

3.3 Magnetization under pressure

For magnetization measurements under hydrostatic pressure a miniature Copper-Beryllium (Cu:Be, Berylco 25A) clamp cell was used as shown in Fig. 3.1. The measurements were performed in the *VSM* system. The pressure cell has an outer diameter of 12 mm and can be mounted on the standard *VSM* sample rod via a PTFE adapter. Its inner diameter is 3 mm allowing to measure samples with a maximum outer dimension of 2.5 mm. The sample is placed in a PTFE cup with a mixture of Fluorinert (FC84:FC72 - 1:1) as pressure medium. The mixture of Fluorinert solidifies continuously (over a wide temperature range) under cooling and hence provides a homogeneous pressure.

[1]Udo Klein is CEO of WissEl, the company retailing the vibrator unit [130].

Pressure is applied with a hydraulic press by pushing a hard metal rod (through the hole in the Cu:Be lock-nut) onto the non-magnetic hard metal stamp and then fixed by tightening the lock-nut. The pressure medium is sealed with two Cu:Be discs with knife edges. Additional PTFE discs are used as spacers to obtain an optimum filling of the cell.

While loading the cell it is important to avoid any air bubbles in the pressure transmitter. The measurements were performed starting from the maximum pressure and consequently reducing the applied pressure by opening the lock-nut. At the highest pressures, 1/8 of a turn of the lock-nut lead to a pressure reduction of ∼1 kbar. The maximum pressure applied in this thesis was 14.9 kbar.

For the determination of the applied pressure two small Sn pieces (99.9999% purity) were used. One was placed inside the PTFE cup in the high pressure region while the other was glued with GE varnish to the outside of the pressure cell providing a reference transition. At the superconducting transition the Meissner flux expulsion is detected. Since the pressure dependence of the superconducting transition of tin is well known (see e.g. [131]), this allows to determine the applied pressure from the measured temperature difference ΔT_C of the superconducting transitions of the Sn pieces:

$$\Delta T_C = -4.63 \times 10^{-5} P + 2.16 \times 10^{-10} P^2 \quad (P \text{ in bar}) \tag{3.2}$$

An example of the induced voltages from the tin pieces is shown in Fig. 3.2.

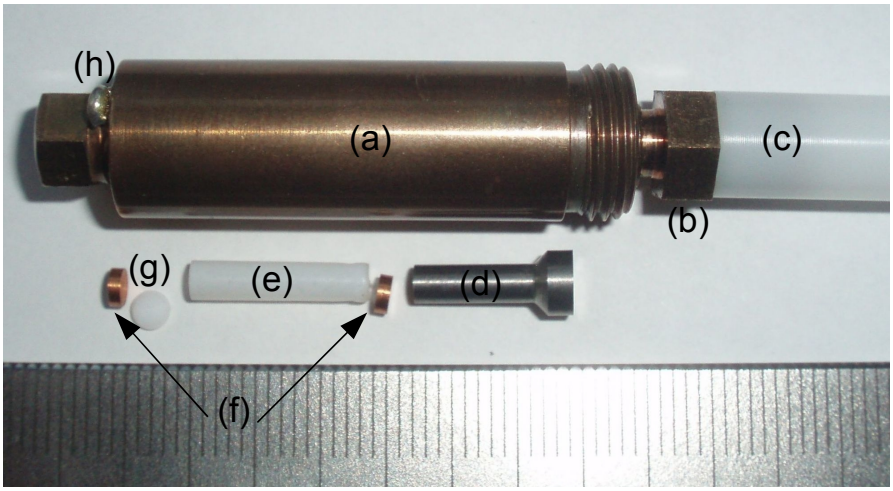

Figure 3.1: Cu:Be clamp cell used for magnetization measurement in the *VSM* system. (a) body of cell; (b) lock-nut with hole; (c) PTFE adapter; (d) non-magnetic stamp; (e) PTFE tube holding the sample and a tin piece, filled with Fluorinert as pressure medium; (f) Cu:Be cutting discs; (g) PTFE spacer; (h) the second tin piece.

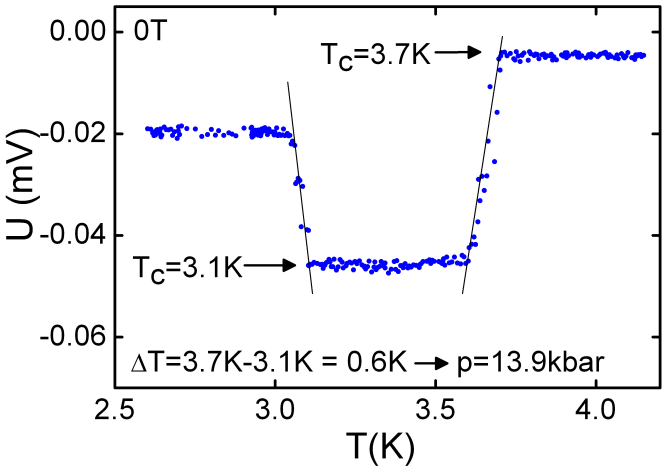

Figure 3.2: Voltage induced in the pick-up coils by the superconducting transition of the tin pellets inside and outside of the pressure cell. The difference in the transition temperature is a measure of the applied pressure, calculated with Eq. (3.2) taken from Ref. [131]. Note that the signal increases or decreases depending on the precise location of the Sn piece in the detection coils.

3.4 AC - susceptibility

The AC - susceptibility, $\chi_{\mathrm{ac}} = \mathrm{d}M/\mathrm{d}H$, i.e. the linear magnetic response function in an alternating field, was measured with the *PPMS* system. A small AC drive magnetic field is superimposed on the applied DC field by an AC current sent through a coil surrounding the sample. The AC magnetic field causes a time-dependent moment in the sample, which in return induces a current in the pickup coils. This allows to measure, without sample motion, both the real (χ') and the imaginary (χ'') part of the AC - susceptibility.

The samples are mounted at the same sample holder and rod as for the magnetization measurement and the same sample environment is used. As for the magnetization measurements at the *PPMS*, the data is recorded at fixed temperature and magnetic field. In general, the AC - susceptibility was measured parallel to the magnetization in the same measurement sequence. Typically, an oscillating frequency of 911 Hz with an excitation amplitude of 1 mT was used.

3.5 Torque magnetization

Torque magnetization of single crystal $NbFe_2$ was measured with a turnable capacitive cantilever in the *Sweet16* system. The technique was recently set-up in our group by Felicitas Birkelbach in collaboration with Werner Biberacher from the Walther Meissner Institute of the Bavarian Academy of Sciences (for a detailed description see Ref. [132]). In general, torque magnetization measures the component of the magnetic moment per-

pendicular to the applied field:

$$\vec{\tau} = \vec{m} \times \vec{B} \tag{3.3}$$

Rotating the sample in fixed field allows to measure the direction dependence of the magnetization, hence it allows to map out the magnetic anisotropies of the material.

In our setup the torque experienced by the sample under field is measured capacitively, i.e., $C \propto \tau$, via the deflection of a leaf spring. The setup is shown in Fig. 3.3 (a) and a schematic cross section of the capacitive cantilever in Fig. 3.3 (b). The oriented single crystal sample (A) is attached with GE varnish to the leaf spring (B). The leaf spring, made from Cu:Be with a thickness of 50 µm, is clamped from one side with a fixed distance to the ground plate (E). The distance of the capacitor plates can be adjusted by a conducting spacer plate (C). This capacitance set-up is mounted on an isolating holder (D) and screwed to a turntable (F) which can be rotated by $\sim 300°$.

The capacitance is measured with a three point set-up as shown in Fig. 3.3 (c); one contact at each capacitor plate (H and L) and an additional contact at the shielding of the set-up (G). This three point measurement avoids disturbing signals and allows to directly measure the capacitance between the capacitor plates with a high resolution. The capacitance was measured with a high precision capacitance bridge (Andeen-Hagerling, AH2770A) at a frequency of 1200 Hz.

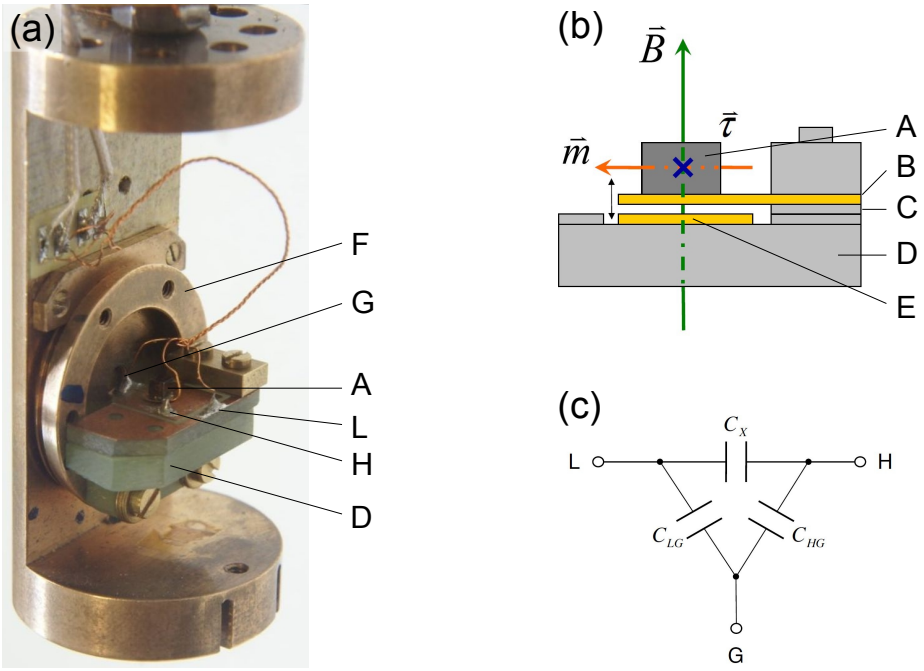

Figure 3.3: (a) Capacitive torque cantilever mounted to a rotable platform (F). (b) Schematic of the cantilever: (A) sample; (B) leaf spring; (C) spacer; (D) isolating support; (E) ground plate. A magnetic moment $\vec{m}$ of the sample perpendicular to the applied field $\vec{B}$ results in a torque $\vec{\tau}$ on the sample (indicated by the blue cross). (c) The capacitance is measured via a three point measurement with (L) and (H) being the contacts at the capacitor plates and (G) the contact of the shielding. Figures taken from Ref. [132].

The torque module (Fig. 3.3 (a)) is connected to a bespoke sample stick. Besides the electrical wiring and a thermometer it contains a spindle which allows to rotate the torque meter within the cryostat. An electric stepper motor, installed on top of the sample holder, allows an automatic rotation of the spindle [2]. For a measurement of the rotation angle of the turntable a Hall sensor was connected to the bottom of the isolating holder (D) and measured with a Lock-In amplifier.

3.6 Specific Heat

The specific heat was measured with the *PPMS* system employing a standard heat pulse technique. It provides the heat capacity at constant pressure

$$C_P = \left(\frac{\mathrm{d}Q}{\mathrm{d}T}\right)_P \tag{3.4}$$

During a measurement, a heat pulse is applied followed by a cooling period of the same duration. From the shape and size of the temperature profile during heating and cooling the specific heat is calculated. For the calculation the *PPMS* offers two routines. A simple model assuming ideal thermal contact between sample and sample platform and the so-called two-tau model in the case of a poor thermal attachment of the sample to the platform.

For the measurement a sample with a weight between 1 to 200 mg is attached (with the help of a sample mounting station) to the sample platform with a thin layer of grease. The platform holds a heater and thermometer and is connected via small wires to the calorimeter puck. Due to the vacuum at the sample chamber the thermal conductance between the sample platform and the thermal bath (puck) is dominated by the conductance of the wires. This establishes a reproducible heat link between the bath and the sample platform. Measurements are taken in step mode and, for a better accuracy, three heat pulse cycles were taken at every measurement point.

3.7 Magnetotransport

Electric transport measurements in applied magnetic field were carried out both in the *VSM* and the *Sweet16* system. Both systems use a similar set-up. A copper gusset holding the sample is mounted to a bespoke sample stick. Each sample rod holds a Cernox thermometer close to the sample position for a precise measurement of the sample temperature. The electrical connections are made of twisted copper pairs. Typical currents of 5 mA were applied at typical frequencies of 67.1 Hz or 11.137 Hz. The measurement signals were amplified by two low-noise impedance matching transformers (model 1900, Signal Recovery) by a factor of 100 and read out simultaneously by two Lock-In amplifiers (SR830, Stanford Research).

[2] The motor was set up and implemented into LabVIEW by Martin Heimgreiter during an internship.

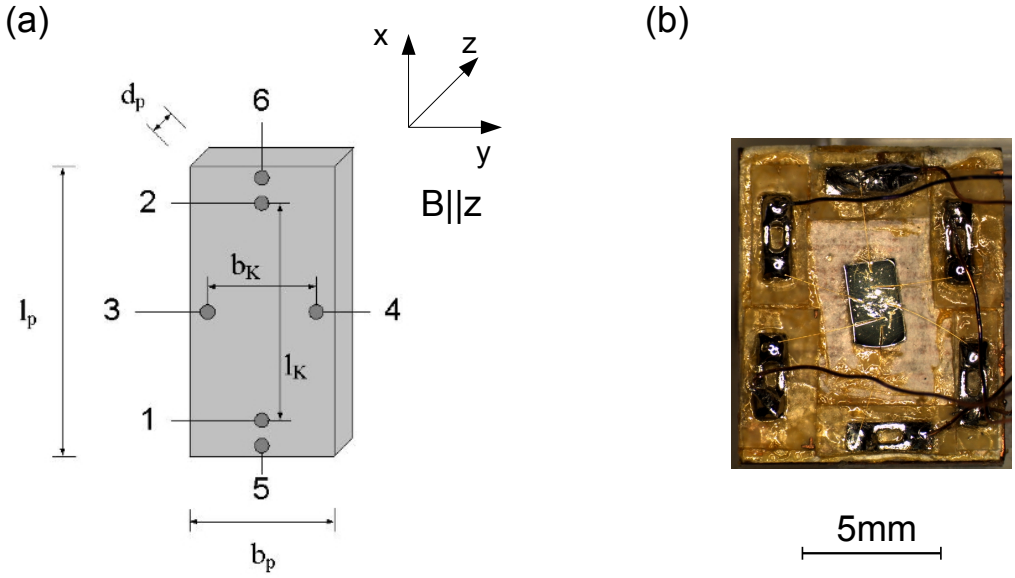

Figure 3.4: (a) Schematic of the 6-point-contact configuration of a Hall bar shaped sample. Sample dimensions (b_P, d_P, l_P) and contact distances (b_K and l_K) are sketched. Magnetic field is applied perpendicular to the sample along the z-direction. (b) Mn_3Si sample on a sample holder.

Samples for the electric transport measurements were typically bar shaped and measured in a 6-point-configuration as shown in Fig. 3.4 (a). The current was applied along the long axis between 5 and 6 and the longitudinal voltage (U_{xx}) was picked up in the same direction (1 and 2). The Hall voltage (U_{xy}) was measured perpendicular to the current between 3 and 4. The magnetic field was applied perpendicular to the flat side of the sample. This set-up allowed simultaneous measurements of the Hall and longitudinal resistivity.

The electric contacts were made by spot-welding of gold wires (⌀ 25 µm) to the polished sample surfaces. During the course of this thesis a new spot-welding apparatus (UIP1000 digital, Schmidt Instruments) was acquired which made the fabrication of stable contacts much more reliable. The optimal welding parameters for each material were obtained empirically. The contacted samples were attached with GE-varnish to the sample holders with cigarette paper as an insulating layer (see Fig. 3.4 (b)). The gold wires were connected with the electric wiring of the sample holder by means of soldering tags.

Inevitable deviations of the ideal contact symmetry lead to longitudinal contributions in the Hall voltage and, respectively, to Hall contributions in the longitudinal voltage. To correct for undesired signal contributions, the Hall signal was antisymmetrized, while the longitudinal signal was symmetrized as follows:

$$U_{xy} = \frac{1}{2}(U(+B) - U(-B)) \tag{3.5}$$

$$U_{xx} = \frac{1}{2}(U(+B) + U(-B)) \tag{3.6}$$

Throughout this thesis material specific results independent of sample geometry are given in units of resistivity:

$$\rho_{xy} = \frac{U_{xy}}{I}\frac{b_\mathrm{P} d_\mathrm{P}}{b_\mathrm{K}}\frac{1}{V} \tag{3.7}$$

$$\rho_{xx} = \frac{U_{xx}}{I}\frac{b_\mathrm{P} d_\mathrm{P}}{l_\mathrm{K}}\frac{1}{V} \tag{3.8}$$

where the sample and point-contact dimensions b_P, d_P, b_K and l_K are defined as shown in Fig. 3.4. V stands for the amplifying factor of the voltage transformer (typically $V = 100$). The resistivity values in metals are generally given in μΩcm. Field and temperature sweeps were measured with the *VSM* and the *Sweet16* system in continuous mode. Typical sweep rates were less than 0.5 K/min in temperature sweeps and less than 0.1 T/min in field sweeps. Since recently, field sweep measurements in the *Sweet16* system can also be recorded in step mode.

3.8 Magnetotransport under pressure

The resistivity measurements of Fe_2TiSn under pressure were carried out with a Bridgman anvil cell in the *Sweet16* system. This pressure technique was first set-up in our group by Robert Ritz as part of his diploma thesis [128]. A qualitative depiction of the cell is shown in Fig. 3.5. Two tungsten carbide anvils are pressed onto the sample positioned in a pyrophylitte gasket. Steatite, positioned below and above the sample, is used as pressure medium. The electrical contacts are established via platinum wires placed on the sample. Under pressure the wires are pushed onto the sample and yield a good electrical connection. Steatite (or soapstone), due to its softness, allows for quasi-hydrostatic pressure within the cell (pressure anisotropies are less than 10%). The applied pressure is detected via the pressure dependence of the superconducting transition of tin.

Different pictures showing important steps of the preparation of the pressure cell may be seen in Fig. 3.6. The pyrophylitte gasket has an inner diameter of 2 mm and a height of $d \sim 250\,\mu\mathrm{m}$. A steatite disc, polished down to a height of $d \sim 80\,\mu\mathrm{m}$, is positioned within the pyrophylitte gasket. The sample ($d \sim 100\,\mu\mathrm{m}$; overall dimensions of $\sim 1 \times 0.5 \times 0.1\,\mathrm{mm}^3$) and a thin tin plate ($d < 80\,\mu\mathrm{m}$) are positioned and fixed with a small amount of GE varnish to the steatite disc. Thin platinum wires (⌀ 25 μm), are bent and positioned in a 6- and 4-point configuration to the sample and the tin plate, respectively. The platinum wires pass through thin slits in the pyrophylitte gasket and are soldered to tags positioned around the anvil. To avoid electrical shortcuts, the anvil is covered with a thin layer of two-component glue (UHU Endfest) where thin slits guide the platinum wires. Steatite powder is carefully placed on the sample, the tin plate and the platinum wires. On top, a second steatite disc ($d \sim 80\,\mu\mathrm{m}$) is placed. The position of and distance between the platinum wires positioned on the sample are recorded and measured with an optical microscope (see (a), $b_\mathrm{K} \sim 300\,\mu\mathrm{m}$, $l_\mathrm{K} \sim 730\,\mu\mathrm{m}$). Pairs of isolated copper wires are connected to the soldering tags and color-coded according to their position.

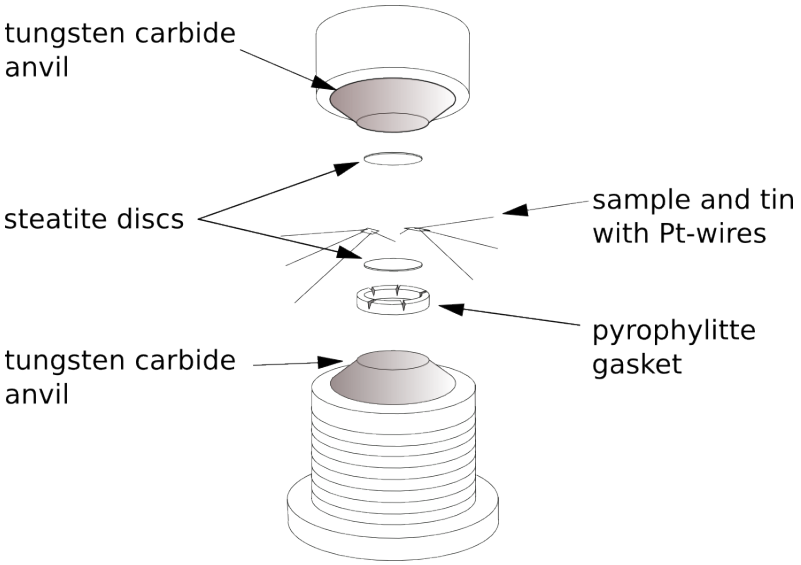

Figure 3.5: Schematic drawing of the Bridgman anvil cell used for pressure dependent magnetotransport measurement of Fe_2TiSn. The illustration is taken from Ref. [128].

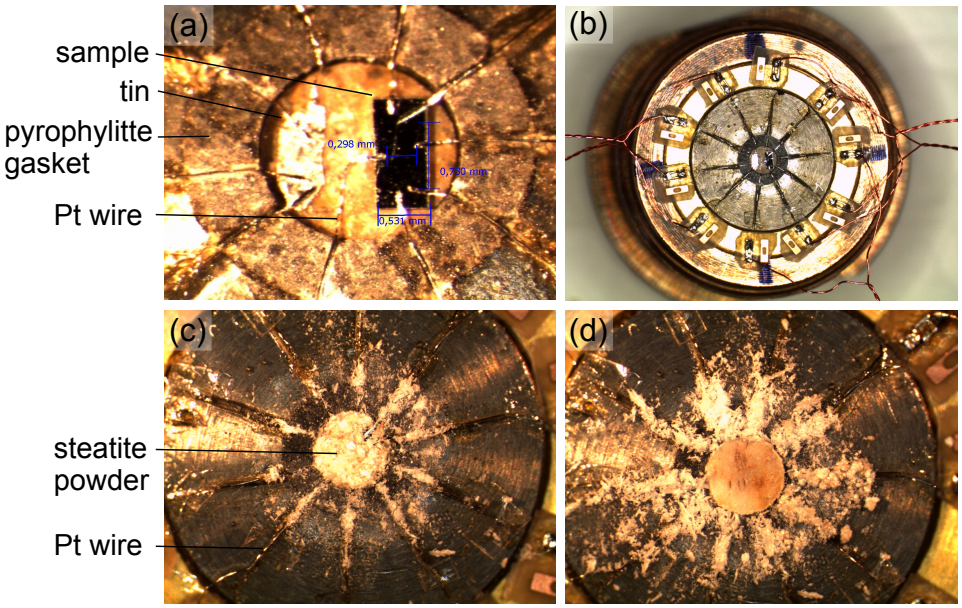

Figure 3.6: Different steps during the preparation of the anvil cell. (a) Tin (left) and sample (right) within the pyrophylitte gasket with the Pt wires positioned in the desired contact configuration. (c) Covered with steatite powder and (d) with an additional steatite disc on top. (b) Overview of the anvil.

After preparation of the sample contacts the pressure cell is loaded. The components of the pressure cell are shown in Fig. 3.7. The outer body (a) is screwed (upside-down) into the anvil onto which the sample (c) is mounted and the pairs of copper wires are passed through to the outside. The second anvil (d) is carefully inserted and placed on top, followed by a plate (e) and the lock-nut (b). Pressure is applied with a hydraulic press pushing a tungsten carbide piston against the plate. The piston is guided through the lock-nut, which is tightened to maintain the pressure. To prevent the upper anvil from turning while pressure is applied, it is fixed with a stud screw. A loaded pressure cell is shown in image (f). For the measurements the cell is bolted to a bespoke sample stick and the copper wires are connected via soldering tags to the electrical wiring of the system. For an exact determination of the temperature during the measurement, an additional thermometer is connected to the bottom of the pressure cell.

Measurements of Fe_2TiSn were performed at 5 different pressures (12 - 51 kbar) with increasing pressure. A summary of the zero field superconducting transitions of tin used to determine the applied pressures is given in Fig. 3.8. The corresponding pressures were calculated according to Eq. (3.2). In order to avoid systematic errors, measurements at the different pressures followed the same sequence.

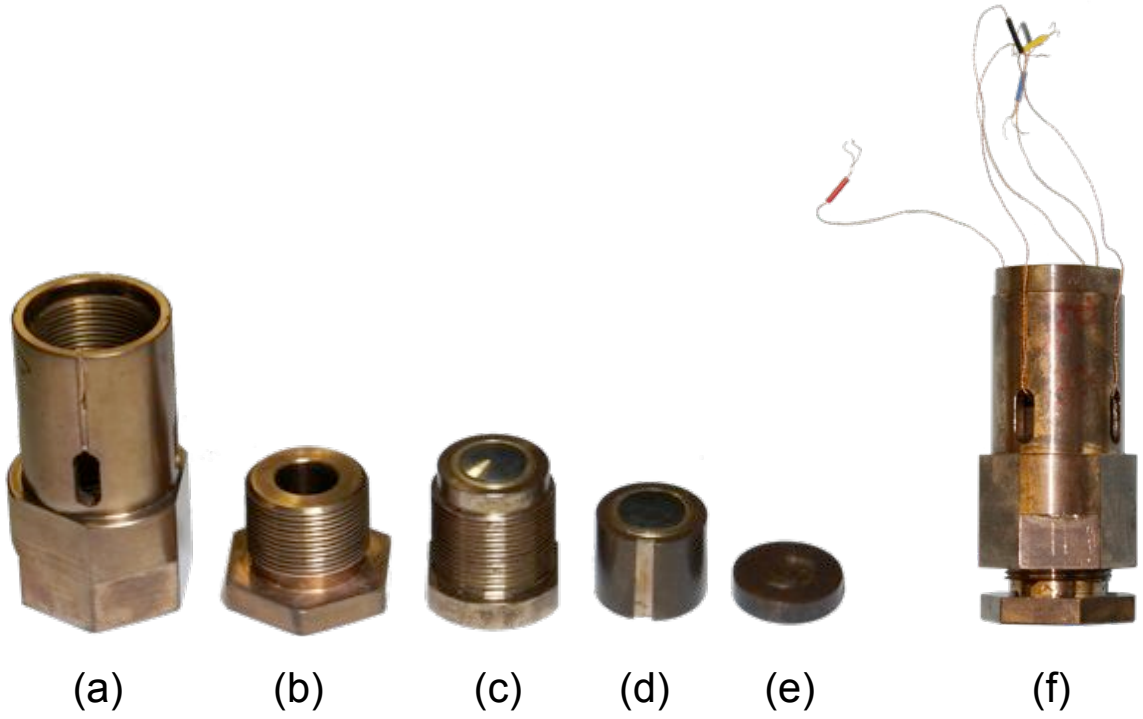

Figure 3.7: Constituent parts of the pressure cell made from Cu:Be (Berylco 25A): (a) outer cover; (b) lock-nut; (c) anvil holding the sample; (d) second anvil with linear slit; (e) intermediate plate. (f) shows an image of a loaded pressure cell with color-coded pairs of copper wires. The illustration is taken from Ref. [129].

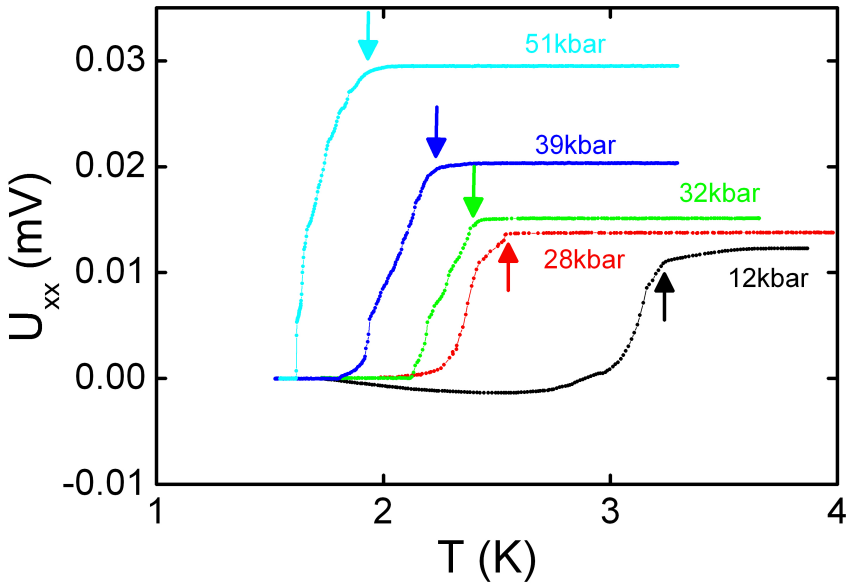

Figure 3.8: Longitudinal resistivity of the tin sample at different pressures. The applied pressure is calculated from the superconducting transition temperature according to Eq. (3.2). The 12 kbar curve was vertically shifted to account for a small set-up dependent offset.

3.9 Neutron depolarization radiography (NDR)

Spin depolarization with polarized neutrons is a powerful new method for non-destructive spatially resolved magnetization measurements of solids. This technique was investigated and installed at the ANTARES beamline [125] at the FRM II by Michael Schulz during his PhD thesis [133]. The NDR measurements of the crystals grown as part of this thesis were carried out in a close collaboration with Michael Schulz. Since it is a new technique the experimental set-up changed and improved while this studies were going on [134, 135]. Here an overview of the fundamental principle of the technique and the latest set-up used for our measurements will be given. For a detailed description of both theory and experiment of NDR we refer to the PhD thesis of Michael Schulz [133].

As sketched in Fig. 3.9 (a), radiography with polarized neutrons is based on the measurement of the beam polarization after transmission of a sample. Within the sample the interaction of the nuclear magnetic moment μ with magnetic field distributions leads to a depolarization of the neutron beam. Thus ferromagnetic regions depolarize the neutron spin depending on the orientation and size of the local magnetization, while paramagnetic regions do not change the polarization of the neutron spin. NDR therefore allows to obtain spatially resolved images of the (ferro)magnetic regimes in bulk materials with the big advantage of being fast and non-destructive, i.e., inhomogeneous samples can be directly studied at once. For materials where the ferromagnetic properties depend strongly on the stoichiometry (as it is the case for Ni_3Al, $NbFe_2$ and Fe_2TiSn studied in this thesis) NDR is an ideal method to determine the crystal homogeneity. It hence provides important information that allows to improve the growth of single crystals.

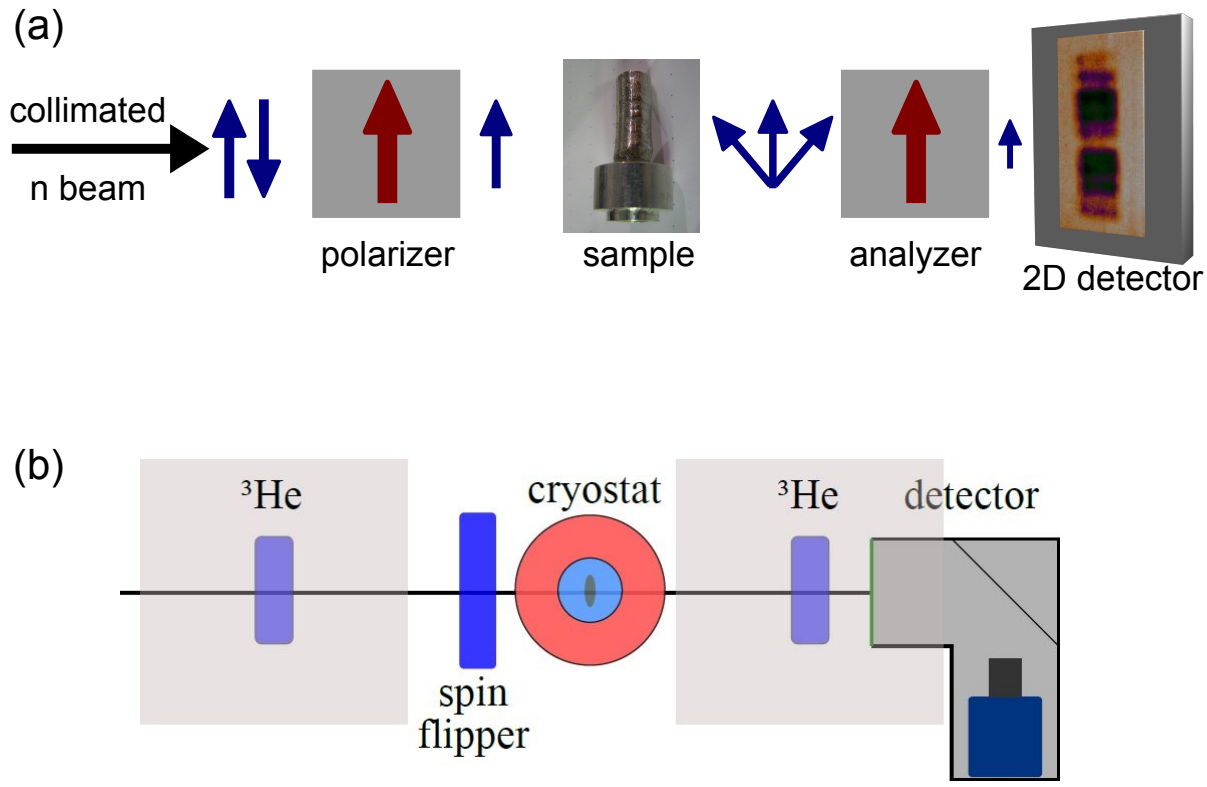

Figure 3.9: (a) Basic principle of neutron depolarization imaging. The neutron spin direction as illustrated by the blue arrows gets depolarized. The depolarization is resolved spatially. (b) Schematic setup for polarized neutron radiography at ANTARES at FRM II consisting of a ^{3}He polarizer with integrated spin flipper, a coldhead with a base temperature of 5 K, a ^{3}He analyzer, a neutron sensitive LiF:ZnS scintillator and a position sensitive CCD detector [133–135].

In a first approximation the polarization P of the neutron beam after transmission of a ferromagnetic sample with no macroscopic magnetization may be given as [133]:

$$P = P_0 \exp(-\frac{1}{3}\gamma^2 \langle B^2 \rangle \frac{\delta}{v^2} \mathrm{d}), \tag{3.9}$$

where P_0 is the neutron polarization prior to the transmission of the sample, γ is the gyromagnetic ratio of the neutron, B is the local magnetic field (or moment) of the magnetic domains with an average size δ, d is the sample thickness and v the neutron velocity. We want to emphasize that the exponential decay of the polarization depends mainly on the square of the local magnetic moment, the sample thickness and the domain size.

The experimental set-up is sketched in Fig. 3.9 (b) and consists of a ^{3}He polarizer[3] with integrated spin flipper, a Helium free closed cycle cryostat with a base temperature of 5 K, a ^{3}He analyzer and a position sensitive CCD detector that records the image of a neutron sensitive scintillator, which is placed behind the analyzer. The minimum distance between sample and detector - the smaller the distance the better the resolution - is restricted to

[3]The ^{3}He cells were provided by Sergey Masalovich from the HELIOS group at the FRM II[136].

around 300 mm by the magneto-static cavity containing the ^{3}He cell. This cavity serves to increase the relaxation time of the polarized ^{3}He. With this setup a spatial resolution of ~ 0.3 mm was obtained.

Measurements were performed both with a monochromatic and a polychromatic neutron beam with wavelengths $\lambda = 3.2$ Å and $\lambda \geq 4$ Å, respectively. Using a polychromatic beam increases the neutron flux and consequently the counting statistics of the measurement compared to a monochromatic beam. In turn it leads to a reduction of the measurement time. The flipping ratio of the ^{3}He cells for a polychromatic beam with wavelengths $\lambda \geq 4$ Å has a sufficiently high value of $R \approx 10$ in order to achieve a good contrast.

For the measurements the samples were mounted in an aluminum can filled with He exchange gas. The aluminum can was bolted to a closed cycle cryostat with a base temperature of 5 K. An additional thermometer connected to the can allowed for precise measurements of the sample temperature. NDR data were taken at fixed temperatures. At each temperature up to 15 images for both spin-up and spin-down were recorded, providing good counting statistics.

For the evaluation of the depolarization measurements, the beam polarization P_B at the detector is given as

$$P_\mathrm{B} = (I_+ - I_-)/(I_+ + I_-), \tag{3.10}$$

with I_+ and I_- being the measured intensities at the detector with the spin flipper turned "off" and "on". In addition, "dark current" of the CCD detector (I_dc) and gamma induced intensities at the detector that are reduced with the gamma filtering function $G(I)$, as well as the polarizing efficiency of the polarizer and analyzer (P_0) have to be taken into account. This leads to the final expression of the polarization of the beam P after transmission of the the sample (see also Ref. [133]):

$$P = \frac{1}{P_0} \frac{\sum_i (G(I_{+,i}) - I_\mathrm{dc}) - \sum_i (G(I_{-,i}) - I_\mathrm{dc})}{\sum_i (G(I_{+,i}) - I_\mathrm{dc}) + \sum_i (G(I_{-,i}) - I_\mathrm{dc})}, \tag{3.11}$$

with i summing over the single images recorded at each temperature. For every image shown in this thesis the above procedure was used to calculate the beam polarization P from the measured intensities.

3.10 Small angle neutron scattering

Small angle neutron scattering experiments with cold neutrons were carried out at the diffractometer MIRA [126] at FRM II. The access to two neutron guides permits experiments with neutron wavelengths λ= 3 - 6 Å and λ = 8 - 30 Å, labeled MIRA1 and MIRA2, respectively. A ^{3}He counter tube and a two dimensional position sensitive detector with a resolution of $1 \times 2\,\mathrm{mm}^2$ are available for neutron detection. For polarization analysis a polarizing multilayer monochromator is available at MIRA1. The polarization may be analyzed by a polarizing bender or a ^{3}He cell. A detailed description of the experimental set-up used for the polarization analysis of Cu_2MnAl (MIRA2) and the B20 gradient crystals (MIRA1) is given in chapter 4 and chapter 8, respectively.

Chapter 4

Results & Discussion: Cu_2MnAl

The growth of Cu_2MnAl single crystals was mainly motivated by its importance for technical applications, notably polarizing monochromators in neutron scattering. In this chapter the growth of large single crystals of Cu_2MnAl by means of optical float-zoning with the high purity image furnace will be presented. The float-zoned crystals show an excellent and highly reproducible crystal quality with a narrow and homogeneous mosaic spread, in stark contrast to the anisotropic mosaic spread observed in Bridgman grown crystals [23]. Investigation of the polarizing properties established indications of a high polarization efficiency of our float-zoned crystals, at least comparable with those obtained for the "good" Bridgman grown crystals.

4.1 Single crystal growth of Cu_2MnAl

The ferromagnetic Heusler alloy Cu_2MnAl was the first compound that was grown in the course of this thesis, since appropriate starting rods of Cu_2MnAl were available prior to the construction of the rod casting furnace. The first two crystals, HKZ361 and HKZ363, were grown in collaboration with Günther Behr in a vertical double ellipsoid image furnace (URN-2-ZM, MPEI, Moscow) at the IFW in Dresden. A growth rate of 15 mm/h and a counter-rotation of 40 rpm (seed) and 25 rpm (feed) were applied. As starting rods for HKZ361, rectangular bars with an edge length of $4 \times 4\,\mathrm{mm}^2$ were used. These bars were cut from large Bridgman grown crystals of Cu_2MnAl provided by Peter Böni. For the growth of HKZ363 poly-crystalline seed and feed rods with a diameter of 6 mm, cast in a rod casting furnace at the IFW in Dresden, were used. The growth processes took place in a high purity flowing Argon gas environment (6 - 10 l/h) of $p \sim 1.1$ bar.

An abundance of oxide contamination flowing on the molten zone disturbed a stable growth process for both crystals. Attrition of oxide layers led to a shaking of the zone that resulted in repeated separations of the zone during the growth process. The strong contamination with oxide on the outside of HKZ361 and HKZ363 can be clearly seen by the grey and brown staining (see Fig. 4.1).

Nevertheless, large single crystal grains were found in the as-grown crystals as shown in Fig. 4.2 (a). The image shows the quenched last zone of HKZ363. The surface was etched with Marble reagent ($2.5\,\mathrm{g}\ CuSO_4 + 30\,\mathrm{cm}^3\ HCl + 25\,\mathrm{cm}^3\ H_2O$) for a better visibility of the grain structure. The growth direction is from the left to the right. In the crystal three grains can be identified with the grain at the center expanding in size. A slightly convex curved growth interface (marked by the dashed red line) separates the crystal that was grown from the poly-crystalline structure of the feed rod. In the poly-crystalline feed large grains already formed in the vicinity of the growth interface. EDX investigation of the surface showed a stoichiometric Cu_2MnAl composition with no indication of secondary phases. These findings indicate Cu_2MnAl as a congruently melting compound that shows a strong tendency to crystallize in a mono-crystalline structure.

With the experience gained at the IFW six more Cu_2MnAl were grown at the TUM with the UHV-compatible 4 - mirror image furnace described in chapter 2.1.2. OFZ1 was grown from rectangular bars as in the case of HKZ361. OFZ3, OFZ4, OFZ5, OFZ6 and OFZ10 were grown from poly-crystalline rods that were prepared with our rod casting furnace (RCF). Cu_2MnAl thereby proved to be an ideal compound for casting with the RCF. Starting with clean material of stoichiometric composition every casting process, carried out in a high purity Argon atmosphere ($p \sim 1.5\,\mathrm{bar}$), was successful, and long, homogeneous rods without signs of impurities could be prepared. For crystals OFZ1-OFZ6 growth rates of 10-12 mm/h were applied as shown in Table 2.1. For OFZ10 the growth rate was increased from 5 mm/h to 10 mm/h during the growth. In each growth process the feed and seed rod were counter-rotated with 10 rpm and 30 rpm, respectively.

Prior to each growth process the image furnace was carefully baked out (10^{-8} mbar) and filled with 6N Argon gas, that was additionally purified with the getter furnace. Each growth process took place in a static Argon atmosphere of $p \sim 1.5\,\mathrm{bar}$. A strong reduction of the oxide layers floating on the molten zone was observed in comparison to the crystals grown at the IFW. Fig. 4.1, that shows crystals HKZ361 and HKZ363 (IFW) as well as OFZ6 and OFZ10 (TUM), clearly illustrates the difference in surface contamination. The high-purity environment enabled us to establish a stable zone during the whole growth process. We attribute the complete grain selection process, that resulted in a mono-crystalline structure across the entire cross section of the rod for all crystals grown in the OFZ, to this improved stability of the zone.

Single-crystallinity was confirmed for all Cu_2MnAl crystals grown in the OFZ by means of X-ray Laue diffraction and light microscopy. As an example the polished and etched cross section of the end of OFZ1 is shown in Fig. 4.2 (b). In addition, single crystal neutron scattering experiments on OFZ5 at the diffractometer RESI at FRM II [122] confirmed bulk single-crystallinity. Fig. 4.3 shows the areas of OFZ5 that were investigated at RESI[1] These measurements nicely illustrated the growth selection process. Starting with several grains at the beginning of the crystal (a), the number of the grains reduced along the crystal (b), resulting in a mono-crystalline structure across the entire cross section of the rod at the end of the crystal (c, d).

[1]The diffraction results, obtained as a set of images of the area detector (see 2.2.3), are not shown, since a crystallographic analysis is necessary in order to obtain information on the single-crystallinity.

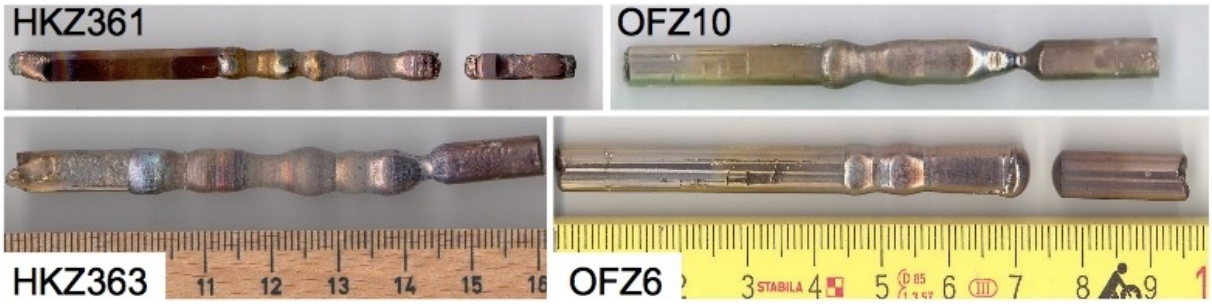

Figure 4.1: Cu_2MnAl crystals HKZ361 and HKZ363 grown at the IFW in Dresden clearly show an abundance of oxide contamination as compared to the Cu_2MnAl crystals OFZ6 and OFZ10 grown with the UHV-compatible image furnace at our institute. The scale at the lower end holds for all crystals.

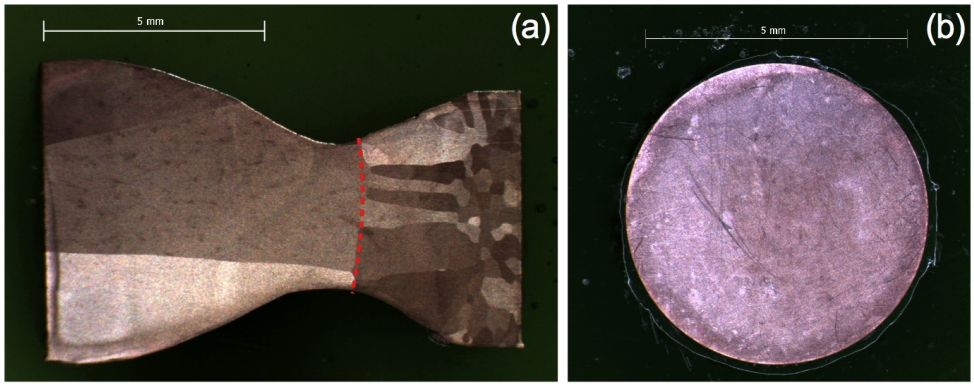

Figure 4.2: (a) Last zone of Cu_2MnAl crystal HKZ363. The growth direction is from the left to the right. Three large grains can be clearly identified to the left hand side of the interface. They are separated by the slightly convex growth interface (see dashed red line) from the polycrystalline feed rod, where large grains already form in the vicinity of the interface. (b) Single-crystalline surface of the cross section at the end of OFZ1. Both surfaces were polished and etched with Marble reagent in order to highlight grain structures.

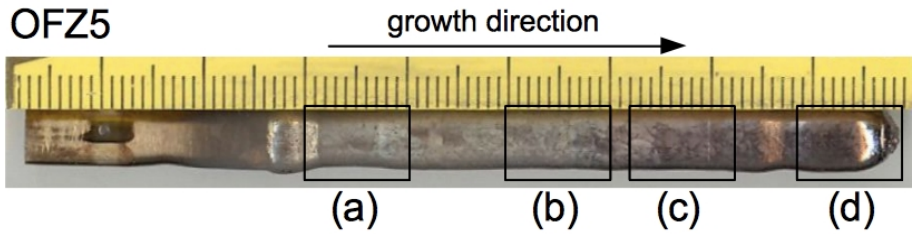

Figure 4.3: Cu_2MnAl crystal OFZ5 investigated with single crystal neutron diffraction at RESI. Black squares mark the areas that were scanned. Several single-crystalline grains were found in (a), a reduced number in (b), and in (c) and (d) only one grain was identified. This measurement nicely illustrates the grain selection process that takes place during crystal growth of Cu_2MnAl.

For further experiments large single-crystalline samples were prepared from OFZ3, OFZ5, OFZ6 and OFZ10, as shown in Fig. 4.4. Single-crystallinity of the samples was confirmed with a light microscope and by means of X-ray Laue diffraction. Any secondary grains were removed, as can be seen by the vertical cuts at the bottom ends of the crystals. The orientation of the crystal structure with respect to the growth direction was investigated by means of X-ray Laue diffraction. A different crystal orientation was found for each crystal. Since poly-crystalline rods rather than oriented crystals were used as seed rods in each growth process, no preferred growth direction could be identified for Cu_2MnAl.

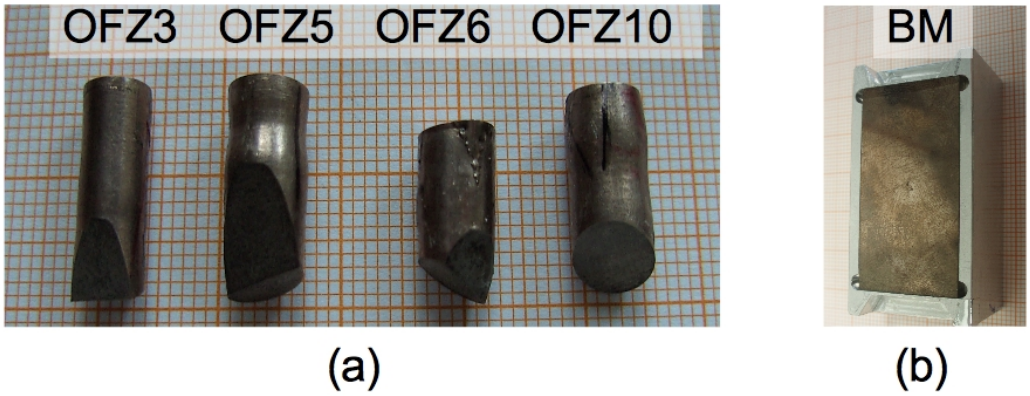

Figure 4.4: (a) Single-crystalline Cu_2MnAl crystals. No preferred growth direction of the crystal structure was identified. (b) Bridgman grown Cu_2MnAl crystal ($40 \times 20 \times 3\,mm^3$) provided by Peter Böni. The disc is mounted to an aluminum holder with the flat side being a crystallographic (111) plane. Note the different scale of the images.

4.2 Magnetization measurements

The ferromagnetic properties of the Cu_2MnAl crystals allow to compare the sample quality. In order to avoid systematic errors due to strong demagnetizing effects in Cu_2MnAl [24] and, hence, to be able to quantitatively compare the magnetic properties, oriented samples of the same dimensions were prepared from OFZ3, OFZ5, OFZ6, OFZ10 and from a Bridgman grown crystal (BM). The samples were cut in a rectangular shape of dimension $5 \times 2.5 \times 2\,mm^3$ with the flat front surface being a (111) crystallographic plane and the small bottom surface a (110) plane.

All five samples were measured in the vibrating sample magnetometer (VSM) with the magnetic field parallel to the long axis, e.g., the configuration that minimizes the demagnetizing effects. Figs. 4.5 (a) and (b) show the field dependent magnetization at 4 K and 300 K for fields up to 9 T and for low fields, respectively. At high fields and 4 K the magnetization saturates for all samples at $m \sim 3.6\,\mu_B$/f.u.. At 300 K the magnetization saturates for all samples at $m \sim 3.2\,\mu_B$/f.u.. Both values are in perfect agreement with values given in the literature [19]. At low fields the magnetization shows a linear slope followed by the onset of saturation at 90 mT for both temperatures and all samples. The curves show no signs of hysteretic behavior.

Fig. 4.6 shows the temperature dependence of the magnetization for all samples at an applied field of 1 T. The magnetization shows a continuous decrease with increasing temperature. All samples show similar behavior. The magnetic moments of the samples differ by less than 3 %. Hence, the magnetic properties of the floating zone grown crystals are in very good agreement with respect to each other and as compared with the Bridgman grown sample. This indicates a good and highly reproducible quality of the floating zone grown crystals.

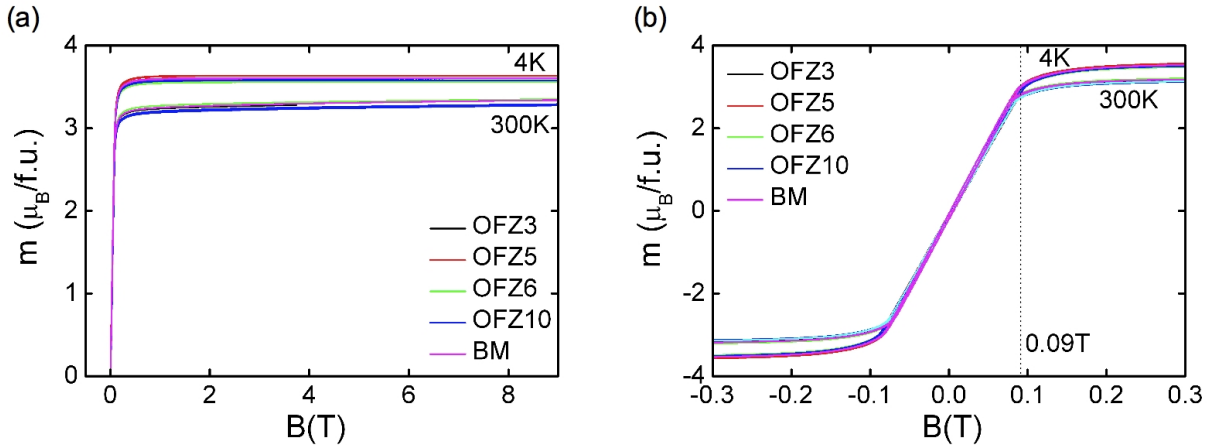

Figure 4.5: (a) Field dependent magnetization for large fields and $T = 4\,\mathrm{K}$ and $T = 300\,\mathrm{K}$. All float-zoned Cu_2MnAl samples, OFZ3, OFZ5, OFZ6, and OFZ10 as well as the Bridgman grown sample (BM) show the same behavior and saturate at $m \sim 3.6\,\mu_B$/f.u. and $m \sim 3.2\,\mu_B$/f.u. at $T = 4\,\mathrm{K}$ and $T = 300\,\mathrm{K}$, respectively. (b) Low field region of the magnetization curves. All samples saturate ferromagnetically for fields $B \geq 90\,\mathrm{mT}$.

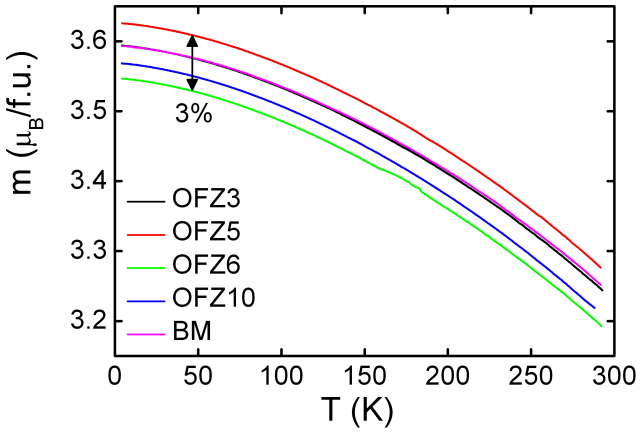

Figure 4.6: Temperature dependence of the magnetic moments of the four floating zone grown (OFZ) and the Bridgman grown (BM) Cu_2MnAl crystals at an applied field of 1 T. With increasing temperature the magnetic moments are decreasing. The low temperature magnetization of the samples is in a range of $3.58 \pm 0.05\,\mu_B$/f.u.. Hence, the absolute deviations of the samples with respect to each other are very small ($\leq 3\%$).

4.3 Neutron single crystal diffraction at HEIDI

The main challenge in the preparation of monochromators for polarized neutron scattering from Cu_2MnAl Heusler crystals lies in the growth of large and homogeneous crystals with a well defined mosaic spread. A mosaic spread in the range of $0.5° - 1°$ is desirable in order to obtain large intensities. However, previous studies established that crystals prepared by the Bridgman technique are characterized by very large anisotropies of the mosaic distribution depending on the growth direction [23], as shown in Fig. 4.7. This sensitivity of the crystal quality on the growth conditions results in a poor success rate of less than 50% in the production of single crystal slabs with excellent polarizing properties suitable for monochromators.

In order to investigate the mosaic spread in our crystals grown by optical float-zoning we carried out neutron scattering experiments at the single crystal diffractometer HEIDI at FRM II [123]. We investigated single crystals of different dimensions prepared from OFZ3, OFZ5, OFZ6 and OFZ10 and, for comparison, a Bridgman grown (BM) single-crystalline disc (see Fig. 4.4).

For each crystal rocking scans with respect to the three main $\langle 400 \rangle$ symmetry directions and the four $\langle 111 \rangle$ directions were carried out. For OFZ10 the $\langle 333 \rangle$ directions were studied and for BM a single [333] direction. Both the integrated and absolute intensities of the Bragg reflections of the different rocking scans vary because different sample volumes were measured for each direction. Nevertheless, the width of the rocking curves, presented in terms of the full-width-have-maximum (FWHM) in Table 4.1, provides information on the isotropy of the mosaic spread. The FWHM values were obtained directly by means

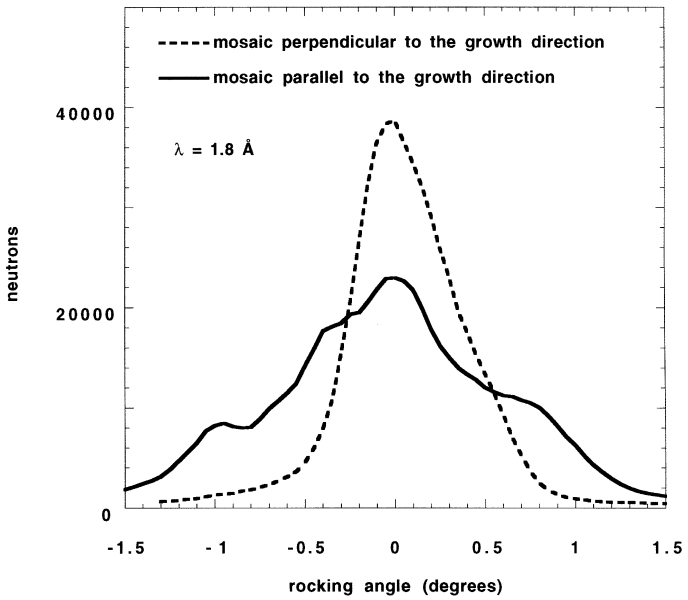

Figure 4.7: Neutron rocking curves from a Cu_2MnAl crystal grown by the Bridgman technique for a scattering plane perpendicular and parallel to the growth direction. The different peak width illustrates the anisotropic mosaic spread. The plot was taken from Ref. [23].

of the measurement software at HEIDI through extrapolation of the measured intensities. This method gives a real illustration of the mosaic distribution in comparison to the FWHM obtained from standard Gauss fits, where a homogeneous mosaic distribution is assumed [105].

An overview of the $\langle 400 \rangle$ and $\langle 111 \rangle$ Bragg scattering intensities as a function of the rocking angle Θ is shown in Fig. 4.8. OFZ3 (a, b) and OFZ5 (c, d) show similar, very homogeneously shaped rocking curves for all $\langle 400 \rangle$ and $\langle 111 \rangle$ directions. This is confirmed by the very homogeneous distribution of the FWHM values around 0.31° ($\langle 400 \rangle$) and 0.41° ($\langle 111 \rangle$) for OFZ3 and 0.26° ($\langle 400 \rangle$) and 0.41° ($\langle 111 \rangle$) for OFZ5, respectively. The instrumental resolution of the FWHM is $\pm 0.1°$. The values are summarized in Table 4.1. The rocking curves for OFZ6 (e, f) are slightly broadened with a small second peak. This also shows up in terms of the larger divergence of the FWHM for the different scattering directions. Nevertheless, in comparison to the data obtained for the Bridgman grown crystals (see Fig. 4.7), OFZ6 shows a more or less isotropic mosaic distribution.

Clear deviations from an isotropic mosaic spread are found for OFZ10 (g, h), where two intensity maxima are seen for most of the directions. This signature is most likely due to the application of two different growth velocities (10 mm/h and 5 mm/h) during the growth of OFZ10. This sensitivity of the mosaic distribution to variations of the growth rate might be advantageous, if varied in a more moderate way, for the preparation of optimized monochromator crystals. As mentioned above, a mosaic spread ($0.5° < \mathrm{FWHM} < 1.0°$) is necessary in order to ensure high neutron intensities.

Finally, Fig. 4.9 shows the rocking scan of the [333] direction of the large Brigdman grown sample (cf. Fig. 4.4 (b)). The (111) plane was prepared perpendicular to the growth direction. In comparison to the float-zoned crystals OFZ3 and OFZ5 the rocking scan of the Bridgman grown crystal is less homogeneous and has a larger FWHM value.

Crystal	OFZ3	OFZ5	OFZ6	OFZ10	BM
FWHM $\langle 400 \rangle$	0.31° 0.34° 0.27°	0.25° 0.26° 0.28°	0.49° 0.42° 0.27°	0.52° 0.33° 1.28°	
FWHM $\langle 111 \rangle$ ($\langle 333 \rangle$ for OFZ10 & BM)	0.41° 0.39° 0.42° 0.42°	0.41° 0.41° 0.41° 0.43°	0.43° 0.53° 0.46° 0.73°	0.74° 0.72° 0.65° 0.26°	0.54°

Table 4.1: Summary of the Bragg diffraction FWHM values of different Cu_2MnAl samples measured at HEIDI (see Fig. 4.8 and Fig. 4.9). The accuracy of the FWHM is ± 0.1, as was the step width of the rocking scans. The different values for the $\langle 111 \rangle$ and $\langle 400 \rangle$ directions are due to the resolution function of the instrument [105]. OFZ3, OFZ5, OFZ6 and OFZ10 denote the float-zoned crystals and BM a Bridgman grown crystal.

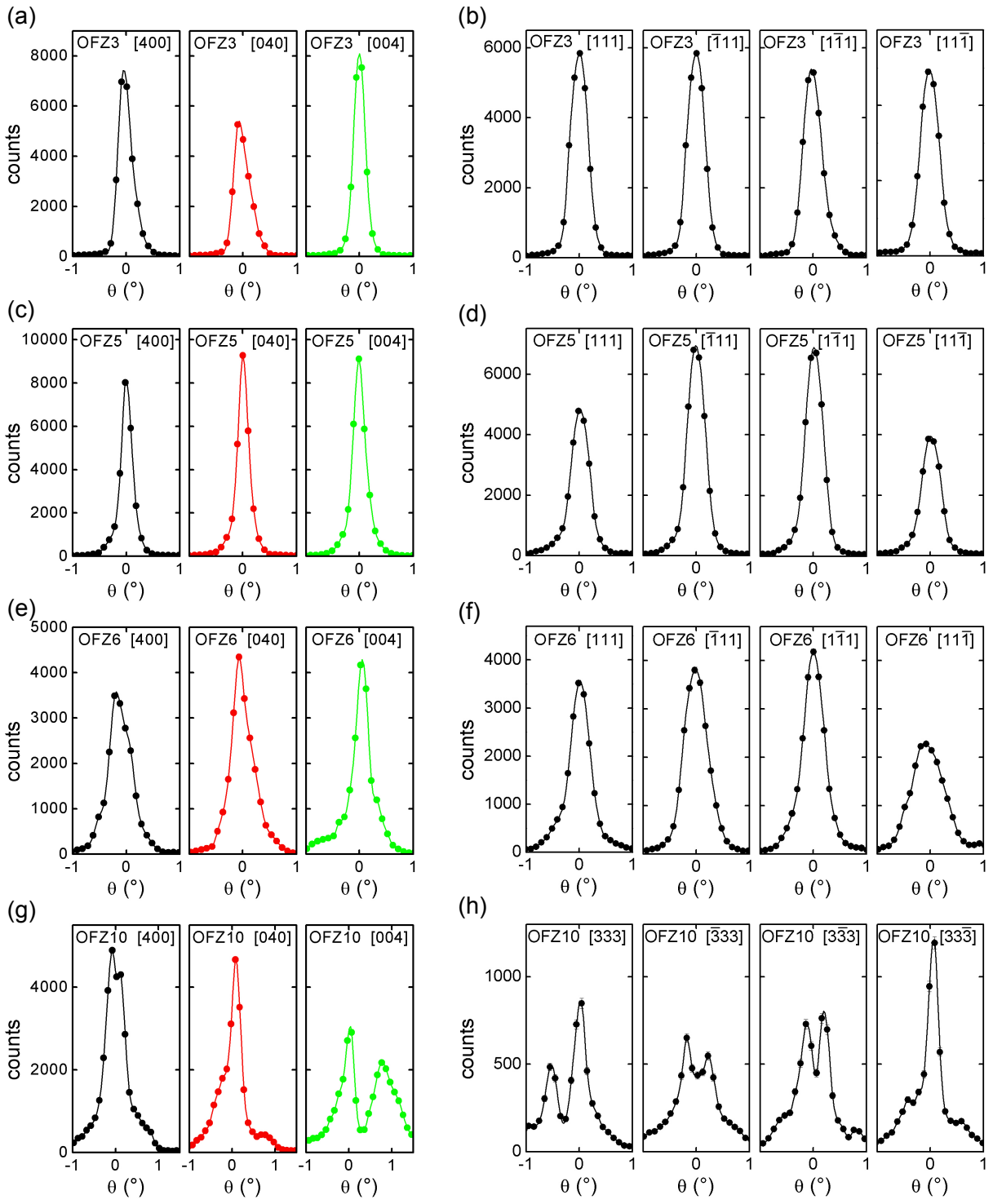

Figure 4.8: Overview of the ⟨400⟩ and ⟨111⟩ Bragg scattering intensities as a function of the rocking angle Θ for the float-zoned crystals. OFZ3 (a, b) and OFZ5 (c, d) show very homogeneously shaped rocking curves for all ⟨400⟩ and ⟨111⟩ directions. For OFZ6 (e, f) the curves are slightly broadened. The inhomogeneous peak structure of crystal OFZ10 (g, h) is most likely due to a change of the growth rate during crystal growth.

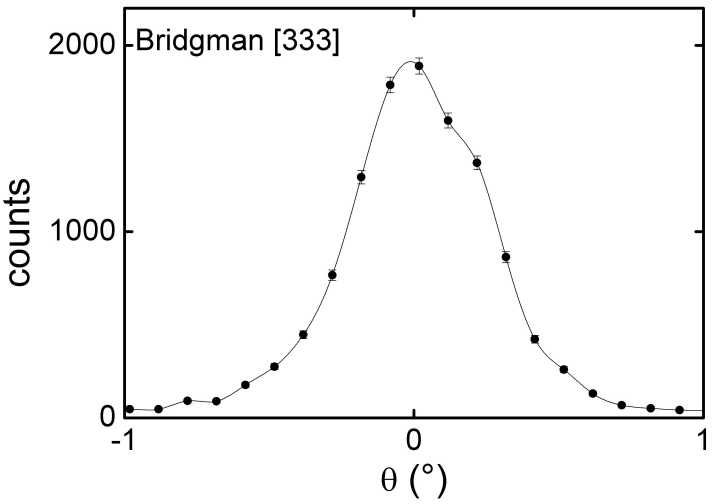

Figure 4.9: [333] Bragg scattering intensity as a function of the rocking angle Θ for the large Bridgman grown disc. The rocking curve is slightly broadened, indicating a coarser mosaic spread in comparison with the float-zoned crystals OFZ3 and OFZ5 (see Fig. 4.8).

The comparison shows that floating zone crystal growth allows to reproducibly grow Cu_2MnAl single crystals with a *homogeneous* mosaic spread that is, at least, comparable to the "good" mosaic spread that is found perpendicular to the growth direction of Bridgman grown crystals.

4.4 Polarization analysis at MIRA

4.4.1 Introduction

As reported in the literature [26], the Bragg (111) reflection from Cu_2MnAl Heusler crystals may be used to generate a monochromatic beam of polarized neutrons. In general, scattering of an unpolarized neutron beam on a ferromagnet results in individual structure factors for nuclear F_{nuc} and magnetic F_{mag} scattering, that sum up individually to a common scattering intensity [137, 138]. For a ferromagnet the scattering intensity is given as

$$I_{\mathrm{zf}} \propto F^2_{\mathrm{tot,zf}} = F^2_{\mathrm{nuc}} + q^2 F^2_{\mathrm{mag}}, \tag{4.1}$$

where $\mathbf{q}$ is the magnetic interaction vector and $q^2 = \sin^2\alpha$. α is the angle between the magnetization and the scattering vectors. In a cubic magnetic crystal without anisotropy, as it is the case for Cu_2MnAl, q^2 takes a value of 2/3.

For a saturated ferromagnet with the magnetization direction perpendicular to the scattering vector, the scattering intensity for neutrons with spin parallel (+) to the magnetization direction is given as

$$I_{+} \propto F^2_{\mathrm{tot},+} = F^2_{\mathrm{nuc}} + F^2_{\mathrm{mag}}, \tag{4.2}$$

while

$$I_- \propto F^2_{\mathrm{tot},-} = F^2_{\mathrm{nuc}} - F^2_{\mathrm{mag}} \tag{4.3}$$

is the scattering intensity for neutrons with spin antiparallel $(-)$ to the magnetization direction.

In the case of Cu_2MnAl the magnetic structure factor for (111) Bragg scattering is comparable to the nuclear structure factor, i.e., $F^{(111)}_{\mathrm{mag}} \simeq F^{(111)}_{\mathrm{nuc}}$ [26]. ConsideringEq. (4.2) and Eq. (4.3), scattering of the (111) plane hence leads to a high flipping ratio $R = I_+/I_-$ and a polarized neutron beam with a high polarization P defined as

$$P = \frac{I_+ - I_-}{I_+ + I_-}. \tag{4.4}$$

4.4.2 Experimental set-up

The measurements were carried out in collaboration with Florian Jonietz at the MIRA2 beamline at FRM II. The set-up used for polarization analysis is shown in Fig. 4.10 (a). An important prerequisite for polarization analysis is a continuous magnetic field along the flight path of the polarized neutrons because strong field gradients and especially zero field regions lead to a strong depolarization of the neutron beam and must be excluded.

The cross section of the monochromatized neutron beam of wavelength $\lambda = 4.2 \pm 0.1$ Å was confined by the source aperture (S1) and the sample aperture (S3). In this experiment the apertures were $\mathrm{S1} = 3 \times 4\,\mathrm{mm}^2$ and $\mathrm{S3} = 5 \times 8\,\mathrm{mm}^2$ (width×height), ensuring that the small samples were entirely illuminated by the neutron beam. A Be filter at a temperature of 30 K was used to remove neutrons with higher order wavelengths. The sample was positioned on a goniometer in an external magnetic field. A magnetic guide field provided a continuous magnetic field for the neutron beam after the (111) Bragg scattering at the sample.

The polarization of the neutron beam was analyzed with a ^{3}He cell that was provided by the HELIOS group of the FRM II [136]. The ^{3}He cell was placed inside a magnetic cavity that acts as a guide field. The cavity furthermore allowed to flip the polarization of the ^{3}He gas with an integrated adiabatic fast passage (AFP) flipper device [139]. A ^{3}He counter tube, right next to the cavity, was used as a detector.

The polarization analysis was carried out with two different arrangements of the ^{3}He cell as shown in Fig. 4.10 (b, c). For the first set of measurements the ^{3}He cell was positioned perpendicular to the neutron beam. With this set-up the flight path of the neutrons through the polarized ^{3}He gas is short and the scattering is reduced. This implies that around 15 - 20% of the neutrons with a polarization other than the polarization of the ^{3}He gas are transmitted. In this configuration the ^{3}He cells have a polarization efficiency $P_0^{\mathrm{rel}} \sim 80$ - 85% [136]. This only allows a relative measure of the polarization efficiency of the Cu_2MnAl crystals, but leads to good counting statistics and was therefore chosen to test the experimental set-up and record rocking scans and field dependencies. For an absolute measure of the polarization efficiency of the crystals, the ^{3}He cell was positioned

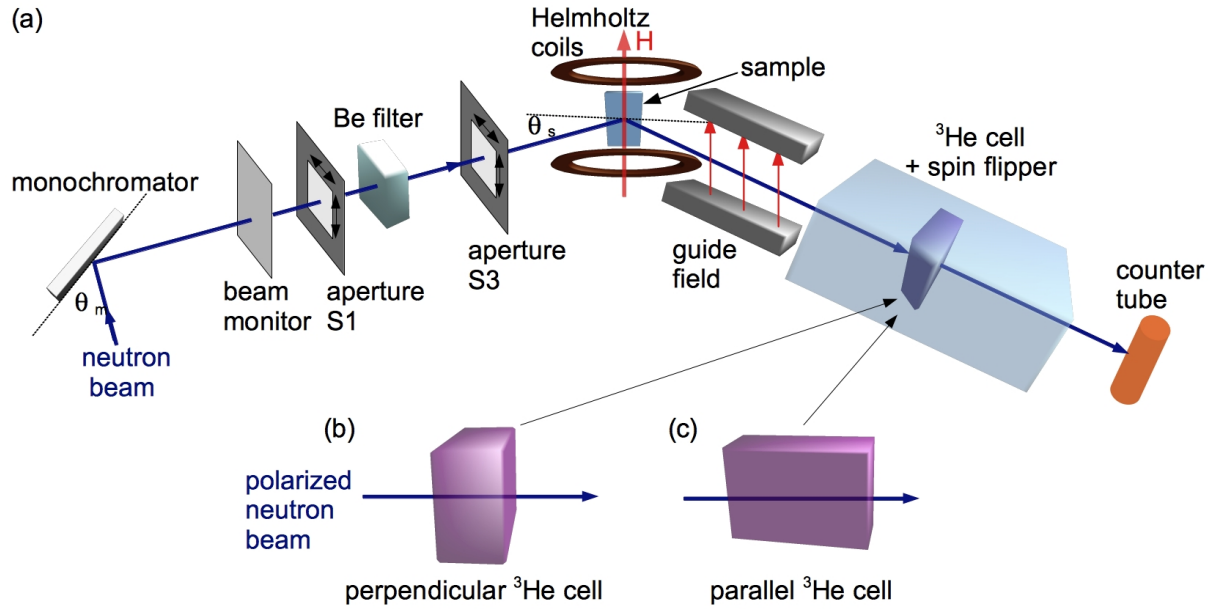

Figure 4.10: (a) Set-up for the polarization analysis of the Cu_2MnAl crystals at the MIRA2 beamline at FRM II. For details see text. (b) ^{3}He cell perpendicular to the neutron beam and (c) parallel to the neutron beam.

parallel to the neutron beam. With this set-up the flight path of the neutrons through the polarized ^{3}He gas is long and only neutrons with a polarization direction parallel to that of the ^{3}He gas are transmitted. In this configuration the ^{3}He cells have a polarization efficiency of $P_0^{\text{abs}} > 99\%$ [140].

The samples grown in the image furnace (OFZ3, OFZ5, OFZ6 and OFZ10) and the small Bridgman grown sample (BMsmall) we investigated here were the same as those used for the magnetization measurements (see section 4.2). These samples were small with dimensions of $5 \times 2.5 \times 2\,\text{mm}^3$. In addition, we investigated the large Bridgman grown (BM) crystal ($40 \times 20 \times 3\,\text{mm}^3$, see Fig. 4.4 (b)) we had characterized at HEIDI and a large inhomogeneously shaped slab (BMlarge, in average $60 \times 30 \times 4\,\text{mm}^3$), from which BMsmall was cut. All samples were prepared and mounted with the large front side being a (111) plane.

In a first test the OFZ samples were mounted in a bespoke aluminum holder designed for our experiment (see Fig. 4.11 (a)). The holder was clamped within a horseshoe magnet, and additional Fe pieces that were placed in the cavities served as pole shoes. This set-up (without the Helmholtz coils) provided a magnetic field of $\sim 180\,\text{mT}$, which is twice the field necessary to saturate the samples (cf. Fig. 4.5). Measurements with this set-up resulted in unexpected low flipping ratios of $R \sim 2$. We believe that field gradients surrounding the sample lead to a depolarization of the beam right after the scattering process and, hence, to the low flipping ratios observed. For that reason the set-up was changed. The horseshoe magnet and pole shoes were removed, and instead a homogeneous magnetic field was generated by a set of Helmholtz coils as shown in Fig. 4.10 (a). With the Helmholtz coils a magnetic field of up to 220 mT could be applied.

Rocking scans were recorded at a 2θ angle of 74.2°, appropriate for the (111) Bragg reflex of a cubic crystal structure with lattice constant $a = 5.996$ Å ($d_{(111)} = a/\sqrt{3}$) and a neutron wavelength $\lambda = 4.2$ Å. Typically the sample was rocked through a range of 3°.

4.4.3 Polarization analysis

^{3}He cell perpendicular to the neutron beam

We recorded rocking scans in an applied field of 220 mT analyzing both spin configurations. The spin-up configuration (I_+, Eq. (4.2)), for which the ^{3}He cell allows neutrons to pass with spin parallel to magnetization direction. And the spin-down configuration (I_-, Eq. (4.3)), for which the ^{3}He cell allows neutrons to pass with spin antiparallel to magnetization direction. In addition, we recorded rocking scans with no applied field (I_{zf}, see Eq. (4.1)). The results for crystals OFZ3, OFZ5, OFZ10 and BM are shown in Fig. 4.12. The curves are Gaussian fits to the data.

Similar to the results of the measurements at HEIDI we observed a narrow (111) Bragg peak for OFZ3 and OFZ5 with a FWHM of 0.28° and 0.35°, respectively, as well as the double peak structure for OFZ10 and the slightly broadened peak for the Bridgman grown sample (BM). As expected from Eq. (4.1)−(4.3) we obtained the maximum intensity for the spin-up configuration, the minimum intensity for the spin-down configuration and an intensity maximum close to the spin-up configuration for the zero field measurements. Analysis of the maximum intensities give a flipping ratio $R \sim 4.5$ for OFZ3, OFZ5 and OFZ10 and a flipping ratio of $R \sim 10$ for the Bridgman crystal.

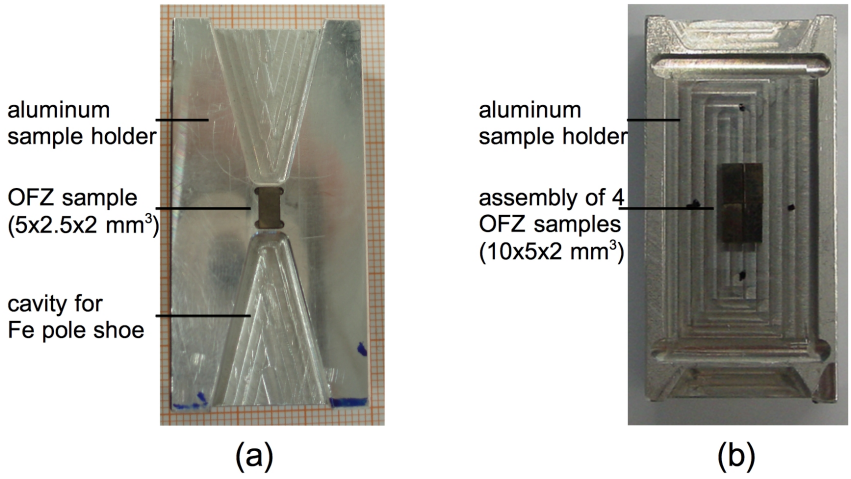

Figure 4.11: (a) Floating zone grown Cu_2MnAl sample mounted to an aluminum holder. The holder can be clamped within a horseshoe magnet and Fe pole shoes, placed in the cavities, provided a magnetic field of 180 mT at the sample position. Nevertheless, for the measurements we used the sample holder without the horseshoe magnet and pole shoes (for details see text). A magnetic field was provided by a set of Helmholtz coils instead. (b) Assembly of the four float-zoned crystals on an aluminum holder as arranged for the polarization analysis.

In addition, we measured the field dependence of the maximum Bragg intensity of crystals OFZ5 and BM, both for the spin-up and the spin-down configuration. As shown in Fig. 4.13 the two crystals show different behavior. For the large BM crystal both intensities remain at the same level for fields below 20 mT. With increasing field the spin-up intensity rises towards its maximum value at around 40 mT and saturates. The spin-down intensity shows a similar field dependence, but decreases more drastically. This behavior is in agreement with Eq. (4.2) and Eq. (4.3), if we assume a ferromagnetic saturation of the sample at around 40 mT. This is plausible due to it's elongated form and, hence, reduced demagnetization factor compared to the OFZ crystals. The slight decrease of both intensities at the highest fields can be assigned to a disturbance of the guide field by the magnetic field of the Helmholtz coils.

Different behavior is observed for the float-zoned crystal OFZ5 (see Fig. 4.13 (b)). Here spin-up and spin-down intensities start at similar intensities at zero field. With increasing fields up to 75 mT both intensities slightly decrease. At 75 mT the curves split and show a

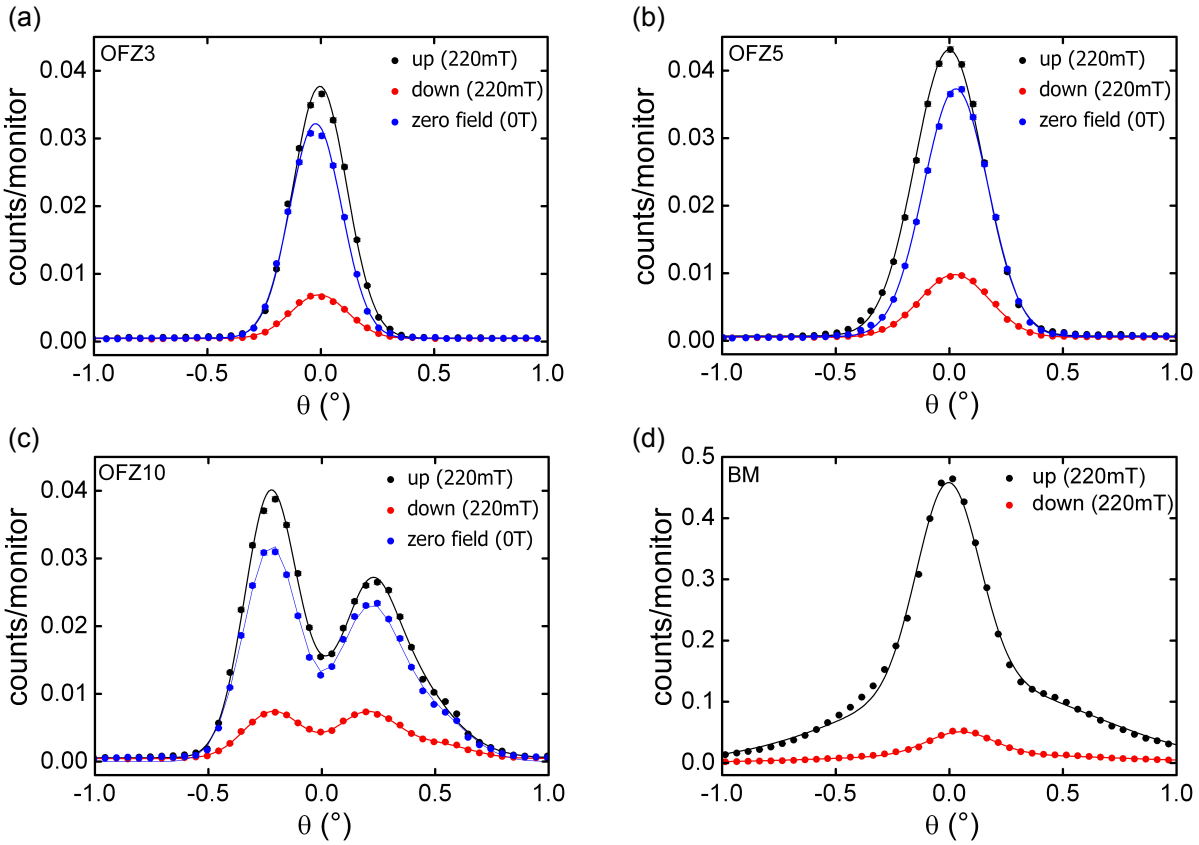

Figure 4.12: Rocking scans along the (111) Bragg reflex of float-zoned crystals OFZ3, OFZ5 and OFZ10 and of the Bridgman grown crystal (BM) with the ^{3}He cell perpendicular to the neutron beam. Measurements were taken in spin-up (I_+) and spin-down (I_-) configuration in an external field of 220 mT and in zero field (I_{zf}) for the OFZ crystals. The intensities are normalized to counts per monitor values. Note that the intensities for the large BM crystal are around 10 times larger than those for the small OFZ crystals.

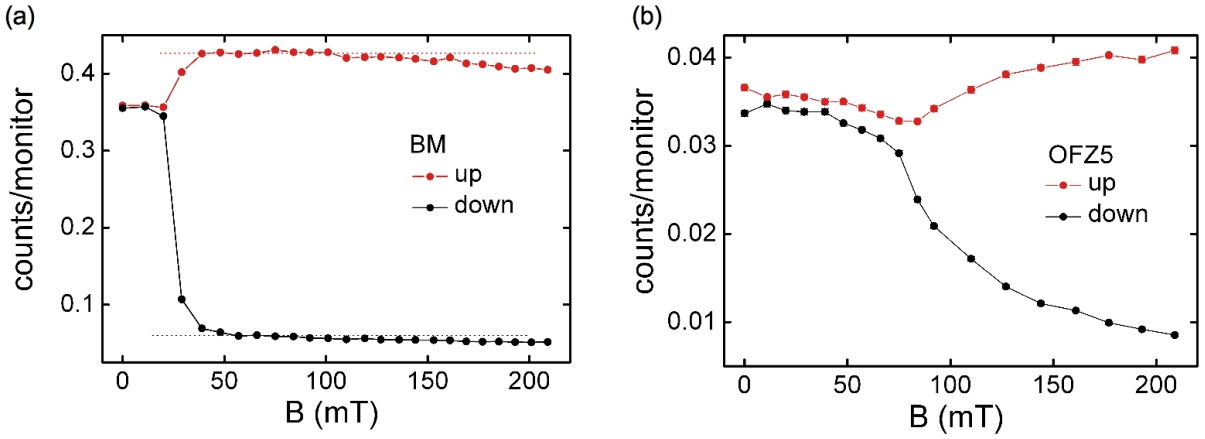

Figure 4.13: (a) Field dependence of the Bragg peak maximum of the large Bridgman grown crystal for the spin-up and the spin-down configuration. For both configurations the intensities start at a similar value, split step-like at a field above 20 mT and saturate at fields exceeding 40 mT. (b) Field dependence of the maximum of the Bragg peak of the float-zoned crystal OFZ5 for both spin configurations. With increasing field both intensities slightly decrease and split for fields above 75 mT. The splitting is gradually with no clear saturation up to fields of 220 mT.

curved increase (spin-up) and decrease (spin-down) to higher fields. No clear saturation is found for fields up to 220 mT. This behavior is in stark contrast to what we expected from the magnetization curves (see Fig. 4.5). At a field of 90 mT both the spin-up and spin-down intensities were expected to saturate. We believe that the small sample dimensions are responsible for the unconventional field dependence of the intensities and, hence, for the low flipping ratio. The geometry of the sample might lead to a not fully polarized sample, inhomogeneous field distributions within the sample or to stray fields next to the sample surface that depolarize the scattered neutrons.

^{3}He cell parallel to the neutron beam

In order to measure the absolute polarization, the last set of measurements was taken with the ^{3}He cell parallel to the neutron beam (see Fig. 4.10 (c)). We recorded the intensities at the maximum Bragg peak positions of each sample for both spin-up and spin-down configuration as well as the background. The measurement times were thereby increased in order to obtain good counting statistics. The flipping ratio was determined from the measured intensities as

$$R = \frac{I_+ - I_0}{I_- - I_0}, \tag{4.5}$$

with I_0 being the background intensity. The efficiency of the polarization, P, was calculated as

$$P = \frac{R-1}{R+1}. \tag{4.6}$$

The resulting flipping ratios and polarization efficiencies are shown in Table 4.2. A low polarization efficiency of $P \sim 80\%$ for the small float-zoned crystals was obtained as compared to the very good $P \sim 97\%$ for the large Bridgman grown crystal.

Crystal	OFZ3	OFZ5	OFZ6	OFZ10	BM
Sample dimension (mm^3)	$5 \times 2.5 \times 2$	$5 \times 2.5 \times 2$	$5 \times 2.5 \times 2$	$5 \times 2.5 \times 2$	$40 \times 20 \times 3$
Flipping ratio R	8.6	8.3	8.1	9.8/5.2	60.3
Polarization efficiency P (%)	79	79	78	81/68	97

Table 4.2: Sample dimensions, flipping ratios and polarization efficiencies for the small float-zoned crystals (OFZ) and the large Brigdman grown crystal (BM).

In order to investigate the influence of the sample geometry on the polarization efficiency we performed two independent measurements. First, we measured a large Bridgman grown sample (BMlarge) and a small sample (BMsmall) prepared from BMlarge with dimensions similar to the OFZ crystals. As a second test we measured an assembly of the float-zoned crystals OFZ3, OFZ5, OFZ6 and OFZ10, as shown in Fig. 4.11 (b).

From the first measurements we obtained a flipping ratio $R = 33$ for BMlarge in comparison to $R = 8.2$ for BMsmall. The flipping ratio $R = 8.2$ for the small Bridgman grown sample is similar to the low value obtained for the small float-zoned crystals.

The rocking scan of the assembly, as the second test, is shown in Fig. 4.14. The rocking curve shows a clear double peak structure that results from a slight misalignment of the (111) planes of each crystal. Nevertheless, the flipping ratios of each of the two Bragg peaks are 23 and 20 (see Table 4.3).

The increase of the flipping ratios from $R \sim 8$ of each OFZ sample by itself to $R \sim 20$ for an assembly of the same samples and the reduced flipping ratio $R = 8.2$ of the small Bridgman sample compared to $R = 33$ of the large Bridgman sample clearly identify the sample dimension as the origin of the low flipping ratios and polarization efficiencies of our float-zoned crystals. Since the small float-zoned crystals and the small Bridgman sample show a similar flipping ratio $R \sim 8$, we expect the float-zoned crystals to achieve high polarization efficiencies comparable to those obtained for Bridgman grown crystals if the problems that arise due to the sample geometry are avoided. This may be achieved by growing larger crystals, by an assembly of several samples, or by a suppression of the stray fields or field inhomogeneities by embedding the Cu_2MnAl crystals in an adequate ferromagnetic material.

Crystal	OFZ assembly	BM large	BM small
Sample dimension (mm^3)	$10 \times 4 \times 2$	$\sim 60 \times 30 \times 4$	$5 \times 2.4 \times 1.8$
Flipping ratio R	23/20	33	8.2
Polarization efficiency P(%)	92/90	94	79

Table 4.3: Sample dimensions, flipping ratios and polarization efficiencies of Cu_2MnAl samples OFZassembly, BMlarge and BMsmall additionally measured at MIRA in order to analyze the dependence of the polarization efficiency on sample geometry.

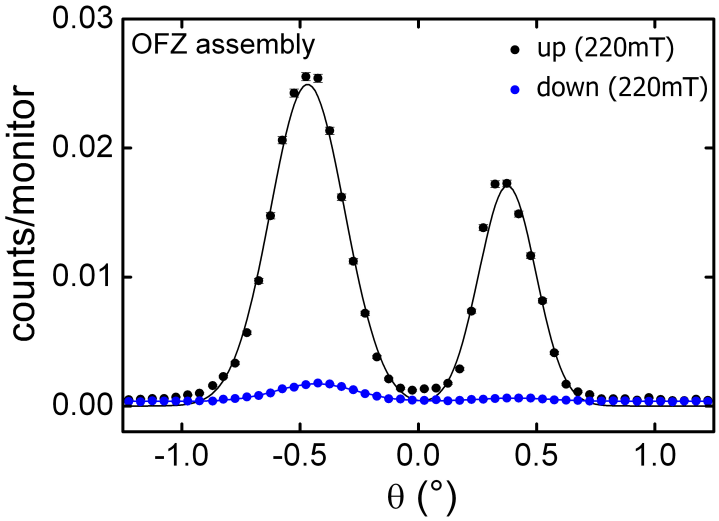

Figure 4.14: Rocking scan of the assembly of float-zoned crystals OFZ3, OFZ5, OFZ6 and OFZ10 for both spin-up and spin-down configuration. Misalignment of the (111) planes of each crystal with respect to each other leads to the double peak structure. The assembly shows increased flipping ratios of $R = 23$ and $R = 20$ for each of the two Bragg peaks compared to $R \sim 8$ for each OFZ sample by itself.

4.5 Summary and Outlook

The Heusler alloy Cu_2MnAl was chosen as the first compound for single crystal growth because starting rods were available before the RCF was set up and because of its importance for technical applications, notably polarizing monochromators in neutron scattering.

Altogether eight crystals were grown in the course of this thesis. Two in a vertical double ellipsoid image furnace in collaboration with Günther Behr at the IFW in Dresden and six with our UHV-compatible image furnace. We found that Cu_2MnAl shows a strong tendency to crystallize in the cubic $L2_1$ crystal structure, indicating a congruent melting formation. The high purity static inert gas environment in our image furnace was thereby indispensable in order to reduce the oxygen formation on the molten zone. High purity conditions allowed us to establish stable growth conditions and, hence, to obtain single crystals across the entire diameter for each of the six crystals grown with our image furnace. No preferred growth direction of the floating zone grown crystals could be identified.

Comparison of the magnetic properties of four crystals established a reproducible magnetic moment of $m \sim 3.6\,\mu_B$/f.u. at 4 K and $m \sim 3.2\,\mu_B$/f.u. at 300 K for each crystal (within 3%). This is in perfect agreement with the magnetic moments measured for a Bridgman grown crystal and those reported in literature [19].

Neutron diffraction of the $\langle 400 \rangle$ and $\langle 111 \rangle$ Bragg intensities established an isotropic mosaic spread of the float-zoned crystals when constant growth parameters were applied. This

is a clear advantage compared to Bridgman grown crystals where an anisotropic mosaic spread is reported [23]. In addition, we found that a variation of the growth rate during the growth process results in a variation of the mosaic distribution. This effect might be useful in order to optimize the mosaic spread for technical applications.

Further, we performed a study of the polarizing properties at the beamline MIRA2 at FRM II. For a large Bridgman grown crystal that was provided by Peter Böni we found a high polarization efficiency of 97%. The lower polarization efficiency of our float-zoned crystals was found to be due to their small sample dimensions and could be raised to 91% by an assembly of four small crystals.

Single crystal growth of Cu_2MnAl with the crucible free vertical floating zone technique allows to reproducibly grow crystals with a homogeneous mosaic distribution, hence avoiding the main drawback of the Bridgman grown crystals [23]. For technical applications it will be necessary to grow single crystals with a larger diameter starting with a larger feed rod. Furthermore, a seed with a predefined orientation will allow to prepare larger samples with a (111) plane from the crystals grown. Since the size of polarizing crystals typically used for technical applications in neutron scattering starts at around $10 \times 20\,\mathrm{mm}^2$ [141], these dimensions should be accessible.

Chapter 5

Results & Discussion: Mn_3Si

Mn_3Si was the first peritectic system addressed in the course of this thesis. Three large single crystals were successfully grown by the "self-flux" traveling solvent floating zone crystal growth. In addition, traveling solvent floating zone growth with a preset off-stoichiometric zone was attempted. The metallurgical properties of the float-zoned single crystals were found to be of high quality. Investigation of the specific heat and resistivity established similar physical properties of our float-zoned single crystals as reported for high quality polycrystals [15, 31, 33]. In the magnetization a sample dependent tiny additional signal below 65 K was observed, that was not reported before. As the origin of the signal, that may only be resolved in the magnetization, two possible scenarios are proposed: (i) the existence of a small volume fraction of an impurity phase or (ii) an intrinsic subtle form of magnetic order.

5.1 Crystal growth

5.1.1 Single crystal growth of Mn_3Si

The Heusler compound Mn_3Si forms via a peritectic reaction, as shown in the binary Mn-Si phase diagram (Fig. 1.4). The composition of the peritectic point ($x_p = 76$ at.% Mn) is situated close to the stoichiometric composition (75 at.% Mn). The temperature difference between the neighboring peritectic and eutectic reaction is roughly 30 K. Due to this relatively large temperature difference and the vicinity of the relevant compositions we first attempted to grow Mn_3Si single crystals by the so-called "self-flux" version of traveling solvent floating zone crystal growth. In other words, starting with stoichiometric rods the composition of the molten zone adjusts itself during crystal growth without using an additional pill as solvent medium. With this "self-flux" method three Mn_3Si crystals (OFZ7, OFZ8 and OFZ19, see Fig. 5.1) were grown. In addition, we attempted traveling solvent floating zone crystal growth of Mn_3Si (OFZ56) by starting the growth with an off-stoichiometric pill of $Mn_{79}Si_{21}$ at the zone.

For crystals OFZ7, OFZ19 and OFZ56 stoichiometric starting rods were prepared with the rod casting furnace (RCF). The feed rod of OFZ8 was prepared with a slight excess of manganese ($\sim$ 75.5 at.% Mn), since evaporation of manganese was observed during crystal growth. For the starting rods of OFZ19 and OFZ56 the manganese was additionally purified prior to the casting process. The off-stoichiometric pill for crystal growth of OFZ56 was prepared from a rod that was cast in the RCF with a starting composition $Mn_{79}Si_{21}$.

The parameters for the growth of the four Mn_3Si crystals with the image furnace are summarized in Table 5.1. Due to the peritectic formation of Mn_3Si relatively slow growth rates of 2-3 mm/h were applied. The crystals grown are shown in Fig. 5.1. For crystals OFZ7 and OFZ8 relatively stable growth conditions were obtained after a short time, although the power of the lamps had to be increased continuously (+1%) due to evaporation onto the quartz tube. For crystal OFZ19 the height and the diameter of the molten zone had to be adapted continuously in the first half of the growth process (this caused the bulge in crystal OFZ19). Stable conditions were obtained not until the second half of the crystal. Both, the use of the 1000 W lamps and the enhanced growth rate might be responsible for the instability of the zone. The purified manganese used for the starting rods of OFZ19 resulted in a reduced amount of impurities on the surface of the molten zone.

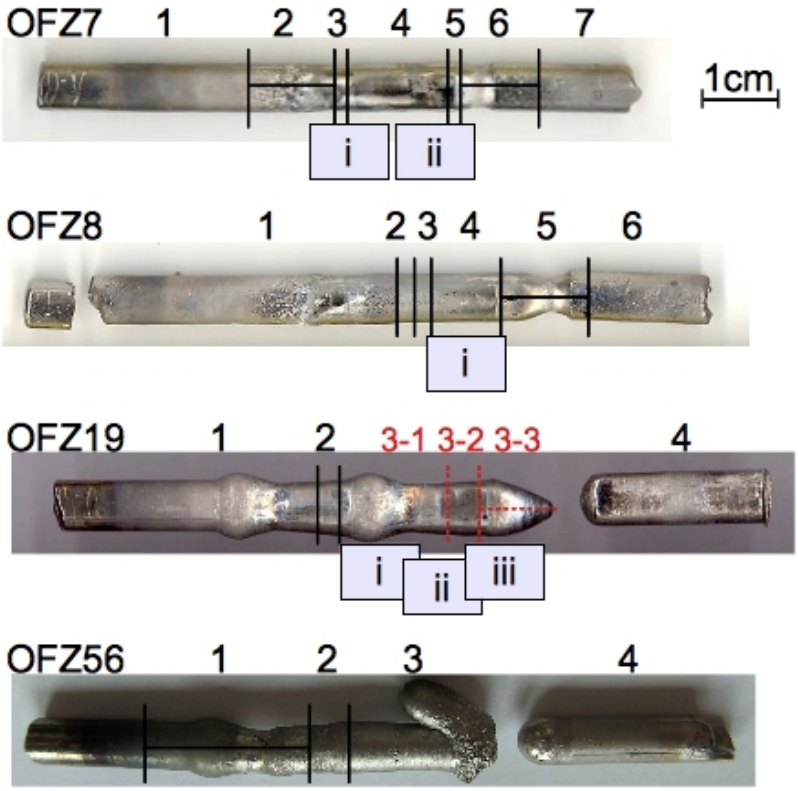

Figure 5.1: The four Mn_3Si crystals grown with the OFZ. The growth direction is from left to right. Samples prepared from the crystals are labeled in the usual way. The blue squares indicate the sections investigated with the neutron diffractometer RESI at FRM II.

Growth Parameter	OFZ7	OFZ8	OFZ19	OFZ56
Growth rate	2 mm/h	2 mm/h	3 mm/h	2 mm/h
Counter-rotation (seed/feed)	22/10	30/10	25/10	20/10
Argon pressure	2 bar	2 bar	2.2 bar	4.8 bar
Lamp type	300 W (72%)	300 W (74%)	1000 W (39%)	500 W (53-60%)

Table 5.1: Growth parameters for the four Mn_3Si crystals grown with the image furnace.

For crystal OFZ56 no stable growth conditions were obtained. The heating power had to be changed continuously and over a wide range (53-60%) and the molten zone shifted below the focus of the lamps during the growth process. This implies that during the growth process no equilibrium composition of the molten zone was achieved. As a result the molten zone separated several times in the second half of the growth process, causing a large amount of material at the top of the rod to drip off (see Fig. 5.1).

5.1.2 Characterization of the single-crystalline properties

Single-crystallinity of the crystals was first established by means of X-ray Laue diffraction. In the last section of crystals OFZ7, OFZ8 and OFZ19 symmetric Laue patterns were obtained at the front (0°) and back (180°) of the crystals as expected of a single crystal. An example of a (110) Laue diffraction pattern for crystal OFZ8-4 is shown in Fig. 5.2. For crystal OFZ56 no clear or multiple diffraction patterns were found along the crystal, indicating, at best, several single crystal grains. Combining X-ray Laue diffraction with an investigation using a light microscope we determined the size of the single crystal (i.e., a single-crystalline structure across the entire rod diameter) as 1 cm, 0.8 cm and 0.5 cm for OFZ7, OFZ8 and OFZ19, respectively.

Neutron diffraction at RESI at FRM II of crystals OFZ7, OFZ8 and OFZ19 at the locations shown in Fig. 5.1 (blue squares) confirmed the results obtained from X-ray Laue diffraction. A clear single crystal diffraction pattern was found for section OFZ7-ii and OFZ8-i, while several large grains were observed for OFZ7-i and along OFZ19 (the mono-crystalline structure at the end of OFZ19 has a with of ~ 5 mm, which is smaller than the scanning area of RESI).

No secondary phase was detected in any of the investigated crystals. Single-crystalline OFZ7 and OFZ8 show a resolution limited excellent mosaic spread of 0.6°. The growth direction for the mono-crystalline structure in OFZ7 was along a $\langle 100 \rangle$ direction within ±4°. In contrast, the growth direction in OFZ8 was tilted away by 13° from a main direction. The lattice constants as measured were $a = 5.73 \pm 0.01$ Å for both crystals, in good agreement with literature [15]. In a recent investigation of the crystal structure of sample OFZ7-4 at HEIDI at FRM II, carried out by Tim Adams, the mosaic spread was determined to be $\sim 0.3°$.

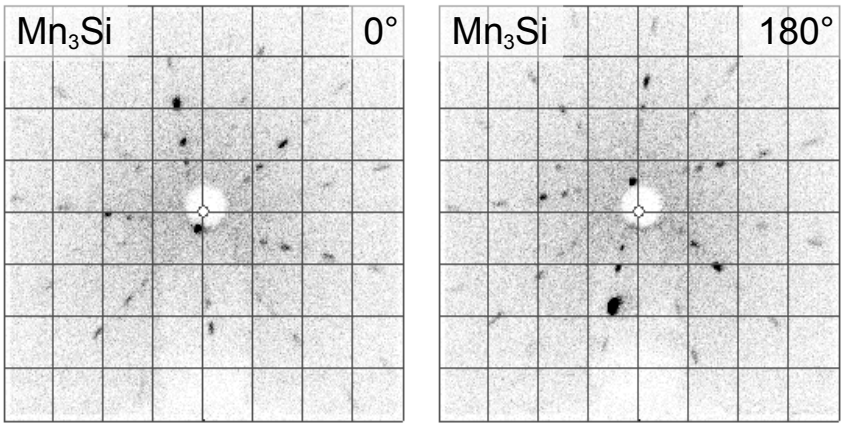

Figure 5.2: (110) X-ray Laue diffraction patterns of crystal OFZ8-4 taken at the front (0°) and the back side (180°) of the rod. The 2-fold symmetry of each pattern identifies a single-crystalline structure. The upside-down symmetry of both patterns with respect to each other indicates scattering from the same single crystal grain.

5.1.3 Metallurgical investigation

The optical appearance of selected sections of crystal OFZ8 is shown in Fig. 5.3. The large grains visible on the etched surface of OFZ8-1 illustrate the fast grain selection that takes place in Mn_3Si at the beginning of the growth. It indicates the tendency of Mn_3Si to crystallize in a mono-crystalline state. Two large grains are visible on the polished discs of neighboring sections OFZ8-2 and OFZ8-3. Along the growth the upper grain dominates and suppresses the lower grain. We note the symmetric surface structures on both grains. Similar surface structures appeared for all polished surfaces of all Mn_3Si crystals. SEM analysis (see white lines in Fig. 5.4 (a)) revealed typical structure dimensions of $\leq 100\,\mu m$. We assume crystal defects like line dislocations or small angle grain boundaries to be responsible for the appearance of these structures as there is no evidence for compositional variations. Image OFZ8-5 shows the quenched last zone. The growth direction is from left to right. The interface, which is not ideally convex, separates the single crystal from the quenched zone. A poly-crystalline structure is found in the feed rod after the quenched zone. This shows that large grains already form in the feed rod due to annealing.

A detailed EDX investigation of OFZ8-5 is shown in Fig. 5.4. The measurements were carried out at IFW in Dresden using a Phillips XL30 scanning electron microscope (SEM) and back scattered electrons. In addition, recent measurements (not shown) were carried out at the radiochemistry institute in Garching with a Zeiss EVO MA25 SEM. It is important to note that the absolute values of the compositions, as recorded without a standard in either instruments, differ by a value of around 2.5 at.%., i.e., the values for Mn determined by the Zeiss SEM are around 2.5 at.% above those determined by the Phillips instrument. To be consistent and to be able to quantitatively compare the results with the binary phase diagram, we corrected the absolute EDX values determined by the two instruments for the single-crystalline areas to the starting composition of stoichiometric $Mn_{75}Si_{25}$. More precisely, we added 1 at.% to the Mn values obtained with the Phillips EDX and subtracted 1.5 at.% of the Mn values obtained with the Zeiss EDX.

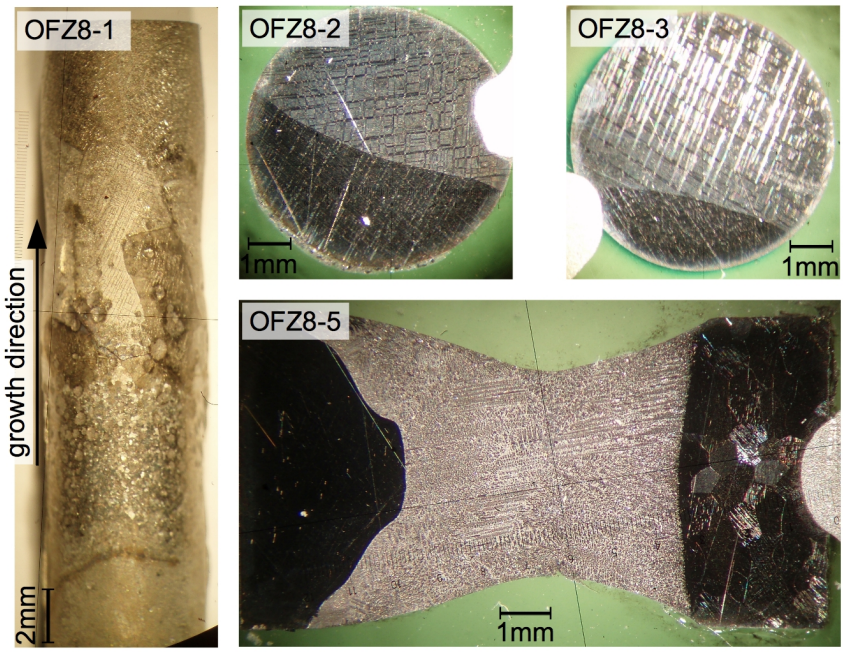

Figure 5.3: Images of crystal OFZ8 taken with an optical light microscope. OFZ8-1: Etched rod at the beginning of the growth. Large grains are visible on the surface. OFZ8-2 and OFZ8-3: Polished surfaces of neighboring discs show two single-crystalline grains. One grain expands during the growth process. OFZ8-5: Last zone of OFZ8. From left to right: single crystal, quenched zone, polycrystal.

Cross-sectional scans of single-crystalline Mn_3Si (see Fig. 5.4 (a)) confirmed the stoichiometric composition for the crystals grown. Additional scans with secondary electrons attributed the origin of the white lines, i.e., the symmetric structure visible on the surface after polishing, to surface effects. This finding confirmed our assumption that crystal defects are responsible for the appearance of these structures. Area scans of the quenched zone (Figs. 5.4 (c,e)) indicated an increased Mn concentration of around 77%. This value represents the self-adjusted composition of the zone due to the peritectic reaction, a value in good agreement with the binary phase diagram (see Fig. 1.4). The images show a dendritic structure (bright color) characteristic of super-cooling of the zone. Detailed EDX-analysis of this structure (Figs. 5.4 (d,f)) revealed a composition of the dendrites close to stoichiometry. The dendrites are imbedded in a Mn-rich matrix (dark color) with a composition of $Mn_{80}Si_{20}$, which corresponds to the ν-phase in the binary phase diagram. EDX area scans of the poly-crystalline feed (Fig. 5.4 (b)) showed a stoichiometric composition. Detailed investigations of the grain boundaries, though, revealed a Si-rich phase with a composition close to Mn_5Si_3. This suggests that Mn_5Si_3, a constituent part of the peritectic formation of Mn_3Si, tends to form at the grain boundaries. With EDX-analysis no traces of this Mn_5Si_3 phase were found in single crystal Mn_3Si.

Fig. 5.5 (a) shows a longitudinal cut through the beginning of crystal OFZ56, the crystal grown with the off-stoichiometric $Mn_{79}Si_{21}$ pill. The growth direction is from left to right. The image illustrates the grain selection that took place in the beginning of the growth. A large grain expands from the center of the rod and is about to dominate the whole crystal,

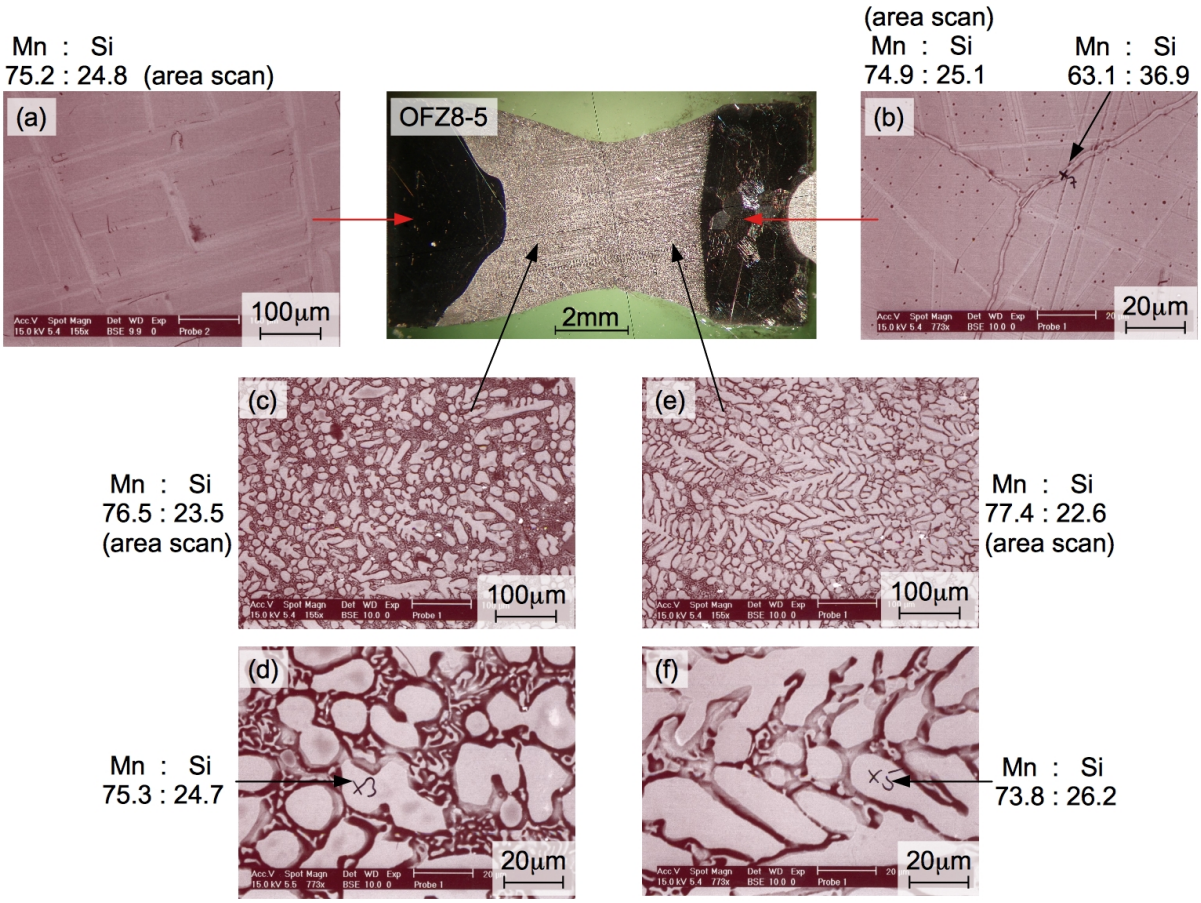

Figure 5.4: EDX-analysis of the final zone (OFZ8-5) of crystal OFZ8. Area scans of the (a) single- and (b) poly-crystalline structure reveal a stoichiometric composition. The formation of a Si rich phase (probably Mn_5Si_3) is found at the grain boundaries of the feed rod (b). Area scans of the dendritic structure of the quenched zone (c, e) show a Mn-rich composition. This indicates the self-adjustment of the zone during crystal growth. Detailed investigations of the quenched zone (d, f) reveal that the stoichiometric dendrites are imbedded in a Mn-rich matrix with composition $Mn_{80}Si_{20}$ (measurements are not shown).

Figure 5.5: Longitudinal cut through crystal OFZ56 at the beginning of crystal growth. The growth direction is from left to right. The grain selection process abruptly stops at a well-shaped convex growth interface marked by the dashed red line. EDX-analysis revealed an excess of manganese to the right hand side of the interface.

when the growth suddenly stops at a well-shaped convex interface (marked by the dashed red line). EDX-analysis revealed a slightly enriched composition of $Mn_{75.5}Si_{24.5}$ for the large grains and an eutectic mixture of $Mn_{76.5}Si_{23.5}$ and $Mn_{80}Si_{20}$ in the region right after the interruption. All values indicate a slight excess of Mn. We hence assume that the Mn concentration in the pill was too high, which resulted in a sudden transition of the equilibrium concentration at the interface. This suggests that a pill with less excess of manganese should be used for future growth attempts of single-crystalline Mn_3Si.

5.2 Physical properties of Mn_3Si

In this section we report the specific heat, magnetization, and resistivity measurements of the float-zoned single crystals. Taken together, we find good agreement of the physical properties of the single crystals with the results reported for polycrystals, e.g., the unusual stability of T_N in high fields [15]. In the magnetization we find a tiny (sample dependent) additional signal, which might be due to a subtle form of magnetic order or a small volume fraction of a second phase. A similar contribution may have also been present in the polycrystals, but was not noticed [142]. The intrinsic features of the antiferromagnetic order below $T_N = 23.5\,K$ in Mn_3Si do not seem to be influenced by the additional contribution, as measured in a recent neutron scattering experiment on crystal OFZ7-4.

5.2.1 Specific heat

Specific heat measurements of sample OFZ8-4 are shown in Fig. 5.6. The distinct anomaly at T_N shows the onset of incommensurate antiferromagnetic order. The transition temperature at $T_N = 23.5\,K$ was determined by an entropy conserving construction [142]. The peak of the specific heat anomaly shows no field dependence for fields up to 8 T. Only for temperatures above T_N the specific heat is slightly reduced with applied field. The low temperature behavior of the specific heat may be accounted for very well by:

$$C = \gamma \cdot T + \beta \cdot T^3, \tag{5.1}$$

as shown in Fig. 5.6 (d) for zero external field. Fitting the data we obtained a Sommerfeld coefficient $\gamma \approx 59\,mJ/mol\,K^2$ and a cubic term $\beta \approx 1.0\,mJ/mol\,K^4$. These values, as well as the absolute peak value, are slightly reduced in comparison to the values reported for poly-crystalline samples ($\gamma_{pc} \approx 69\,mJ/mol\,K^2$, $\beta_{pc} \approx 1.5\,mJ/mol\,K^4$) [15].

Except for the slight reduction of γ and β, we generally found a very good agreement of the specific heat data of our float-zoned single crystals with the data reported for polycrystals [15]. The transition to the antiferromagnetic state takes place at $T_N \approx 23.5\,K$ and also the unusual stability of T_N to high external fields was confirmed.

Fig. 5.6 (a) shows the specific heat in zero applied field for temperatures up to 70 K. No additional anomaly is found at elevated temperatures. This served as a test for a

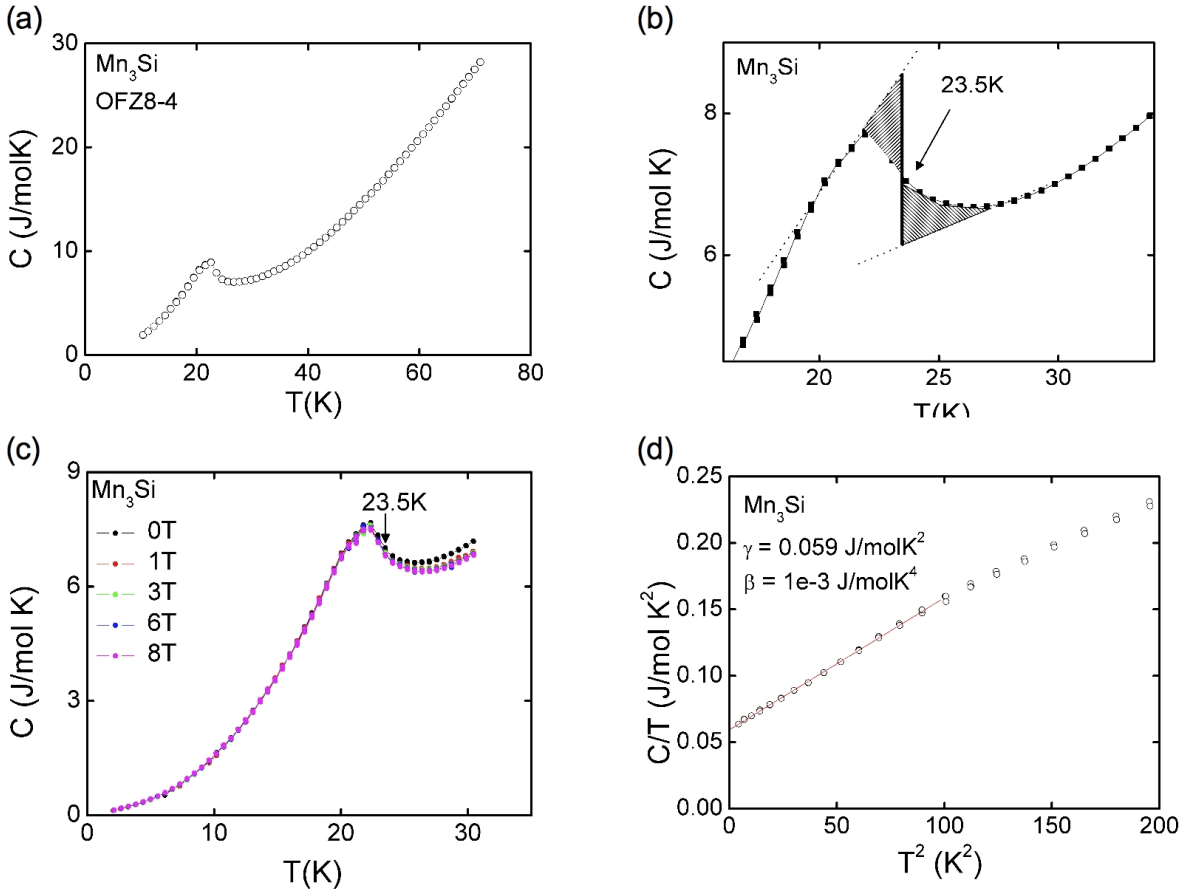

Figure 5.6: (a) Specific heat of OFZ8-4 up to 70 K. A maximum around $T_N \approx 23.5$ K indicates the antiferromagnetic phase transition. No additional signal is found around 55 K, where an additional signal in the magnetization appears. (b) The exact transition temperature T_N was determined by an entropy conserving construction [142]. (c) Specific heat at various fields up to 8 T. No field dependence is found for the distinct anomaly at T_N. (d) C/T vs. T^2 depiction of the specific heat at low temperatures. The data shows a linear behavior.

secondary phase, which appears below 60 K in the magnetization. It either indicates that only a small volume fraction of a secondary phase is responsible for the additional signal found in the magnetization (see the magnetization section below) or that a new magnetic phase forms with a tiny ordered moment.

5.2.2 Electrical resistivity

Zero-field resistivity measurements of samples OFZ8-3 and OFZ19-2 are shown in Fig. 5.7. For both samples the resistivity decreases monotonically with decreasing temperature, as expected for a metallic compound. The strong decrease below 30 K indicates the loss of dominant magnetic scattering mechanism associated with the onset of long range antiferromagnetic order. The broad shoulder below 50 K is more pronounced for sample OFZ8-3. At low temperatures the resistivities show a quadratic temperature dependence

(see Fig. 5.7 (b)). The residual resistivity ratios (RRR $= \rho(290K)/\rho_0(T \to 0)$) are around 6 and 14 for OFZ8-3 and OFZ19-2, respectively. In comparison, a residual resistivity ratio RRR ~ 14 was reported for the best poly-crystalline sample [15].

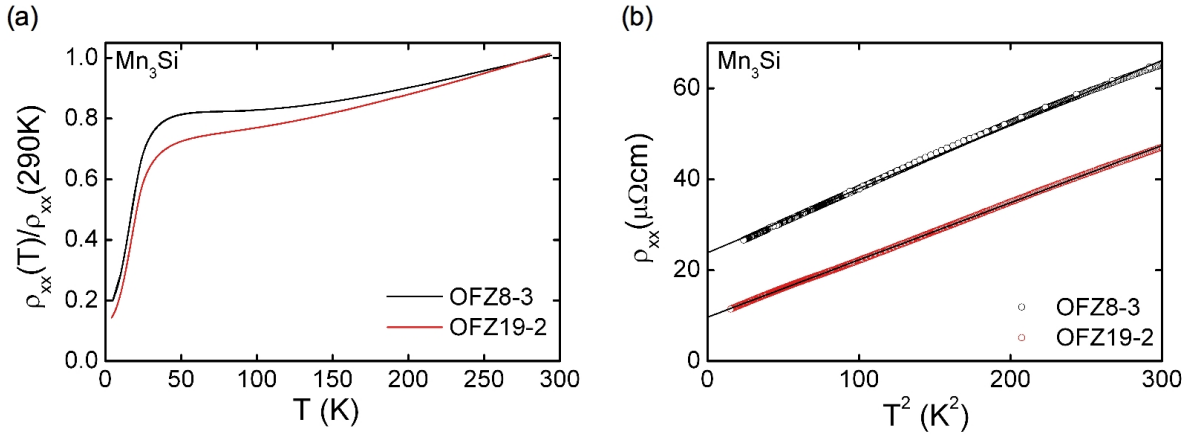

Figure 5.7: (a) Temperature dependence of the longitudinal resistivity for samples OFZ8-3 and OFZ19-2. The resistivity is normalized to the high temperature value. The decrease below 30 K indicates the loss of dominant magnetic scattering associated with the onset of long range antiferromagnetic order. (b) Both samples show a quadratic temperature dependence at low temperatures. OFZ19-2 has a good residual resistivity ratio around 14.

5.2.3 Magnetization

The magnetization of sample OFZ7-3 is shown in Fig. 5.8. We note the tiny absolute size. As a function of temperature the magnetization at small fields shows a cusp between 40 K and 65 K with a peak around 55 K. With increasing fields the maximum shifts to lower temperatures. The field dependence of the magnetic moment is consistent with this observations. At 80 K the magnetization shows an almost linear field dependence. With decreasing temperatures an additional signal appears. This is shown in more detail in Fig. 5.8 (c) for small fields. We first observe a tiny ferromagnetic contribution that turns into an antiferromagnetic hysteresis curve with a metamagnetic transition for temperatures below 50 K. The critical field B_m of the metamagnetic transition is indicated by the black arrows. With decreasing temperature the critical field increases, as well as the width of the hysteresis.

Qualitatively similar magnetic properties are found for all our float-zoned single crystals, but quantitatively large differences are observed as shown in Fig. 5.9 (a). The maximal magnetizations (at the peak position) measured at $B = 0.1$ T vary by almost a factor of four. Sample OFZ19-2 clearly shows the smallest signal with a maximum value $m = 0.007\,\mu_\mathrm{B}$/f.u.. For crystals OFZ7 and OFZ8 we find that samples prepared from the beginning of the crystal (OFZ7-3, OFZ8-3) show an enhanced magnetic contribution in comparison with samples prepared from the end of the crystal (OFZ7-5, OFZ8-4). The same conclusions can be drawn from the field dependent magnetization at $T = 10$ K and

$T = 80\,\mathrm{K}$ shown in Fig. 5.9 (b) and (c), respectively. At $T = 10\,\mathrm{K}$ we additionally find that for fields above 1 T sample OFZ19-2 shows an almost linear behavior, while an increase of the curvature with increasing magnetic moment is observed for the other samples. At 80 K an almost linear field dependence is observed for all crystals. However, the pitch of the lines differs and follows the sample dependence as mentioned above. In addition, the field dependence of a poly-crystalline sample, as reported in [32], is shown in Fig. 5.9 (c). We find that the slope of the magnetization of the polycrystal agrees quite well with single crystal OFZ19-2.

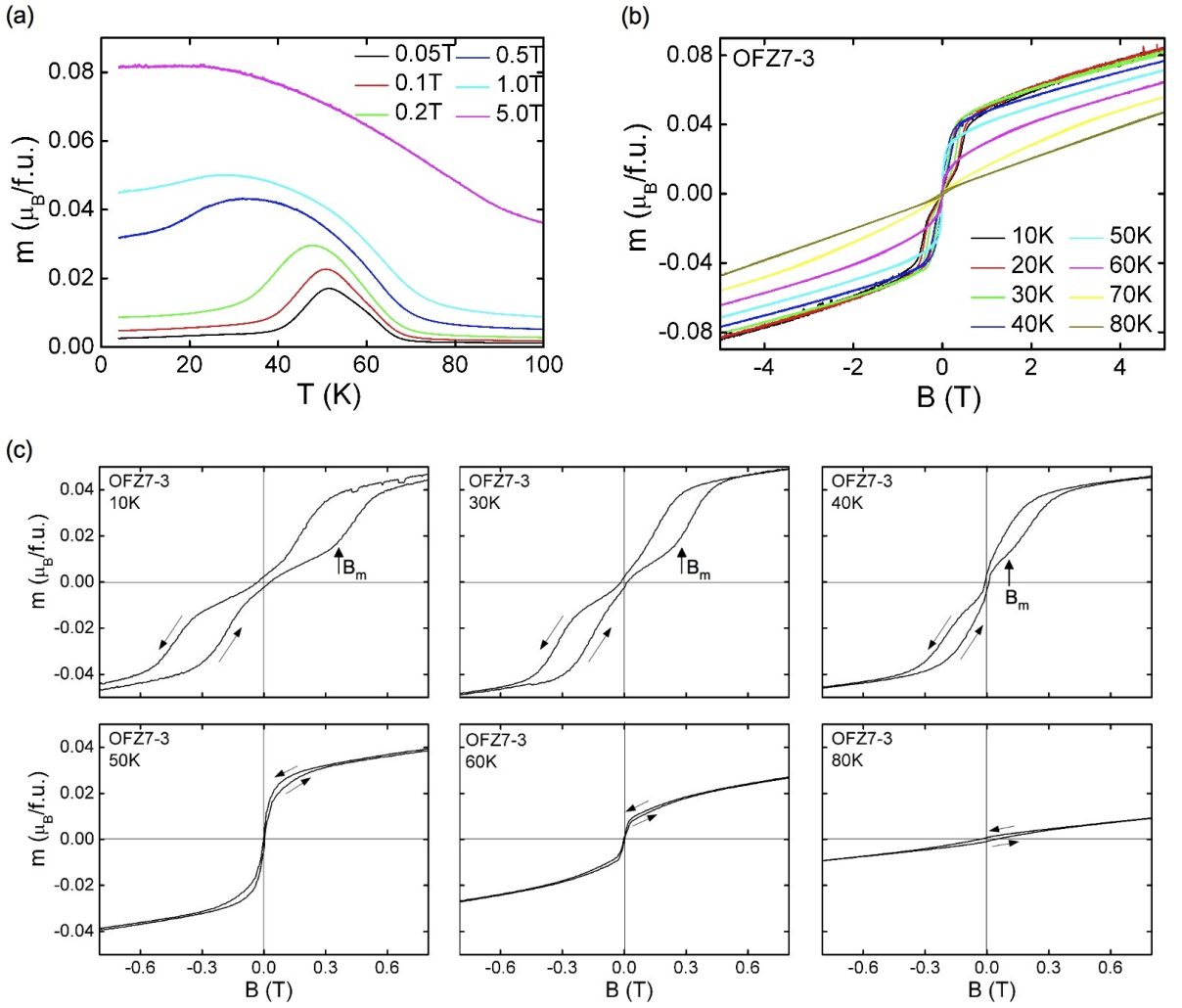

Figure 5.8: (a) Temperature dependent magnetization of sample OFZ7-3 measured at various fields. At small fields a small cusp forms between 40 K and 65 K with a peak around 55 K, reminiscent of an antiferromagnetic ordering. With increasing fields the maximum shifts to lower temperatures. (b) Field dependent magnetization of sample OFZ7-3 measured at various temperatures for fields up to 5 T. The low field dependence is shown in more detail in (c). First a tiny ferromagnetic contribution appears that turns, with decreasing temperature, into an antiferromagnetic hysteresis curve with a metamagnetic transition (indicated as B_m) for temperatures below 50 K.

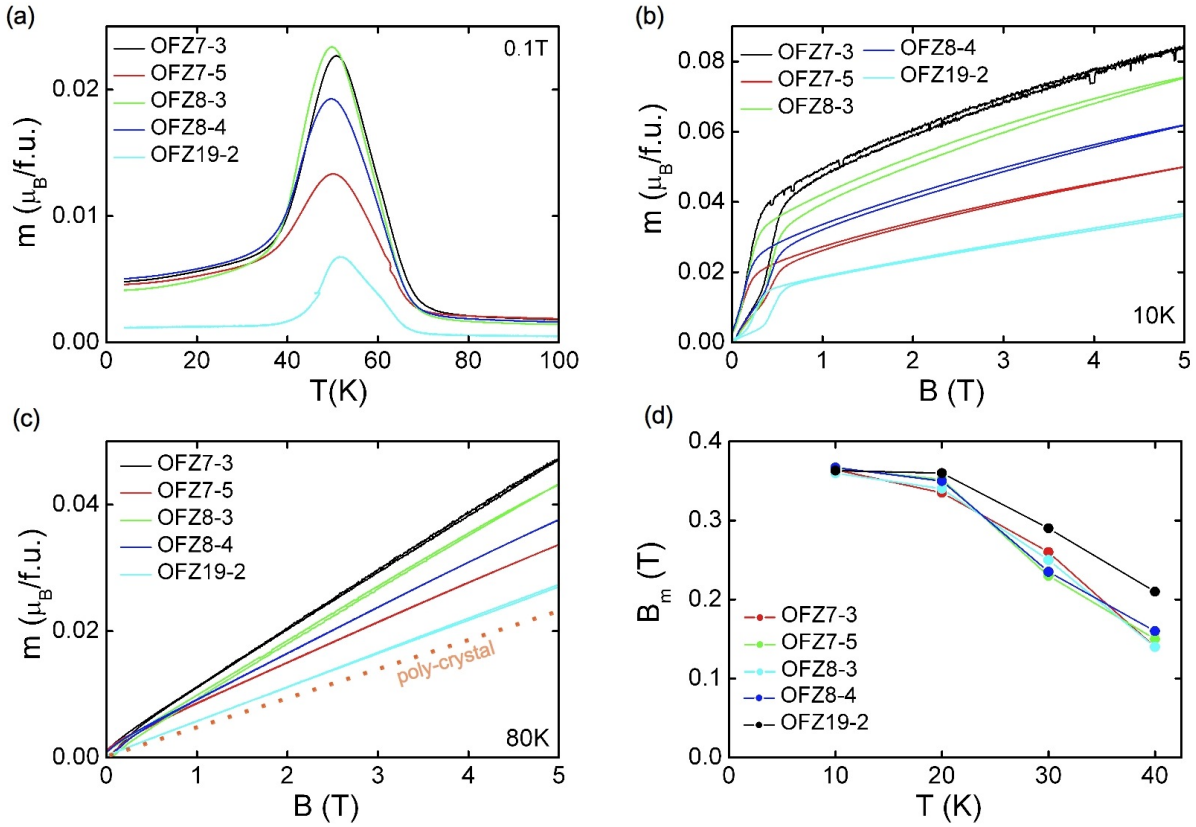

Figure 5.9: Comparison of the magnetic properties of different single-crystalline samples of Mn_3Si: (a) temperature dependence at 0.1 T; (b) field dependence at 10 K; (c) field dependence at 80 K; (d) temperature dependence of the field B_m that indicates the onset of the metamagnetic transition. All samples show qualitative similar behavior. Crystal OFZ19-2 shows the least amount of additional signal. Its linear field dependence is very similar to the field dependence reported for polycrystals [32] shown by the orange dashed line in (c).

As the origin of the magnetic contribution below 60 K we consider two possible scenarios: (i) the existence of a small volume fraction of secondary phase, or (ii) an intrinsic subtle form of magnetic order. We thereby have to keep in mind that the observed magnetic contributions are tiny. Previous studies do not contribute to a clarification. Tomiyoshi *et al.* reported the appearance of a secondary phase of Mn_5Si_3 in their crystals [29]. However, they did not show any corresponding data. Further studies of poly-crystalline Mn_3Si [15, 32] focussed on the magnetization in very high fields (up to 50 T) and did not consider the low field magnetization in any detail. Hence it is possible that a similar contribution may have also been present in the polycrystals, but was not noticed [142].

No clear conclusion in favor of one scenario can be drawn neither from the absence of an additional signal in the specific heat nor from the absence of neutron spin depolarization (NDR was measured on sample OFZ7). In both cases a small volume fraction of a secondary phase or a magnetic phase with a tiny ordered moment would account for the observed behavior. This also accounts for the strong sample dependence of the additional magnetic signal, which is generally taken as evidence of an impurity phase. However,

slight variations of the composition or atomic structure may also lead to pronounced variations of the intrinsic magnetic order, as shown, e.g., for $NbFe_2$ in chapter 7.

An indication in favor of an impurity phase may be the improved residual resistivity ratio of sample OFZ19-2 together with its small magnetic signal, since impurities generally act as scattering centers and hence increase the resistivity. In addition, no orientation dependence of the magnetization was detected, as measured for the $\langle 111 \rangle$ and $\langle 110 \rangle$ direction for OFZ8-3. From an intrinsic antiferromagnetic contribution in a single crystal with the pronounced metamagnetic transition, we would expect some orientation dependence of the magnetization.

Mn_5Si_3 is thereby the most likely candidate for the impurity phase since it forms as a constituent part of the peritectic formation of Mn_3Si. Pure Mn_5Si_3 orders antiferromagnetic at $T = 68\,\mathrm{K}$ [143], with a metamagnetic transition at $B = 4.5\,\mathrm{T}$ around $T = 60\,\mathrm{K}$ [144]. Although the former corresponds quite well with our observations, we did not detect the latter in our crystals. Instead we found a metamagnetic transition for temperatures below 40 K and very low fields, as displayed in Fig. 5.8 (c) and Fig. 5.9 (d). An additional discrepancy is obtained from the uniform magnetic moment. For Mn_5Si_3 a magnetic moment around $0.6\,\mu_\mathrm{B}$/f.u. is reported at $T = 5\,\mathrm{K}$ and $B = 9\,\mathrm{T}$ [144]. This would imply a Mn_5Si_3 volume fraction of up to 10% in our samples, which would definitely have been detected with EDX-analysis. But, as mentioned before, with EDX-analysis we did not detect any secondary phase in our single crystals. Then again, we did detect a Mn_5Si_3-like phase at grain boundaries in the polycrystals (see Fig. 5.4 (b)). From these ambiguous results we cannot assign the impurity phase to pure Mn_5Si_3. Nevertheless, one has to keep in mind that the magnetic properties of clusters of Mn_5Si_3 might differ from that of bulk Mn_5Si_3.

Further growth attempts with traveling solvent floating zone crystal growth with a preset off-stoichiometric zone and with varying starting rod compositions are expected to provide more information. In addition, it will be interesting to investigate the influence of annealing of the single crystals. Nevertheless, we have to keep in mind that the magnetic signal is very small and that no similar contribution in that temperature range has been observed in the resistivity or specific heat. Nor do any other so far measured properties seem to be influenced by the additional signal as seen in the magnetization. A further example is given in the next section where we show the results of a recent neutron scattering experiment.

Concluding the above considerations, we are so far not able to clearly assign the tiny contributions in the magnetization to either an intrinsic form of subtle magnetic order or to a second phase, especially since the magnetic properties of the proposed Mn_5Si_3 impurity phase are not in good agreement with the observed magnetic signals. However, irrespective of the origin of the additional magnetic signal, the linear field dependence of single crystal OFZ19-2 at high fields up to $B = 9\,\mathrm{T}$ and low temperatures is consistent with the unusual stability of the antiferromagnetic state in Mn_3Si as reported for polycrystals [15, 31].

5.2.4 Preliminary neutron scattering results

In a recent small angle neutron scattering experiment on crystal OFZ7-4, carried out by Tim Adams at MIRA at FRM II, magnetic Bragg reflections of the antiferromagnetic order below $T = 25\,\mathrm{K}$ have been observed, as shown in Fig. 5.10. Panel (a) shows the integrated scattering intensity as a function of q along the reciprocal lattice vector G_{111} for different temperatures. The intensity peaks observed correspond to the first harmonic satellite position of the antiferromagnetic spin structure of Mn_3Si. The Bragg peaks appear, in good agreement with literature [30], around $q = 0.425 \cdot G_{111}$ and $q = (1\text{-}0.425) \cdot G_{111}$. However, the Bragg scattering of higher harmonics below 9 K, as reported by Tomiyoshi *et al.* [29], was not observed. We note that the data was recorded in a test experiment using neutron focussing guides that led to a slight broadening of the Bragg peaks. Panel (b) shows the intensity of the magnetic Bragg peaks as a function of temperature, indicating a Néel temperature around $T_N = 23.5\,\mathrm{K}$.

These first neutron scattering experiments confirmed the antiferromagnetic order in float-zoned single-crystalline Mn_3Si. In addition, they illustrated that the additional signal observed in the magnetization does not seem to influence the incommensurate spin structure below T_N. We also carried out q-scans at elevated temperatures around 55 K in order to search for magnetic scattering intensities that corresponds to the additional signal observed in the magnetization. No additional scattering intensities were observed, though.

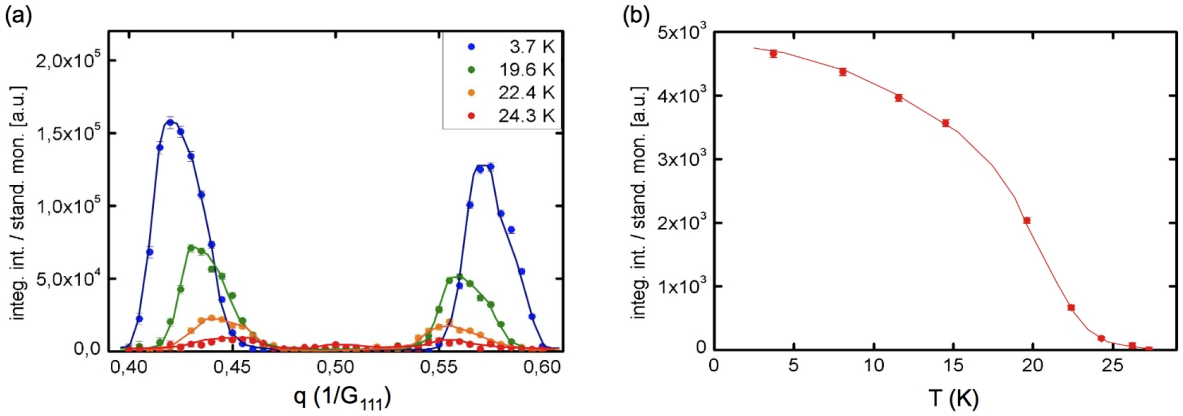

Figure 5.10: (a) Scattering intensity as a function of q in terms of the reciprocal lattice vector G_{111} along the [111] direction. Magnetic Bragg peaks appear around $q = 0.425 \cdot G_{111}$ and $q = (1\text{-}0.425) \cdot G_{111}$ as reported in literature for the antiferromagnetic order in Mn_3Si [30]. (b) The intensity of the magnetic Bragg peaks as a function of temperature indicates a Néel temperature around $T_N = 23.5\,\mathrm{K}$. The data was recorded by Tim Adams [145].

5.3 Summary and Outlook

In this chapter the first single crystal growth of the antiferromagnetic Heusler compound Mn_3Si by means of optical float-zoning was reported. This system forms via a peritectic reaction and was grown by "self-flux" vertical traveling solvent zone crystal growth. It was the first peritectic system we addressed in the course of this thesis. The crystals show very good single-crystalline properties, with a very good structural mosaic spread of $\sim 0.3^\circ$ measured for crystal OFZ7. No secondary phases were detected by means of EDX-analysis in the single crystal samples.

Specific heat measurements confirmed magnetic ordering below $T_N = 23.5\,K$ with a remarkably small magnetic field dependence of the specific heat anomaly, as reported previously for polycrystals [32]. Resistivity measurements showed a strong decrease below 30 K and a quadratic temperature dependence at low temperatures, consistent with a weakly spin polarized Fermi liquid ground state. For our best crystal, OFZ19, we obtained a residual resistivity ratio around 14, similar to the best RRR values obtained for polycrystalline samples [15]. The linear field dependence of the magnetization of single crystal OFZ19-2 at high fields up to 9 T and for all temperatures confirmed the unusual stability of the antiferromagnetic state in Mn_3Si, as reported for polycrystals [15, 31].

In the magnetization we observed a tiny additional signal for temperatures below 60 K that shows antiferromagnetic features with a metamagnetic transition at small fields. The signal is sample dependent and minimal for OFZ19-2. No signs of this signal have been observed in any other properties measured. We are, so far, not able to clearly assign this tiny contribution to either an intrinsic form of magnetic order or to a small volume fraction of a second phase. Further growth attempts with compositional variations, off-stoichiometric pills, as well as annealing are desirable to address this question. We propose a slightly enriched $Mn_{77}Si_{23}$ pill for future traveling solvent floating zone growth attempts.

Recent investigations with neutron scattering of single crystal OFZ7-4, carried out by Tim Adams as part of his PhD thesis, revealed magnetic Bragg scattering below $T_N = 23.5\,K$ characteristic of the antiferromagnetic order along the $\langle 111 \rangle$ direction. Other than Tomiyoshi *et al.* [29], no scattering of the higher-harmonic spin density waves below 9 K was observed, though. Future neutron scattering experiments on our float-zoned Mn_3Si single crystals are in preparation. A main goal thereby is to quantitatively investigate the pressure dependence of the ordered moments up to high pressures using a special neutron focussing set-up.

Chapter 6

Results & Discussion: Fe_2TiSn

In this chapter the growth of single-crystalline Fe_2TiSn is reported. To the best of our knowledge this is the first time single crystals have been grown. The crystalline and magnetic properties of various single crystal samples allowed to attribute the origin of a weak ferromagnetic transition at 250 K, reported in the literature [34], to an impurity phase, and that of a second transition at 125 K to surface effects that depend on sample preparation. In contrast, phase-pure Fe_2TiSn was found to be paramagnetic down to a few Kelvin, where a very weak spin glass transition was observed. In addition, a trend to split-site disorder was identified, that might affect the magnetic and transport properties of phase-pure single crystal Fe_2TiSn.

Following our original idea to establish pressure induced long range magnetic order in Fe_2TiSn, the magnetization and the magnetotransport properties under pressure were investigated. In contrast to an enhancement of the magnetic properties and magnetic order, the susceptibility and magnetization decrease under pressure, characteristic of a paramagnetic state. This is contrasted by the appearance of an unusual anomalous Hall effect with increasing pressure. Supported by band structure calculations that establish the appearance of a Dirac cone at the Fermi energy of Fe_2TiSn, the anomalous Hall signal suggests that Fe_2TiSn may, in fact, become a topological insulator.

6.1 Crystal growth

In the course of this thesis we grew four crystals of Fe_2TiSn as shown in Fig. 6.1. We thereby performed, to the best of our knowledge, for the first time crystal growth of Fe_2TiSn with optically heated vertical float-zoning. Since no metallurgical phase diagram was available for the Fe-Ti-Sn ternary system we analyzed the first crystals OFZ13 and OFZ14 in great detail before we attempted the growth of crystals OFZ31 and OFZ41. Following this approach, we will first present the results for the polycrystals OFZ13 and OFZ14, and then focus on the growth of the single crystals OFZ31 and OFZ41.

Figure 6.1: The four Fe_2TiSn crystals grown in the course of this thesis. The first crystals OFZ13 and OFZ14 were grown with a growth rate of 10 mm/h and 5 mm/h, respectively, resulting in a poly-crystalline structure. Crystals OFZ31 and OFZ41 were grown with a reduced growth rate of 0.7 - 1 mm/h, resulting in large single-crystalline grains. The dashed lines mark the beginning of the growth with the growth direction to the left. The formation of oxides causes the weak yellow staining of the crystals.

6.1.1 Preparation of starting rods

The poly-crystalline starting rods were prepared with the rod casting furnace, described in section 2.1.1, taking into account the typical requirements to achieve high purity. As starting material we used 6N Sn, 4N Fe and 4N5 Ti. Initially, the pure starting material had to be heated slowly, since the low melting point of Sn caused a mechanical motion when heated too fast.

The as-cast rods of Fe_2TiSn turned out to be extremely brittle, causing them to fracture easily in the casting mold. This made it difficult to obtain long starting rods. Both the copper and the stainless steel molds were tested, but no difference in the stability of the rods was observed. Therefore several poly-crystalline rods were prepared from stoichiometric composition and the longest parts were used for crystal growth. For the growth of crystal OFZ31, several small rods were joined by inductive heating in the horizontal cold finger (HCF) described in section 2.1.3. This long rod served as feed rod for the optical float-zoning.

6.1.2 Polycrystals OFZ13 & OFZ14

Crystals OFZ13 and OFZ14 were grown in an Argon atmosphere of 1.5 bar after pumping and baking out the image furnace. The 1000 W lamps were used at a power setting of ∼36 %. A growth rate of 10 mm/h and 5 mm/h was chosen for OFZ13 and OFZ14, respectively. The seed and feed rods were counter-rotating with 38 rpm and 13 rpm, respectively. For OFZ13 stable growth conditions were obtained, that is, the molten zone was stable and the lamp power had to be adjusted only slightly during growth. Prior to crystal growth, OFZ14 was zone-refined, i.e., the molten zone was driven through the feed rod with 18 mm/h. The zone-refining resulted in an inhomogeneous shape of the feed rod. This is most probably the reason for the unstable growth conditions during the growth of OFZ14. The molten zone dripped off twice and the growth process had to be restarted.

The optical inspection of crystals OFZ13 and OFZ14 revealed a poly-crystalline grain structure with an abundance of thermal cracks, inclusions and secondary phases. Panel (a) of Fig. 6.2 shows a longitudinal cut through the final section of crystal OFZ14 and panels (b - d) show SEM images with EDX analysis at the locations indicated. At the point

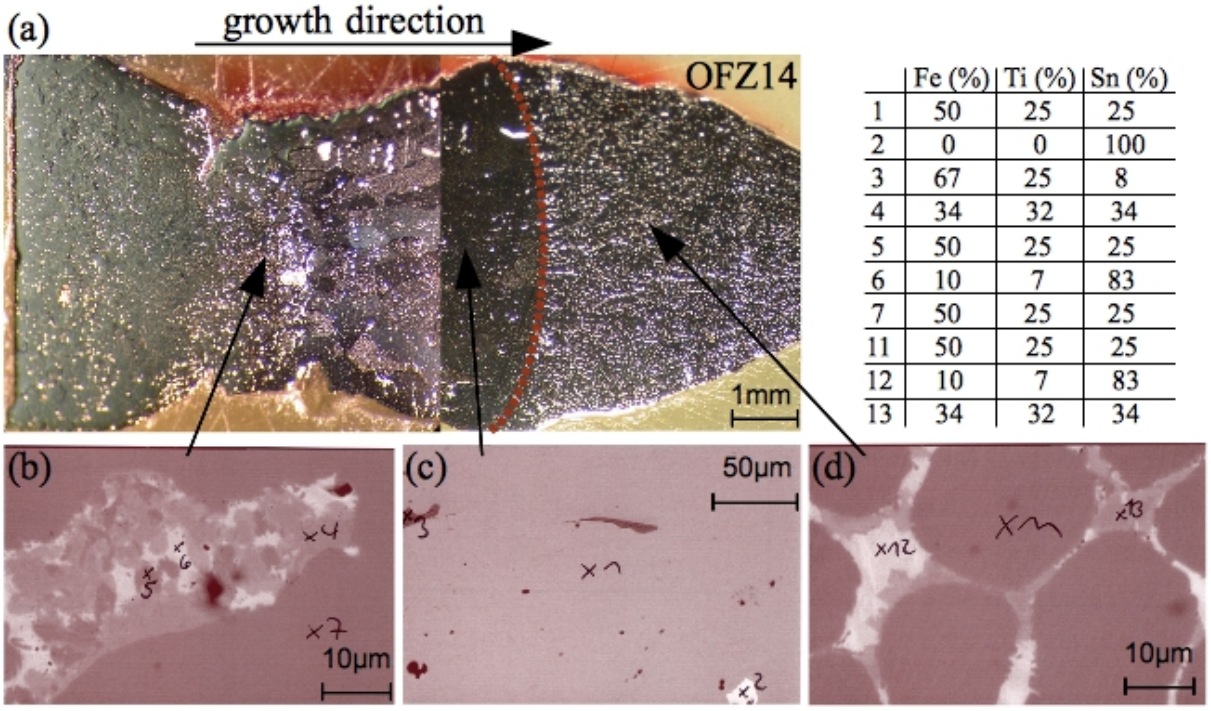

	Fe (%)	Ti (%)	Sn (%)
1	50	25	25
2	0	0	100
3	67	25	8
4	34	32	34
5	50	25	25
6	10	7	83
7	50	25	25
11	50	25	25
12	10	7	83
13	34	32	34

Figure 6.2: (a) Longitudinal cut through the final section of OFZ14. The shape of the convex growth interface is marked with a red dashed line. After restarting the growth at the bottle-neck of the crystal the formation of grains may be observed. (b - d) SEM images of different crystal positions. EDX analysis at the tagged positions was carried out at the IFW in Dresden. The composition values for each position are presented in the table. (b) Various inclusions embedded in a stoichiometric matrix are visible in the "unstable" growth regions. (c) A reduced amount of inclusions, primarily pure tin and an iron rich secondary phase ($Fe_{67}Ti_{25}Sn_8$), is found in the larger grains. (d) In the quenched last zone a cellular structure shows up.

where the growth was restarted (left arrow), a coarse structure with cracks and various inclusions is visible. Along the growth direction the formation of small stoichiometric grains is observed, that show a reduced amount of secondary phases. This grain structure is separated from the quenched last zone by a convex growth interface which is favorable for crystal growth. The quenched zone on the right is again dominated by an abundance of secondary phases, that are arranged in a honeycomb-like structure. The occurrence of inclusions, especially in the quenched last zone, strongly indicates that the growth rate was too high. We therefore decided to reduce the growth rate in subsequent growth attempts.

The compositions of the phases investigated are summarized in the table in Fig. 6.2. Note the formation of the $Fe_{67}Ti_{25}Sn_8$ secondary phase. Besides pure tin, it is the main impurity phase across the crystalline grain structure (see dark areas labeled as 3 in Fig. 6.2 (c)). As shown in section 6.2.1, this impurity phase is responsible for the observed weak ferromagnetic transition at $\sim 250\,\mathrm{K}$.

Magnetization measurements of different samples confirmed the strong sample dependence reported in the literature [34, 39, 40]. Fig. 6.3 shows the temperature dependence of the magnetic moment at a field of 0.1 T for samples taken from the starting rods L21, L22, and crystal OFZ13. Qualitatively similar behavior with an increase around 250 K and an additional increase at low temperatures is observed. Quantitatively, though, the magnetic moments differ strongly, which is due to differing volume fractions of the $Fe_{67}Ti_{25}Sn_8$ impurity phase. These differences were also found for different samples prepared from crystals OFZ13 and OFZ14. These measurements hence confirmed the low sample quality as expected from the optical inspection.

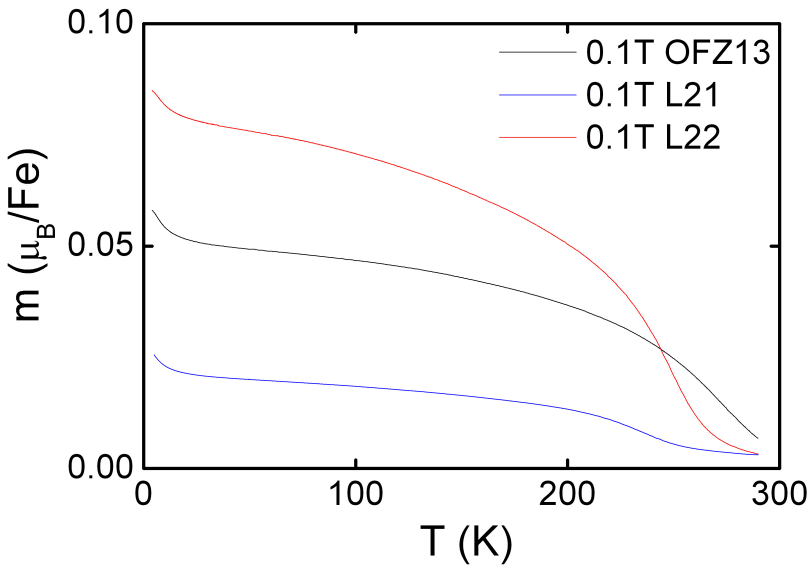

Figure 6.3: Temperature-dependent magnetization of three different samples of Fe_2TiSn taken from the float-zoned crystal OFZ13 and from its starting rods L21 and L22 at a field of $B = 0.1\,\mathrm{T}$. Qualitatively a similar behavior with an increase around 250 K is observed, but quantitatively a large difference of the measured moments may be noticed.

This first characterization may be compared with neutron depolarization radiography (NDR) measurements. Fig. 6.4 shows NDR images of crystal OFZ13 at various temperatures between 5 K and 300 K. The dark areas indicate ferromagnetic domains. On the one hand we observe strong depolarization (dark areas) up to high temperatures. On the other hand, though, there also exist areas where no depolarization of the neutron beam is observed at all down to the lowest temperatures studied. Interestingly, these regions seem to coincide with the areas of crystal OFZ13 where a stable morphology without cracks is observed. This was our first indication that Fe_2TiSn may be a paramagnetic metal as predicted by theory and that the ferromagnetic behavior is presumably observed in regions with structural imperfections.

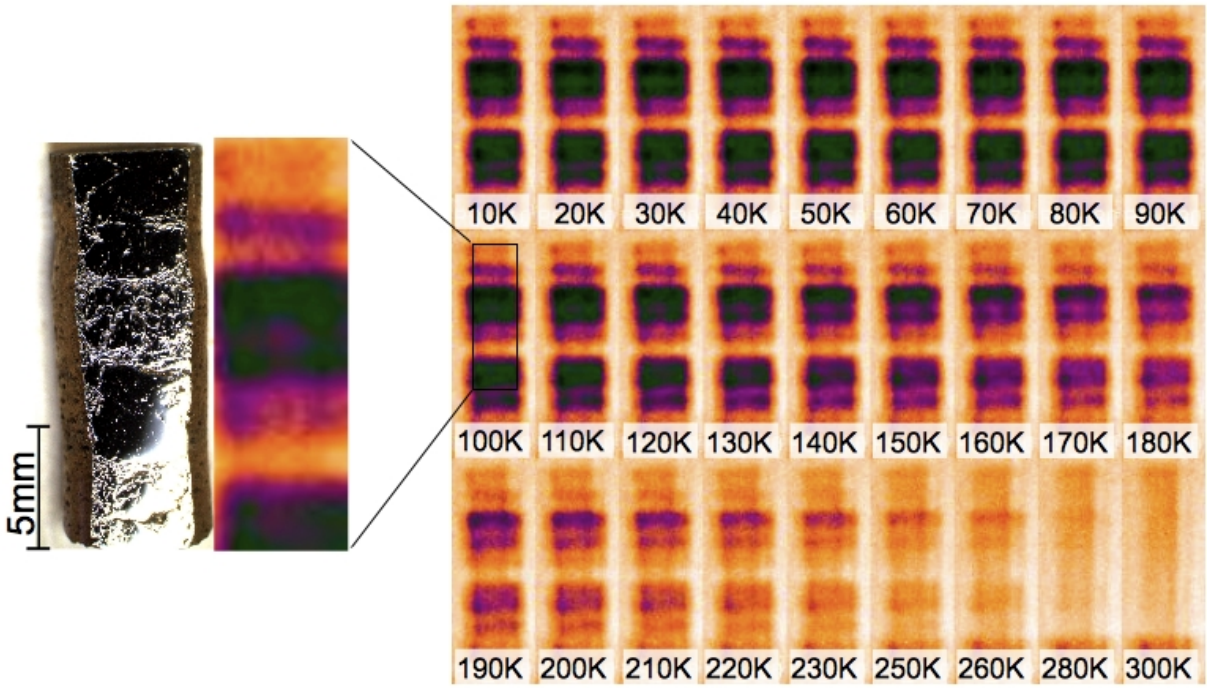

Figure 6.4: NDR images at various temperatures between 5 K and 300 K of crystal OFZ13. The images show layers of ferromagnetic (dark) and paramagnetic (bright) regions perpendicular to the direction of growth. Surprisingly, paramagnetic regions persists down to the lowest temperatures measured, indicating the vicinity to a paramagnetic ground state. A comparison with the polished surface of the crystal strongly suggests that the ferromagnetic behavior is related to the morphology with cracks while the smooth areas exhibit paramagnetic behavior.

6.1.3 Non-magnetic single crystals OFZ31 & OFZ41

Based on the results obtained in OFZ13 and OFZ14, we used a reduced growth rate of 0.7 mm/h and 0.8 mm/h for the growth of crystals OFZ31 and OFZ41, respectively. In addition, we used the 500 W lamps at a power of $\sim 57\,\%$ to reduce the size of the zone. Feed and seed rod were rotating with 13 rpm and 31 rpm, respectively. For crystal OFZ31 we used a long feed prepared with the HCF as shown in Fig. 2.12. At the beginning of the

growth of OFZ31 the molten zone dropped off once. The position is indicated by the black arrow in Fig. 6.5. Following this dripping-off stable growth conditions were obtained, even though the feed rod stopped rotating for six hours due to a loose bolt. For crystal OFZ41 the growth conditions were found to be even more stable and only minor changes of the lamp power had to be carried out. Stable growth conditions were essential, since the overall duration of crystal growth was 34 and 26 hours for crystals OFZ31 and OFZ41, respectively. Similar to the first crystals, minor contamination of the molten zone with impurities was observed, resulting in the yellow staining of the crystals.

A first optical inspection of the float-zoned crystals revealed the appearance of large single-crystalline grains in both crystals, as shown in Fig. 6.5 and Fig. 6.6 for OFZ31 and OFZ41, respectively. Similar behavior is found for both crystals. At the beginning of the growth the crystals show a coarse structure that is dominated by cracks. However, within a few millimeters the number of cracks is reduced and large single-crystalline grains with a smooth crystal structure and no signs of secondary phases appear. At the end of each crystal an almost mono-crystalline section across the crystal diameter is found for both OFZ31 and OFZ41, as shown in Fig. 6.5 (b) and Fig. 6.6 (b), respectively. We were hence able to prepare large single-crystalline samples for further experiments.

The single-crystallinity of the large grains prepared from the crystals was verified by means of X-ray Laue diffraction. Fig. 6.7 shows Laue diffraction patterns of the main (100) and (110) crystal plains of an oriented sample of crystal OFZ31. The clear diffraction spots of the 4-fold symmetric (100) and 2-fold symmetric (110) direction confirm the mono-crystallinity and indicate a good sample quality.

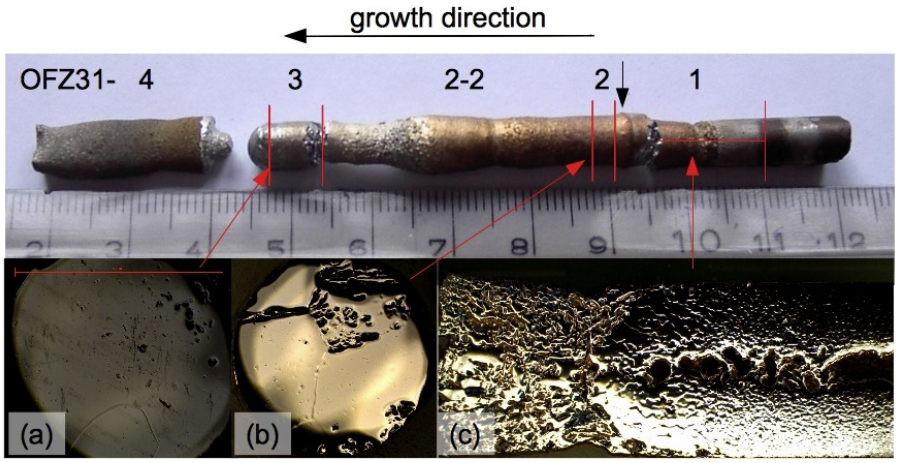

Figure 6.5: Crystal OFZ31 grown with a reduced growth rate of 0.7 mm/h. The growth direction was from the right to the left. The black arrow marks the restart of the growth after the zone dripped off. The red lines denote the polished metallurgical cuts investigated by light microscopy (a - c). (c) A brittle poly-crystalline structure with many cracks is found at the beginning of the growth. (b) After a short distance the formation of several large grains is observed. (a) One big grain prevails at the end of the crystal. Only one additional small grain is found, observable by the grain boundary at the lower end. Investigations of the physical properties were mainly carried out on samples prepared from OFZ31-2 and OFZ31-3.

A non-ferromagnetic ground state of high quality Fe_2TiSn crystals was confirmed by neutron depolarization radiography. NDR measurements of crystals OFZ31-2-2 and OFZ41 showed no depolarization of the neutron beam at the float-zoned single-crystalline regions for temperatures down to 5 K, the lowest temperature studied. Fig. 6.8 (a) shows NDR images of crystal OFZ41 at different temperatures. The brittle part at the beginning of the crystal (OFZ41-2, cf. Fig. 6.6) fell off during cooling the sample, as shown in the image. It is interesting, that both this brittle part and the poly-crystalline feed rod (OFZ41-5, lower end) depolarize the neutron beam up to high temperatures, while no depolarization

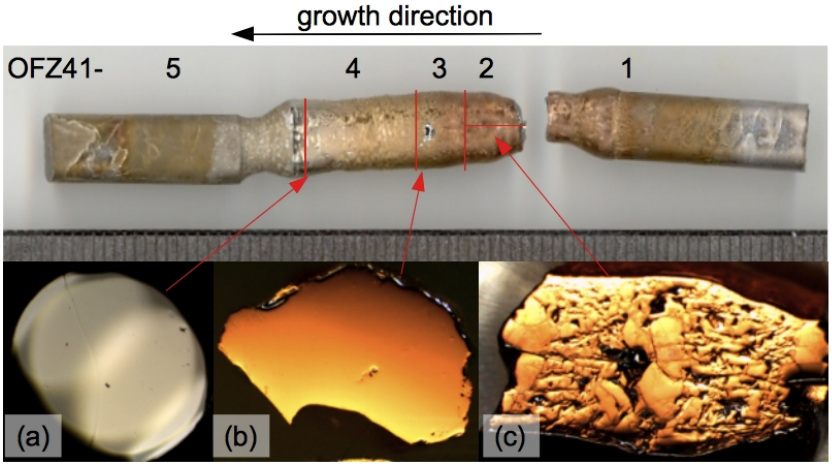

Figure 6.6: Crystal OFZ41 grown with a reduced growth rate of 0.8 mm/h. The growth direction was from the right to the left. The red lines denote the polished metallurgical cuts investigated by light microscopy (a - c). (c) A brittle poly-crystalline structure with many cracks is found at the beginning of the growth. At the left side the formation of larger grains is observable. (b) Already after a short distance large single-crystalline grains are found. (a) Two big grains prevail until the end of growth. The grain boundary crosses the surface vertically. Investigations of the physical properties were carried out on samples prepared from OFZ41-3.

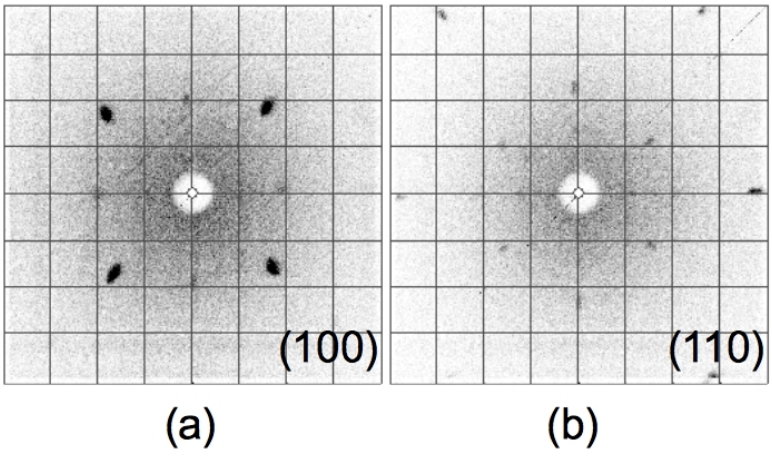

Figure 6.7: Laue X-ray diffraction pattern for (a) (100) and (b) (110) crystal planes of an oriented single-crystalline Fe_2TiSn sample cut from OFZ31-3. The clear diffraction spots indicate a good sample quality.

shows up for the float-zoned crystal (except for left overs of the brittle part at the top of the crystal). Annealing of poly-crystalline Fe_2TiSn seems to reduce ferromagnetism, since the part of the feed rod next to the quenched zone shows less depolarization. For comparison Fig. 6.8 (b) shows the NDR results for the Fe_2TiSn rod L50, that was used as feed for the growth of OFZ41. For L50 a homogeneous depolarization of the neutron beam for temperatures up to 225 K is found. These findings imply once more that the ferromagnetism in Fe_2TiSn is connected to a low sample quality and probably due to secondary phases.

Measurements of the AC - susceptibility confirmed the absence of high temperature ferromagnetism in single crystal Fe_2TiSn. Fig. 6.9 (a) shows the temperature dependence of the zero field AC - susceptibility of a single crystal sample prepared from OFZ31-2. Other than the data reported in the literature [34], the susceptibility shows no visible transition around 250 K. At low temperatures a strong continuous increase is observed to a maximum

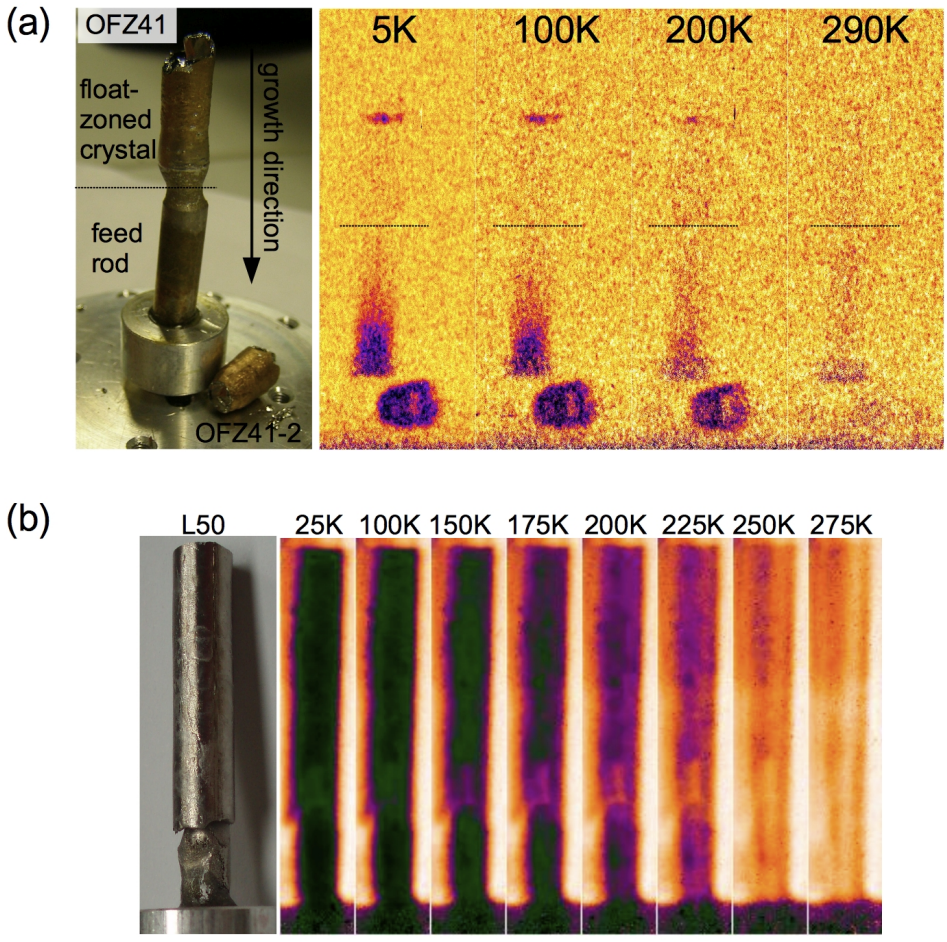

Figure 6.8: (a) NDR images of crystal OFZ41. The feed rod and the brittle part OFZ41-2 depolarize the neutron beam up to high temperatures. No depolarization is measured for the float-zoned crystal. There is a smooth transition of the depolarization across the quenched last zone, which is indicated by the dashed line. (b) NDR images of rod L50, that was cast in the RCF and used as a seed for OFZ41. L50 shows a homogeneous depolarization up to 225 K.

around 4.3 K as shown in Fig. 6.9 (b). We believe that this maximum marks a spin-glass transition as shown in section 6.3.1. The inverse susceptibility, shown in Fig. 6.9 (c), shows a linear Curie-Weiss behavior over the entire temperature range, that extrapolates to zero at $T \sim 0$ K, as shown in detail in Fig. 6.9 (d). We find this remarkable, since it resembles the behavior observed of weak ferromagnets at a quantum critical point.

To summarize, we succeeded to grow for the first time large single crystals of Fe_2TiSn. We found that the float-zoned single crystals do **not** show a ferromagnetic transition around 250 K. Instead, these Fe_2TiSn single crystals show a linear Curie-Weiss behavior over a large temperature range that extrapolates to zero at $T \sim 0$ K, resembling the behavior expected of weak ferromagnets at a quantum critical point. In addition, we observed a maximum of the AC - susceptibility at low temperatures which we attribute to a spin-glass state, as described in section 6.3.1.

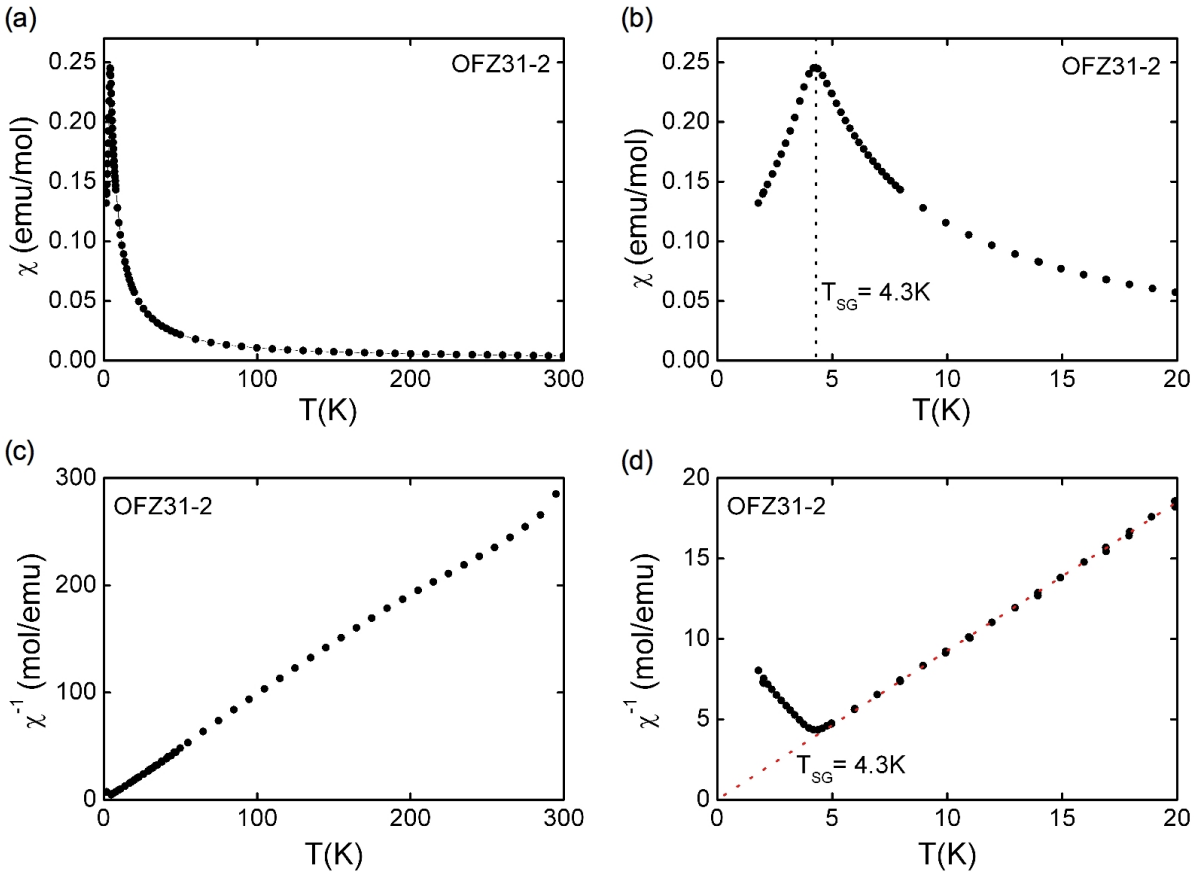

Figure 6.9: (a) Temperature dependence of the AC - susceptibility at zero magnetic field for single crystal OFZ31-2. No transition around 250 K is observed. (b) At low temperatures the susceptibility shows a strong increase, up to a maximum around 4.3 K. (c, d) Temperature dependence of the inverse susceptibility at zero field. The inverse susceptibility shows a remarkable linear Curie-Weiss behavior over the entire temperature range, that extrapolates to zero for $T_C \approx 0$ K. This resembles the behavior expected of weak ferromagnets at a quantum critical point.

6.2 Extrinsic magnetic properties

Measuring the AC - susceptibility and magnetization of more than twenty samples prepared from crystals OFZ31 and OFZ41, we were able to identify two distinct extrinsic effects that influence the magnetic properties of Fe_2TiSn single crystals. The appearance of the impurity phase $Fe_{67}Ti_{25}Sn_8$ leads to the ferromagnetic transition around 250 K, while surface effects that depend on the sample preparation result in a transition around 125 K. It is important to note that these transitions are observable in the AC - susceptibility, which is a very sensitive probe of the magnetic properties, especially since the intrinsic high temperature susceptibility of Fe_2TiSn is very low. In the magnetization these small effects did not show up.

6.2.1 Impurity phase $Fe_{67}Ti_{25}Sn_8$

For various samples prepared from our float-zoned crystals OFZ31 and OFZ41 we found an increase of the zero field AC - susceptibility around 250 K, similar to the observations reported by Ślebarski *et al.* [34]. This effect is particularly evident in the inverse AC - susceptibility as shown in Fig. 6.10 for different samples prepared from OFZ31-2. Optical inspection of the samples revealed that the appearance and size of the additional signal can be related to the appearance and amount of grain boundaries in the samples. In contrast, single-crystalline samples were found to show hardly any additional signal.

EDX analysis, as shown by the line-scan in Fig. 6.11 for a polished and etched Fe_2TiSn sample (OFZ31-2), revealed the appearance of an Fe-rich and Sn-poor impurity phase at the grain boundaries. For some crystals this impurity phase was additionally present as small inclusions in the single crystal. The same impurity phase with an average composition of 67:25:8 (Fe:Ti:Sn) was also observed in OFZ13 and OFZ14 (cf. Fig. 6.2).

In order to confirm the role of the impurity phase we prepared a specimen of $Fe_{67}Ti_{25}Sn_8$ (nominal composition) by inductive melting with the RCF. This specimen was found to be ferromagnetic up to room temperature, as shown in Fig. 6.12 (a). From the temperature dependence of the magnetization, which is shown as m^2 vs. T^2 in Fig. 6.12 (b), we determined $T_C \approx 335$ K. Figs. 6.12 (c) and (d) show the AC - susceptibility and the inverse AC - susceptibility of $Fe_{67}Ti_{25}Sn_8$ measured in zero field. The drop of the AC - susceptibility at around 200 K and the increase of the inverse AC - susceptibility at that temperature are reminiscent of the effects seen in many Fe_2TiSn samples.

Comparison of the absolute values of the susceptibility of $Fe_{67}Ti_{25}Sn_8$ ($\chi(200\,\mathrm{K}, 0\,\mathrm{T}) \sim 30$ emu/mol) with that of nominal Fe_2TiSn ($\chi(200\,\mathrm{K}, 0\,\mathrm{T}) \sim 0.005$ emu/mol) shows that already small volume fractions of less than 0.1% of $Fe_{67}Ti_{25}Sn_8$ will contribute noticeably to the AC - susceptibility of Fe_2TiSn at high temperatures. The contributions of such a volume fraction to the magnetization (at low temperatures) are, in contrast, negligible small consistent with our experiments.

Taken together, this strongly suggests that the impurity phase $Fe_{67}Ti_{25}Sn_8$ is responsible for the ferromagnetic transition observed in Fe_2TiSn at high temperatures in contrast

to atomic disorder as proposed by Ślebarski *et al.* [34]. This finding is supported by the observation of strong depolarization effects at crystal positions that show an abundance of inclusions, since the impurity phase was found primarily at grain boundaries.

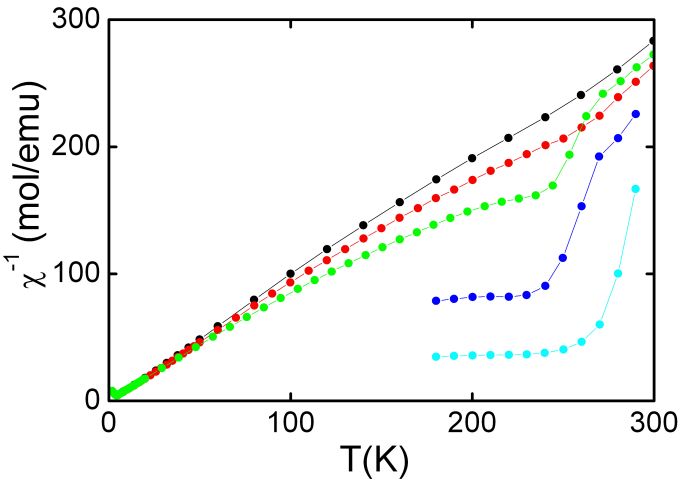

Figure 6.10: Temperature dependence of the inverse AC - susceptibility for different samples prepared from OFZ31-2. Samples that contain grain boundaries show an additional magnetic response around 250 K, as illustrated by the drop of the inverse AC - susceptibility.

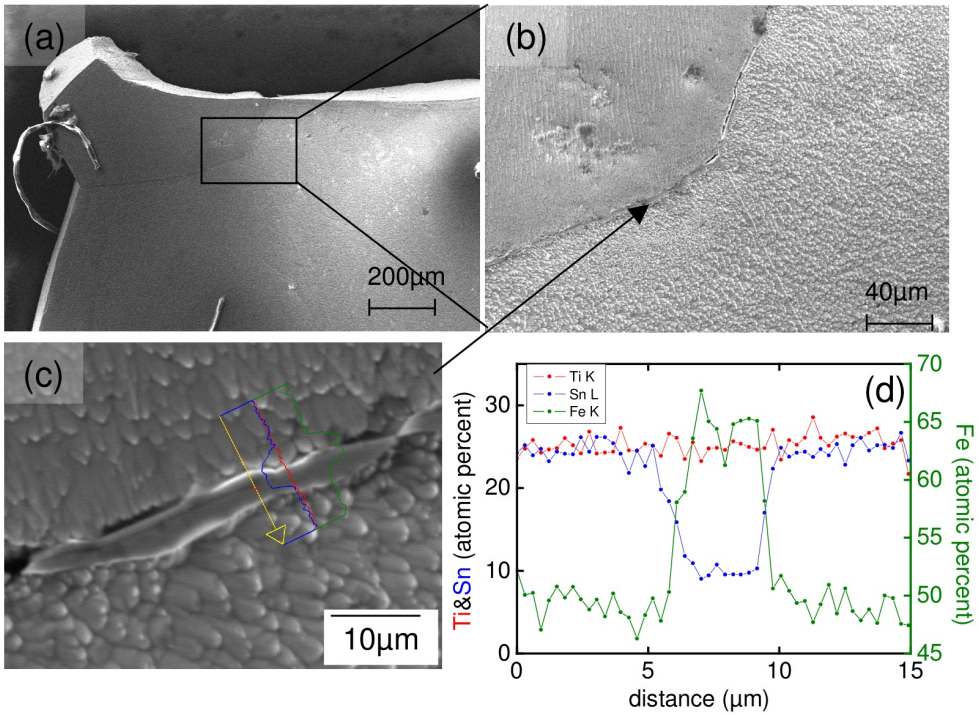

Figure 6.11: Detailed investigation of the grain boundaries of a polished and etched Fe_2TiSn sample (OFZ31-2) with SEM and EDX analysis. (a - c): Zoom into the grain boundary. (c) Line sweep with EDX analysis across the grain boundary. The composition at the grain boundary is Fe-rich and Sn-poor as shown in (d). The approximate composition is $Fe_{68}Ti_{25}Sn_7$.

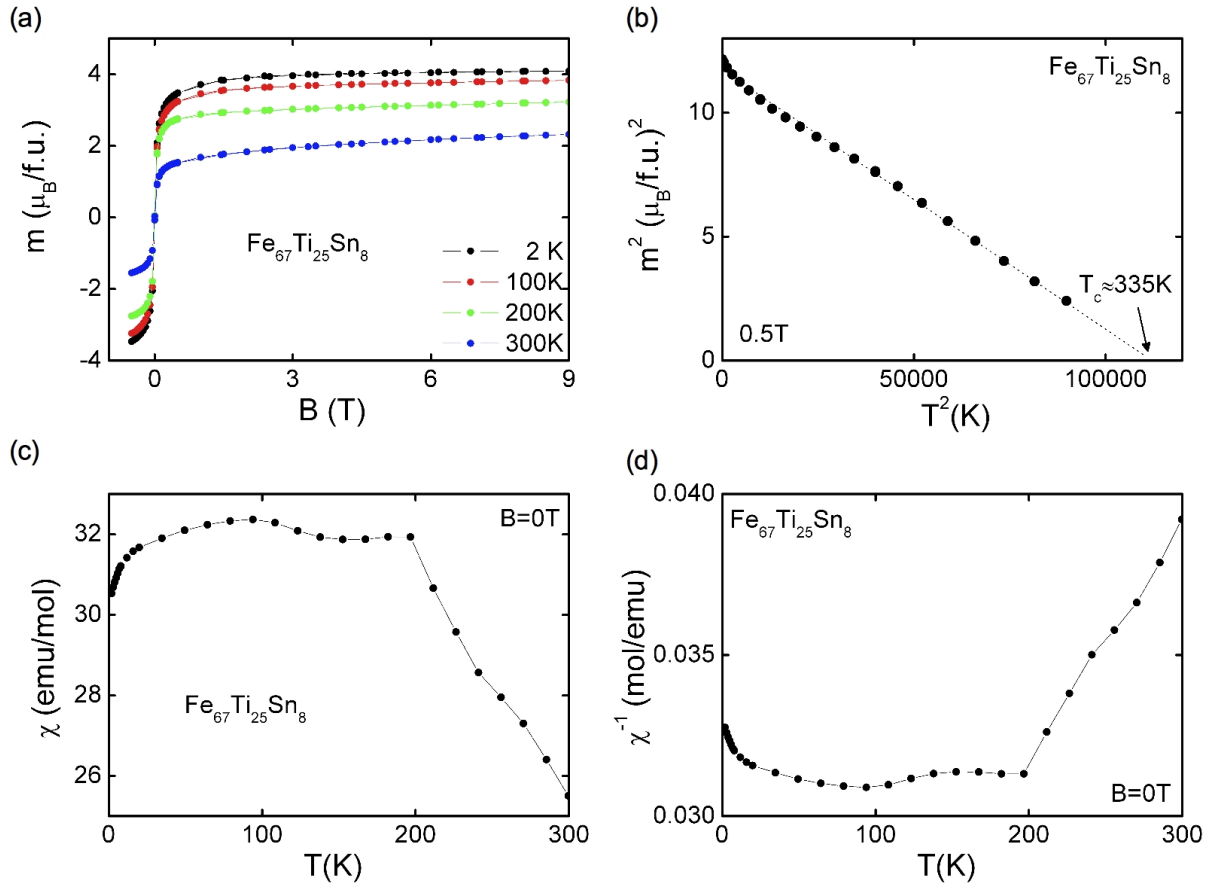

Figure 6.12: (a) Magnetic field dependence of the magnetization of poly-crystalline $Fe_{67}Ti_{25}Sn_8$. Ferromagnetic behavior is observed up to room temperature. (b) m^2 as a function of T^2 for $B = 0.5\,\mathrm{T}$. From the point of intersection with the x-axis we estimate $T_C \approx 335\,\mathrm{K}$. (c) AC-susceptibility and (d) inverse AC-susceptibility at zero field as a function of temperature. A drop of the AC-susceptibility around $T = 200\,\mathrm{K}$ and an increase of the inverse AC-susceptibility at that temperature are observed. This behavior is reminiscent of the effects seen in many Fe_2TiSn sample. The magnetic moment and the AC-susceptibility are given in units of formula unit Fe_2TiSn.

6.2.2 Surface contamination

Besides the transition around 250 K we found in several single crystal samples an additional signal in the AC-susceptibility around $T = 125\,\mathrm{K}$, which we attribute to surface effects that arise from sample preparation. The additional contribution is displayed by the kink in the inverse AC-susceptibility in Fig. 6.13 that appears for the polished and, especially, the powder sample.

Fig. 6.13 shows the temperature dependent inverse AC-susceptibility for a sample prepared from OFZ31-2-2. The data was recorded for the same sample at different stages of its preparation. First the sample surface was roughly polished with a coarse grained sand paper. In this state a weak additional magnetic signal was observed around $T = 125\,\mathrm{K}$,

indicated by the kink in the inverse AC - susceptibility (black dots). Then, the sample surface was polished with a fine grained sand paper and subsequently etched. The additional signal vanished and the inverse AC - susceptibility showed a linear behavior in the entire temperature range studied (red dots). At last, the sample was finely ground. For this powder sample a pronounced increase of the AC - susceptibility appeared, which is shown by the small signal of the inverse AC - susceptibility in Fig. 6.13 (blue spots). It is similar to the behavior observed for the roughly polished sample.

Similar preparation effects, especially regarding the polishing process, were observed for several samples. We hence attribute the additional magnetic response in Fe_2TiSn at around 125 K to surface contamination. While this effect was found experimentally, a microscopical identification has not been carried out.

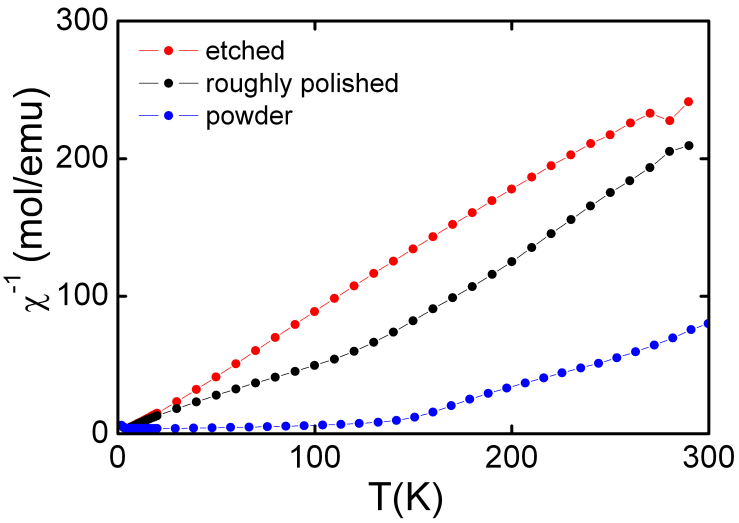

Figure 6.13: Temperature dependence of the zero field inverse AC - susceptibility for a sample prepared from OFZ31-2-2. The data was recorded for the same sample at different stages of its preparation; with a roughly polished surface (black), fine polished and etched surface (red), and as a powder (blue). For the polished and the powder sample a magnetic transition around 125 K is observed, while the etched sample shows the linear Curie-Weiss behavior observed in phase-pure single crystals.

6.3 Properties of phase-pure Fe_2TiSn

In this section the experimental results of phase-pure Fe_2TiSn single crystals are presented. It will be shown that the AC - susceptibility, the magnetization and the specific heat indicate Fe_2TiSn to be on the border of magnetism and in the vicinity to a quantum critical point. However, other than in weak itinerant ferromagnets, the resistivity increases with decreasing temperatures, pointing at isolating behavior at low temperatures. In addition, the phase-pure Fe_2TiSn single crystals display an unusual large sample dependence of the magnetization. In combination with structural disorder effects observed in X-ray synchrotron radiation and with a sample dependent low temperature spin-glass transition, this observation suggests a highly unconventional paramagnetic state in Fe_2TiSn.

For clearness only the experimental results obtained from phase-pure single crystal samples prepared from crystal positions OFZ31-2, OFZ31-3, and OFZ41-3 (cf. Fig. 6.5 and Fig. 6.6) are presented. These samples are referred to as phase-pure, since no impurity phases were identified by means of EDX analysis and synchrotron X-ray diffraction. Likewise, these crystals show no or only very weak additional signals in the AC - susceptibility around 250 K, which was assigned to extrinsic effects as described in the previous section.

6.3.1 Magnetization and AC - susceptibility

Quantum critical weak ferromagnetic properties

The AC - susceptibilities and the inverse AC - susceptibilities at zero field for samples OFZ31-2, OFZ31-3 and OFZ41-3 are shown in Fig. 6.14. All samples show qualitatively similar behavior, notably a Curie-Weiss behavior up to room temperature that extrapolates through zero for $T \approx 0\,\mathrm{K}$ (see Figs. 6.14 (b, d, f) and insets). All samples also display a maximum of the AC - susceptibility at low temperatures (see Figs. 6.14 (a, c, e) and insets). Although qualitatively similar, we note that quantitatively both the temperature of the maximum and the slope of the inverse susceptibility differ for each sample. The effective Curie-Weiss moments determined from the slopes of the inverse susceptibilities are $\mu_{\mathrm{eff}} \approx 2.07$, 2.34, and $2.58\,\mu_{\mathrm{B}}$/Fe for OFZ31-2, OFZ41-3 and OFZ31-3, respectively. These quantitative differences will be discussed below. Irrespective of the quantitative differences, we emphasize the Curie-Weiss behavior up to room temperature that extrapolates to zero for $T_{\mathrm{C}} \approx 0\,\mathrm{K}$ as an important intrinsic property of Fe_2TiSn. This remarkable feature resembles the behavior expected of weak itinerant magnets at a quantum critical point.

The magnetization as a function of field of samples OFZ31-2 and OFZ31-3 is shown in Figs. 6.15 (a) and (b), respectively. For OFZ31-2 data at various temperatures up to 100 K are shown; for OFZ31-3 data at various temperatures up to 30 K are shown. Again qualitatively similar behavior is observed for both samples. At low temperatures the magnetization shows the non-linear behavior of a paramagnetic state without a sign of saturation up to $B = 9\,\mathrm{T}$, the highest field studied. The magnetic moments at $T = 2\,\mathrm{K}$

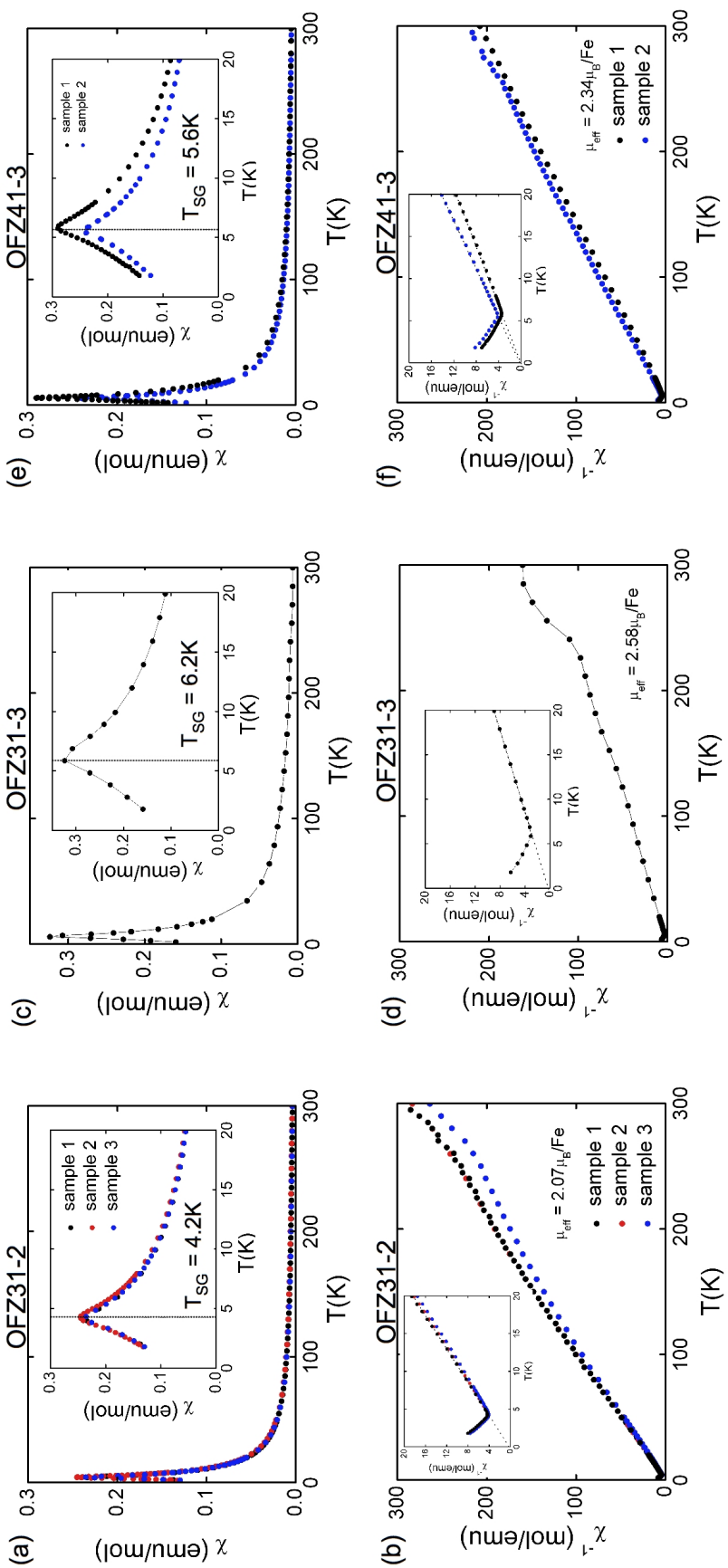

Figure 6.14: Temperature dependent zero field AC - susceptibility and inverse AC - susceptibility of single-crystalline samples prepared from OFZ31-2 (a,b), OFZ31-3 (c,d) and OFZ41 (e,f). All samples show a steep increase of the susceptibility at low temperatures, reaching a maximum at slightly varying temperatures T_{SG} (see insets). The inverse susceptibilities (b,d,f) reveal a linear Curie-Weiss-behavior over the entire temperature range characteristic of good sample quality. The inverse susceptibilities extrapolate to zero for $T_C \approx 0\,K$ (see insets), as expected empirically for quantum critical behavior. Quantitatively the different samples show different slopes of χ^{-1}, resulting in different effective Curie-Weiss moments μ_{eff}. Empirically T_{SG} appears to increase with increasing μ_{eff} as shown in Fig. 6.20.

and $B = 9\,\mathrm{T}$ are $m = 0.12\,\mu_\mathrm{B}$/f.u. and $m = 0.18\,\mu_\mathrm{B}$/f.u. for OFZ31-2 and OFZ31-3, respectively. They are hence by far smaller than the effective Curie-Weiss moments. With increasing temperatures the magnetization decreases and shows a more linear behavior. The unsaturated non-linear behavior of the magnetization at low temperatures may be roughly captured in Arrott plots, i.e., B/m vs. m^2, as shown in Fig. 6.15 (c) and (d). For temperatures above 30 K a linear behavior is observed for OFZ31-2. At lower temperatures both samples show quasi-linear behavior with a slightly positive curvature.

A linear behavior of the magnetization illustrated in Arrott plots is a prominent feature of weak itinerant ferromagnets. These materials also exhibit a large difference of the saturated and effective magnetic moments. As shown above, both features are also present in Fe_2TiSn single crystals. From magnetization and AC - susceptibility we hence may characterize single-crystalline Fe_2TiSn as a weak ferromagnet at a quantum critical point. In the following we will therefore explore if this conjecture is consistent with other properties of Fe_2TiSn.

Intrinsic sample dependent magnetic properties

As mentioned above, a strong sample dependence of both the AC - susceptibility and the magnetization was observed. This is illustrated in Fig. 6.16 (a), that shows the magnetization at $T = 2\,\mathrm{K}$ for samples OFZ31-2, OFZ31-3, and OFZ41-3. As illustrated in Fig. 6.16 (b), all three samples qualitatively show very similar behavior. This raises the question for the origin of the quantitative differences.

Comparing the magnetization with the AC - susceptibility data, we note that the crystal with the smallest effective moment (OFZ31-2) shows the smallest magnetic moment at $T = 2\,\mathrm{K}$ and $B = 9\,\mathrm{T}$, while the crystal with the highest μ_eff(OFZ31-3) shows the highest magnetic moment $m(9\mathrm{T}, 2\mathrm{K})$. This relation is displayed in Fig. 6.17 (b), where empirically a linear dependence of μ_eff^2 and $m(9\mathrm{T}, 2\mathrm{K})$ is found.

A linear dependence of μ_eff^2 and m would be consistent with a variation of the volume fraction of a magnetic impurity phase in a non-magnetic material. However, such a large variation of $m(9\mathrm{T}, 2\mathrm{K})$ would imply the existence of a large volume fraction of an impurity phase, which we did not observe in EDX analysis. Hence, we speculate that the origin of the sample dependence of the magnetic properties is more subtle. Possibilities are compositional variations or disorder effects as will be discussed below. In any case, we want to emphasize that such a large variation of the magnetic moment in a phase-pure single crystal is a remarkable feature.

Spin-glass state at low temperatures

Finally, we turn to the nature of the low temperature transition as indicated by the maximum in the AC - susceptibility. Fig. 6.18 shows the real and imaginary part of the AC - susceptibility as a function of temperature at various fields for OFZ31-2 and OFZ31-3. The maxima in the AC - susceptibility are observed around 4.3 K and 6.2 K for OFZ31-2

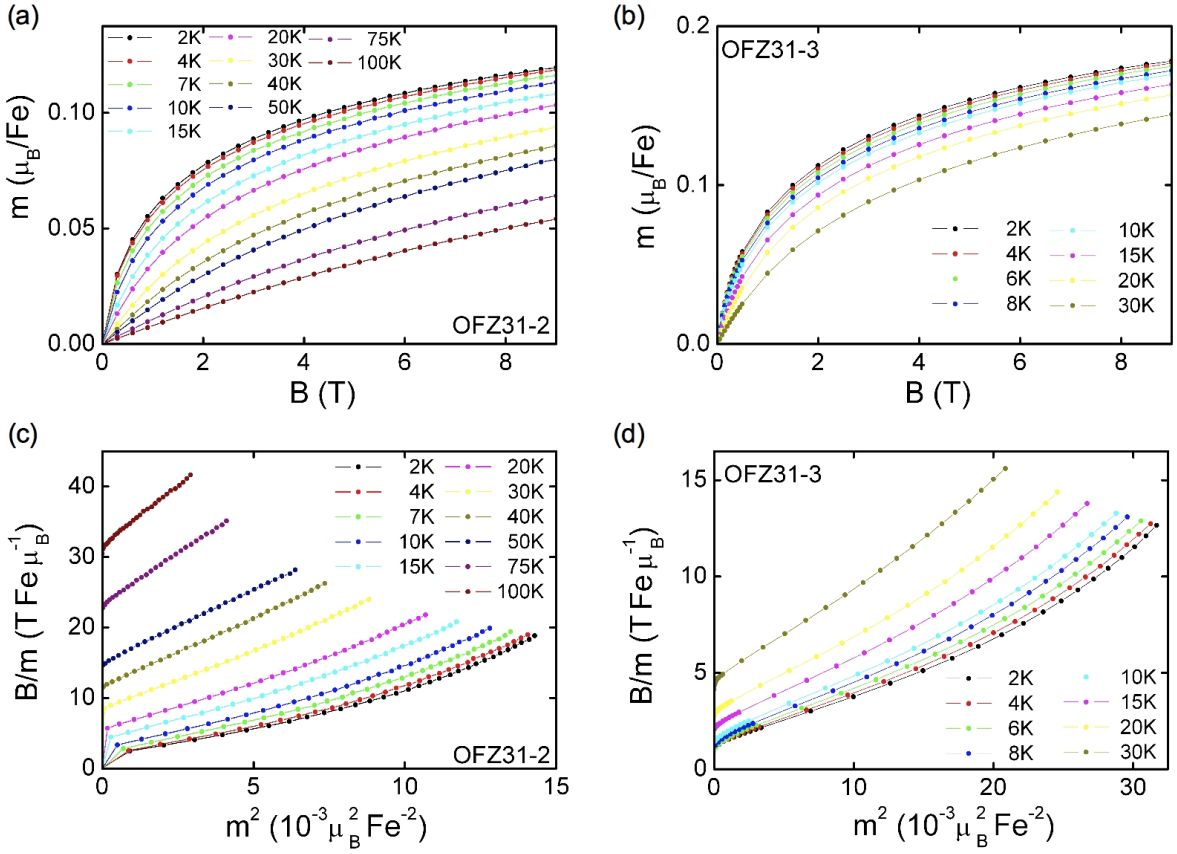

Figure 6.15: (a, b) Magnetization as a function of field for single crystal samples OFZ31-2 and OFZ31-3. The magnetic moments of OFZ31-3 are around 50% larger than those of OFZ31-2. At low temperatures the magnetization of both samples shows the non-linear behavior of a paramagnetic state without a sign of saturation. (c, d) Magnetization presented as Arrott plots for OFZ31-2 and OFZ31-3. At temperatures above 30 K a linear behavior is observed for OFZ31-2. Below, the data for both samples shows sub-linear behavior with a positive curvature.

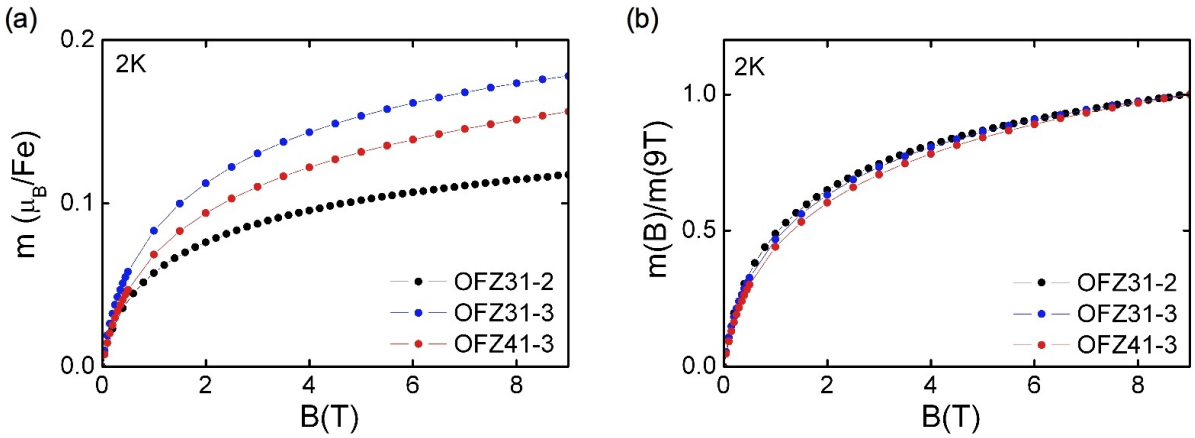

Figure 6.16: (a) Field dependence of the magnetic moments of single-crystalline samples prepared from OFZ31-2, OFZ31-3 and OFZ41-3, measured at $T = 2$ K. No hysteresis is observed. The absolute moments differ by 50%. (b) The magnetization at $T = 2$ K for all three samples scaled to their high field values, illustrating qualitatively similar behavior of all three samples.

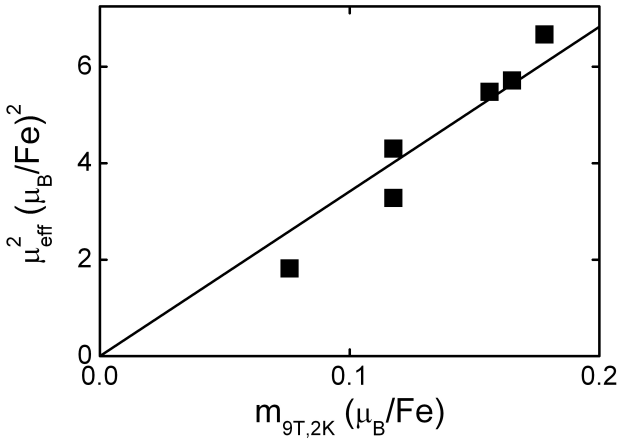

Figure 6.17: Empirically we find a scattered linear dependence of μ_{eff}^2 and $m(9\text{T}, 2\text{K})$. This linear dependence suggests that a variation of the magnetic volume fraction is responsible for the quantitative differences observed. However, EDX analysis did not show any impurity phase.

and OFZ31-3, respectively. Besides these differences, both samples show qualitatively similar behavior. With increasing field the maximum in the AC - susceptibility is suppressed and flattened. At 500 mT the maximum vanished and an almost constant susceptibility is observed. The imaginary part of the AC - susceptibility is finite below T_{SG} characteristic of dissipative behavior, as shown in Figs. 6.18 (c) and (d). At zero external field a sharp increase appears around the transition temperature. With increasing external field the the increase becomes less pronounced and shifts to lower temperatures. This behavior confirms the suppression of the low temperature state with increasing field.

Fig. 6.19 shows the temperature dependent AC - susceptibility for OFZ31-3 measured at three different frequencies. With increasing frequency the maximum is slightly suppressed and shifts to higher temperatures. This weak frequency dependence as well as the dissipative signal in the imaginary part of the AC - susceptibility suggest a spin-glass state of Fe_2TiSn at low temperatures. A tiny signal in the specific heat (see Fig. 6.24) around T_{SG} shows that this spin-glass state is accompanied by a very weak reduction of entropy.

Fig. 6.20 (a) shows the B - T -phase diagram of the spin-glass state for OFZ31-2 and OFZ31-3. The data represent the point of inflection of the imaginary part of the AC - susceptibility, indicated by the black arrows in Figs. 6.18 (c) and (d). For OFZ31-2 the data is shifted to lower temperatures. However, qualitatively the same field dependence is observed (not shown). The relationship of the spin-glass temperature and the effective moment is shown in Fig. 6.20 (b). Curiously, we observe a linear relation of T_{SG} and μ_{eff}^2. This sample dependence of the spin-glass state suggests that the properties are somehow connected. The origin of the relationship is presently open. However, if the spin-glass state is primarily due to weak disorder it does not seem plausible that this disorder can account for the large fluctuating moments in each unit cell. Thus the spin-glass temperature depends also on the size of the fluctuating moments. To explore the role of disorder further we performed annealing and a structural refinement presented in the following.

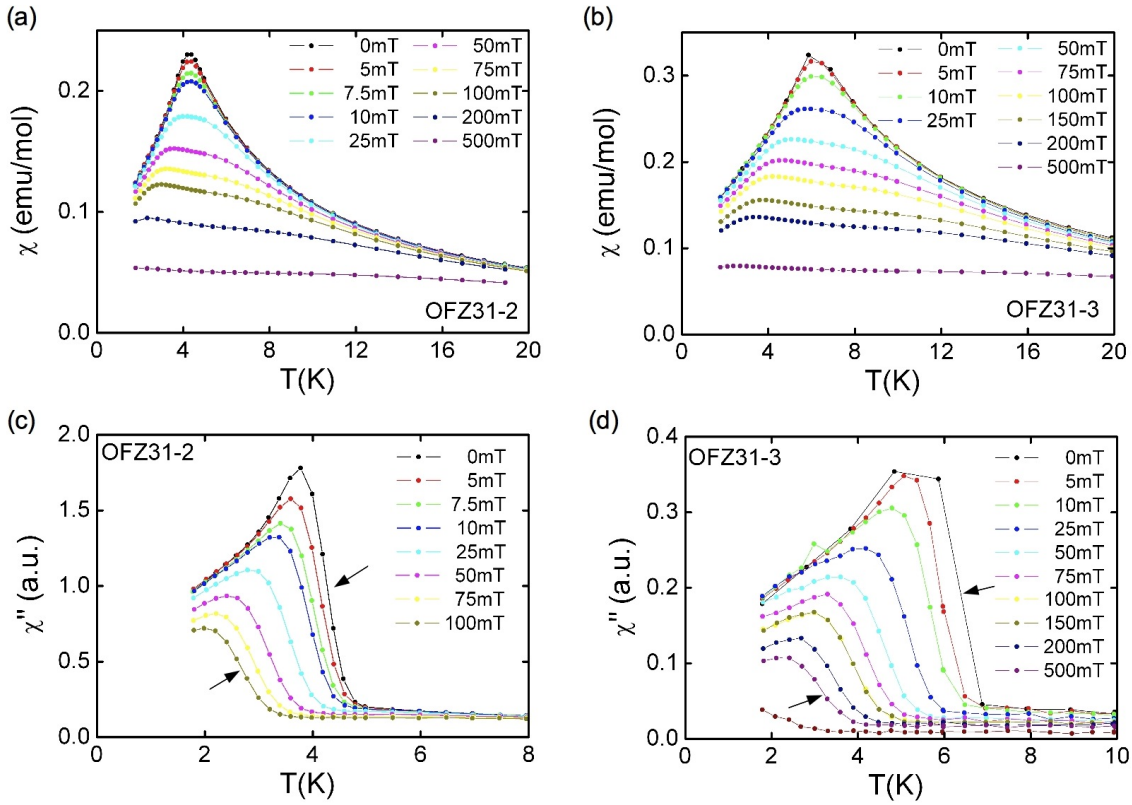

Figure 6.18: Low temperature real and imaginary part of the AC - susceptibility at small fields. Panels (a) and (c) show data for single crystal OFZ31-2, while panels (b) and (d) show data for single crystal OFZ31-3. Besides the transition temperature T_{SG} both samples show very similar behavior. With increasing field T_{SG} is suppressed and the maximum flattens. The steep increase in the imaginary part of the AC - susceptibility at the transition temperature indicates a spin-glass-like behavior. With increasing field this increase is also suppressed. The black arrows indicate the point of inflection of the increase of χ''.

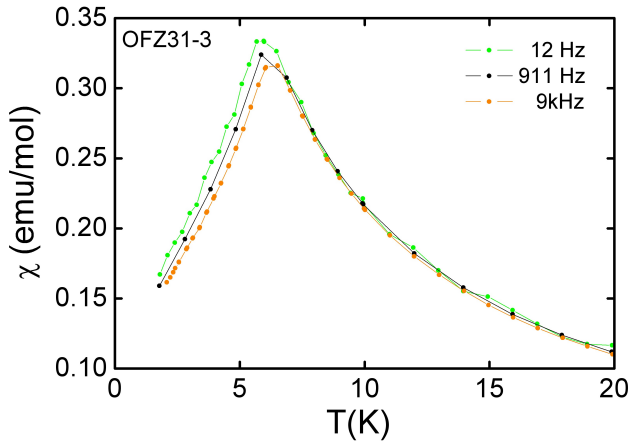

Figure 6.19: Temperature dependence of the AC - susceptibility of OFZ31-3 measured at three different frequencies. Below the transition the AC - susceptibility shows a weak frequency dependence and is suppressed with increasing ac-frequency. This resembles the typical behavior observed for spin-glass transitions.

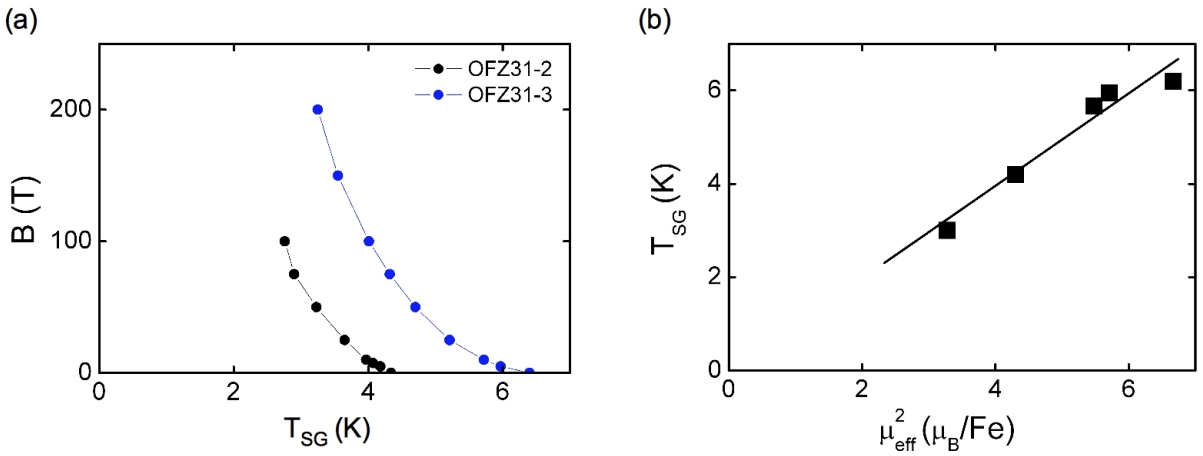

Figure 6.20: (a) Temperature-field phase diagram of the spin-glass state in OFZ31-2 and OFZ31-3. The data is derived from the point of inflection of the imaginary part of the AC-susceptility, as indicated by the black arrows in Figs. 6.18 (c) and (d). Qualitatively a similar field dependence is observed (not shown). (b) Empirically T_{SG} appears to increase linearly with the square of the effective moment μ_{eff}^2.

6.3.2 Role of annealing

Since high temperature treatment can have a strong influence on the physical properties of materials, notably disorder, we investigated the effects of annealing on single-crystalline Fe_2TiSn samples. In general, annealing at the appropriate temperature may reduce strains and crystal defects and therefore may be used as a method to optimize the crystal properties.

Two samples prepared from OFZ41-3 were annealed for 10 days by inductive heating in the horizontal cold finger (HCF) system in high purity Argon atmosphere. In order to reduce temperature gradients the Fe_2TiSn samples were placed on a Ta slab. The two samples OFZ41-3A and OFZ41-3B with a mass of 669 mg and 148 mg, respectively, were positioned next to each other. The temperature was controlled by a pyrometer, that allowed to measure temperatures between 500° and 2200° C. The large sample OFZ41-3A was kept at a constant temperature of 870° C. The temperature of the small sample OFZ41-3B was below 500° C, i.e., below the limit of the pyrometer. The different annealing temperatures were chosen in order to investigate the effects of the temperature of the annealing. After the heat treatment, the temperature of the large sample was reduced manually in steps of $\sim$ 20° C every 15 minutes. A similar cooling rate is expected for the smaller sample. No mass loss was observed during annealing.

Fig. 6.21 shows the temperature dependent AC-susceptibility and inverse AC-susceptibility, and the field dependent magnetization for both samples (left row: OFZ41-3A; right row: OFZ41-3B). Data for the as-grown single crystal prior to annealing, for the annealed crystal, and for the annealed crystal after polishing are shown.

For OFZ41-3A, that was annealed at $T = 870°$ C, the appearance of an additional magnetic signal in the AC - susceptibility around 250 K was observed, as shown in Figs. 6.21 (a) and (c). This additional signal resembles the behavior attributed to the $Fe_{67}Ti_{25}Sn_8$ impurity phase. EDX analysis confirmed the appearance of extended $Fe_{67}Ti_{25}Sn_8$ regions in the vicinity of a grain boundary in this sample. After polishing the additional signal was found to be slightly reduced. In addition, we found a reduction of the spin-glass temperature from 5.8 K to 4.8 K for the annealed sample, as illustrated in the inset of Fig. 6.21 (c). Regardless of the additional impurity signal we found a reduction of the magnetization at $T = 2$ K for the annealed sample, as shown in Fig. 6.21 (e). The magnetization curves of the as-grown and the annealed sample show qualitatively identical behavior as illustrated by the scaled curve (red triangles), where the scaling factor was 1.2.

For OFZ41-3B, which was annealed below 500° C, the AC - susceptibility data is less conclusive. An additional signal in the AC - susceptibility appears with a maximum around 15 K, as shown in Fig. 6.21 (d). This behavior may be attributed to some surface effect, since it vanishes after polishing. Nevertheless, an additional contribution persists for the polished and etched sample, as illustrated by the non-linear behavior of the inverse susceptibility in Fig. 6.21 (b). As for OFZ41-3A we also observed a reduction of the spin-glass temperature of the annealed sample from 5.6 K to 4 K, as well as a strong reduction of the magnetization, shown as a function of field at $T = 2$ K in Fig. 6.21 (f). Again, the magnetization of the annealed sample can be scaled to match that of the as-grown sample as indicated by the green triangles. The scaling factor was 1.73.

Summarizing the observed effects of the high temperature treatment on the magnetic properties in Fe_2TiSn single crystals, we found that annealing leads to a reduction of the magnetic moment, measured as $m(9\mathrm{T}, 2\mathrm{K})$. This effect was observed for annealing at high and low temperatures. Since annealing at $T = 870°$ C promotes the formation of a $Fe_{67}Ti_{25}Sn_8$ impurity phase we propose a reduced annealing temperature for further heat treatment experiments. However, the origin of the additional magnetic response observed for the sample annealed at lower temperatures must be investigated.

We also found a reduction of the spin-glass temperature T_{SG} after annealing. Since both T_{SG} and $m(9\mathrm{T}, 2\mathrm{K})$ were found to scale with the effective magnetic moment (see previous section), we also assume a reduction of μ_{eff} of the annealed samples. An experimental determination of μ_{eff} was not possible, however, due to the non-linear inverse AC - susceptibility of the annealed samples which was caused by impurity phases. The reduction of both the magnetic moments and the transition temperature T_{SG} in annealed samples favors a disorder effect as the origin of the unusual sample dependence of the magnetization. Compositional variations as the origin are unlikely, since we did not observe a loss of mass during annealing nor large phase differences in EDX. In order to investigate the role of disorder in Fe_2TiSn we carried out a structural refinement of synchrotron powder diffraction data as shown in the next section.

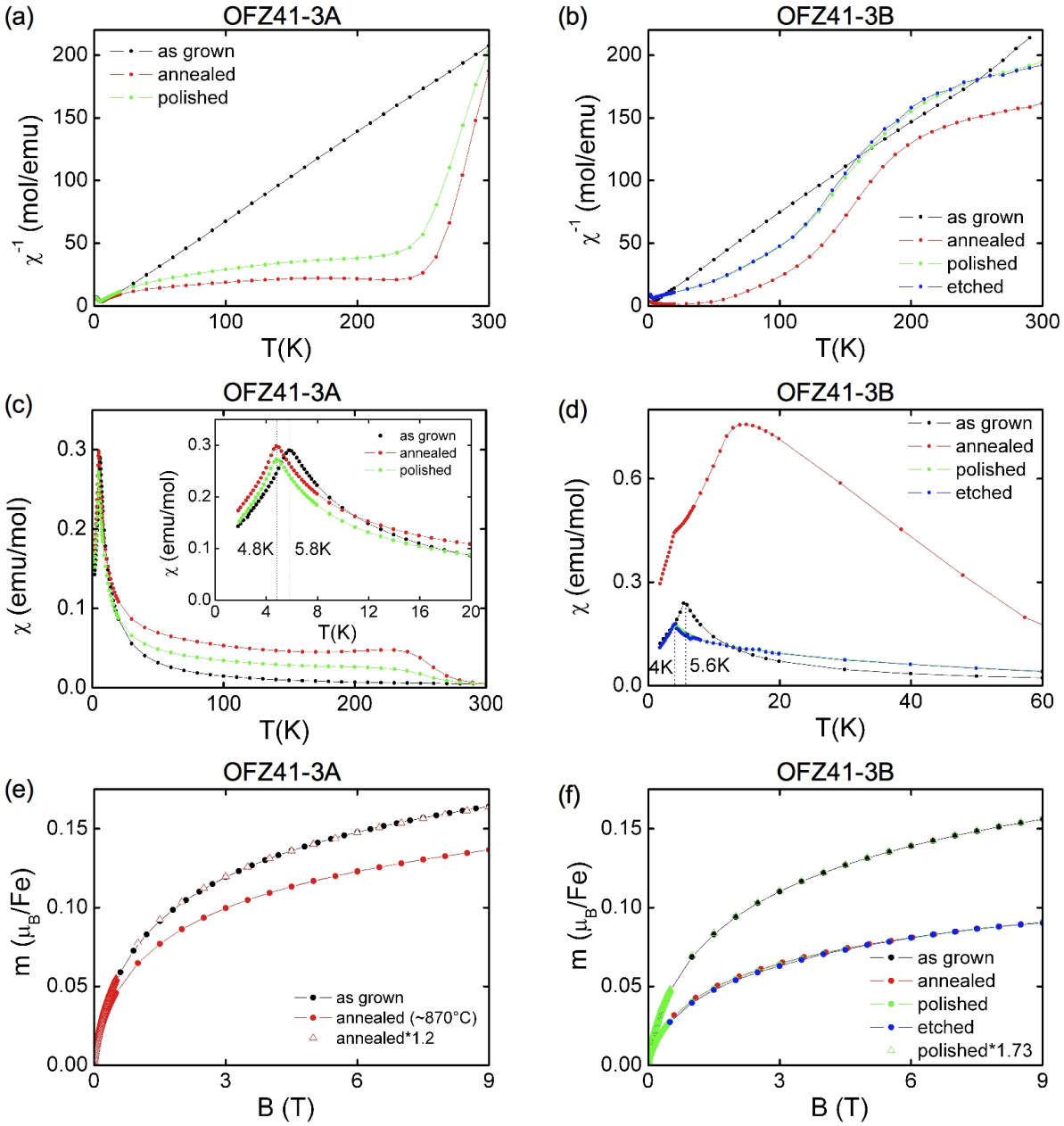

Figure 6.21: AC-susceptibility and magnetization data for two single-crystalline samples prepared from OFZ41-3 after high temperature treatment for 10 days. Panels on the left (a, c, e) show data for OFZ41-3A (667 mg), which was annealed at 870°C. Panels on the right (b, d, f) show data for OFZ41-3B (148 mg), which was annealed below 500°C in the same set-up. Data is shown for the annealed samples (red), the annealed samples after polishing (green) and etching (blue, OFZ41-3B only), and, in comparison, the same samples prior to the heat treatment (black). (a-d) For the annealed samples additional contributions in the AC-susceptibility appear. In addition, the spin-glass temperature, indicated by the maximum in the AC-susceptibility, is reduced. (e, f) The magnetization as a function of field at $T = 2\,\mathrm{K}$. The annealed samples show a reduced magnetization that scales with the as-grown samples prior to annealing, as illustrated by the open triangles. The scaling factor is 1.2 and 1.73 for OFZ41-3A and OFZ41-3B, respectively.

6.3.3 Synchrotron powder diffraction

In order to investigate the influence of disorder on the magnetic properties of Fe_2TiSn, especially with respect to the anti-site disorder proposed by Ślebarski *et al.* [37], we carried out detailed X-ray powder diffraction (XRD) experiments in collaboration with Anatoliy Senyshyn[1] and Klaudia Hradil[2]. The Rietveld refinement and analysis of the XRD data was carried out by Anatoliy Senyshyn.

The first XRD diffraction experiments on samples from crystals OFZ13 and OFZ14 using Cu radiation indicated a small amount of a secondary Fe phase, whereas XRD diffraction with Cu radiation on two samples from OFZ31-2 and one from OFZ41-3 did not reveal any secondary phase. However, a detailed analysis of the crystal structure with Cu radiation was limited by the strong fluorescence caused by the iron atoms in Fe_2TiSn. Subsequent investigation with Co radiation did not yield satisfying results either, since only a limited number of Bragg reflections was observed due to the high symmetry of the system. In the case of Mo radiation, a poor resolution was the limiting factor.

Using Cu, Co and Mo radiation, we were, hence, able to show that XRD patterns of high quality Fe_2TiSn powder did not yield any evidence for impurity phases. However, for a detailed analysis of the crystal structure these experiments did not provide data of sufficient quality. Therefore synchrotron radiation with a wavelength of $\lambda_s \approx 0.7\,\text{Å}$ (close to Mo) at the beamline B2 (Hasylab, Hamburg) was used for a detailed structural investigation of samples prepared from single crystals OFZ31-2 (two samples) and OFZ41-3 (one sample). The measurements were carried out in transmission geometry and the powder was placed in a small quartz capillary ($\varnothing\,0.3\,\text{mm}$).

Figs. 6.22 (a) and (b) show the XRD patterns obtained with synchrotron radiation on samples OFZ31-2a and OFZ41-3, respectively. The data for sample OFZ31-2b are very similar (not shown). The red dots show the experimentally observed intensities and the black line the calculated intensity after Rietveld refinement. The blue line at the bottom shows the difference between both intensities, thus indicating a good agreement for both samples.

A standard analysis of the peak positions in the XRD pattern revealed that all three samples crystallize in the $L2_1$-type Heusler structure with lattice parameters $a = 6.063 \pm 0.002\,\text{Å}$ (see Table 6.1). The small differences in the lattice parameters might indicate either defect formation or may be caused by experimental effects due to sample mounting. The lattice parameters for our float-zoned single crystals are systematically smaller than those reported by Ślebarski *et al.* [34] for polycrystals ($a = 6.074\,\text{Å}$).

The results of the Rietveld refinement for all three crystals are summarized in Table 6.1. The following conclusions may be drawn [146]: (i) The changes in the "U Caglioti" parameters may be assigned to microstrains. Grinding of the single crystal samples might have an effect on the formation of microstrains in the material, and on the magnetic properties as well. Further investigation and control of single crystals ground, e.g., in liquid nitrogen,

[1] Dr. Anatoliy Senyshyn is instrument responsible at SPODI at FRM II.
[2] Dr. Klaudia Hradil is instrument responsible at PUMA at FRM II.

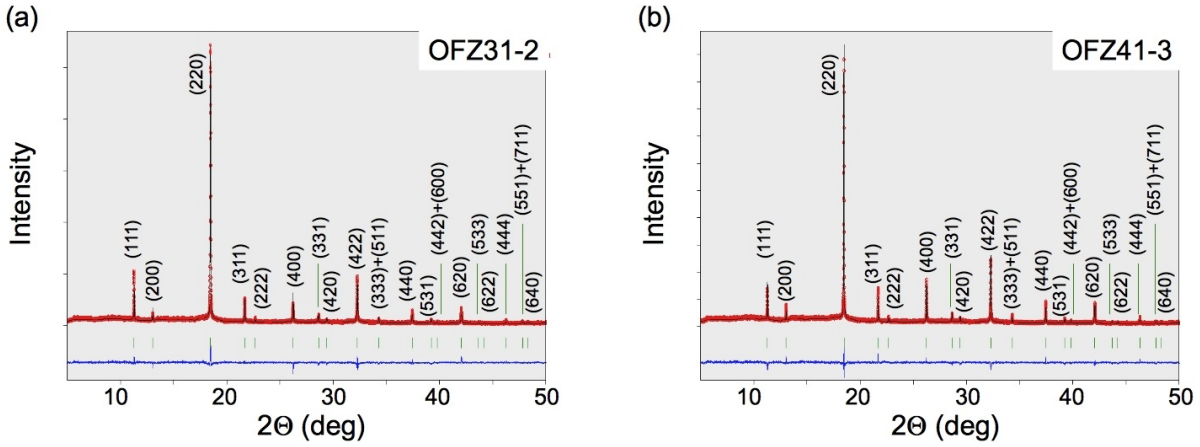

Figure 6.22: Observed (red dots) and calculated (black line) XRD patterns of OFZ31-2 (a) and OFZ41-3 (b) obtained with synchrotron radiation ($\lambda_s \approx 0.7$ Å) at Hasylab. The bottom pattern is the difference between the experimental and calculated intensities after Rietveld refinement. It illustrates a good agreement for both samples.

would be desirable. (ii) A significant difference in the isotropic displacement parameters $\mathbf{B}_{iso}$ for Fe, Ti and Sn occurs. As both scattering power and weight of constituents are similar, this might correspond to positional disorder. The most stable refinement was obtained by simulation of the observed disorder phenomena with a split-site model as shown in Fig. 6.23. In this split-site model the Fe and Ti sites at 8c $(\frac{1}{4},\frac{1}{4},\frac{1}{4})$ and 4a (0,0,0), respectively, have been split into 32f (x,x,x). Due to the usual correlations between atomic positions, isotropic displacement parameters and site occupancies an overall displacement parameter has been used instead of an isotropic displacement parameter. Site occupancies have been fixed to their nominal values. As splitting of the Sn site resulted in a divergent fit, no site splitting has been applied for this case, i.e., only Fe and Ti positions underwent disorder modeling.

Application of the split-site approach did not result in a significant improvement of the fit residuals, which is rather normal [146]. Nevertheless, from the split site positions in Table 6.2 one can see that sample OFZ31-2b has the smallest magnitude of disorder. For this sample Ti is probably in the ordered state. OFZ31-2a, in this sense, is the most disordered sample (one can expect a little disorder on the Sn site as well) and sample OFZ41-3 possesses an intermediate level of disorder.

	OFZ31-2A	OFZ31-2B	OFZ41-3
Lattice parameter a	6.06328(16)	6.06493(15)	6.06139(15)
Overall $\mathbf{B}_{Fe}$	2.222(72)	0.948(43)	1.263(69)
Overall $\mathbf{B}_{Ti}$	0.502(44)	0.153(30)	0.027(44)
Overall $\mathbf{B}_{Sn}$	1.832(105)	0.190(60)	0.856(99)
Caglioti parameter $\mathbf{U}$	0.12(1)	0.21(1)	0.062(7)
Fit residuals (R_p, R_{wp}, R_{exp})	12.0, 14.3, 3.09	11.1, 13.5, 3.46	11.5, 13.5, 2.93

Table 6.1: Fitting parameters obtained from Rietveld refinement of float-zoned Fe_2TiSn.

	OFZ31-2A	OFZ31-2B	OFZ41-3
Fe site disorder	0.25 → 0.2734(4)	0.25 → 0.2338(4)	0.25 → 0.2298(5)
Ti site disorder	0.00 → 0.0206(8)	0.00 → 0.003(3)	0.00 → 0.0167(9)
Fit residuals (R_p, R_{wp}, R_{exp})	11.9, 14.3, 3.09	11.1, 13.5, 3.46	11.5, 13.4, 2.93

Table 6.2: Fitting parameters obtained for the split-site model.

Since the AC - susceptibility and magnetization were only measured for samples OFZ31-2b and OFZ41-3 (see previous section), no conclusive relation between the observed disorder phenomena and the variations of the magnetic properties can be drawn at this stage. Especially since samples OFZ31-2a and OFZ31-2b, which are expected to show similar magnetic properties, showed the most and the least amount of disorder, respectively. Comparing the amount of disorder and the size of the magnetic moments (see Fig. 6.16) for samples OFZ31-2b and OFZ41-3, we may speculate, however, that the magnetic moment increases with the amount of disorder. Further structural investigation of sample OFZ31-3, the sample with the largest magnetic moment, as well as of annealed samples would be desirable to confirm this speculation.

Finally, during the sample preparation for single crystal diffraction experiments a twinning of the crystallites along the <111> direction was noticed, which is rather common for Heusler compounds [147]. Preliminary single crystal diffraction experiments using Cu radiation, carried out by Klaudia Hradil, showed diffraction patterns with diffuse stripes. This finding is in good agreement with the proposed split-site model [147].

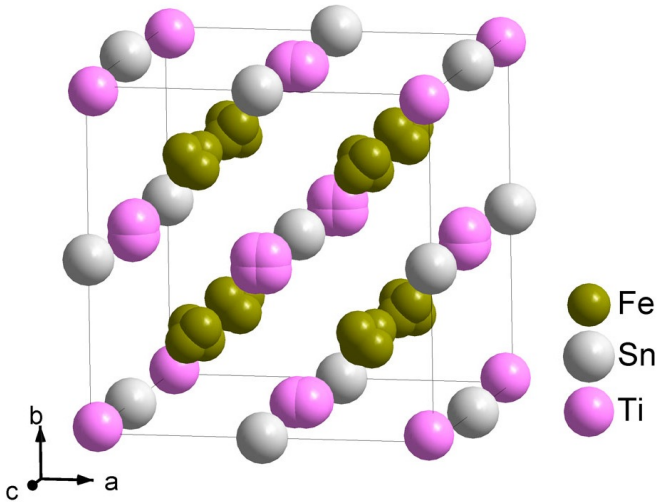

Figure 6.23: Proposed Fe_2TiSn crystal structure for OFZ41-3 with split-site disorder as derived from the pronounced disorder phenomena observed in the XRD patterns. The Fe and Ti sites, 8c $(\frac{1}{4},\frac{1}{4},\frac{1}{4})$ and 4a (0,0,0), respectively, have been splitted into 32f (x,x,x) sites. No split-site has been applied to Sn.

To summarize, Rietveld refinement of synchrotron X-ray powder diffraction data revealed a structural disorder in our float-zoned Fe_2TiSn crystals, which can be modeled to a first approximation by a split-site ansatz. A microscopic relationship between this structural disorder and the magnetic properties may not been given yet. Nevertheless, taking into account the linear dependence of $m(9\mathrm{T}, 2\mathrm{K})$ and μ_{eff}^2, as well as T_{SG} and μ_{eff}^2, we suspect a subtle microscopic origin of the sample dependence that is strongly connected to the observed disorder phenomena. Finally, in order to exclude or elucidate possible anti-site disorder effects as proposed by Ślebarski *et al.*[34], powder diffraction with neutrons is of essential importance and planned in the near future.

6.3.4 Specific heat

So far we found that the AC - susceptibility and magnetization indicate single-crystalline Fe_2TiSn as a weak ferromagnet at a quantum critical point. In addition to this intrinsic feature we found a strong sample dependence of the magnetic properties as well as the low temperature spin-glass-like state. The effect of annealing as well as the observation of split-site structural disorder imply the importance of disorder for the magnetic properties of Fe_2TiSn. In order to examine the nature of the quantum criticality in Fe_2TiSn in detail, we investigated the specific heat and the resistivity as shown in this and in the next section, respectively.

The specific heat of a single-crystalline sample prepared from OFZ31-2 was measured in zero field between $T = 2\,\mathrm{K}$ and $T = 300\,\mathrm{K}$ as shown in Fig. 6.24 (a). At room temperature the specific heat approaches the Dulong-Petit threshold of $C = 4 \times 3Nk_{\mathrm{B}} \approx 100\,\mathrm{Jmol^{-1}K^{-1}}$. At low temperatures between 10 K and 40 K the specific heat is very well described by $C = \gamma T + \beta T^3$. Fitting the data we obtained an electronic contribution $\gamma \approx 11.8\,\mathrm{mJ\,mol^{-1}K^{-2}}$ and a phonon contribution $\beta = 0.14\,\mathrm{mJ\,mol^{-1}K^{-4}}$. The coefficient β of the low-temperature lattice contribution corresponds to a Debye temperature $\Theta_{\mathrm{D}} \sim 380\,\mathrm{K}$. In comparison to the data reported by Ślebarski *et al.* [34], the Sommerfeld coefficient γ determined for OFZ31-2 is in good agreement, while β is slightly larger than the value $\beta = 0.11\,\mathrm{mJ\,mol^{-1}K^{-4}}$ reported for polycrystals.

Fig. 6.24 (b) shows C/T vs. T for OFZ31-2 at low temperatures and different fields. Note that the temperature is presented on a logarithmic scale. At low fields C/T increases with decreasing temperature and shows a logarithmic dependence between 3 K and 9 K. Such a logarithmic increase is predicted by spin-fluctuation theory for 3-dimensional ferromagnetic quantum critical systems [87, 148–150]. With increasing field the upturn in C/T is suppressed, resulting in a constant C/T at a field of 9 T, with an increased $\gamma = 35\,\mathrm{mJ\,mol^{-1}K^{-2}}$. In addition, we observe a small additional reduction around 4.5 K and low fields, that indicates the phase transition to the spin-glass state. From the small size of the reduction we infer that the spin-glass state causes only a small reduction of entropy. We therefore denote it as a weak spin-glass state.

Qualitatively similar behavior was also found for sample OFZ31-3 (not shown). C/T for OFZ31-3 shows a logarithmic dependence with a slightly less pronounced increase. Further, the specific heat around 10 K, i.e., above the upturn in C/T, is slightly enhanced for

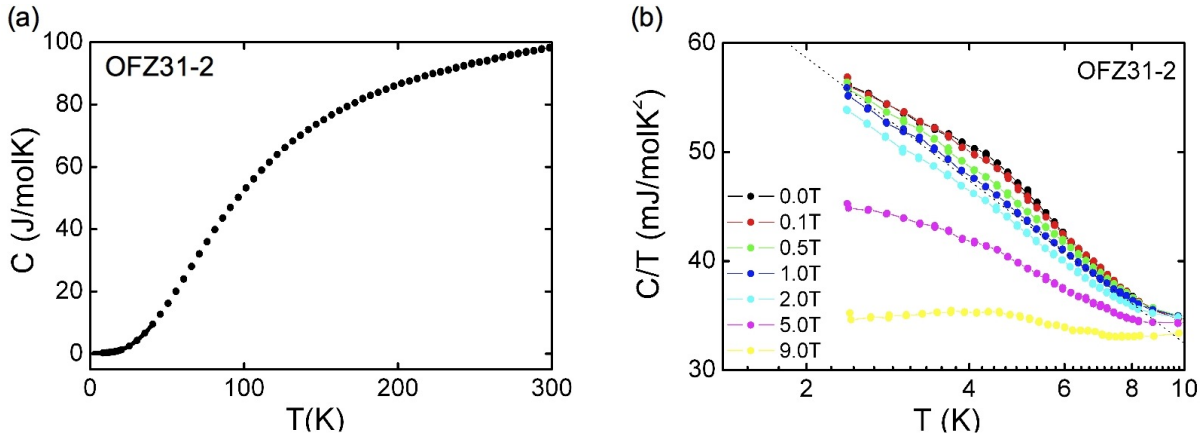

Figure 6.24: (a) Temperature dependent specific heat for a single-crystalline sample prepared from OFZ31-2. (b) The upturn in C/T at low temperatures follows a logarithmic increase as indicated by the black dotted line. The reduction around $T = 4\,\mathrm{K}$ at lowest fields corresponds to the transition observed in the susceptibility. With increasing field the upturn is suppressed.

OFZ31-3 in comparison to OFZ31-2. We attribute this enhancement of the specific heat to the slightly larger magnetic moments in sample OFZ31-3. The additional reduction in C/T that appears at the spin-glass transition is again very weak.

The surprisingly high Sommerfeld coefficient γ in Fe_2TiSn single crystals at low temperatures indicates the presence of strong spin fluctuations. In addition, the logarithmic increase of the specific heat (C/T) at low temperatures is consistent with the behavior reported for other quantum critical d-metal compounds, e.g., $Nb_{1-x}Fe_{2+x}$ [62]. Hence, measurements of the specific heat also support that single crystal Fe_2TiSn is intrinsically at a quantum critical point at ambient pressure.

6.3.5 Electrical transport

To address the question if Fe_2TiSn supports itinerant electron magnetism we measured the electrical transport. The zero field temperature dependence of the longitudinal resistivity for single crystal samples prepared from OFZ31-2 and OFZ31-3 is shown in Figs. 6.25 (a) and (b), respectively. At high temperatures OFZ31-2 shows a metallic decrease of the resistivity with decreasing temperature. Below a minimum around 125 K the resistivity increases with decreasing temperature, showing a semiconductor-like behavior. Qualitatively, the resistivity of OFZ31-2 resembles the behavior observed for polycrystals reported by Ślebarski *et al.* [34], although the minimum is shifted to higher temperatures. For polycrystals the minimum was found to be around 50 K.

In contrast, crystal OFZ31-3 shows no minimum and the semiconductor-like increase of the resistivity prevails in the entire temperature range investigated. The absolute value of the resistivity is similar for both samples. Interestingly, for the poly-crystalline samples an elevated room temperature resistivity of $\sim 480\,\mu\Omega$cm was reported. This high value may be related to cracks in the polycrystals and an erroneous geometry factor.

From the linear Hall resistivity ρ_{xy} at room temperature, shown in the insets in Figs. 6.25 (a) and (b), a negative Hall coefficient R_0 is derived for both samples indicating an electron-like conduction. From R_0 a charge carrier concentration of $n \approx 2.5 \times 10^{21}\,\mathrm{cm}^{-3}$ and $n \approx 4.1 \times 10^{21}\,\mathrm{cm}^{-3}$ may be inferred for samples OFZ31-2 and OFZ31-3, respectively. This difference may be easily explained by the uncertainty of the location of the electrical contacts. We note that the charge carrier concentration suggests a metallic state.

In the previous sections we proposed that OFZ31-3, the sample that shows larger magnetic moments, is more disordered than sample OFZ31-2. This suggests that the qualitative difference of the temperature dependent resistivity of both samples is due to disorder. We propose that disorder suppresses the metallic behavior of the resistivity at high temperatures. This would be consistent with the minimum of the resistivity at 50 K reported for polycrystals [34], since these samples were annealed which we assume to reduce disorder. Resistivity measurements of our annealed single crystals are in preparation in order to test this conjecture. Irrespective of these differences, we observed a strong increase of the resistivity at low temperatures for both samples. We note that this increase to low temperatures is in stark contrast with weak itinerant-electron ferromagnets, e.g., MnSi, Ni_3Al, or $ZrZn_2$, for which the resistivity decreases with decreasing temperature resulting in very low residual resistivities ρ_0 [93, 151, 152].

Fig. 6.26 (a) shows the field-dependent magnetoresistance for crystal OFZ31-3 at various temperatures. A negative magnetoresistance is observed in the entire temperature range studied. With decreasing temperature the magnetoresistance increases. At $T = 4\,\mathrm{K}$ and $B = 14\,\mathrm{T}$ the resistivity is suppressed by around 7%. We note that the linear suppression of the resistivity with applied field at low temperatures is highly unusual. For sample OFZ31-2 (not shown) similar behavior was observed .

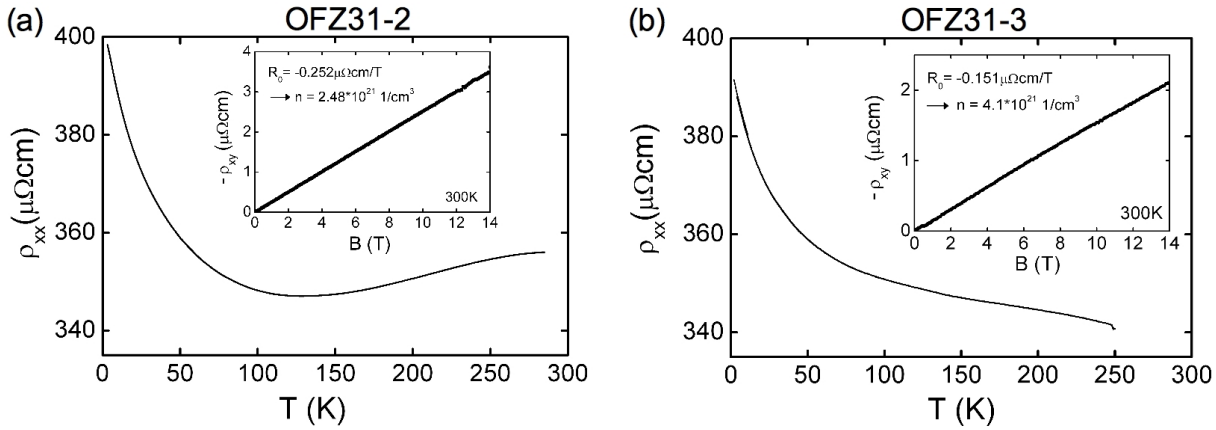

Figure 6.25: Temperature dependence of the longitudinal resistance of a single-crystalline sample prepared from OFZ31-2 (a) and OFZ31-3 (b). OFZ31-2 shows a decreasing (metallic) resistivity down to 125 K, followed by an increase (semiconductor-like) to lower temperatures. In contrast, OFZ31-3 shows an increasing (semiconductor-like) resistivity with decreasing temperatures for the entire temperature range studied. At room temperature both show a negative linear Hall resistivity ρ_{xy} (see insets and note that the data is presented as $-\rho_{xy}$). From the slope an electron-like charge carrier density $n \sim 3.5 \times 10^{21}\,\mathrm{cm}^{-3}$ is derived.

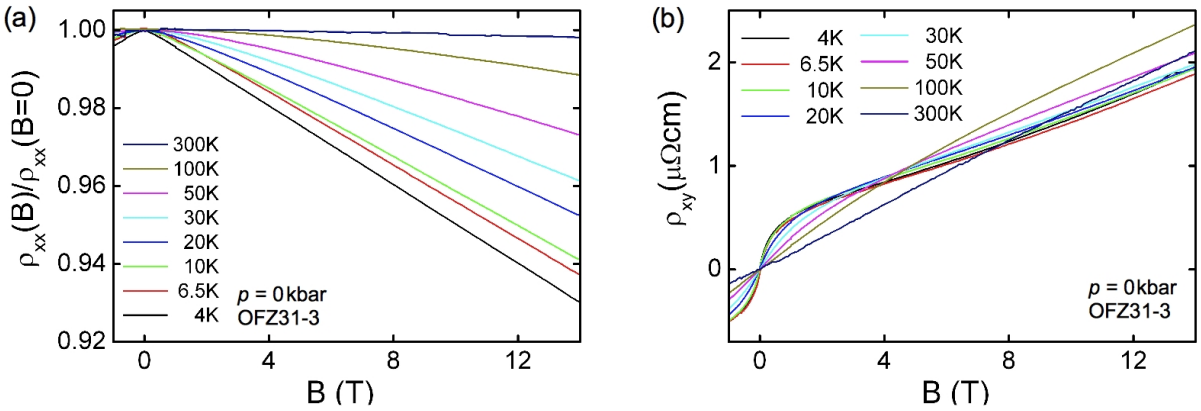

Figure 6.26: (a) Field dependence of the magnetoresistance (MR) of single-crystalline OFZ31-3 at various temperatures. A negative MR is observed for all temperatures. The MR increases with decreasing temperature. At low temperature the MR exhibits a highly unusual linear field dependence. (b) Field dependence of the Hall resistivity for various temperatures. With decreasing temperature deviations from a linear Hall resistivity are observed; an additional contribution at low fields followed by a faint change of curvature at high fields.

Fig. 6.26 (b) shows the Hall resistivity as a function of field for different temperatures for crystal OFZ31-3. With decreasing temperature a deviation from the linear behavior of the normal Hall resistivity is observed. The additional contribution at low fields is reminiscent of the anomalous Hall effect observed for ferromagnetic materials, where the Hall resistivity is typically described as $\rho_{xy} = R_0 B + R_a \mu_0 M$. R_a is known as the anomalous Hall coefficient. Nevertheless, a fit of the low temperature Hall resistivity following this equation with the measured magnetization did not yield satisfying results. The Hall resistivity will be discussed in more detail in section 6.4.2.

6.3.6 Discussion

We may now summarize the properties of the Fe_2TiSn single crystals at ambient pressure and compare them to general properties expected of weak itinerant-electron ferromagnets at quantum criticality. As typical examples of weak itinerant-electron magnets we consider, e.g., Ni_3Al [151], $ZrZn_2$ [152, 153], $NbFe_2$, and MnSi. Similarities are: (i) a large ratio of $\mu_{\text{eff}}/m(9\text{T}, 2\text{K})$, which is ~ 16 for Fe_2TiSn; (ii) a Curie-Weiss behavior of χ^{-1}, that extrapolates to zero for $T_C \approx 0\,\text{K}$; (iii) an unsaturated non-linear magnetization that may be described as quasi-linear in Arrott plots (B/m vs. m^2); (iv) a logarithmic dependence of the specific heat at low temperatures; and (v) an elevated Sommerfeld coefficient. Considering those properties, Fe_2TiSn may be described in the standard context of weak itinerant-electron ferromagnets in the vicinity of a quantum critical point. A remarkable feature of Fe_2TiSn thereby is its vicinity to a putative quantum critical point without need for tuning by an external control parameter. However, carrying out electric transport measurements we found an unusual semiconductor-like increase of the resistivity. This observation contrasts all other intermetallic weak ferromagnets investigated so far. Hence, Fe_2TiSn may display properties of a new class of quantum critical materials.

In addition, we found that phase-pure Fe_2TiSn single crystals exhibit a peculiar sample dependence of the magnetic and transport properties. The square of the effective magnetic moment scales both with the magnetic moment $m(9\mathrm{T}, 2\mathrm{K})$ and with the transition temperature of the low temperature spin-glass state. EDX analysis rules out impurity phases as possible origin. We speculate that a new, more subtle form of interaction is responsible for the variations observed. Possibilities are compositional variations or subtle forms of structural disorder, e.g., anti-site or split-site disorder. The latter is supported by Rietveld refinement of synchrotron X-ray powder diffraction data. However, further experimental studies are necessary to resolve the origin of the sample dependence.

6.4 Physical properties under pressure

Following our initial interest of a pressure induced transition from paramagnetism to ferromagnetism in Fe_2TiSn we carried out magnetization and transport experiments under pressure. The magnetization was measured up to a pressure of 13.9 kbar using a Cu:Be clamp cell. In this pressure range we found, in contrast to our expectations, a reduction of the magnetic moment with pressure. The magnetotransport was measured up to an elevated pressure of 51 kbar using a Bridgman pressure cell. With increasing pressure we found an increase of the longitudinal resistivity accompanied by a highly anomalous behavior of the Hall effect. These properties will be discussed in the framework of topological insulators in the next section.

6.4.1 Magnetization under pressure

The pressure dependent magnetization was measured with a Cu:Be clamp cell in the *VSM* as described in section 3.3. We initially applied the highest pressure of 13.9 kbar and reduced it in subsequent measurements. The magnetization was measured at seven different pressures, following the same routine at each pressure point. For the analysis we subtracted the signal of the empty pressure cell. The ambient pressure data was measured for the same single-crystalline sample (OFZ31-2) without a pressure cell.

Fig. 6.27 (a) shows the field dependence of the magnetization for various pressures at $T = 2.7\,\mathrm{K}$. The lower blue line depicts the signal of the empty pressure cell. The ambient pressure data (black curve) is slightly higher in comparison to the data recorded under pressure. As our main result we found that the magnetization slightly reduces with increasing pressure (from top to bottom). The suppression of the magnetic moment from $p = 2.4\,\mathrm{kbar}$ to $p = 13.9\,\mathrm{kbar}$ at $B = 8\,\mathrm{T}$ is around 5%. Other than the suppression of the absolute value of the magnetic moments, no change of the shape of the magnetization curves was observed under pressure. Hence, we did not find any indication for the expected stabilization of a long range magnetic order with applied pressure.

A similar behavior was observed in the temperature dependent magnetization measurements shown in Fig. 6.27 (b). The data was recorded after zero field cooling with increas-

ing temperature at fields of 0.1 T, 0.5 T, and 1 T. For all fields the magnetization was suppressed with pressure. No additional signals indicating a transition were observed.

Fig. 6.28 (a) shows the pressure dependence of the effective magnetic moment, which we determined from the inverse temperature dependent magnetization divided by magnetic field, $\chi_{\mathrm{DC}}^{-1} \propto (m/H)^{-1}$. For all fields, $B = 0.01\,\mathrm{T}$, 0.1 T, and 0.3 T, we found a decrease of the effective moment with pressure that extrapolates to zero for pressures around 150 kbar. We note that a linear extrapolation of $m(8\mathrm{T}, 2.7\mathrm{K})$ as a function of pressure (not shown) yields $p \sim 220\,\mathrm{kbar}$ for which $m(8\mathrm{T}, 2.7\mathrm{K})$ is suppressed to zero. The decrease of the effective moment with pressure is in pronounced contrast to the pressure independent effective moment reported for $ZrZn_2$ [153]. Fig. 6.28 (b) shows the square of the effective moment μ_{eff}^2 as a function of the magnetic moment measured at $T = 2.7\,\mathrm{K}$ and $B = 8\,\mathrm{T}$ for the different pressures. With increasing pressure the data is shown from top to bottom and from the right to the left. Interestingly, we observe a linear dependence that is similar to the sample dependence of the magnetic properties shown in Fig. 6.17.

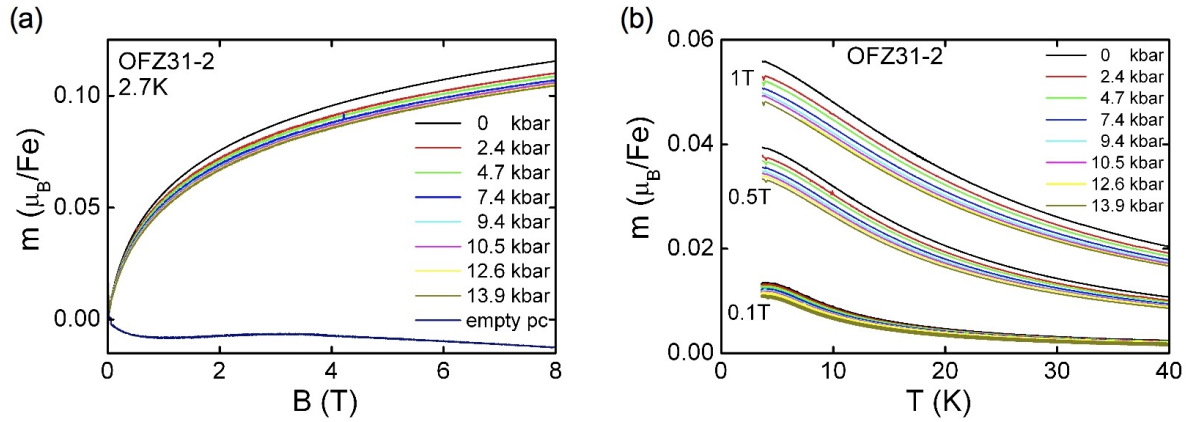

Figure 6.27: (a) Field and (b) temperature dependent magnetization of single crystal OFZ31-2 at various pressures. A slight reduction of the magnetization with increasing pressure (from top to bottom) is observed. No signal indicating the expected ferromagnetic transition is found.

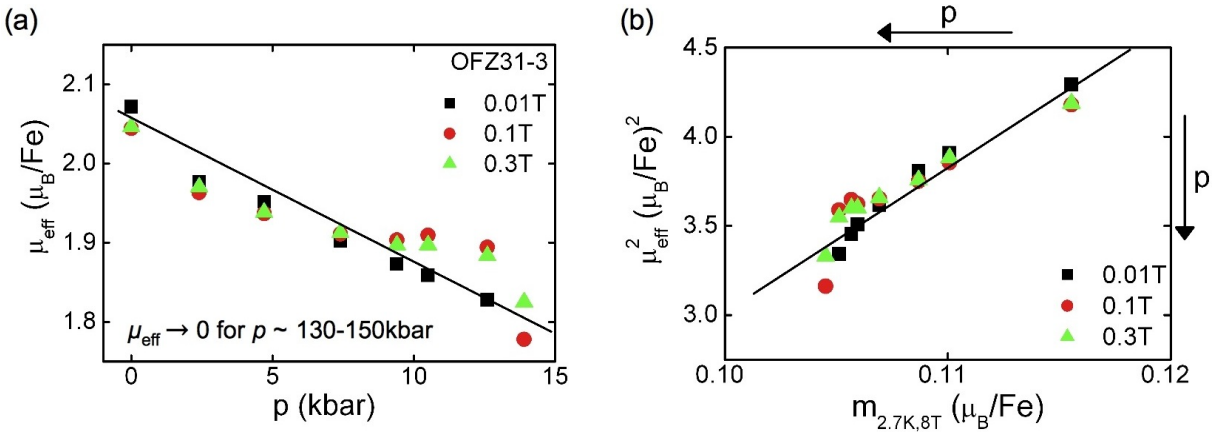

Figure 6.28: (a) The effective moment μ_{eff} as a function of pressure. With increasing pressure μ_{eff} decreases. (b) μ_{eff}^2 as a function of the magnetic moment $m(8\mathrm{T}, 2.7\mathrm{K})$ for $p = 0 - 13.9\,\mathrm{kbar}$.

6.4.2 Magnetotransport under pressure

The pressure dependence of the magnetotransport of a single-crystalline sample prepared from OFZ31-3 was measured with a Bridgman pressure cell in the *Sweet 16* system. The set-up is shown in section 3.8 in detail. The 6-point-configuration allowed a simultaneous measurement of the longitudinal resistance ρ_{xx} and the Hall resistance ρ_{xy}. The pressure was increased subsequently. We started from a pressure $p \sim 12$ kbar and reached $p \sim 51$ kbar as the highest pressure.

Fig. 6.29 (a) shows the zero field longitudinal resistivity measured at different pressures. In addition, the ambient pressure data (0 kbar) of single-crystalline OFZ31-3 measured without the pressure cell is shown (see previous section). The large difference of the 0 kbar and 12 kbar data is most probably due to a systematic error of the position of the sample contacts in the pressure cell[3]. The longitudinal resistivity increases with increasing pressure in the entire temperature range studied. We also find that the semiconductor-like increase to low temperatures becomes more pronounced with increasing pressure, as illustrated in Fig. 6.29 (b). Here data are scaled to the value at 250 K. At ambient pressure an increase of the resistivity of around 15% is observed at the lowest temperatures, while the increase at 51 kbar is more than 40%.

Figs. 6.30 (a - d) show the field dependent magnetoresistance for various temperatures measured at 12 kbar, 28 kbar, 38 kbar, and 51 kbar, respectively. The 32 kbar data is very similar to the 28 kbar data and hence not shown. Similar behavior is observed for all pressures, reminiscent of the measurements at ambient pressure (cf. Fig. 6.26). The negative MR increases with decreasing temperatures and it shows a highly unusual linear dependence at the lowest temperatures. With increasing pressure the absolute size of the MR is slightly reduced and also a small deviation from the linear field dependence emerges.

Other than in the magnetoresistance, the behavior of the Hall resistivity changes distinctly under pressure as shown in Fig. 6.31. At a first glimpse it appears that the overall Hall resistivity is decreasing with increasing pressure and that a pronounced curvature emerges at low temperatures and high fields. At 300 K a linear Hall resistivity (dark blue line) is observed at all pressures. The slope of this linear Hall effect constantly reduces with increasing pressure, indicating a slight increase of the charge carrier concentration under pressure. This observation is inconsistent with the increase of the longitudinal resistivity under pressure.

With decreasing temperatures an additional contribution appears at low fields, that becomes most pronounced at the lowest temperatures. This increase merges, with a change of the curvature, into a distinct sub-linear behavior at high fields. With increasing pressure both features become more pronounced, as shown in Figs. 6.32 (a) and (b) for the 4 K data. The slightly curved high field data at 0 kbar and 12 kbar change drastically to high pressures, where a pronounced curvature with a local minimum at high fields is observed.

[3]When preparing the Bridgman cell the wires are only loosely placed on top of the sample. Under loading the initial position may be shifted slightly, causing changes of the geometry factor. Further pressure changes do not change the geometry factor.

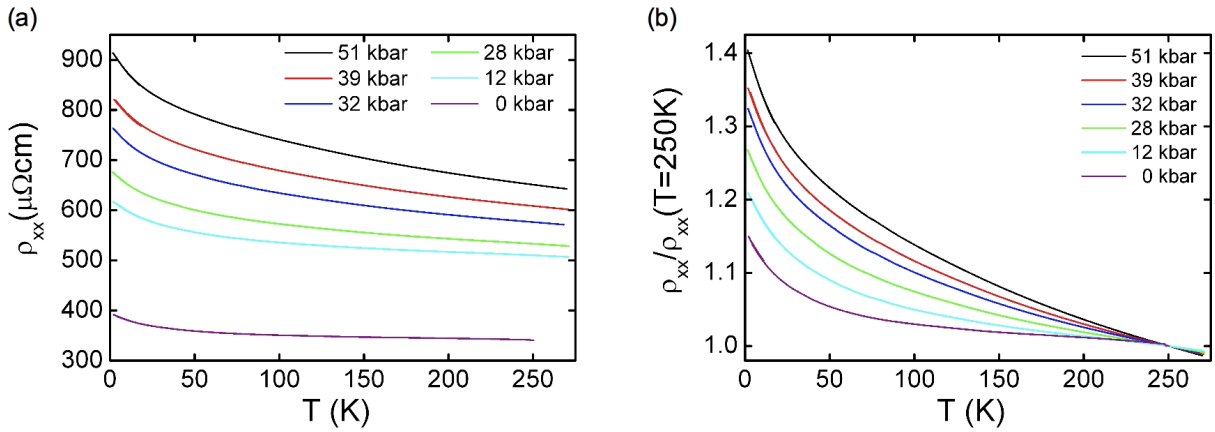

Figure 6.29: (a) Temperature dependence of the longitudinal resistivity at zero field. The resistivity increases in the entire temperature range with increasing pressure. The large gap between the 0 kbar and 12 kbar data is most likely due to a displacement of the sample contacts in the pressure cell. (b) With increasing pressure the semiconductor-like increase of the resistivity with decreasing temperature is amplified. Each resistivity data is scaled to the value at 250 K.

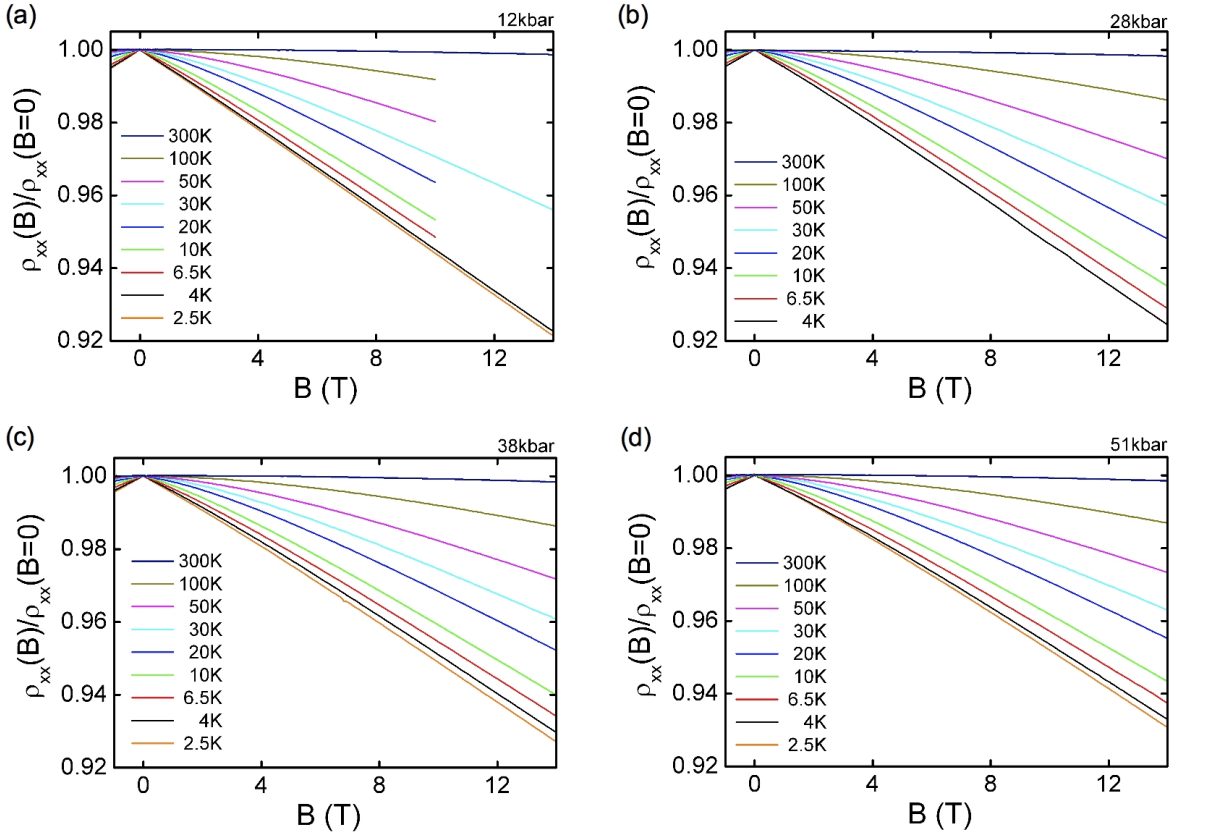

Figure 6.30: Field dependent magnetoresistance measured at various temperatures and at a pressure of (a) 12 kbar, (b) 28 kbar, (c) 38 kbar, and (d) 51 kbar. The MR is very similar for all pressures. With increasing pressure the MR is slightly reduced. In addition, a slight deviation from the linear field dependence is observed at the highest pressures.

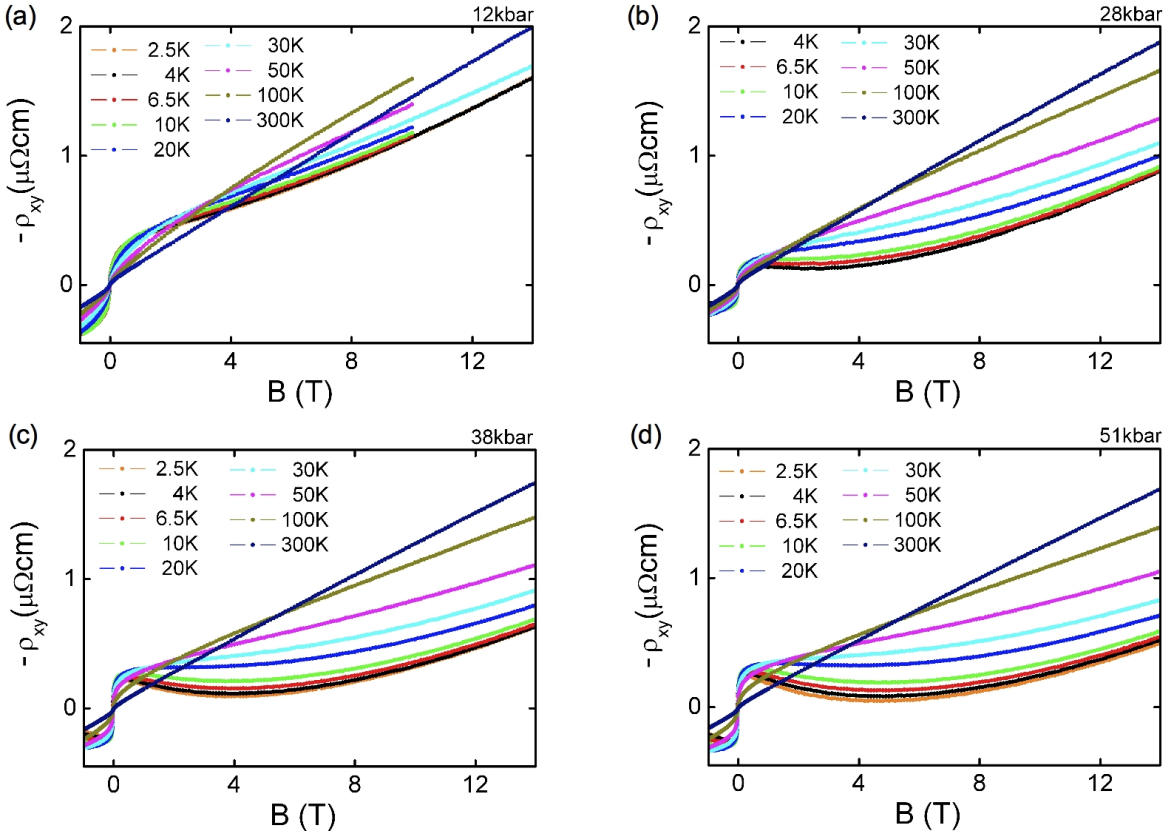

Figure 6.31: Field dependent Hall resistivity for various temperatures at pressures of (a) 12 kbar, (b) 28 kbar, (c) 38 kbar, and (d) 51 kbar. The linear Hall resistivity at 300 K decreases with increasing pressure. At low temperatures a distinctive change of the Hall resistivity is observed with pressure, especially between 12 kbar and 28 kbar. With increasing pressure a pronounced curvature appears at high fields. Details are shown in Fig. 6.32.

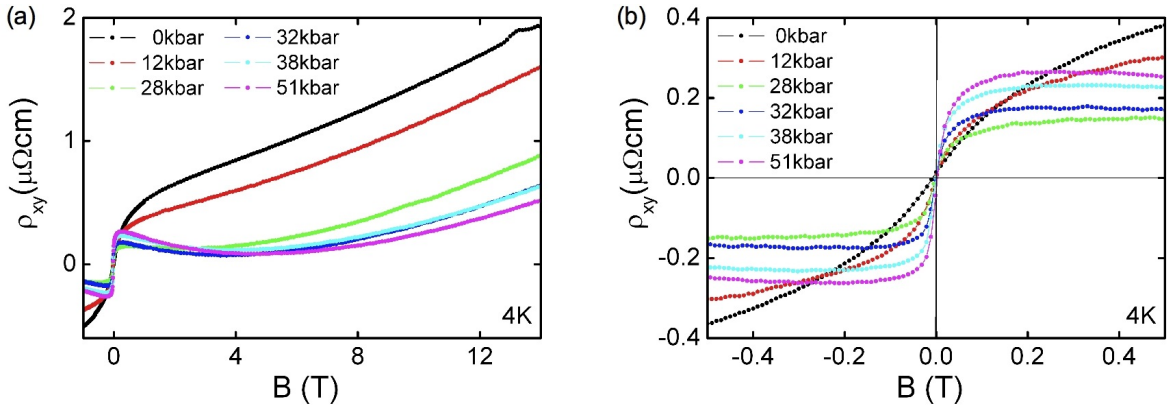

Figure 6.32: Hall resistivity at $T = 4\,\mathrm{K}$ and different pressures. High and low field data are shown in (a) and (b), respectively. (a) With increasing pressure the high field resistivity is suppressed and a pronounced curvature with a local minimum around $4 - 5\,\mathrm{T}$ appears. (b) At low fields the increase of the resistivity becomes more pronounced with increasing pressure. For pressures above 28 kbar a step-like feature is observed. The size of the step increases with increasing pressure from 28 kbar to 51 kbar.

At low fields the increase changes from gradual at 0 kbar and 12 kbar to step-like at higher pressures, as shown in detail in Fig. 6.32 (b). Curiously, the size of the step increases with increasing pressure from 28 kbar to 51 kbar although the overall Hall resistivity decreases. In order to account for the increasing longitudinal resistivity under pressure we plotted the Hall conductivity, $\sigma_{xy} = \rho_{xy}/(\rho_{xx}^2 + \rho_{xy}^2) \approx \rho_{xy}/\rho_{xx}^2$, as shown in Fig. 6.33 for 4 K. The Hall conductivity clearly illustrates the step-like feature observed at low fields and pressures above 28 kbar. Interestingly, the Hall conductivity indicates a pressure threshold above which no change of the low field Hall conductivity is observed. To higher fields, though, different curvatures are found for different pressures.

We note that we corrected the field dependent pressure cell data for a small hysteresis of ~ 20 mT, which is a well known relict of the magnetic piston in the pressure cell. We also rescaled the Hall resistivity data measured in the pressure cell in order to account for the geometrical error mentioned above. We divided the Hall resistivity ρ_{xy} by 2.4. This factor was derived by scaling R_0, i.e., the slope of the normal Hall effect at room temperature, of the 12 kbar data to R_0 at ambient pressure (cf. Fig. 6.26 (b)).

The unusual step-like feature in the Hall resistivity of Fe_2TiSn that emerges under pressure is reminiscent of the anomalous Hall effect observed in ferromagnets. As already mentioned in section 6.3.5, the anomalous Hall effect is phenomenologically described as $\rho_{xy} = R_0 B + R_a \mu_0 M$, where the anomalous part scales with the magnetization. In the case of a ferromagnetic ordered state, this leads to a step-like feature in ρ_{xy} at low fields. However, the suppression of the magnetization under pressure and the absence of any sign for long-range magnetic order (see previous section) contradicts this scenario in Fe_2TiSn. Instead we propose in the next section that the anomalous behavior of the Hall resistivity of Fe_2TiSn under pressure may be described in terms of a topological insulator.

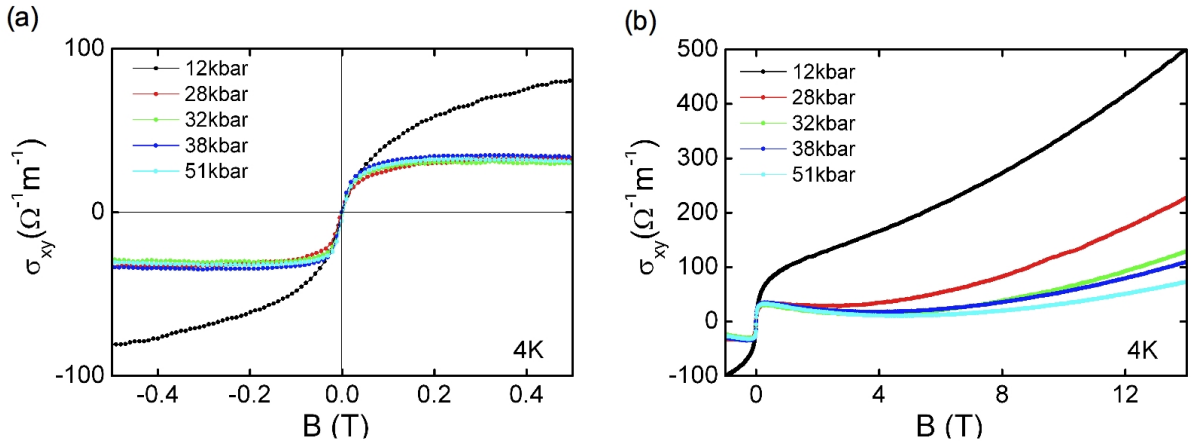

Figure 6.33: Hall conductivity at $T = 4$ K and different pressures at low fields (a) and high fields (b). The anomalous step-like feature at small fields for pressures above 28 kbar is clearly illustrated.

6.5 Is Fe_2TiSn a weak topological insulator?

In this section we speculate that under pressure Fe_2TiSn may be characterized as a topological insulator. In the framework of a topological insulator, the conductance in Fe_2TiSn may be separated into a bulk and a surface conductance with distinctly different mobilities, the latter being substantially higher. This separation of the conductance may account for the Hall anomaly observed in weak field and high pressure in Fe_2TiSn single crystals.

Our speculation is based on qualitative similarities to Hall anomalies observed in the topological insulator Bi_2Te_3 as reported recently [154]. Further support is given by preliminary band structure calculations in the local density approximation (LDA) carried out by Jürgen Kübler [155], in which he identifies a Dirac-like linear dispersion in the band structure around the Γ-point. In addition, he finds that the first Chern number ν_0, which is a classification of the topology of a three dimensional system, changes from 0 to 1 with decreasing lattice constant.

In this section we first give a short introduction to topological insulators. We then present the Hall anomaly observed in the topological insulator Bi_2Te_3 and compare it with the anomaly in Fe_2TiSn. For both compounds the Hall conductance may be separated into a surface and bulk contribution as expected for a topological insulator. In the last part we summarize the preliminary band structure calculations for Fe_2TiSn carried out by Jürgen Kübler [155].

6.5.1 What is a topological insulator?

Since a general description of topological insulators exceeds the scope of this thesis, we restrict ourselves to the most important properties and refer to the literature for a detailed introduction, e.g., [156–159] and references therein.

Other than common ordered states of matter such as the crystalline solids and magnets, topological states of quantum matter are characterized by their topology and not by a spontaneously broken symmetry. The quantum Hall (QH) state, discovered in 1980, provided the first example of such a topological quantum state [160]. Its behavior was found to depend only on its topology and not on its specific geometry, as illustrated in the quantized integer quantum Hall effect.

Recently, a new class of topological states has emerged called quantum spin Hall states or topological insulators (TI). Other than the QH states, for those TIs no large magnetic field is necessary to break time reversal symmetry and realize the same "robust" edge or surface states. In the TIs spin-orbit effects take the role of the external magnetic field. TIs have been theoretically predicted and experimentally observed in HgTe quantum wells [161, 162], in $Bi_{1-x}Sb_x$ alloys [163, 164] and in Bi_2Se_3 and Bi_2Te_3 bulk crystals [165, 166]. Very recently TIs have also been predicted for a large number of Heusler compounds [167, 168]. However, there is so far no experimental evidence for a topological insulator among the Heusler compounds.

Three dimensional topological insulators, such as Bi_2Te_3, are insulating in the bulk - they have an energy gap separating the valence and conduction bands - but on the boundary they have gapless surface states that are topologically protected. This means that the metallic surface of a 3D TI is immune to impurities or geometric perturbations. The gapless surface states appear due to band inversion between two orbitals with opposite parity, driven by strong spin orbit coupling. The dispersion of the surface states is linear and described by a so-called Dirac cone. This expression originates from the description of a linear dispersion of a massless relativistic fermion in quantum field theory by the Dirac equation. The massless Dirac-like surface states, in which the electrons have only one spin degree of freedom on each surface, have been imaged for Bi_2Te_3 by means of angle resolved photo emission spectroscopy [166].

6.5.2 Hall anomaly in the topological insulator Bi_2Te_3

Very recently, Qu *et al.* [154] reported the observation of quantum oscillations and a Hall anomaly in the topological insulator Bi_2Te_3. It is instructive to revisit those results in the following. In their paper Qu *et al.* [154] expressed the Hall conductivity (see Fig. 6.34 (a)) as the sum of two contributions

$$\sigma_{xy} = \sigma_{xy}^{\mathrm{b}} + \frac{G_{xy}}{t}\,, \tag{6.1}$$

where σ_{xy}^{b} is the bulk Hall conductivity and G_{xy} the surface Hall conductance. t denotes the thickness of the crystal. For the bulk term they used the semiclassical expression

$$\sigma_{xy}^{\mathrm{b}} = p_{\mathrm{eff}}\, e\, \mu_{\mathrm{b}}\, \frac{\mu_{\mathrm{b}}\, B}{[1 + (\mu_{\mathrm{b}}\, B)^2]}\,, \tag{6.2}$$

where p_{eff} is an "effective" bulk carrier concentration and μ_{b} is the bulk mobility. The Hall conductance of the surface states may be expressed as

$$G_{xy} = \frac{2\pi e^3}{h^2}\frac{B\, l^2}{[1 + (\mu B)^2]}\,, \tag{6.3}$$

where $l = v \cdot t$ is the charge carrier mean free path and μ the surface mobility.

Using Eq. (6.1) Qu *et al.* separated the surface and the bulk contribution to the Hall conductivity. A fit to the Hall conductivity of Bi_2Te_3 using the above equations is shown in Figs. 6.34 (a) and (b). Panel (b) thereby plots both the surface term G_{xy} and the bulk term σ_{xy}^{b}. The fits illustrate that the anomaly in the Hall conductivity in Bi_2Te_3 may be very well described by a sum of a surface and a bulk conductivity.

We note that the semi-classical treatment of the surface term does not capture quantum oscillations as observed in the high field regions of the Hall conductivity. From the fit parameters Qu *et al.* obtained a surface mobility $\mu = 9000\,\mathrm{cm}^2/\mathrm{Vs}$ that is substantially higher than the bulk mobility $\mu_{\mathrm{b}} = 860\,\mathrm{cm}^2/\mathrm{Vs}$. The high surface mobility was confirmed by quantum oscillation measurements which show the angular dependence of a two-dimensional Fermi surface. Hence the anomaly in the Hall conductance in Bi_2Te_3 provides direct evidence of the surface current of a topological insulator by means of transport measurements.

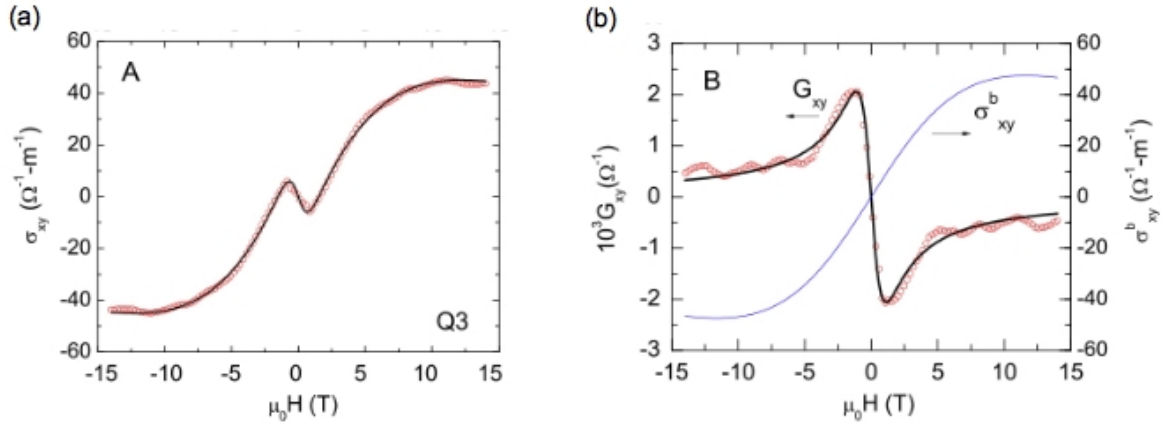

Figure 6.34: (a) The red circles show the Hall conductivity of Bi_2Te_3. The solid curve is a fit to Eq. (6.1). The Hall conductivity displays a pronounced anomaly at low fields. (b) Separation of the bulk and surface contributions to the Hall conductivity. The solid blue line illustrates the bulk term σ^{b}_{xy} as calculated from Eq. (6.2). The open circles show the experimental data after subtraction of σ^{b}_{xy} (blue line) and the black line illustrates the surface term G_{xy} as calculated from Eq. (6.3). The images were taken from Ref. [154].

6.5.3 Hall effect in Fe_2TiSn revisited

Following the approach of Qu *et al.*, we tried to describe the anomalous Hall conductivity observed in Fe_2TiSn by the sum of a bulk and a surface term. However, since the curvature at high fields is distinctly different for Fe_2TiSn in comparison to Bi_2Te_3, a description of the high field behavior of Fe_2TiSn with Eq. (6.2) did not yield satisfying results. We note, though, that Qu *et al.* did not take the field dependence of the longitudinal resistivity into account in their expression of the bulk conductivity.

In order to account for the linear negative magnetoresistance observed in Fe_2TiSn, we empirically introduced this field dependence into the Drude expression for the resistivity: $\rho_{xx} = e^{-1}\, p_{\mathrm{eff}}^{-1}\, \mu_{\mathrm{b}}^{-1}(1-zB)^{-1}$. The empirical parameter z thereby determines the size of the suppression of the resistivity in applied field. From the magnetoresistance in Fe_2TiSn at low temperatures we expect $z \approx 0.005\,\mathrm{T}^{-1}$. p_{eff} is an "effective" bulk carrier concentration and μ_{b} is the bulk mobility, as introduced above. This leads to the following expression for the bulk conductivity:

$$\sigma^{\mathrm{B}}_{\mathrm{xy}} = \frac{\rho_{\mathrm{xy}}}{\rho^2_{\mathrm{xx}} + \rho^2_{\mathrm{xy}}} \approx \frac{\rho_{\mathrm{xy}}}{\rho^2_{\mathrm{xx}}} = p_{\mathrm{eff}}\, e\, \mu_{\mathrm{b}}\, \frac{\mu_{\mathrm{b}}\, B}{(1-zB)^2} \tag{6.4}$$

Using this empirical expression for the bulk conductivity as well as the surface term from Eq. (6.3), we obtained a fit to the Hall conductivity data as shown in Fig. 6.35. Panel (a) and (b) show the experimental Hall conductivity (black circles) and the fit to the data (red line) at $T = 4\,\mathrm{K}$ for $p = 28\,\mathrm{kbar}$ and $p = 51\,\mathrm{kbar}$, respectively. For $p = 28\,\mathrm{kbar}$ the experimental data is very well described by the fit, while slight deviations of the experimental data and the fit are observed for $p = 51\,\mathrm{kbar}$.

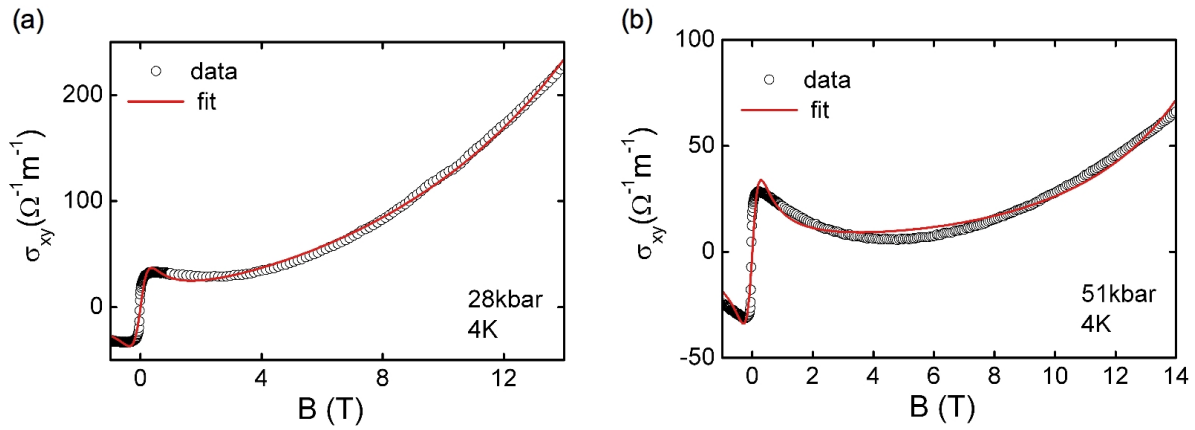

Figure 6.35: Field dependence of the Hall conductivity of Fe_2TiSn at $T = 4\,\mathrm{K}$ and a pressure of 28 kbar (a) and 51 kbar (b). The black circles represent the experimental data and the red lines a fit to the data following Eq. (6.1), yet with the bulk conductivity term as given in Eq. (6.4). For $p = 28\,\mathrm{kbar}$ the experimental data may be very well described by the fit. For $p = 51\,\mathrm{kbar}$ slight deviations of the experimental data and the fit are observed.

From the fits to the data we obtained a charge carrier mean-free-path $l = 600\,\mathrm{nm}$ and $l = 640\,\mathrm{nm}$ for $p = 28\,\mathrm{kbar}$ and $p = 51\,\mathrm{kbar}$, respectively, as well as a surface conductivity $\mu = 30000\,\mathrm{cm}^2/\mathrm{Vs}$ and $\mu = 35000\,\mathrm{cm}^2/\mathrm{Vs}$. These fit parameters are larger than those obtained by Qu *et al.* for Bi_2Te_3 ($l = 235\,\mathrm{nm}$, $\mu = 9000\,\mathrm{cm}^2/\mathrm{Vs}$). In contrast, for the bulk conductivity we obtained a very low bulk carrier mobility $\mu = 1.2\,\mathrm{cm}^2/\mathrm{Vs}$ and $\mu = 0.8\,\mathrm{cm}^2/\mathrm{Vs}$ as well as an effective charge carrier concentration $p_{\mathrm{eff}} = 2.6 \times 10^{21}\,\mathrm{cm}^{-3}$ and $p_{\mathrm{eff}} = 0.9 \times 10^{21}\,\mathrm{cm}^{-3}$ for $p = 28\,\mathrm{kbar}$ and $p = 51\,\mathrm{kbar}$, respectively. We note that p_{eff} is in the same range as the charge carrier concentration obtained from the linear Hall effect at 300 K. For the empirical parameter we obtain $z = 0.028$ and $z = 0.043$ for $p = 28\,\mathrm{kbar}$ and $p = 51\,\mathrm{kbar}$, respectively.

We conclude from these preliminary fits to the data that the Hall conductivity in Fe_2TiSn may be described by the sum of a surface and a bulk contribution. We find that the expression for the surface states (cf. Eq. (6.3) accounts very well for the low field anomaly and, similar to Bi_2Te_3, yields a high surface mobility μ. Further we find that the empirical expression for the bulk conductivity given in Eq. (6.4) describes the high field data very well and yields very low values for the bulk conductivity, as expected for a topological insulator. However, the fit results for the parameter z, that was empirically introduced to account for the field dependence of the longitudinal resistivity, are far larger than $z \approx 0.005$ obtained from experiment.

We suspect that also the magnetization of Fe_2TiSn has to be considered for a better description of the bulk contribution to the high field Hall conductivity. The magnetization will give rise to an anomalous Hall contribution that has not been taken into account yet.

6.5.4 Preliminary LDA results

In the following we summarize the results of preliminary band structure calculations of Fe_2TiSn in the local density approximation (LDA) that were recently carried out by Prof. Jürgen Kübler [155].

The LDA calculations taking into account spin-orbit coupling (SOC) revealed a Dirac-like linear dispersion. The Dirac-point, i.e., the point where the linear bands cross, is centered at the Γ symmetry point and situated above the Fermi energy. In addition, the calculations show a small hole Fermi surface centered at the Γ-point. With increasing SOC this Fermi surface pocket is suppressed and a band gab opens. However, the Dirac-like point remains because of time-reversal symmetry. These calculations revealed that the band structure of Fe_2TiSn shows properties akin those observed in topological insulators.

A characterization whether the Dirac-like linear dispersion leads to topological stable surface states, may be given in terms of the Chern numbers [163]. In general, four Chern numbers are necessary to classify the topology of a 3D-system. Nevertheless, as pointed out by Kübler [155], the first Chern number ν_0 with $\nu_0 = 1$ allows to distinguish the topologically *interesting* cases.

In order to comment on the pressure dependent properties we observed in Fe_2TiSn, Kübler further carried out calculations of the total energy as a function of the atomic volume. In addition, he calculated the first Chern number for different atomic volumes. At first sight these calculations appeared to deviate from experiments. The experimental volume was not seen to occur in the total energy minimum, i.e., the experimentally observed lattice constant $a \approx 0.6063\,\text{nm}$ is larger than the calculated value $a = 0.5984\,\text{nm}$. However, this may be explained by a well-known discrepancy of LDA, commonly referred to as the "LDA overbinding". More important, though, was the observation that the first Chern number changes from $\nu_0 = 0$ at large volumes to $\nu_0 = 1$ at small volumes. This result illustrates that with decreasing lattice constant the topological properties of Fe_2TiSn become characteristic of a topological insulator. A further discrepancy with experiment is the observation of the change of the Chern number from 0 to 1 prior to the experimental lattice constant. Again, this might be due to the overbinding problem.

To summarize, the preliminary LDA calculations indicate that Fe_2TiSn shows a trend to exhibit topologically interesting properties. A Dirac-like linear dispersion is observed in the electronic band structure, as well as a change of the first Chern number as a function of lattice parameter. However, quantitatively the change of the Chern number is calculated to occur at a lattice parameter larger than that observed experimentally.

6.6 Summary and Outlook

We succeeded to grow for the first time large single crystals of Fe_2TiSn. We found that phase-pure float-zoned single crystals do not show a ferromagnetic transition at 250 K, as reported previously [34]. In fact, we were able to attribute the ferromagnetic transition around 250 K to the presence of an $Fe_{67}Ti_{25}Sn_8$ impurity phase that primarily forms at grain boundaries.

We found that phase-pure Fe_2TiSn single crystals display quantum critical behavior at the border to magnetism. A linear Curie-Weiss behavior over the entire temperature range that extrapolates through zero for $T_C \approx 0$ K is observed in the inverse AC - susceptibility. The magnetization shows an unsaturated non-linear behavior and the Sommerfeld contribution to the specific heat displays a logarithmic divergence at low temperatures. These properties, as well as a large difference of the effective magnetic moment μ_{eff} and the ordered moment $m(9\text{T}, 2\text{K})$, suggest an analogy of Fe_2TiSn with weak itinerant-electron ferromagnets in the vicinity of a ferromagnetic quantum critical point. The resistivity of Fe_2TiSn, however, contrasts this observation and shows a semiconductor-like increase to low temperatures. A remarkable feature of Fe_2TiSn is its vicinity to a putative quantum critical point without need for tuning by an external control parameter.

In addition to the properties suggesting quantum criticality, we observed an unusual sample dependence of the magnetic and transport properties in Fe_2TiSn. The magnetic moments at large fields and low temperatures, $m(9\text{T}, 2\text{K})$, were found to vary by up to a factor of two. As the origin of this sample dependence we ruled out impurity phases. Instead, this might be consistent with split-site disorder of the Fe and Ti atoms as inferred from the refinement of synchrotron X-ray powder diffraction data.

Finally, we observed a reduction of the magnetic moments with applied pressure, contradicting our initial expectations of pressure induced ferromagnetic order in Fe_2TiSn. In the resistivity we observed an anomaly in the Hall effect under pressure, which suggests that Fe_2TiSn is a weak topological insulator.

The possibility of a topologically insulating state of Fe_2TiSn would be of great general interest and might open new insights to the entire field of topological insulators. For instance, since Heusler compounds are known to be functional materials, this finding might even trigger possible applications in the field of quantum computing. Hence further measurements under pressure are planned for the future. Besides measurements of the electric transport and the magnetization, an investigation of the topological magnetoelectric effect [169] is just one of the many phenomena that may be pursued.

Chapter 7

Results & Discussion: $NbFe_2$

The C14 Laves phase $Nb_{1-y}Fe_{2+y}$ can be driven through a ferromagnetic (FM) quantum phase transition by a slight modification of the composition y. Near the quantum critical point (QCP) deviations from conventional Fermi liquid behavior have been observed in the resistivity and heat capacity: a logarithmic dependence of the low temperature specific heat, $C/T \propto \ln T$, that is consistent with predictions for a FM QCP, and a $\rho \propto T^{3/2}$ power law dependence of the resistivity [61]. Stoichiometric $NbFe_2$ has been reported as a rare example of low-temperature spin density wave (SDW) order in a d-metal system, although direct evidence from neutron scattering is so far missing [170]. The appearance of the SDW state in the vicinity of a FM QCP nominates $NbFe_2$ as a candidate for the Belitz-Kirkpatrick phase, a theoretical model suggesting that the ferromagnetic order transforms into a long wavelength helical spiral driven by a QCP [171]. This scenario has not been realized experimentally so far. It is shown schematically in Fig. 7.1.

Since most of the above mentioned features of $Nb_{1-y}Fe_{2+y}$ were observed in polycrystals, the aim pursued in this thesis was to grow high quality single crystals of $Nb_{1-y}Fe_{2+y}$ of various compositions in the vicinity of stoichiometric $NbFe_2$ in order to address the following questions: (i) Is the composition dependent magnetic phase diagram of single crystals similar to that of polycrystals? (ii) Do single crystals show similar deviations from conventional Fermi liquid behavior at low temperatures? (iii) Where are the 1^{st} and 2^{nd} order phase transitions in the magnetic phase diagram (cf. Fig. 7.1 (b)) for single crystals? (iv) What is the nature of the SDW state?

The investigation of $NbFe_2$ was carried out in collaboration with William Duncan from Royal Holloway, University of London, the group of Manuel Brando at the Max-Planck-Institute in Dresden, and the group of Malte Grosche at the University of Cambridge. Our main contribution concerned the growth of single crystals, the characterization of the crystalline properties, and the investigation of the distribution of the ferromagnetic properties in the crystals by means of neutron depolarization radiography. In addition, we carried out magnetization and AC - susceptibility measurements on crystal OFZ29-2, as well as preliminary angle dependent torque magnetization measurements as a sensitive probe for the magnetic anisotropy. A comprehensive study of the bulk properties of $Nb_{1-y}Fe_{2+y}$ was carried out by William Duncan as part of his PhD thesis [172].

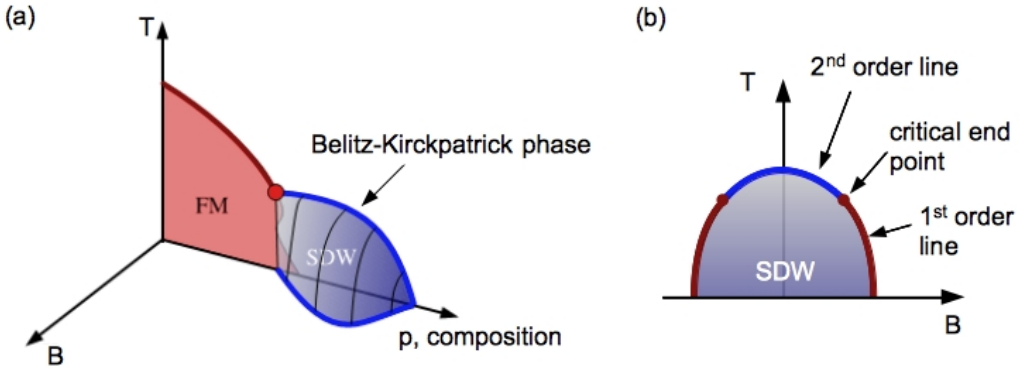

Figure 7.1: (a) Schematic temperature versus field and pressure phase diagram illustrating the transformation of the ferromagnetic phase into a long wavelength spiral, the Belitz-Kirkpatrick phase, as the quantum critical point is approached. Image taken from Ref. [172]. (b) Field versus temperature phase diagram of the Belitz-Kirkpatrick phase. At elevated temperatures the transition to the SDW state changes from first to second order. Images taken from Ref. [172]

7.1 Crystal growth

In the course of this thesis we grew six crystals of $Nb_{1-y}Fe_{2+y}$ of various compositions. The nominal compositions of our float-zoned crystals are indicated in the composition dependent magnetic phase diagram shown in Fig. 7.2. First we grew two crystals, OFZ11 and OFZ12, with nominally stoichiometric composition followed by four crystals, OFZ27 to OFZ30, with $y = 0.01$, 0.006, -0.007, and 0.018.

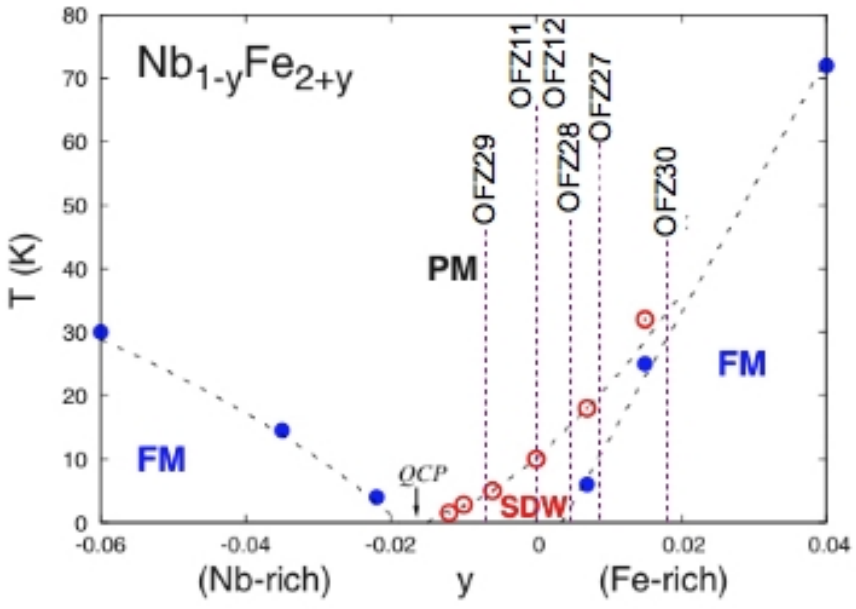

Figure 7.2: Composition dependent magnetic phase diagram of $Nb_{1-y}Fe_{2+y}$ as discussed in the introduction (cf. section 1.2.2), taken from Ref. [60]. The nominal starting compositions of our float-zoned crystals OFZ11, OFZ12, OFZ27, OFZ28, OFZ29, and OFZ30 are shown.

7.1.1 Preparation of starting rods

Starting rods for the crystal growth in the optical floating-zone furnace (OFZ) were prepared by William Duncan at Royal Holloway in a horizontal cold crucible furnace with radio-frequency (RF) induction heating. The system is similar to the horizontal cold finger described in section 2.1.3. The starting rods for OFZ11 and OFZ12 were synthesized from annealed 99.95% Nb and 99.99% Fe, which was melted under vacuum. The rods for OFZ27 through OFZ30 were synthesized from 99.99% Nb powder and 99.995% Fe powder. The powders were first degassed in ultra high vacuum (UHV) before they were melted into Nb and Fe rods. The Nb rods were further purified by annealing in a UHV RF furnace. From the raw materials poly-crystalline pellets of $\sim 5\,\mathrm{g}$ were prepared, that were turned over and re-melted several times. The seed rods consisted of one of those ingots while the feed rods were composed of typically four of these pellets. In order to avoid the formation of cracks the feed rods were cooled slowly once they had been molten. The shape of the resulting rods deviated from the ideal homogeneous form as shown in Fig. 7.3. In addition, we also attempted to cast $NbFe_2$ rods with our rod casting furnace. However, due to the brittleness of the material the as-cast rods always broke into several small pieces in the copper mold and could not be used further.

7.1.2 Optical float-zoning of $Nb_{1-y}Fe_{2+y}$

Prior to each growth the OFZ was baked out for typically two days and flushed several times with purified Argon gas. The growth was carried out in an overpressure Argon atmosphere of $\sim 2\,\mathrm{bar}$. Due to the high melting temperature of $NbFe_2$ of $1670^\circ\,\mathrm{C}$ the $1000\,\mathrm{W}$ lamps at a power of around 75% had to be used. The crystals were grown at constant rates of $5 - 10\,\mathrm{mm/h}$ with a counter-rotation of around $25\,\mathrm{rpm}$ and $10\,\mathrm{rpm}$ of the seed and feed rod, respectively. No signs of evaporation were found on the quartz tube. An overview of the growth parameters is given in Table 7.1 and the six crystals that were grown are shown in Fig. 7.4.

In order to account for the irregular shape of the feed rods and to maintain a stable size of the molten zone both the lamp power and the speed of translation of the feed rod had to be adjusted continuously during the growth process for all crystals. The maximal

Figure 7.3: $NbFe_2$ starting rods for crystal OFZ12 prepared by William Duncan in a horizontal furnace with RF induction heating.

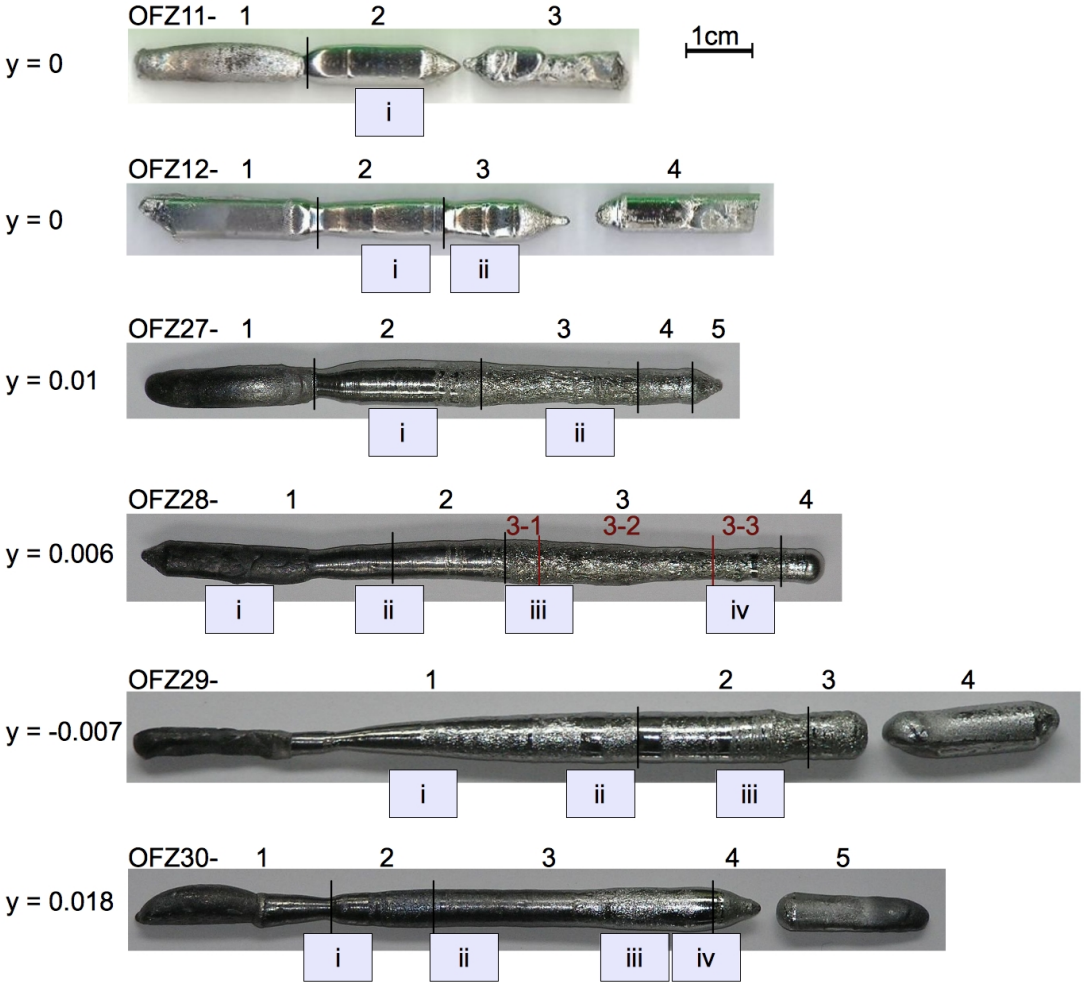

Figure 7.4: The six $Nb_{1-y}Fe_{2+y}$ crystals grown with the image furnace. Growth direction was from the left to the right. The crystals are labeled in the usual way. The blue squares mark the areas that were investigated by neutron diffraction at RESI at FRM II.

	OFZ11	OFZ12	OFZ27	OFZ28	OFZ29	OFZ30
Feed rod comp.	$y = 0$	$y = 0$	$y = 0.01$	$y = 0.006$	$y = -0.007$	$y = 0.018$
Growth rate	5 mm/h	8 mm/h	5 mm/h	6-8 mm/h	6 mm/h	10 mm/h
Rotation (seed/feed)	25/10	30/10	30/12	25/11	30/12	25/12
Lamp power	74.2 – 76.1 %	75.6 – 78.6 %	76.5 – 78.2 %	73.4 – 81.8 %	77.1 – 83.3 %	73.7 – 79.0 %
Argon pressure	1.5 bar	2.0 bar	2.0 bar	2.2 bar	2.2 bar	2.2 bar

Table 7.1: Growth parameters for the $Nb_{1-y}Fe_{2+y}$ crystals grown in the image furnace.

variation of the lamp power for each crystal is given in Table 7.1. In order to support the grain selection we introduced a moderate necking at the beginning of each growth.

For all crystals there was a minor disruption during the growth processes. For crystals OFZ11 and OFZ12 the turning rod of the feed rod stopped turning several times due to a loose bolt. The later growths (OFZ27 - OFZ30) were disturbed by a grinding of the turning rods against the baffles as they had become warped over time. This grinding led to minor shaking of the crystals and the molten zone during the growth process. Nevertheless, stable growth conditions with a stable molten zone could be maintained during the entire growth.

For crystals OFZ11 and OFZ12 no impurities were found on the molten zone, with a very clean surface of the crystals as shown in Fig. 7.4. Curiously, an extra phase appeared floating on the molten zone for the later crystals (OFZ27 - OFZ30). This extra phase shows up as small crystallites on the surface. Fig. 7.5 shows a SEM image of the surface phase. EDX analysis identified this phase to contain a large amount of Nb (56%) and oxygen (40%) and only small traces of Fe (4%). The amount of this extra phase generally increased along the crystals with occasional clear patches. Optical investigations of cuts perpendicular through the crystals confirmed that the extra phase is only found on the surface and does not penetrate into the crystal. The origin of the appearance of this impurity phase is unclear, since all crystals were grown in a similar way.

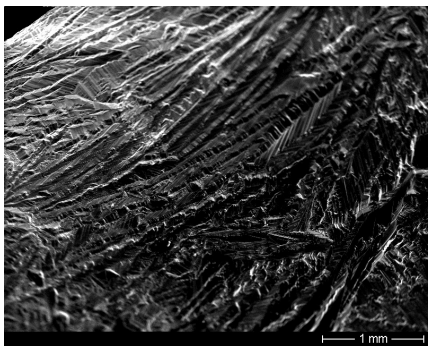

Figure 7.5: SEM image of the impurity phase on the surface of crystal OFZ27. EDX analysis identified this phase to contain a large amount of Nb (56%) and O (40%) and only a small amount of Fe (4%).

7.1.3 Morphology and crystal structure

The single-crystallinity of the float-zoned crystals was first investigated by X-ray Laue diffraction. The appearance of sharp diffraction patterns over extended areas indicated the existence of large single crystal grains in each $Nb_{1-y}Fe_{2+y}$ crystal.

A detailed investigation of the single-crystallinity and the crystal structure of the float-zoned crystals was then carried out by neutron diffraction at RESI at FRM II (cf. section 2.2.3). The blue squares in Fig. 7.4 illustrate the areas investigated. The results may be summarized as:

- OFZ11: Section (i) contains one large single crystal grain and, in addition, several small grains.
- OFZ12: Section (i) contains several single crystal grains, while in section (ii) only two large single crystal grains with different orientations are present.
- OFZ27: Section (i) contains several single crystal grains with one being dominant. Section (ii) contains one single crystal grain, that has the same orientation as the dominant grain in (i), along with an unidentified weak signal that might be the impurity phase or a small second grain.
- OFZ28: Section (i) is a polycrystal. Section (ii) contains three single crystal grains that reduce to two single crystal grains in section (iii) with one already being dominant. It finally turns into a single crystal throughout the rod in section (iv).
- OFZ29: Section (i) contains one main single crystal grain and, in addition, several small grains. The same main grain is present and growing in size in sections (ii) and (iii), with a reduced amount of small additional grains.
- OFZ30: Section (i) contains numerous small grains that reduce in number in section (ii). Sections (iii) and (iv) contain two equally sized single crystal grains.

All crystals grown hence show similar structural properties. Despite the disruptions and changes of the parameters during crystal growth, a continuous grain selection process was observed in all crystals, resulting in the formation of large single crystal grains at the end of each rod. We were hence able to prepare large oriented single crystal samples from the float-zoned crystals for further measurements. As an example, the Laue diffraction patterns along the main c - and a - axes of an oriented sample (OFZ29-3) of hexagonal $Nb_{1-y}Fe_{2+y}$ are shown in Fig. 7.6.

The single crystal diffraction patterns recorded at RESI provide rough information about the crystal mosaicity and the lattice parameters for each crystal. Except for OFZ27 and OFZ30 all crystals show a small mosaic spread of less than 0.5°, indicating an excellent

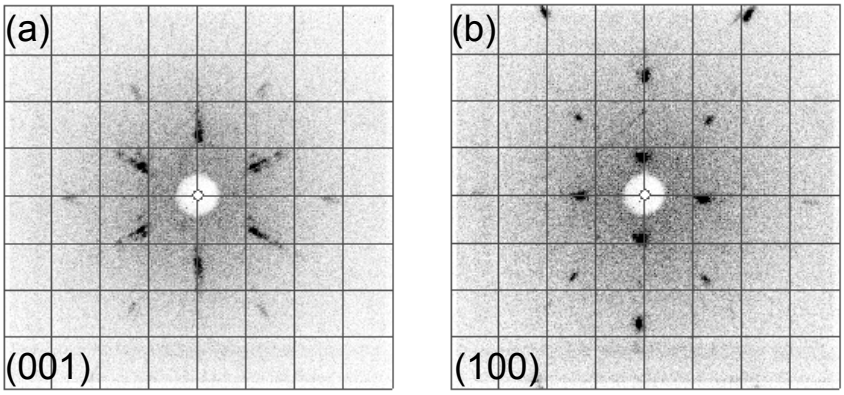

Figure 7.6: X-ray Laue diffraction pattern of the c - (a) and a - axes (b) of an oriented single crystal sample prepared from OFZ29-3.

	OFZ11	OFZ12	OFZ27	OFZ28	OFZ29	OFZ30
Feed rod comp.	$y = 0$	$y = 0$	$y = 0.01$	$y = 0.006$	$y =$ -0.007	$y = 0.018$
Mosaic	$\leq 0.4°$	$\sim 0.5°$	$\sim 1°$	$\leq 0.4°$	$\leq 0.4°$	$\sim 1°$
Lattice parameters	$a = 4.85$Å $c = 7.89$Å	$a = 4.86$Å $c = 7.88$Å	$a = 4.82$Å $c = 7.87$Å	$a = 4.81$Å $c = 8.03$Å	$a = 4.79$Å $c = 7.94$Å	$a = 4.87$Å $c = 7.81$Å
T^*_{nom}	10 K	10 K	17 K	20 K	5 K	35 K
T_{NDR}	-	-	$15 - 24$ K	$20 - 30$ K	-	$30 - 40$ K

Table 7.2: Summary of crystalline and magnetic properties of the float-zoned $Nb_{1-y}Fe_{2+y}$ crystals. T^*_{nom} denotes the transition temperature as expected from the nominal composition. T_{NDR} denotes the transition temperatures measured with NDR.

crystal quality. The increased mosaic spread in OFZ30 might be due to the increased growth rate. A summary of the mosaic and the lattice parameters of each crystal is given in Table 7.2. Note that the reported values are only a rough estimation due to the low number of diffraction patterns recorded during the measurements. For a more accurate determination additional measurements are necessary.

7.2 Neutron depolarization radiography

In addition to the structural characterization of our float-zoned single crystals we carried out neutron depolarization radiography (NDR) measurements (cf. section 3.9) at ANTARES at FRM II in order to investigate the distribution of the (ferro)magnetic properties. Since the magnetic properties of $Nb_{1-y}Fe_{2+y}$ are extremely sensitive to composition, NDR measurements provide important information about the compositional distribution during the crystal growth process. In addition, NDR is an ideal tool to identify large areas with homogeneous magnetic properties from which samples may be prepared for further studies.

(i) OFZ11, OFZ12 & OFZ29

NDR measurements of single-crystalline samples prepared from OFZ11-2 and OFZ12-3 did not yield any depolarization down to temperatures of 400 mK[1]. A similar result was obtained for OFZ29-2, where no depolarization was found down to 4 K, the lowest temperature studied.

AC - susceptibility measurements indicated a transition to the SDW state for all three crystals around 10 K. The exact transition temperatures are given in Table 7.3. The absence of neutron depolarization in the SDW state is not surprising, since antiferromagnetic materials and materials with a modulated spin structure, e.g., MnSi, do in general not depolarize the neutron beam.

[1]NDR measurements to 400 mK were carried out by Phillip Schmakat as part of his diploma thesis.

Curiously, also no depolarization showed up for sample OFZ11-2 at low temperatures, although AC - susceptibility identified a second transition at 4.3 K (see Fig. 7.10, which is believed to be a transition to the ferromagnetic state. An explanation for the absence of depolarization for temperatures below this transition might be the small ordered magnetic moment in the ferromagnetic state. As shown in Eq. (3.9), the ordered moments have to be sufficiently large in order for the sample to depolarize the neutron beam.

(ii) OFZ27

The results of the NDR measurements of OFZ27-2 and OFZ27-3 for different temperatures are shown in Fig. 7.7. The images show the measured polarization in gray scales. Dark areas resemble parts of the crystals where the neutron beam is depolarized, hence the ferromagnetic regions. For the bright areas no depolarization occurs. In the following we focus on the temperature dependent onset of depolarization which we attribute to the onset of ferromagnetic ordering.

Three regions with different magnetic transition temperatures may be distinguished in OFZ27. The lower part of OFZ27-2, at the beginning of the crystal growth, shows no depolarization down to 4 K. For the upper part of OFZ27-2 the onset of depolarization occurs between 15 K and 18 K. Recent measurements of OFZ27-2 with a better temperature resolution reveal a homogeneous transition in the range $T = 16.5 - 17.5$ K. For most of OFZ27-3 the onset of depolarization occurs between 21 K and 24 K, with two stripe-like depolarizing features remaining above 24 K. At 26 K no depolarization occurs along the entire rod.

Interestingly, the increase of the transition temperature seems to coincide with the appearance of the secondary phase on the outside of the rod. Since no depolarization was measured for crystal OFZ29, which also contains the impurity phase, we do not believe that it is the impurity phase itself that depolarizes the neutron beam. We rather attribute the increase of the transition temperatures to a slight increase of the Fe content in the single crystal which is driven by the segregation of the Nb-rich impurity phase.

Referring to the phase diagram obtained from polycrystals (cf. Fig. 7.2), we expected a transition to the SDW state at $T^* \sim 17$ K and a second transition to the ferromagnetic state at $T_C \sim 4$ K for a nominal composition $Nb_{0.99}Fe_{2.01}$. If we assign the transition temperatures $T_{NDR} = 16 - 24$ K to the ferromagnetic transition and refer to the same phase diagram, this would imply an increase of the Fe content of $\delta y = 0.008 - 0.01$ for the ferromagnetic part of float-zoned crystal OFZ27.

As may be seen in Fig. 7.7, crystal OFZ27 broke into two pieces during handling - into OFZ27-2 and OFZ27-3. The line of breakage thereby coincides with the observation of different magnetic properties for both rods. During recent measurements OFZ27-2 broke again. Interestingly, the line of breakage again coincides with the transition of the magnetic properties. These findings suggest, that sudden changes in the composition lead to strain in the crystal structure.

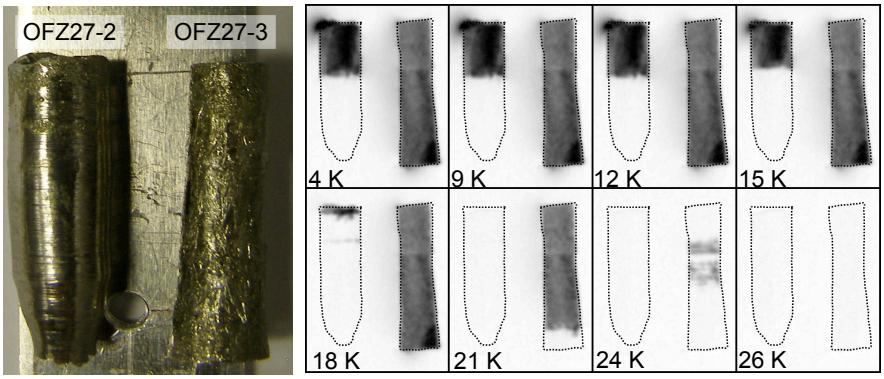

Figure 7.7: Neutron depolarization radiography images of crystals OFZ27-2 and OFZ27-3 for different temperatures. NDR reveals three regions with different magnetic transition temperatures. A photograph of the crystals is shown on the left.

(iii) OFZ28

The results of NDR measurements of OFZ28, that broke during handling into two parts denoted OFZ28-1 and OFZ28-2/3, are shown in Fig. 7.8. For the measurement the crystals were mounted as shown in the photograph on the left. The growth direction is from bottom to top, starting with OFZ28-1.

As for crystal OFZ27, no depolarization is observed at the beginning of the growth of OFZ28-1. For the rest of the crystals, the onset of depolarization and hence the ferromagnetic transition temperature varies between 20 K and 30 K. For the central section of OFZ28-2/3 depolarization of the neutrons even persists at 30 K, the highest temperature studied. A clear coincidence of the transition temperature with the onset of the impurity phase is not found for crystal OFZ28.

From the magnetic phase diagram we expected $T^* \sim 20\,\mathrm{K}$ and $T_\mathrm{C} \sim 5\,\mathrm{K}$ for the nominal composition $Nb_{0.994}Fe_{2.006}$. The transition temperatures $T_\mathrm{NDR} = 20 - 30\,\mathrm{K}$ measured by NDR hence would imply an increase of the Fe content of $\delta y = 0.005 - 0.007$ for the float-zoned crystal OFZ28.

(iv) OFZ30

The results of NDR measurements of OFZ30 are shown in Fig. 7.9. Note the large temperature interval between the first two images. Again a small area at the beginning of the growth exists where no depolarization is found down to the lowest temperatures studied. For most of the crystal the onset of depolarization is found between 30 K and 40 K with an inhomogeneous distribution along the crystal. Only the seed and the top end of the crystal depolarize the neutron beam at 40 K. The appearance of stripes implies variations of the composition that may be caused by changes of the growth parameters. The expected ferromagnetic transition temperature $T_\mathrm{C} \sim 35\,\mathrm{K}$ for the nominal composition $Nb_{0.982}Fe_{2.018}$ agrees quite well with the observed transition temperatures $T_\mathrm{NDR} = 30 - 40\,\mathrm{K}$.

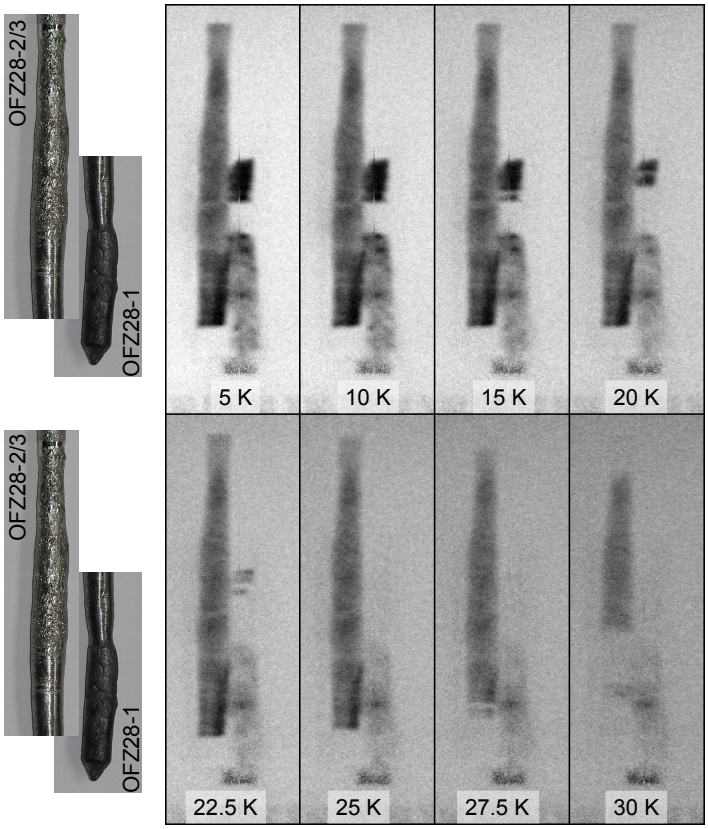

Figure 7.8: NDR images of crystal OFZ28 for various temperatures. Crystal OFZ28 broke during the preparation of the NDR measurements into two parts denoted OFZ28-1 and OFZ28-2/3. For the NDR measurements the crystals were mounted as shown on the left, with the growth direction from bottom to top. The onset of depolarization varies over a large temperature interval.

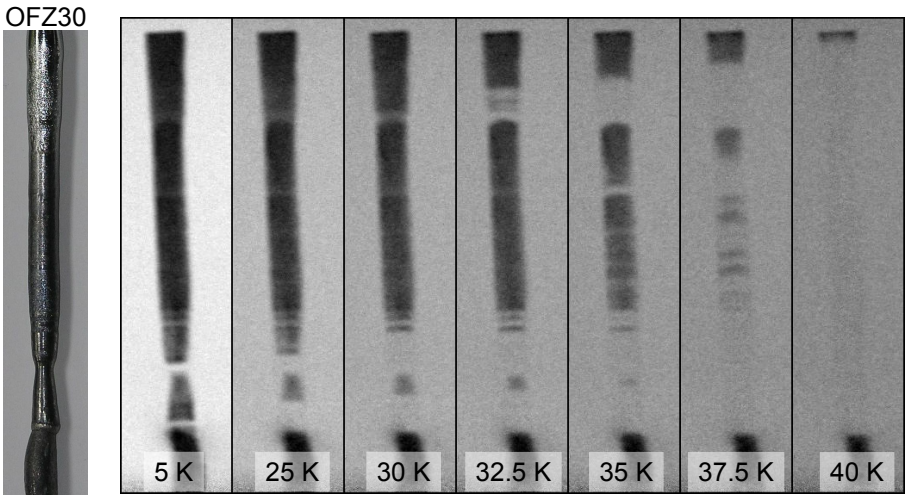

Figure 7.9: NDR images of crystal OFZ30 for different temperatures. Note the large temperature difference between the first two panels. For most of the crystal the depolarization vanishes between 30 K and 40 K.

7.3 Physical properties

In the following section experimental studies of the physical properties of oriented single crystal samples will be presented. The magnetization, AC - susceptibility and torque magnetization of OFZ29-2, as well as the AC - susceptibility of OFZ27-2 were measured at TUM as part of this thesis. The magnetization, AC - susceptibility, specific heat and resistivity of samples OFZ11-2, OFZ12-3, and OFZ28-4 were measured by William Duncan at Royal Holloway. In addition, William Duncan carried out small angle neutron scattering experiments on OFZ11-2 at MIRA at FRM II. Magnetization measurements on crystals OFZ28-4 and OFZ29-3 were carried out by the group of Manuel Brando at the MPI for chemical physics of solids in Dresden.

7.3.1 AC - susceptibility

Magnetic phase diagram

Measurements of the real part of the AC - susceptibility typically show a double-peak structure as a function of temperature as shown in Figs. 7.10 (a) and (b) for crystals OFZ11-2 and OFZ28-4, respectively. At high temperatures the transition from the paramagnetic state to the SDW state is denoted by T^*. The transition at lower temperatures from the SDW state to the ferromagnetic state is denoted by T_C. As known from measurements on polycrystals both transitions (starting from the Fe-rich side) shift to higher temperatures with increasing Fe content. The transition temperatures of our float-zoned single crystals as compared with the magnetic phase diagram in Fig. 7.11 of polycrystals suggest the following true compositions. Crystals OFZ11-2, OFZ12-3 and OFZ29-2 are situated around the stoichiometric composition, while OFZ27-2 and OFZ28-4 are on the Fe-rich side of the phase diagram. We find that OFZ28-4 and both parts of OFZ27-2 do agree very well with the phase diagram of polycrystals. Curiously, the lower transition temperature $T_C = 4.3\,\mathrm{K}$ of crystal OFZ11-2 is higher as compared to the polycrystals. For crystals around the stoichiometric composition T_C generally shifts to very low temperatures and the ferromagnetic transition becomes very weak [124]. For crystals OFZ12-3 and OFZ29-2 a ferromagnetic transition could so far not be resolved. The magnetic properties of the float-zoned crystals investigated are summarized in Table 7.3.

Crystal quality

The zero-field AC - susceptibility also provides information about the quality of the samples [173]. High quality crystals were found to show well-defined transitions and no frequency dependence. In this respect, as shown in Fig. 7.10, our float-zoned crystals were found to be of very good quality. In fact, crystal OFZ28-4 was the first crystal that did not show any frequency dependence of the AC - susceptibility in zero field.

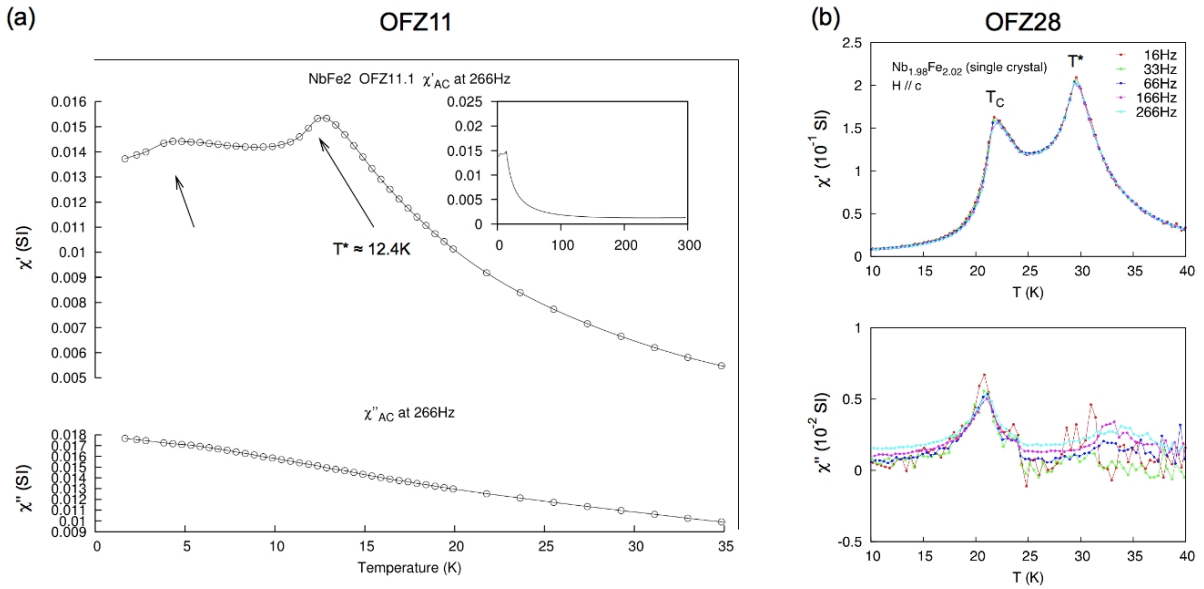

Figure 7.10: AC - susceptibility of single crystals OFZ11-2 (a) and OFZ28-4 (b). The high temperature transition at T^* denotes the transition from the paramagnetic to the SDW state. The transition at the lower temperature T_C may be assigned to the transition from the SDW to the ferromagnetic state. The transition temperatures are higher for the Fe-rich sample OFZ28. The clear signals of the transitions and the lack of frequency dependence shown in panel (b) indicate the excellent quality of the float-zoned crystals. Images were taken from Ref. [172].

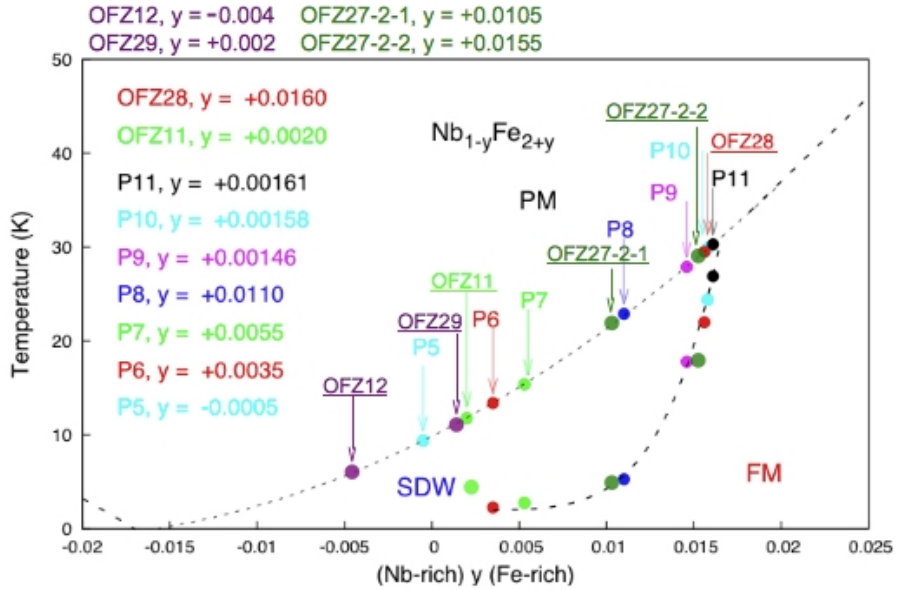

Figure 7.11: Composition dependent magnetic phase diagram of $Nb_{1-y}Fe_{2+y}$ as compiled by William Duncan [172]. The measured transition temperatures of our float-zoned single crystals are superimposed on the dashed lines that indicate the dependence of the transition temperatures in poly-crystalline samples. The Fe content (y) of each float-zoned crystal inferred from this comparison is shown in the graph. OFZ27-2-1 and OFZ27-2-2 denote the lower and, respectively, upper part of rod OFZ27-2 as shown in Fig. 7.7.

Magnetic anisotropy

Measurements of the AC - susceptibility in oriented single crystals indicated a strong magnetic anisotropy in $Nb_{1-y}Fe_{2+y}$ [170]. Fig. 7.12 shows the temperature dependent inverse AC - susceptibility for sample OFZ29-2 measured with field along the a - axis ($B||a$) and c - axis ($B||c$). For both directions the inverse AC - susceptibility follows a Curie-Weiss behavior for temperatures above T_C. For $B||a$ (black dots) the inverse AC - susceptibility is noticeable higher than for $B||c$ (red dots). An effective magnetic moment $\mu_{\rm eff}$ may be inferred from the slope of the inverse susceptibilities. The effective moment $\mu^a_{\rm eff} = 0.96\,\mu_B$/atom for $B||a$ is thereby found to be slightly larger than $\mu^c_{\rm eff} = 0.92\,\mu_B$/atom for $B||c$. From the intercept of the slope with the x - axis we obtain Curie-Weiss temperatures of $T^c_{\rm CW} = 9\,$K and $T^a_{\rm CW} = -0.6\,$K for field along the c - and the a - axis, respectively. Similar behavior is found for all single crystals. An overview of the effective moments and Curie-Weiss temperatures obtained for our float-zoned single crystals is given in Table 7.3. Curiously, it is found that $T^c_{\rm CW}$ for $B||c$ corresponds quite well to T^*, while $T^a_{\rm CW}$ for $B||a$ relates to T_C. In addition, we note that the Curie-Weiss temperatures obtained for polycrystals of similar compositions generally correspond to the Curie-Weiss temperatures of single crystals with field along the a - axis.

The temperature dependence of the real part of the AC - susceptibility for various fields and both directions of OFZ29-2 is shown in Figs. 7.13 (a) and (b). The maximum value of the AC - susceptibility for $B||c$ ($\chi^c_{B=0}$) is by a factor of five larger than the maximum value for $B||a$ ($\chi^a_{B=0}$). This difference clearly identifies the c - axis as the easy axis. For field along the easy axis a maximum in the AC - susceptibility denotes the transition to the SDW state. This maximum is suppressed to lower temperatures with small fields. Already at a field of 0.5 T no maximum is observed. In contrast, for $B||a$, where the transition to the SDW state is denoted by a broad shoulder, the transition is found to be more stable under magnetic field. At $B = 1\,$T the transition is only suppressed to $T \sim 6\,$K.

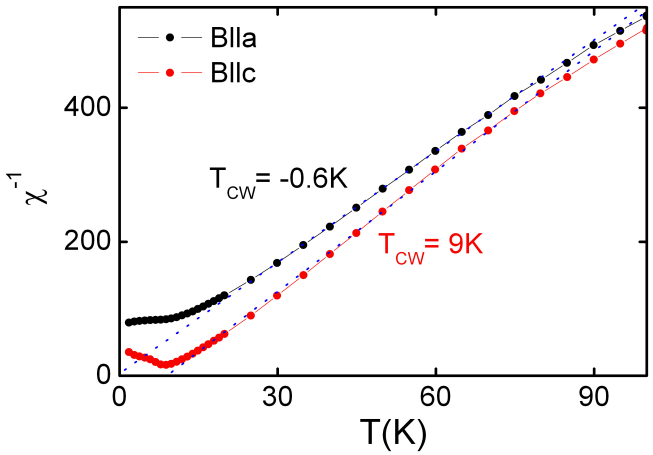

Figure 7.12: Inverse AC - susceptibility of crystal OFZ29-2 with field along the a - and the c - axis indicating the anisotropic behavior of $Nb_{1-y}Fe_{2+y}$. For both directions the inverse susceptibility follows a linear Curie-Weiss behavior for $T > T_C$.

Figs. 7.13 (c) and (d) show the field dependence of the AC - susceptibility for various temperatures and both directions for single crystal OFZ29-2. For $B||c$ and 1.8 K the SDW state is suppressed by an external field of $B_c^c = 0.19$ T as indicated by the maxima of the AC - susceptibility. With increasing temperature the critical field decreases and the double peak structure merges into a single peak around $T^* = 9$ K, consistent with the transition temperature as observed in Figs. 7.13 (a). For $B||a$ no distinct signature other than the weak maximum at zero field appears in the AC - susceptibility for fields up to $B = 1$ T. As we will see below in the field dependent AC - susceptibility of crystal OFZ11-2, data up to high fields are necessary to reveal a double peak structure of the AC - susceptibility for $B||a$. From a kink in the magnetization (not shown) we derived a critical field around 2.5 T for crystal OFZ29-2 and $B||a$.

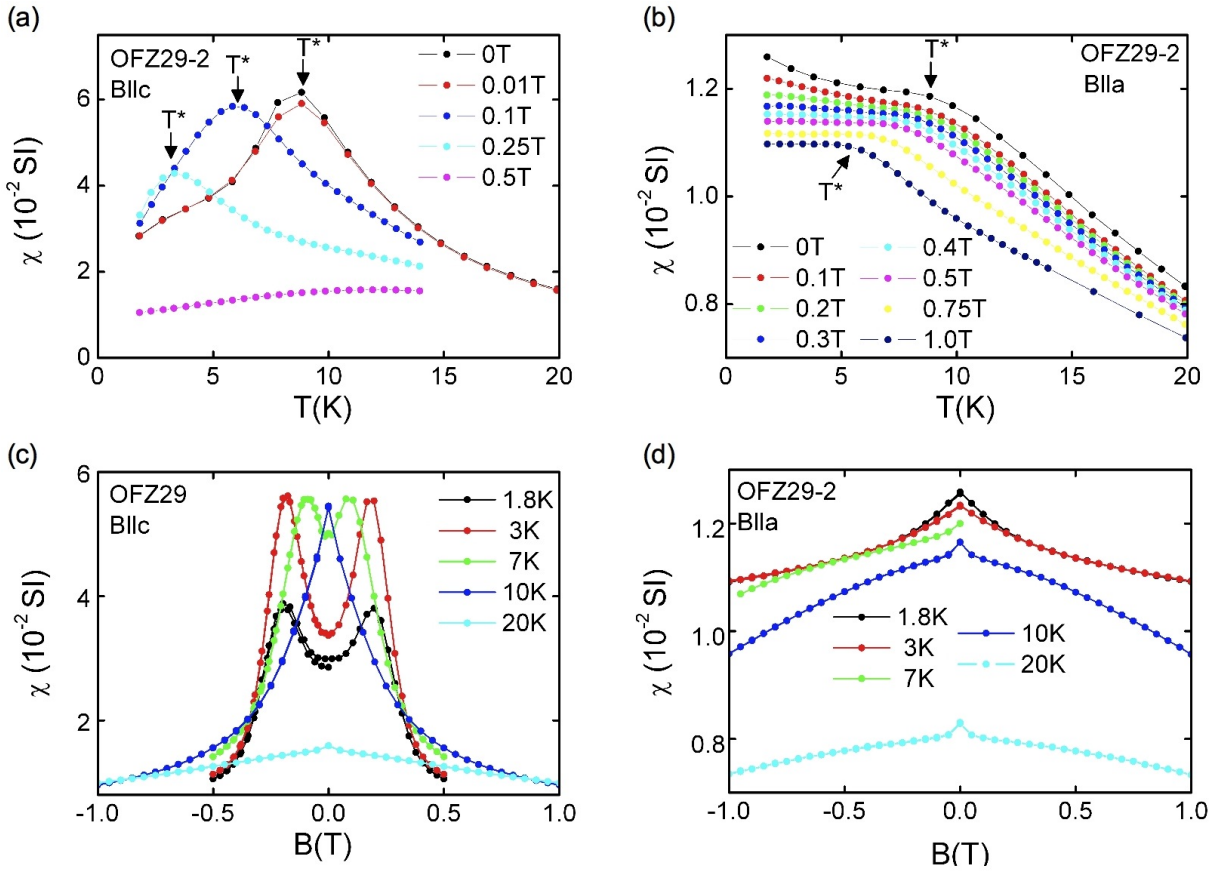

Figure 7.13: Temperature and field dependence of the AC - susceptibility for both orientations of single crystal OFZ29-2. (a) For $B||c$ the transition temperature is suppressed in small fields. (b) For $B||a$ the transition temperature is more stable under magnetic field, i.e., the transition temperature is only suppressed to around 6 K at $B = 1$ T. (c) For $B||c$ and low temperatures, the SDW state is suppressed by an external field of $B_c^c = 0.19$ T. With increasing temperature B_c^c decreases and the double peak structure merges into a single peak around $T^* = 9$ K. (d) For $B||a$ no distinct signature in the AC - susceptibility is found for fields up to $B = 1$ T.

AC - susceptibility measurements to high fields were carried out by William Duncan on crystal OFZ11-2 as shown in Fig. 7.14. The transition temperature $T^* = 12.4\,\mathrm{K}$ of OFZ11-2 is slightly higher than $T^* = 9\,\mathrm{K}$ of OFZ29-2. Data of the real and the imaginary part of the AC - susceptibility are shown for both orientations of OFZ11-2. In addition, Fig. 7.14 (c) shows data for a poly-crystalline sample P5 of similar composition ($T^* = 9.4\,\mathrm{K}$).

For $B||c$ the AC - susceptibility of OFZ11-2 shows qualitatively similar behavior as for OFZ29-2. A double peak structure at low temperatures that merges into a single peak at the transition temperature. Interestingly, though, is the large critical field $B_c^c = 0.45\,\mathrm{T}$ suppressing the SDW state in comparison to $B_c^c = 0.19\,\mathrm{T}$ observed for OFZ29-2. This indicates that the stability of the SDW under magnetic field increases quite drastically when the transition temperature increases from 9 K to 12.4 K. For $B||a$ additional peaks are observed at high fields and low temperatures. At $T = 1.8\,\mathrm{K}$ the critical field is $B_c^a = 2.3\,\mathrm{T}$. As for $B||c$ the peaks shift to smaller fields with increasing temperature. We note that the size of the critical fields B_c^a are similar for OFZ11-2 and OFZ29-2. For the poly-crystalline sample P5 a behavior similar to OFZ11-2 with $B||c$ is found. However, the peaks are smeared out and no clear transition shows up at high fields (not shown).

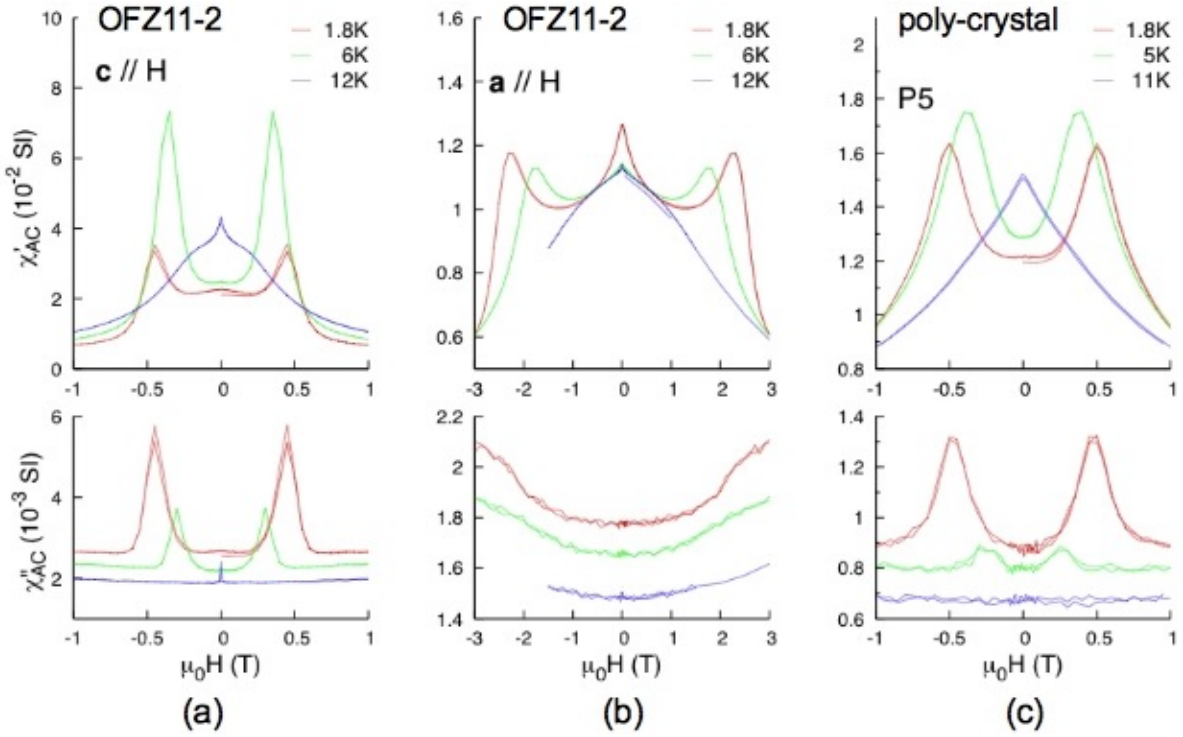

Figure 7.14: Field dependence of the real and imaginary part of the AC - susceptibility for both orientations of single crystal OFZ11-2 (a, b) and for a poly-crystalline sample P5 (c) with similar composition. The transition temperatures are 12.4 K and 9.4 K for OFZ11-2 and P5, respectively. The critical field suppressing the SDW is different for $B||a$ and $B||c$. At the lowest temperatures studied we obtain $B_c^c = 0.45\,\mathrm{T}$ and $B_c^a = 2.3\,\mathrm{T}$. The polycrystal P5 shows a behavior similar to OFZ11 with $B||c$. The maxima in the imaginary part for single crystal OFZ11-2 with $B||c$ at low temperatures suggest the transition to be first order. Image taken from Ref. [172].

The imaginary part of the AC - susceptibility (see bottom row of Fig. 7.14) shows clear peaks for OFZ11-2 with $B||c$ and slightly smeared out peaks for the polycrystal. The peaks in the imaginary part of the AC - susceptibility indicate losses and suggest a first order phase transition with magnetic field along the c - axis. On approaching the transition temperature, the imaginary part of the signal decreases, suggesting that the transition changes from first to second order. For $B||a$, the small increase of the imaginary part suggests a second order phase transition in this direction.

7.3.2 Magnetization

Fig. 7.15 shows magnetization isotherms of the single crystal OFZ11-2 along both directions and of the poly-crystalline sample P5. A jump in the magnetization of the single crystal with $B||c$ indicates a metamagnetic transition at the critical field $B_c^c = 0.45\,\mathrm{T}$. The jump decreases in size and shifts to lower fields with increasing temperatures and vanishes around the transition temperature T^*=12.4 K. The metamagnetic transition indicates the SDW state at low fields. In addition, the appearance of hysteresis is observed for low temperatures (1.8 K and 3 K), indicating ferromagnetic order. This agrees very well with the ferromagnetic transition at $T_\mathrm{C} = 4.3\,\mathrm{K}$ observed in the AC - susceptibility (cf. Fig. 7.10). For $B||a$ a kink in the magnetization is observed at $B_c^a = 2.3\,\mathrm{T}$ and 1.8 K. This kink, indicating the metamagnetic transition with $B||a$, shifts to lower fields with increasing temperature and smears out. The poly-crystalline sample again resembles the behavior of the single crystal with $B||c$. It shows a metamagnetic transition at small fields and low temperatures and a small hysteresis at low temperatures. In general, the features are not as pronounced as for the single crystal. Therefore it is not surprising that no kink is observed at high fields (not shown).

To summarize, the magnetization measurements resemble the anisotropic magnetic behavior of the $Nb_{1-y}Fe_{2+y}$ single crystals observed in the AC - susceptibility. Along the c - axis, the easy axis, the SDW state at low temperatures is suppressed in weak magnetic fields of $B_c^c = 0.45\,\mathrm{T}$ and $B_c^c = 0.19\,\mathrm{T}$ for crystals OFZ11-2 and OFZ29-2, respectively. In contrast, with field along the a - axis, the SDW state in both single crystals is only suppressed at high fields around $B_c^a = 2.5\,\mathrm{T}$. For a polycrystal of similar composition only the lower critical field was observed, with the signal being smeared out. Hence the float-zoned single crystals allowed us to identify a strong magnetic anisotropy in $Nb_{1-y}Fe_{2+y}$ with two distinct critical fields suppressing the SDW state.

For crystal OFZ28 similar results were obtained in the magnetization and AC - susceptibility. The transition temperatures were shifted to higher temperatures and a more pronounced ferromagnetic state appeared. Further details of measurements on crystal OFZ28 are reported by William Duncan [172]. An overview of the magnetic properties of all float-zoned single crystals investigated is given in Table 7.3.

	OFZ11-2	OFZ12-3	OFZ27-2-1	OFZ27-2-2	OFZ28-4	OFZ29-2
T^*	12.4 K	6.4 K	21.5 K	29 K	29.5 K	9 K
T_C	4.3 K	-	4.8 K	17.8 K	22.0 K	-
T^c_{CW}	12.1 K	-	-	-	33.9 K	9 K
T^a_{CW}	-2.1 K	(-4.2) K	-	-	23.4 K	-0.6 K
μ^c_{eff} (μ_B/at.)	0.91	-	-	-	0.92	0.92
μ^a_{eff} (μ_B/at.)	1.00	(0.96)	-	-	0.98	0.96
$\mu^c_{9T,2K}$ (μ_B/at.)	0.062	-	-	-	0.078	0.042
$\mu^a_{9T,2K}$ (μ_B/at.)	0.067	-	-	-	0.08	0.047
B^c_c ($B\|\|c$)	0.45 T	(0.5T)	-	-	0.35 T	0.19 T
B^a_c ($B\|\|a$)	2.3 T	-	-	-	2.5 T	2.5 T

Table 7.3: Summary of the magnetic properties of the float-zoned single crystals. The orientation dependent properties of single crystal OFZ12-3 are given in brackets since the crystal was not oriented when measured.

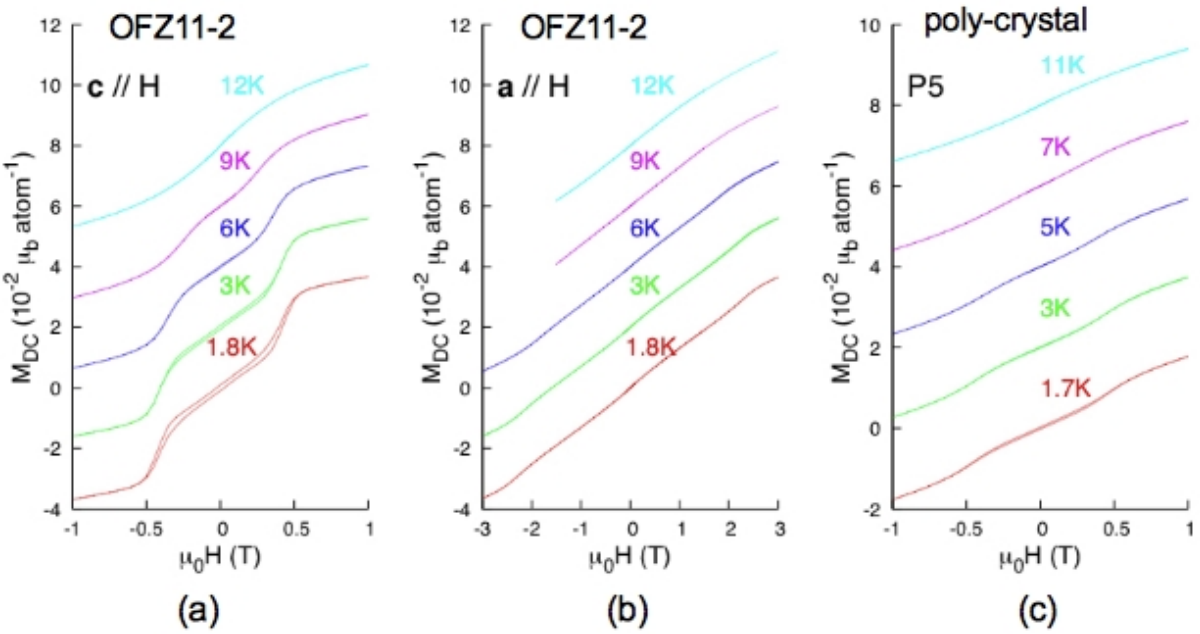

Figure 7.15: Magnetization isotherms of single crystal OFZ11-2 with $B||c$ (a) and $B||a$ (b) and of the polycrystal P5 (c). The transition temperatures are 12.4 K and 9.4 K for OFZ11-2 and P5, respectively. The curves are shifted for clarity. A jump in the magnetization of the single crystal indicates a metamagnetic transition at the critical fields $B^c_c = 0.45$ T and $B^a_c = 2.3$ T for for $B||c$ and for $B||a$, respectively. At low temperatures hysteretic behavior is observed for $B||c$. The polycrystal resembles the behavior of the single crystal with $B||c$. The image was taken from Ref. [172].

7.3.3 Torque magnetization

In order to investigate the magnetic anisotropy the torque magnetization of an oriented single crystal sample of OFZ29-2 was measured. The rectangular sample ($m = 71\,\mathrm{mg}$) was cut from the sample we used for the magnetization and AC - susceptibility measurements reported above. Unfortunately, the transmission spindle that allows to rotate the torque set-up broke during the first measurements. Hence only preliminary results could be obtained. Detailed measurements are planned for the future.

Fig. 7.16 shows the angular dependence of the capacitance of the torque meter in an applied field of 1 T for three different temperatures. Note that the capacitance is proportional to the magnetic moment ($m_\perp$) perpendicular to the applied field:

$$C \propto |\mathbf{m} \times \mathbf{B}| \propto m_\perp B. \tag{7.1}$$

The x - axis of Fig. 7.16 defines the angle between the direction of the applied field **B** and the c - axis of $NbFe_2$. The sample is rotated in the a - c - plane. Hence, at an angle of 90° the magnetic field is aligned parallel to the a - axis. Note that the capacitance represents a relative measure since the zero-field capacitance has not been subtracted. The zero-field capacitance varies between 2.9 pF to 3 pF due to the mass of the sample. For an absolute measure and for the determination of the anisotropy coefficients an angle dependent background correction is indispensable, but missing here due to the broken spindle.

However, Fig. 7.16 clearly shows that the size of the magnetic anisotropy increases with decreasing temperature. At 30 K the capacitance shows sine-like behavior with a minimum around 45°. The preliminary 20 K data suggests that this sine-like behavior changes and that the minimum shifts to higher angles. At 4 K the minimum is clearly shifted to higher angles. This resembles the behavior we expected since at 90° the capacitance C measures the magnetization along the easy axis of $NbFe_2$. We note that at 90° (and at 0°) the torque changes its sign since the magnetization direction is changed and hence the minimum can not be centered at 90°, but shifts to its vicinity.

Figs. 7.17 (a) and (b) show the field dependence of the normalized capacitance with field along the c - axis and a - axis, respectively. Note that five-point loops are shown and that the curves are shifted vertically for clarity. For $B||c$, hence measuring the magnetic moment along the a - axis ($m_\perp^a$), a kink of $m_\perp^a$ is observed at $\sim 0.25\,\mathrm{T}$ (see black arrow). With increasing temperature this kink smears out and eventually a gradual increase of $m_\perp^a$ is observed. For $B||c$ no hysteresis is observed. In contrast, for $B||a$, hence measuring the magnetic moment along the c - axis ($m_\perp^c$), a strong hysteresis is observed in the ordered state with a large coercive field of around 1.8 T at $T = 2\,\mathrm{K}$. The 2 K curve shows a maximum around $B = 2.5\,\mathrm{T}$. At 8 K the signal appears as a broad shoulder. As a preliminary result we found that the transitions observed in the field dependent torque magnetization resemble the critical fields $B_c^c \approx 0.2\,\mathrm{T}$ and $B_c^a \approx 2.5\,\mathrm{T}$ observed in the magnetization and susceptibility. The origin of the large coercive field is unclear. We also note that the size of the capacitance measured is strongly angle dependent, especially around 0° and 90°.

Fig. 7.18 shows the temperature dependence of the capacitance at various fields with $B||a$. With increasing field (0 - 2.5 T, from top to bottom) the minimum that denotes the transition to the SDW state is shifted to lower temperatures. At 2.5 T no minimum is observed in the temperature range studied. We note that the evolution of T^* observed here is consistent with measurements of the AC - susceptibility shown in Fig. 7.13.

Both the temperature and the field dependent measurements of the torque magnetization illustrated that this technique allows to sensitively track the critical fields. Further investigations at various angles of the applied field may be an excellent method to precisely track the angular dependence of the critical fields and possibly identify an angle-dependent quantum critical point as proposed in the discussion.

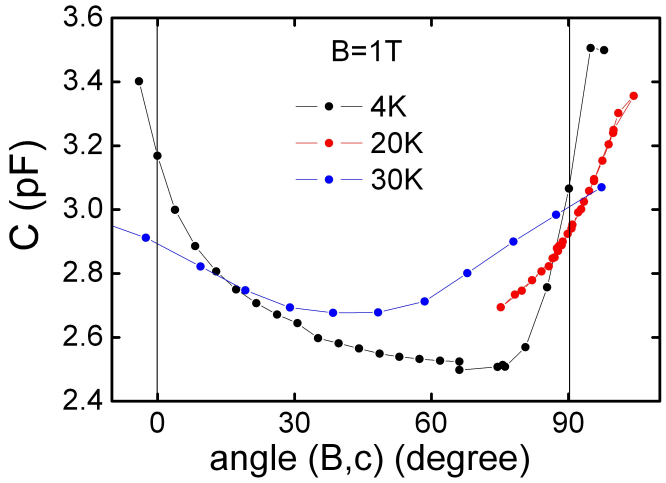

Figure 7.16: Angular dependence of the capacitance at a constant field of 1 T for 4 K, 20 K and 30 K. The angle is defined by the angle between the direction of the applied field **B** and the c - axis of the crystal. The sample is rotated in the a - c - plane. At low temperatures the minimum shifts towards 90°, indicating the c - axis as the easy axis.

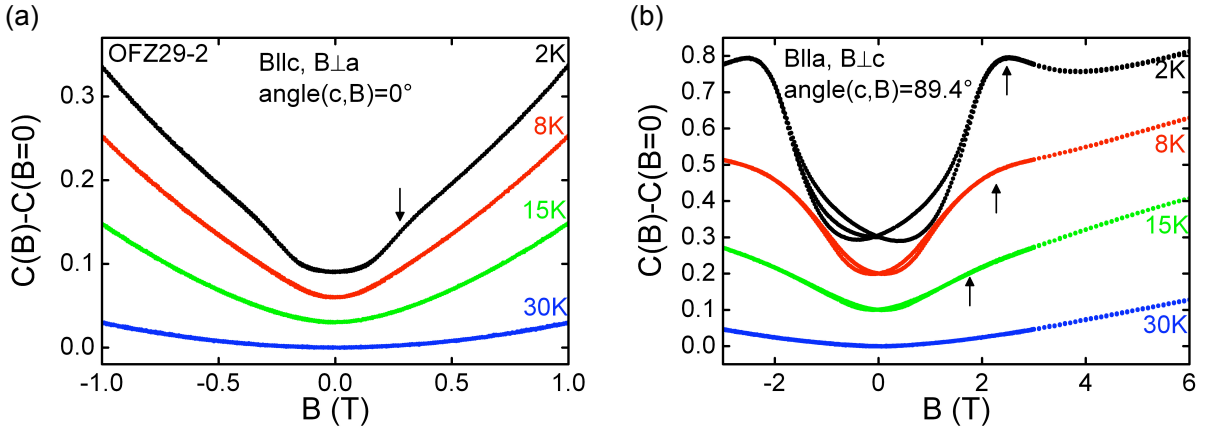

Figure 7.17: Five-point loops of the normalized capacitance with field along the c - axis (a) and a - axis (b). The curves are shifted for clarity. For $B||a$ hysteretic behavior appears. A kink at 0.25 T in (a) and the maximum at 2.5 T in (b) resemble the critical fields measured in the AC - susceptibility and the magnetization.

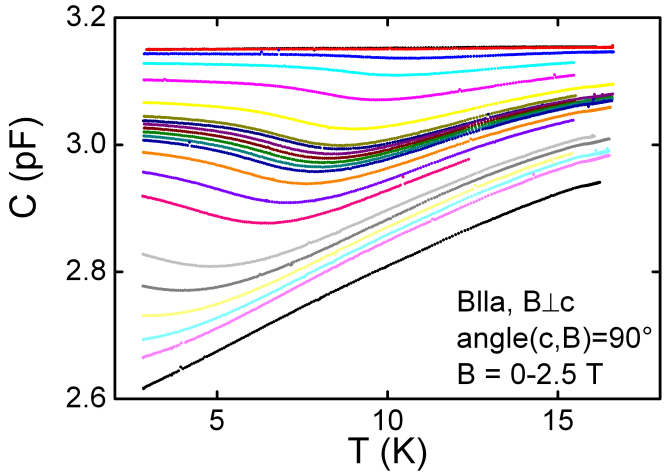

Figure 7.18: Temperature dependence of the torque capacitance of crystal OFZ29-2 with $B||a$. With increasing field the minimum that resembles the transition temperature T^* is shifted to lower temperatures. From top to bottom fields between 0 T and 2.5 T are shown.

7.3.4 Magnetoresistance

Resistivity measurements on samples OFZ11-2 and OFZ28-4 were carried out by William Duncan in a 4-point configuration. As in the previous section, we will focus on the results for crystal OFZ11. Further details on crystal OFZ28 are reported by William Duncan [172].

The resistivity for sample OFZ11-2 was only measured in the configuration with the current applied parallel to the a-axis ($I||a$). The temperature dependent zero-field resistivity measured from room temperature to $T = 2$ K showed metallic behavior in the whole temperature range (not shown). At low temperatures the resistivity seems to follow a $T^{1.5}$ temperature dependence. No anomalies of the resistivity were observed around the transition temperatures T^* and T_C. The residual resistivity ratio (RRR) was around 8.

The magnetoresistance for single crystal OFZ11-2 was measured in two different field configurations, $B||c$ and $B||a$-b, with the magnetic field always perpendicular to the applied current. As shown in Fig. 7.19, for both field configurations a negative magnetoresistance was observed for all temperatures studied. The magnetoresistance reveals the similar anisotropic features as reported above in the susceptibility and magnetization. For $B||c$ (cf. Fig. 7.19 (a)) a pronounced drop of the resistivity is observed at a critical field $B_c^c \approx 0.45$ T and $T = 1.8$ K. The resistivity is considerably suppressed by around 20%. With increasing temperatures up to T^*, the drop in the resistivity shifts to smaller fields and broadens. In addition, hysteresis is observed for temperatures below T_C. For $B||a$-b (Fig. 7.19 (b)), i.e., B perpendicular to the c-axis, the low temperature magnetoresistance decreases continuously up to a kink around $B = 3$ T. This field is slightly larger than the critical field $B_c^a \approx 2.5$ T observed in the susceptibility and magnetization. With increasing temperatures the kink shifts to lower fields and its pronounced signature is lost.

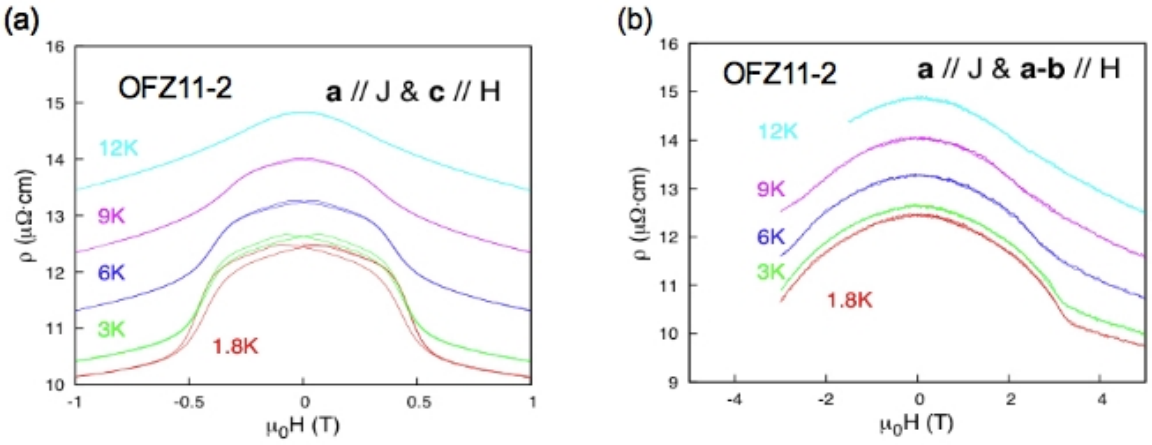

Figure 7.19: Magnetoresistance isotherms with the current applied along the a-axis and field along (a) and perpendicular (b) to the c-axis. The magnetoresistance reveals the similar anisotropic features as observed in the magnetization and susceptibility. Image taken from Ref. [172].

7.3.5 Specific heat

The low temperature specific heat of crystal OFZ11-2 with $B||c$ is shown in Fig. 7.20. The data is plotted as C/T vs. T. The measurements were carried out by William Duncan. For all fields C/T shows a minimum around 11 K and an increase to low temperatures. An extrapolation to zero yields an elevated Sommerfeld coefficient around 50 mJ mol^{-1}K^{-2}. The low temperature increase seems to follow a logarithmic dependence [124], similar to the behavior reported by Brando *et al.* [61]. However, for a reliable statement further measurements to lower temperatures are necessary. Furthermore, around 13 K and in zero field an additional signal is observed. This additional magnetic contribution in the specific heat indicates the transition to the SDW state. In magnetic fields above the critical field B_c^c the magnetic contribution is suppressed.

7.3.6 Small angle neutron scattering

In order to identify the nature of the small-moment ordered state (SDW) in $Nb_{1-y}Fe_{2+y}$, single crystal OFZ11-2 was investigated by means of small angle neutron scattering at MIRA at FRM II. The experiment was carried out by William Duncan in collaboration with Robert Georgii, Philipp Niklowitz and Malte Grosche.

The single crystal OFZ11-2 had a diameter of around 6 mm and a height of around 10 mm. The crystal was kept at a constant temperature of 4 K and scans were conducted both in zero field and in an applied field of 0.2 T with the field parallel to the neutron beam. The parameters where chosen in order to ensure that OFZ11 is in the SDW state. The use of two different detector positions and scans over a large angular range (-7 to 108 degrees with a scan at every degree) allowed to cover a large q-range of 0.002 to 0.59 Å^{-1} around the c-axis with a neutron wavelength $\lambda = 4.8$ Å.

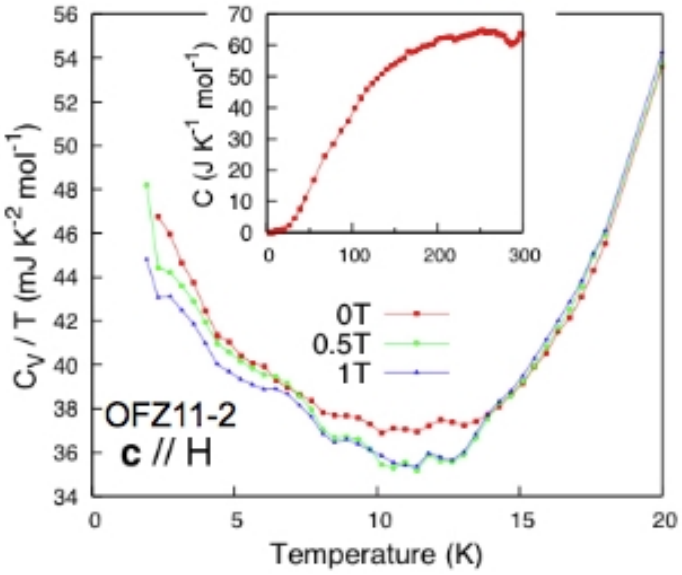

Figure 7.20: Heat capacity of crystal OFZ11 with $B||c$. Around 13 K an additional contribution is observed in zero field, indicating the transition to the SDW state. At fields above the critical field this magnetic contribution is suppressed. The image was taken from Ref [172].

No signs of magnetic order were observed in the q - range investigated. One explanation might be that the magnetic ordering wave vector lies outside of this q - range, although Brando *et al.* estimated the wave vector to be $\sim 0.05\,\text{Å}^{-1}$ [61]. Another explanation might be the small ordered moment, which may be estimated from the jump in the magnetization at the critical field to be $\sim 0.02\,\mu_B$/atom. Hence, the measurement time of 300 s may have been insufficient to detect the magnetic scattering intensities.

7.4 Discussion

The magnetic properties of single crystal OFZ11-2 and of the poly-crystalline sample P5 are summarized in contour plots shown in Fig. 7.21. The row at the top shows the DC - susceptibility derived from the magnetization. The middle and the bottom row show the real and imaginary part of the AC - susceptibility, respectively. In addition, the maximum values of the derivative of the magnetoresistance are indicated by blue points.

The clearest signal is found for OFZ11-2 with $B||c$ (Fig. 7.21 (a)), where a dome, defined by a low critical field $B_c^c \leq 0.45\,\text{T}$, illustrates the boundary of the SDW state. The large signal in the imaginary part of the AC - susceptibility for low temperatures identifies the quantum phase transition (SDW-PM) to be first order. This signal vanishes to higher temperatures indicating the transition to become second order. For $B||c$ the magnetic data coincides perfectly with the data obtained from the resistivity measurements. For the single crystal with $B||a$ (Fig. 7.21 (b)), the dome representing the SDW state is limited by a much larger critical field $B_c^a \leq 2.3\,\text{T}$. The magnetic signatures are smaller in size and less well defined as for $B||c$. The broad distribution of the imaginary part of the

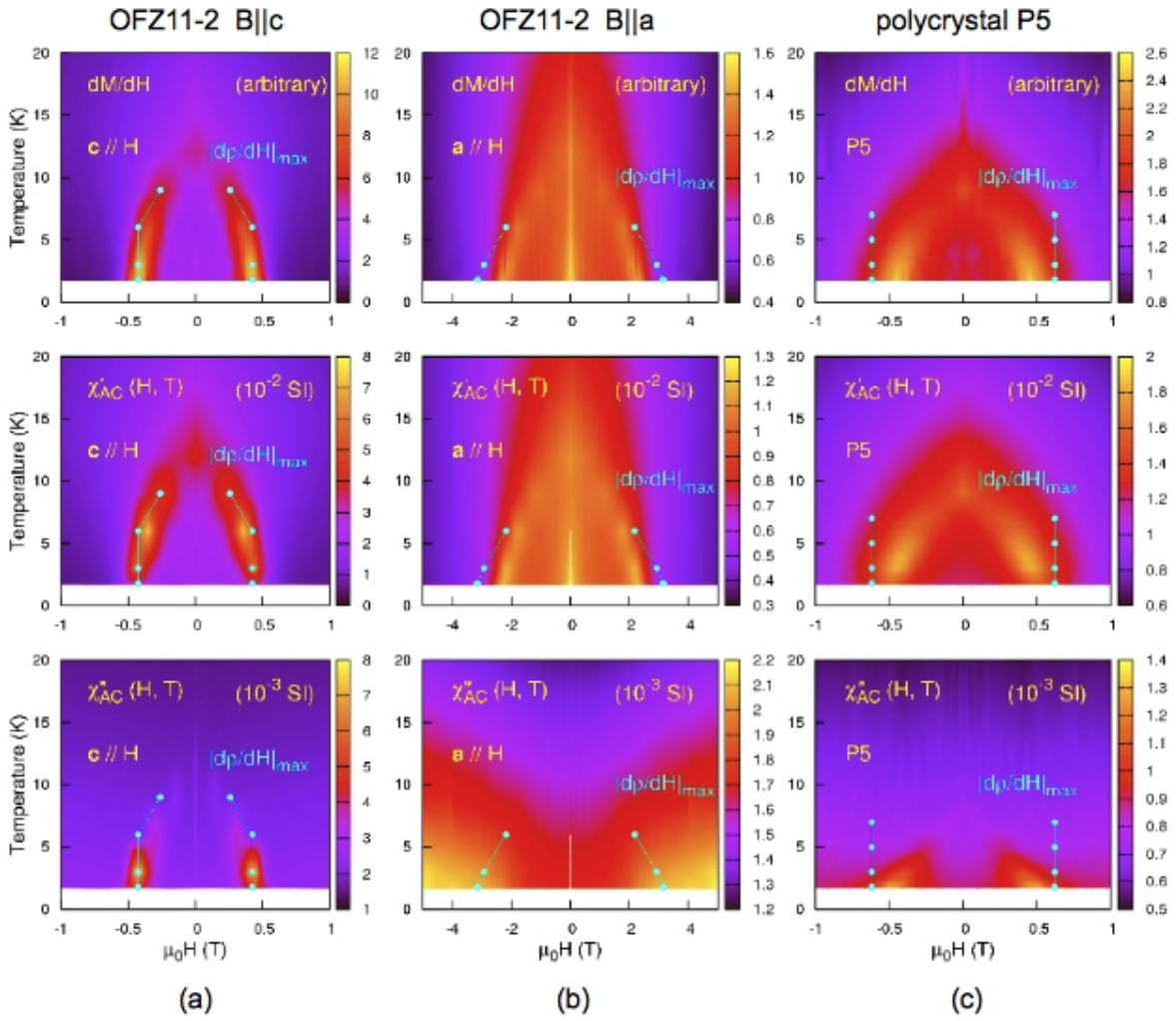

Figure 7.21: Contour plots of the dc-susceptibility and the real and imaginary part of the AC - susceptibility (from top to bottom) for single crystal OFZ11-2 with $B||c$ (a) and $B||a$ (b) and for polycrystal P5 (c). In addition, the maxima of the derivative of the magnetoresistance are shown as blue points. Two distinct critical fields confine the SDW state along the $B||c$ and $B||a$ direction. For the polycrystal the signals are smeared out. Image taken from Ref. [172].

AC - susceptibility suggests the quantum phase transition (SDW-PM) to be second order for $B||a$. The dome representing the SDW state in the polycrystal (Fig. 7.21 (c)) is similar to the dome for the single crystal with $B||c$, but with less well defined boundaries. For large fields no clear signal was detected for the polycrystal.

The observation of the strong magnetic anisotropy in single crystal $NbFe_2$ allowed us to expand the schematic magnetic phase diagram from 2 dimensions to 3 dimensions, as shown in Fig. 7.22. For polycrystals so far only one critical field value suppressing the SDW-state was found. For single crystals we were able to find two orientation dependent critical fields, B_c^c and B_c^a, suppressing the ordered state, with $B_c^a \gg B_c^c$. The values for the critical fields are summarized in Table 7.3. At low temperatures the large imaginary part

of the AC-susceptibility indicates the transition for $B||c$ to be first order while at higher temperatures the transition seems to become second order. For $B||a$ the transition appears to be second order for all temperatures. These findings also suggest the existence of a critical angle of the suppression of the first order transition in $Nb_{1-y}Fe_{2+y}$, as illustrated in Fig. 7.22 (c). Torque magnetization measurements may be an excellent method in order to identify this angle-dependent suppression of the transition.

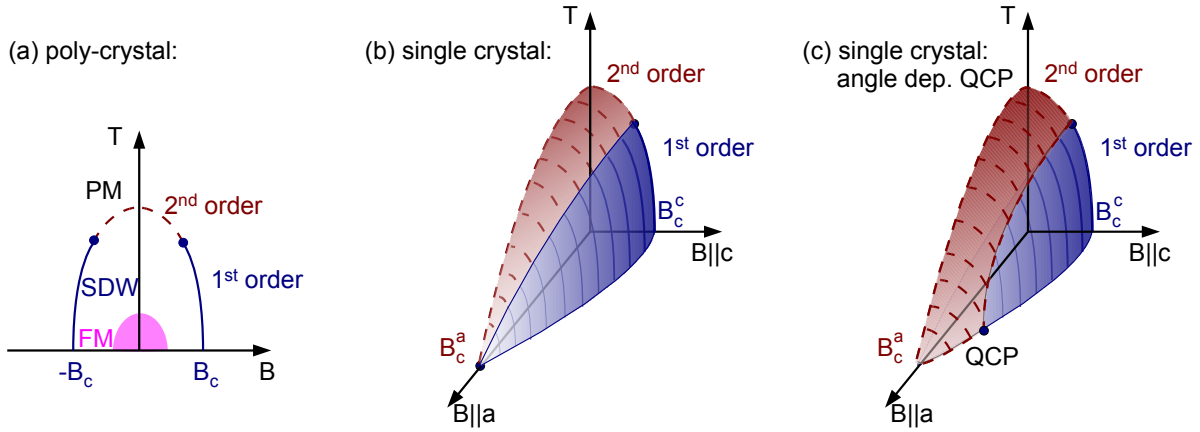

Figure 7.22: Schematic of the magnetic phase diagram of $NbFe_2$. (a) 2D phase diagram as derived from polycrystals. With increasing temperature the transition from the SDW state to the paramagnetic state changes from 1^{st} to 2^{nd} order. At low fields and low temperatures $NbFe_2$ orders ferromagnetic. (b) 3D phase diagram as derived from single crystals, illustrating the strong magnetic anisotropy. For $B||a$ the magnetic transition is second order for all temperatures. This suggests the existence of a critical angle of the suppression of the first order transition as shown in (c).

7.5 Summary and Outlook

We were able to grow six large crystals of $Nb_{1-y}Fe_{2+y}$ with our UHV-compatible image furnace starting with slightly irregular shaped rods of various compositions. Single crystal neutron diffraction at RESI confirmed excellent crystal properties indicated by the narrow mosaic spread. At least one large single-crystalline grain was observed in every crystal. For crystal OFZ28 we obtained a mono-crystalline structure across the entire cross-section of the rod.

Neutron depolarization radiography revealed an inhomogeneous distribution of the ferromagnetic transition temperatures along the float-zoned crystals. Nevertheless, taking into account the strong composition dependence of the transition temperature, the homogeneity of the float-zoned crystals can still be considered as very good. With the help of NDR we were able to prepare homogeneous single crystal samples for further measurements. A tendency of the composition to shift to the Fe-rich side during crystal growth was found, which was probably driven by the precipitation of a Nb-rich impurity phase on the surface of the crystals.

The well-defined transitions of the temperature dependent zero-field AC - susceptibility in float-zoned single crystals are a further proof of an excellent crystal quality. For samples OFZ27-2-1, OFZ27-2-2, and OFZ28-4 the transition temperatures derived from the double peak structure in the AC - susceptibility agree well with the y - T - phase diagram derived by William Duncan for polycrystals (cf. Fig. 7.11). The ferromagnetic phase is found to show a quadratic composition dependence, in contrast to the linear dependence as reported before (see Fig. 7.2) [60]. However, for sample OFZ11-2 an unusual elevated ferromagnetic transition temperature T_C was observed. For nearly stoichiometric samples OFZ12-3 and OFZ29-2 the lower transition temperatures could not be resolved. Hence, the exact progress of T_C around stoichiometric $NbFe_2$ remains elusive.

Bulk measurements of oriented single crystals revealed a strong anisotropic behavior of the magnetically ordered state in $Nb_{1-y}Fe_{2+y}$. Investigations of the single crystals allowed us to expand the schematic magnetic phase diagram from 2D to 3D, as shown in Fig. 7.22 (b). The absence of a first order transition for $B||a$ suggests the existence of a critical angle of the suppression of the first order transition in $Nb_{1-y}Fe_{2+y}$, i.e., an angle-dependent quantum critical point as shown in Fig. 7.22 (c). A continuation of the torque magnetization measurements may be an excellent method to identify this angle-dependent suppression of the transition in the near future.

No signs of magnetic order of the SDW state were observed in neutron diffraction experiments on single crystal OFZ11-2. A microscopic identification of the nature of the small-ordered moment state is essential in order to establish $NbFe_2$ as a candidate for the Belitz-Kirkpatrick phase of a ferromagnetic quantum critical transition. Hence further neutron diffraction experiments are in preparation. We plan to investigate the SDW state in OFZ28-4, since the magnetic moments increase in size with increasing Fe content. This may increase the chances to resolve the magnetic order of the SDW state. In addition, investigations of the imaginary part of the susceptibility by inelastic neutron scattering as a measure of the spin fluctuations are planned. As proposed by Subedi *et al.* [63], from inelastic neutron scattering important insights into the behavior of $NbFe_2$, specifically the identification of competing magnetic states that may exist in relation to the quantum critical behavior, may be obtained.

Chapter 8

Results & Discussion: B20 compounds

As described in the introduction, the investigation of B20 compounds that show helical magnetic order, i.e., MnSi, $Mn_{1-x}Fe_xSi$, $Mn_{1-x}Co_xSi$, and $Fe_{1-x}Co_xSi$ (shown in blue in Fig. 1.9), has been of major interest to our group in the last couple of years. Since the first floating zone crystal growth of MnSi in our group was carried out as part of this thesis, the growth parameters and basic properties of the MnSi single crystal is reported in the first part of this chapter. The growth and investigation of the $Mn_{1-x}Fe_xSi$ and $Fe_{1-x}Co_xSi$ gradient crystals, that constitute the main part of our investigations on the B20 compounds, is described in the subsequent parts of this chapter.

8.1 MnSi

8.1.1 Crystal growth

Starting rods with a stoichiometric composition of pure Mn (4N) and Si (> 6N) were cast in pure Argon atmosphere ($p = 1.5\,\mathrm{bar}$) in the rod casting furnace. The Mn pieces were etched with a mixture of ethanol and nitric acid (25:1) prior to the casting process. Special care had to be taken to cast the molten compound at the optimum RF power and temperature to avoid brittle fracture of the starting rods after casting them. Rods of MnSi tend to be partly hollow and, as a result, tend to break easily.

Prior to single crystal growth the image furnace was baked out and evacuated to a pressure of $2 \cdot 10^{-8}\,\mathrm{mbar}$ and subsequently filled with high purity Argon gas at a pressure of $p = 1.5\,\mathrm{bar}$. The melting of the MnSi rods started at a power of 72% of the image furnace with the 300 W lamps mounted. The crystal (OFZ9) was grown at a growth rate of 10 mm/h with a counter-rotation of 25 rpm and 10 rpm of the seed and feed rod, respectively. Stable growth conditions were obtained straight from the start and only a minimal adjustment of the lamp power was necessary during the growth due to the

evaporation of Mn on the quartz glass. The crystal was grown without a necking process, but a strong grain selection resulted in single crystal growth across the entire rod diameter after a distance of less than 1 cm. The crystal grown is shown in Fig. 8.1. Mono-crystalline MnSi was obtained along the last 2 cm of the crystal. Slight oxide contamination on the surface of the molten zone was observed during the growth process. The resulting contamination appears as dim gray areas on the crystal surface. The amount of oxide contamination on the surface of the molten zone reduced during the growth process.

Single-crystallinity of the crystal was confirmed optically, by means of X-ray Laue diffraction and neutron diffraction at RESI at FRM II. No preferred growth direction along a main crystallographic direction was found.

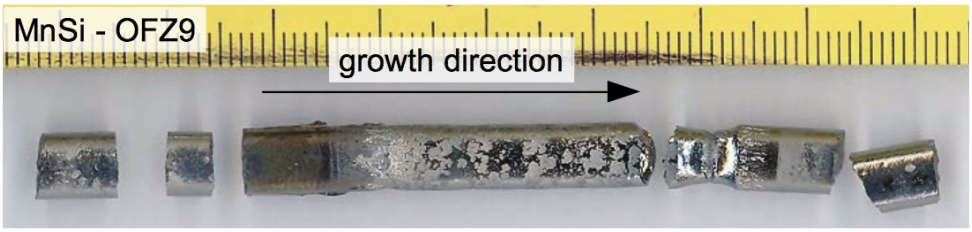

Figure 8.1: MnSi crystal grown with the vertical floating zone technique. Mono-crystalline MnSi was obtained for the last 2 cm. A small amount of oxide impurities floating on the molten zone during the growth process resulted in the grey shaded islands on the surface of the crystal. The impurity amount reduced during the growth process. Both feed and seed rod broke during cooling after the growth process had been finished.

8.1.2 Physical properties of MnSi

Resistivity measurements (see Fig. 8.2 (a)) show the well-established metallic behavior of MnSi reported in the literature [93]. The transition at T_c=29.5 K to the magnetically ordered state is illustrated by a drop of the resistivity. At low temperatures the resistivity shows a quadratic temperature dependence $\rho(T) = \rho_0 + AT^2$ as expected from Landau Fermi liquid theory. The crystal has a relatively low residual resistivity ratio RRR $= \rho(293\,\mathrm{K})/\rho_0 = 34$, which is attributed to the insufficient purity of Mn. Measurements of the specific heat at zero field are shown in Fig. 8.2 (b). The maximum at $T_c = 29.5$ K indicates the phase transition to the magnetically ordered state. The broad shoulder in the specific heat next to the maximum, shown in the inset, is a typical feature of MnSi that awaits further classification [98, 174, 175].

8.1.3 Summary

We found that congruently melting MnSi is very well-suited for crystal growth with the optical float-zoning technique. Stable growth conditions were obtained at a relatively high growth rate of 10 mm/h. A strong grain selection leads to a mono-crystalline structure

throughout the cross-section of the rod after a short growth distance. Measurements of the resistivity and the specific heat reproduced the typical physical properties reported for MnSi in literature and, hence, confirmed the good crystal quality of the floating zone grown crystal. Further crystals of MnSi were grown by Wolfgang Münzer and Andreas Bauer as part of their diploma theses [78, 95]. In their work they took special care in the preparation of high purity Mn prior to the casting process and were thus able to improve the residual resistivity ratios to RRR = 70 − 330. It is important to note that this excellent RRR values were already obtained without any further heat treatment of the crystals grown.

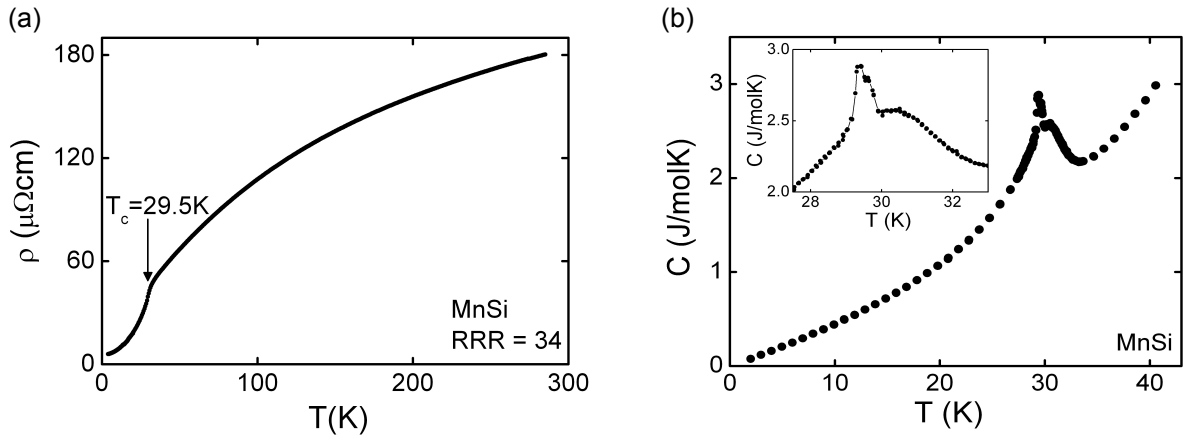

Figure 8.2: (a) The temperature dependent resistivity of MnSi at zero field shows the typical behavior reported for MnSi [93]. The transition to the magnetically ordered state is accompanied by a sudden drop in the resistivity. (b) Temperature dependence of the specific heat in zero field. The maximum at $T_c = 29.5\,\mathrm{K}$ indicates the magnetic phase transition. The broad shoulder next to the maximum (see inset) is an anomalous behavior characteristic of MnSi [98, 174, 175].

8.2 Gradient crystals: $Mn_{1-x}Fe_xSi$ & $Fe_{1-x}Co_xSi$

In order to examine the claim of a composition dependent chirality in $Mn_{1-x}Fe_xSi$ and $Fe_{1-x}Co_xSi$ crystals reported by Grigoriev *et al.* [100, 101], four crystals with a gradient of the composition were grown in the course of this thesis. In addition to the growth with the crucible free vertical float-zoning technique, any interactions with the surrounding were reduced to a base minimum by a systematic growth procedure. Single-crystallinity of the float-zoned crystals was checked by neutron single crystal diffraction at RESI at FRM II. The change of composition along the crystals was determined by detailed EDX analysis. The chirality of the magnetic order was investigated by small angle neutron scattering (SANS) with polarized neutrons at MIRA at FRM II.

8.2.1 Crystal growth

For the investigation of the composition dependence of the handedness of the magnetic helix in $Mn_{1-x}Fe_xSi$ and $Fe_{1-x}Co_xSi$ four gradient crystals were prepared, where the arrow indicates the growth direction:

- $MnSi \rightarrow Mn_{0.85}Fe_{0.15}Si$ (OFZ45)
- $Mn_{0.85}Fe_{0.15}Si \rightarrow MnSi$ (OFZ46)
- $Fe_{0.7}Co_{0.3}Si \rightarrow Fe_{0.9}Co_{0.1}Si$ (OFZ47)
- $Fe_{0.9}Co_{0.1}Si \rightarrow Fe_{0.7}Co_{0.3}Si$ (OFZ48)

The growth procedure was exactly the same for all four crystals. It is illustrated in Fig. 8.3. Starting rods of the initial (A) and final (B) composition were prepared with the rod casting furnace. At first, a short piece of rod A was attached to rod B with the image furnace. Subsequently, this rod was used as a feed rod for crystal growth with a seed of composition A, as shown schematically in Fig. 8.3 (b). An example of the rods mounted for crystal OFZ46 is shown in Fig. 8.3 (a). The dashed line shows the joint of compositions A and B. For the rest of the chapter this will be referred to as the initial joining point of compositional difference or $\Delta z = 0$. A list of the compositions of rods A and B for all four gradient crystals is shown in Fig. 8.3 (c).

Starting the crystal growth with seed A and feed A allows to establish a mono-crystalline structure prior to passing the zone across the onset of the steep compositional gradient. This way the nucleation of different grains with a different chirality at the steep compositional gradient may be avoided. For all four crystals a growth rate of 5 mm/h and a counter-rotation of 23 rpm and 10 rpm for the seed and feed rod, respectively, was applied. The crystals grown are shown in Fig. 8.4, with the dashed red line indicating the position of the initial joining point of compositional difference. Except for OFZ47, a slight necking process was applied in the beginning of the growth in order to promote the grain selection.

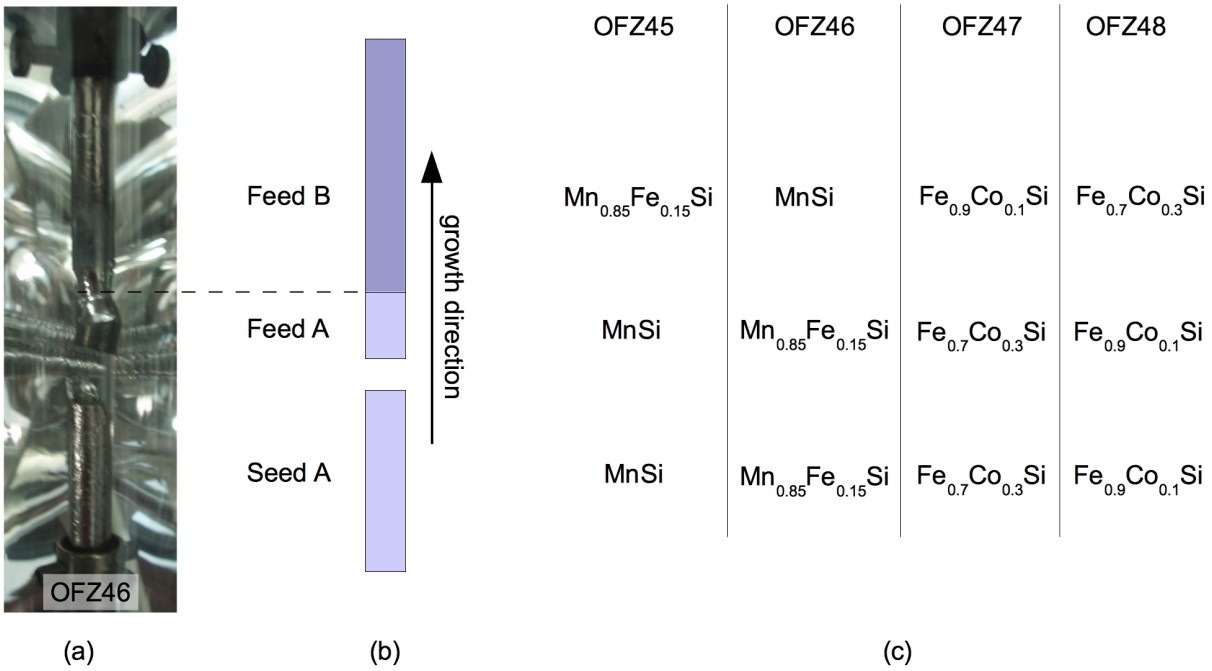

Figure 8.3: (b) The gradient crystals were grown in a systematic way, starting with crystal growth of composition A prior to the onset of the steep compositional gradient. (a) Picture of seed A and composite feed (A+B) mounted in the image furnace. Feed A and B were previously joint with the OFZ. The dashed line indicates the initial joining point of compositional difference ($\Delta z = 0$). (c) Overview of the compositions of the starting rods for all four gradient crystals.

Figure 8.4: Overview of the four gradient crystals grown with the floating zone technique. The red dashed lines mark the initial joining point of compositional difference. Growth direction was from left to right. Single-crystallinity was confirmed for large parts of each crystal.

Single-crystallinity of the rods was checked with X-ray Laue diffraction and neutron single crystal diffraction (except for OFZ45) at RESI at FRM II. At RESI areas below the initial joining point of compositional difference, at the initial joining point and well above the initial joining point were investigated, as shown in Fig. 8.5 for OFZ47. The crystals were mounted to sample holders as used for the investigation of the magnetic helicity at MIRA at FRM II. The top of the cadmium marker is located at the initial joining point of compositional difference. The yellow squares mark the areas investigated. In the case of OFZ47 the crystal broke during preparation and was therefore held in position for neutron scattering with an aluminum bar. The results of the measurements at RESI are summarized in Table 8.1.

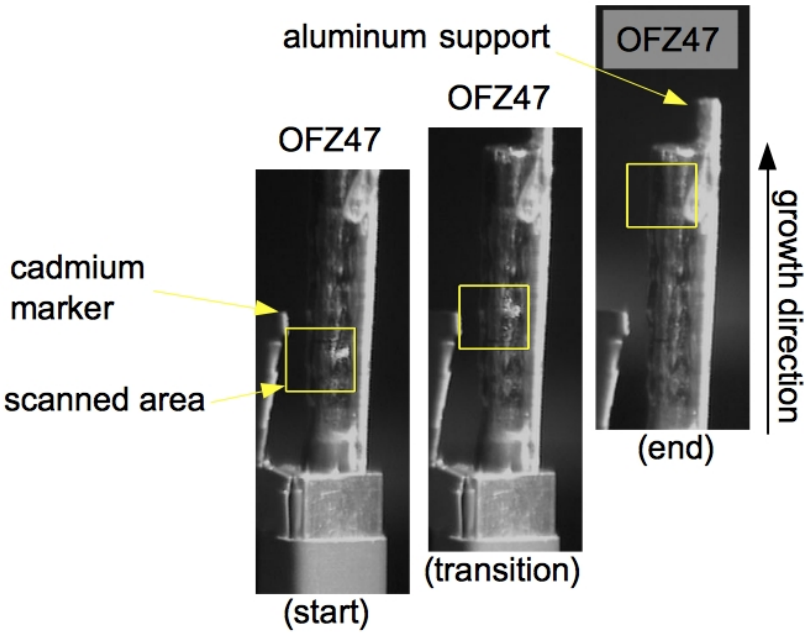

Figure 8.5: Images of crystal OFZ47 as investigated by single crystal neutron diffraction at RESI at FRM II. The samples were mounted as for the SANS measurements at MIRA. The top of the cadmium marker is located at the initial joining point of compositional difference. The yellow squares mark the areas that were scanned - before (start), at (transition), and well after (end) the initial joining point of compositional difference. OFZ47 broke during the preparation; the two parts were hold in position for the neutron measurements by a thin aluminum bar.

Scan Position	OFZ46	OFZ47	OFZ48
start	-	second grain (20 Vol.%)	second grain (5 Vol%)
transition	single crystal	second grain (20 Vol.%)	single crystal
end	single crystal	single crystal	single crystal

Table 8.1: Overview of single-crystallinity of crystals OFZ46, OFZ47 and OFZ48 as investigated by neutron diffraction at RESI. A description of the scan positions is given in Fig. 8.5.

8.2.2 EDX analysis

The compositions of all four gradient crystals were determined in a detailed EDX analysis in cooperation with Rainer Jungwirth using a SEM Zeiss EVO MA25 at the institute for radiochemistry of TUM. An illustration of the EDX measurements is shown in Fig. 8.6 for crystal OFZ47. The surface of the crystals was polished on one side. EDX area scans (yellow squares) were performed along the crystal as marked by the red crosses. In the vicinity of the initial joining point of composition A and B line-scans were performed in order to obtain a better spatial resolution. The relative accuracy of the EDX analysis is of the order of 1 %. Note that EDX is only surface sensitive and, hence, does not provide information on the compositional gradient perpendicular to the growth direction.

An overview of the position dependence of the composition (in atomic %) is given in Fig. 8.7 and Fig. 8.8 for $Mn_{1-x}Fe_xSi$ and $Fe_{1-x}Co_xSi$, respectively. The x-axis shows the distance Δz to the initial joining point of compositional difference. Δz increases along the growth direction. The vertical dashed lines mark the initial joining point at $\Delta z = 0$. The horizontal dashed lines indicate the theoretical starting compositions. For clearness error-bars are not shown.

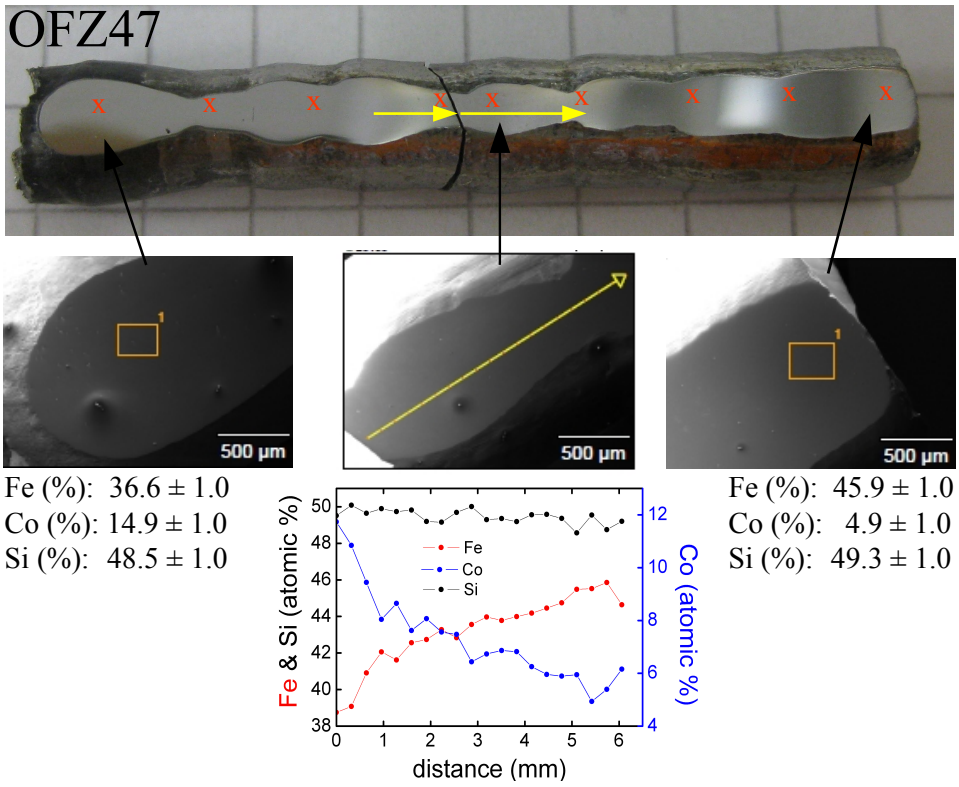

Figure 8.6: Illustration of the EDX measurements, shown for OFZ47. Area scans were recorded along the crystal at positions marked by the red x. At the initial joining point of compositional difference line-scans, indicated by the yellow arrows, were recorded, since they allow a better spatial resolution. The spacing of the measurement points during the line-sweeps was less than 0.5 mm.

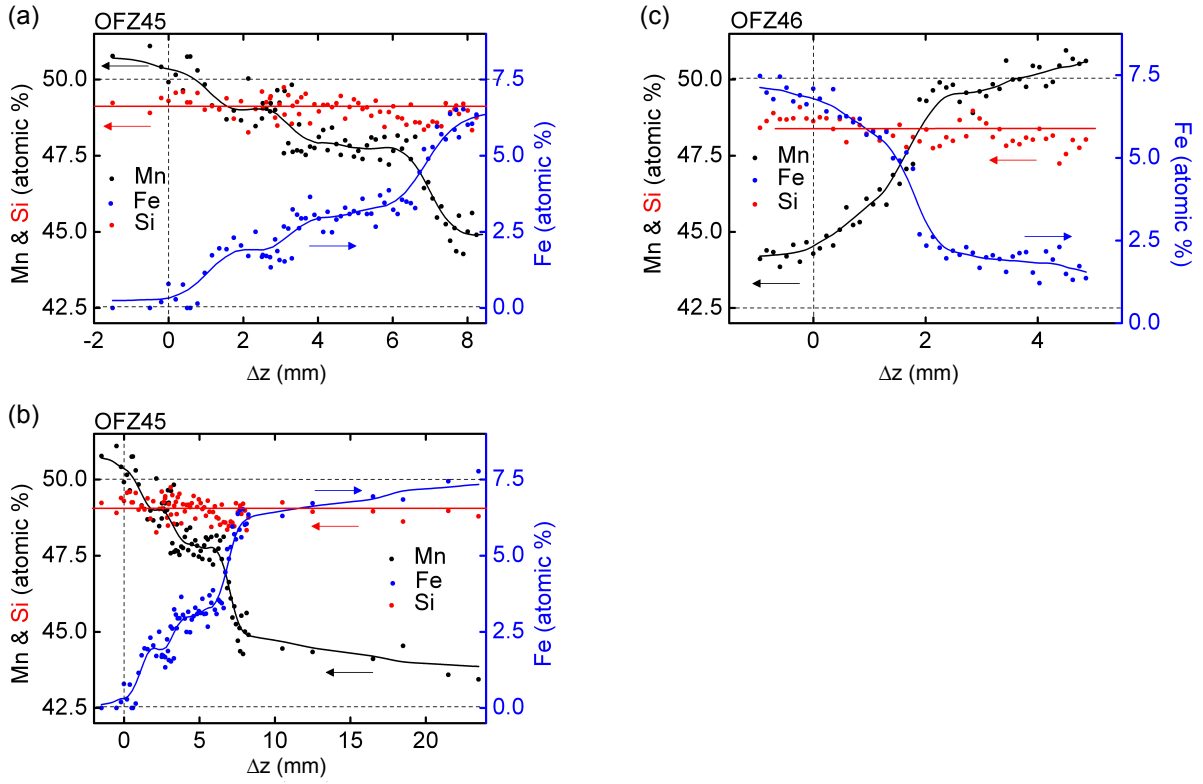

Figure 8.7: Composition of the $Mn_{1-x}Fe_xSi$ gradient crystals OFZ45 (a, b) and OFZ46 (c) as a function of the distance Δz from the initial joint of the starting rods, A and B, marked by the vertical dashed lines. The solid lines serve as a guide to the eye. Panel (a) shows the concentration dependence of OFZ45 at the transition, while panel (b) shows it over a larger distance. The main compositional transition in OFZ45 and OFZ46 takes place within ~ 8 mm and ~ 3 mm, respectively. The horizontal dashed lines indicate the expected initial compositions of rods A and B.

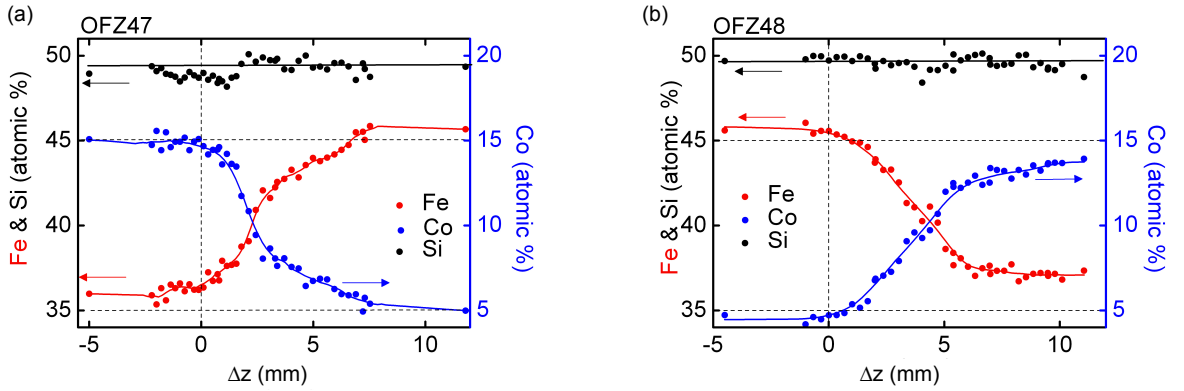

Figure 8.8: Composition of the $Fe_{1-x}Co_xSi$ gradient crystals OFZ47 (a) and OFZ48 (b) as a function of the distance Δz from the initial joint of the starting rods, A and B, marked by the vertical dashed lines. The horizontal dashed lines indicate the expected initial compositions of rods A and B. The solid lines serve as a guide to the eye. For both crystals the main compositional transition takes place within ~ 7 mm.

The position dependence of the composition of OFZ45 ($MnSi \rightarrow Mn_{0.85}Fe_{15}Si$) as determined by EDX analysis is shown in Figs. 8.7 (a) and (b). Initially a steep increase (decrease) with step like features of the Fe (Mn) composition is observed in the first 8 mm as shown in panel 8.7 (a). It is followed by a gradual increase, shown in panel 8.7 (b), for the next 15 mm. Crystal OFZ46 ($Mn_{0.85}Fe_{15}Si \rightarrow MnSi$), shown in panel 8.7 (c), displays an even steeper evolution of the composition with a step-like feature at $\Delta z = 2$ mm. The main transition of the composition takes place within ~ 3 mm. For OFZ46 no measurements further away from the initial interface were carried out. An analysis of the origin of the different transitions for both crystals is difficult. The height of the molten zone during the preparation of the joint feed rod as well as the duration of the melting process is assumed to play a decisive role. In addition, the exact growth parameters (e.g. height of molten zone) and, hence, the exact transport of matter during the passage of the gradient transition during single crystal growth are difficult to determine and control. A more systematic investigation would be necessary to comment on factors like the diffusion velocities of the Fe and Mn atoms.

Figs. 8.8 (a) and (b) show the distribution of the composition of OFZ47 ($Fe_{0.7}Co_{0.3}Si \rightarrow Fe_{0.9}Co_{0.1}Si$) and OFZ48 ($Fe_{0.9}Co_{0.1}Si \rightarrow Fe_{0.7}Co_{0.3}Si$), respectively. In OFZ47 the complete transition takes place within a distance of ~ 8 mm. In OFZ48 the main transition also takes place in the first 8 mm, but the final concentrations expected are not reached. This either might be due to a very smooth gradient or to a slight deviation of the final composition of the feed rod.

8.2.3 Polarized neutron scattering at MIRA

8.2.3.1 Experimental Setup

The chirality of the magnetic helix of the gradient crystals was investigated in collaboration with Tim Adams at the beamline MIRA1 at FRM II by means of a small angle neutron scattering set-up with polarized neutrons as illustrated in Fig. 8.9. The neutron beam was monochromatized ($\lambda = 9.7$ Å) and polarized by a supermirror polarisator. The initial spin direction of the polarized neutrons was parallel to the z-direction ($\mathbf{p}_z \| +z$, "up", red arrows) and could be flipped to anti-parallel ($\mathbf{p}_z \| -z$, "down") by a spin flipper positioned between the source and the sample aperture. The apertures were set to $5 \times 1\,mm^2$ (source) and $5 \times 0.5\,mm^2$ (sample), restricting the height of the beam to < 1 mm. The flight path of the neutrons before the sample went through a magnetic guide field conserving the spin direction.

The sample was mounted vertically in a cryostat (we used two different closed cycle cryostats with base temperatures of 450 mK and 3 K). A set of Helmholtz coils provided an external magnetic field along the z-direction. The temperature and the magnetic field were chosen such that the compounds were in the magnetically ordered conical state. This way, the wave vector $\mathbf{Q}$ of the helix was aligned in z-direction (anti-) parallel to the polarization $\pm\mathbf{p}_z$ of the neutrons. As described in the introduction (see section 1.2.3.3), this leads to a magnetic scattering vector $\pm\mathbf{q}_z$ depending on the handedness of the helix

and the polarization direction $\pm\mathbf{p}_z$ of the neutrons, i.e., $\mathbf{q}_z \| -\mathbf{p}_z$ for a right-handed helix and $\mathbf{q}_z \| +\mathbf{p}_z$ for a left-handed helix. The scattering intensities were recorded by an area detector at a distance L from the sample. The distance of the scattered intensity from the center is proportional to the scattering vector $|\mathbf{q}_z|$ and, hence, to the wave vector of the helix $|\mathbf{Q}| = |\mathbf{q}_z|$.

The cryostat and the Helmholtz coils were mounted on the same sample stage. For measurements along the gradient crystals the sample stage was moved along the z-direction. The growth direction corresponds to a positive z-direction. The beginning of the compositional gradient was marked by a piece of cadmium as shown in Fig. 8.5. In addition, the sample stage (and hence $\mathbf{Q}$) could be tilted by an angle ($\pm\Phi$) around the x-direction in order to rock through the Ewald sphere. Rocking the wave vector $\mathbf{Q}$ allowed us to account for changes of the magnetic mosaicity and the length of the wave vector, both of which depend on the composition. The rocking angles and stepwidth, as well as further experimental parameters of the measurements of each crystal, are summarized in Table 8.2.

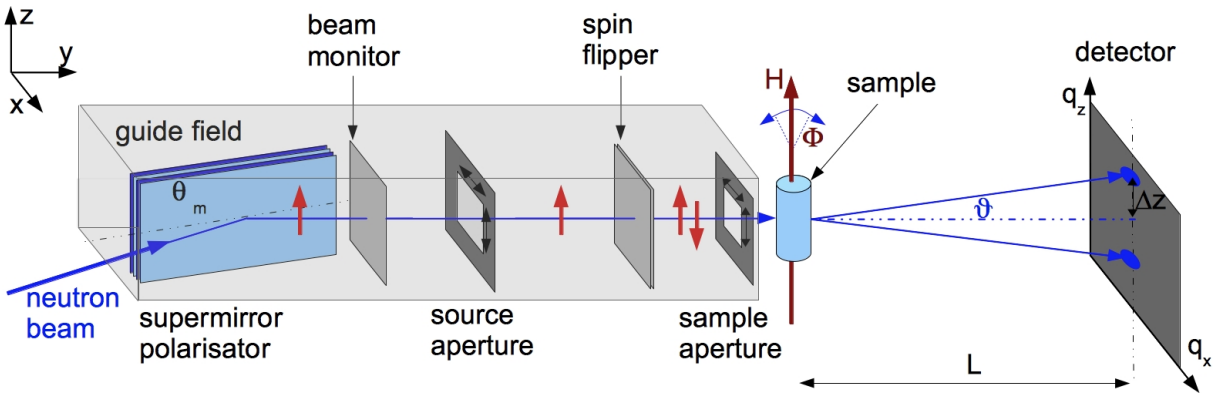

Figure 8.9: Illustration of the SANS set-up with polarized neutrons at MIRA1 as used for the investigation of the handedness of the helices in the gradient crystals. Scattering of the polarized neutrons ($\mathbf{p}$ along z) at the magnetic helix ($\mathbf{Q}$ along z) results in only one allowed scattering intensity $I(\mathbf{p}_z, \mathbf{q}_z)$ depending on the handedness of the helix.

	OFZ45	OFZ46	OFZ47	OFZ48
Temperature	450 mK	450 mK	3 K	3 K
External Field	110 mT	180 mT	5 mT	5 mT
Rocking Angle 2Φ	7° stepwidth: 0.5°	5° stepwidth: 0.5°	3° stepwidth: 0.75°	6° stepwidth: 1.0°
Measurement Time (polarized)	60 s	70 s	480 s	480 s

Table 8.2: Experimental parameters as generally applied during the polarized small angle neutron scattering measurements of the B20 gradient crystals at MIRA at FRM II.

8.2.3.2 $Fe_{1-x}Co_xSi$ gradient crystals

The $Fe_{1-x}Co_xSi$ gradient crystals were scanned at a temperature of 3 K and in an external field of 5 mT. In order to preserve the conical magnetic state, the crystals were field-cooled in an external field of 180 mT down to 3 K before reducing the field to 5 mT. For details of the phase diagram of $Fe_{1-x}Co_xSi$ see Ref. [95–97]. At each z-position measurements were taken for different rocking angles Φ of the sample stage, as given in Table 8.2. The magnetic mosaicity of the $Fe_{1-x}Co_xSi$ gradient crystals thereby permits large angular steps of the rocking scans. Scanning times for the $Fe_{1-x}Co_xSi$ gradient crystals were typically 480 seconds for measurements with polarized neutrons and half that time for unpolarized neutrons.

Fig. 8.10 shows a typical set of diffraction patterns from the z-scan of OFZ47. The left row shows measurements at the beginning of the crystal, i.e., for $Fe_{0.7}Co_{0.3}Si$. The middle row shows measurements at the initial joining point of compositional difference and the right row measurements at the end of the crystal, i.e., at a composition close to $Fe_{0.9}Co_{0.1}Si$. From top to bottom measurements with neutron polarization "up", with unpolarized neutrons, and with neutron polarization "down", i.e., spin-flipped neutrons with polarization in negative z-direction, are shown. The scattering intensities that are shown are the sum of the intensities over all rocking angles measured at that crystal position. The position of the scattering intensities is given in terms of the scattering vector $\mathbf{q}_z$.

The following conclusions can be drawn from the diffraction patterns shown in Fig. 8.10. While neutron diffraction with unpolarized neutrons leads to two diffraction spots as expected for the conical state, diffraction with polarized neutrons only results in one diffraction spot. The position of the diffraction spots, i.e., $+\mathbf{q}_z$ for positive spin polarization ($+\mathbf{p}_z$, "up"), and $-\mathbf{q}_z$ for negative spin polarization ($-\mathbf{p}_z$, "down"), identifies the magnetic helix to be left-handed for crystal OFZ47. We note that the weak diffraction spot at $+\mathbf{q}_z$ for spin "down" polarization (see Fig. 8.10 (g, h)) appears due to not spin-flipped neutrons. The flipping ratio of the spin flipper was measured to be around 14. In addition, the scattering vector $\mathbf{q}_z$ changes its length with changing composition, illustrating the composition dependence of the wave vector $\mathbf{Q}$ of the helix. From $Fe_{0.7}Co_{0.3}Si$ to $Fe_{0.9}Co_{0.1}Si$ the wave vector first increases and then decreases. We also find that the intensities of the diffraction spots for $Fe_{0.9}Co_{0.1}Si$ (OFZ47-end) are very weak, indicating small magnetic moments of the spin structure since the scattering cross section is proportional to the square of the spin moments (see Eq. (1.2)).

In order to quantify the handedness of the magnetic helix in all four gradient crystals we followed a routine introduced by Grigoriev *et al.* [100]. They used the difference of intensities obtained at the same $\mathbf{q}_z$ with different polarization $\pm\mathbf{p}_z$ normalized to their sum,

$$\gamma = \frac{I(+\mathbf{p}_z, \mathbf{q}_z) - I(-\mathbf{p}_z, \mathbf{q}_z)}{I(+\mathbf{p}_z, \mathbf{q}_z) + I(-\mathbf{p}_z, \mathbf{q}_z)}, \tag{8.1}$$

as a measure of the helix chirality γ. For our analysis we integrated the intensities at the upper diffraction spot ($+\mathbf{q}_z$), as indicated by the yellow boxes in Fig. 8.10. In addition, we subtracted the background signal I_{BG} and took the flipping ratio R of the spin flipper

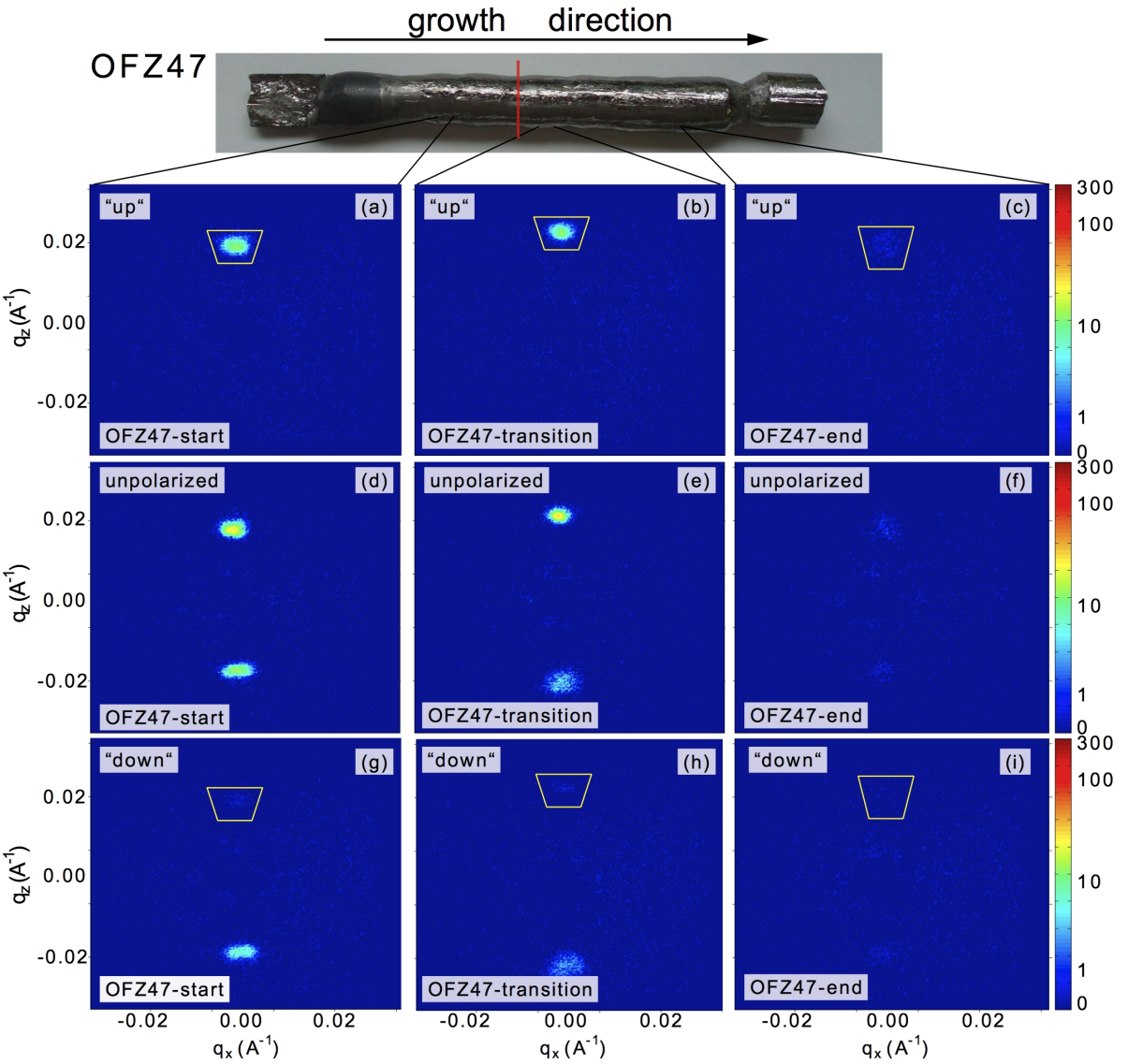

Figure 8.10: SANS measurements with polarized neutrons at the beamline MIRA1 of gradient crystal OFZ47. Measurements were taken at three positions of the gradient crystal with polarization in z-direction ("up", not spin-flipped), unpolarized neutrons and polarization opposite to the z-direction ("down", spin-flipped). Left row: measurements taken before the initial joining point of the rods, i.e., $Fe_{0.7}Co_{0.3}Si$; middle row: next to the initial joining point; right row: well after the initial joining point, i.e., a composition close to $Fe_{0.9}Co_{0.1}Si$. The scattering intensities are illustrated color-coded. With unpolarized neutrons (d, e, f) both intensity spots $\pm\mathbf{q}_z$ appear as expected for the conical state with the helix aligned in z-direction. With polarized neutrons scattering intensities appear only for $+\mathbf{q}_z \| +\mathbf{p}_z$ (top row) and $-\mathbf{q}_z \| -\mathbf{p}_z$ (bottom row), indicating a left-handed helix. The residual upper scattering intensity for "down" spin polarization is due to the not fully spin polarized neutron beam. The scattering vector $\mathbf{q}_z$ first increases (start to transition) and then decreases (transition to end). The absolute scattering intensities decrease along the crystal. The yellow squares illustrate the integrated areas for the determination of the helix chirality γ.

into account. This leads to the following expression to determine the chirality γ of the magnetic helix:

$$\gamma = \frac{I(+\mathbf{p}_z, +\mathbf{q}_z) - I(-\mathbf{p}_z, +\mathbf{q}_z) + \frac{I(+\mathbf{p}_z, +\mathbf{q}_z)}{R}}{I(+\mathbf{p}_z, +\mathbf{q}_z) + I(-\mathbf{p}_z, +\mathbf{q}_z) - 2I_{\mathrm{BG}} - \frac{I(+\mathbf{p}_z, +\mathbf{q}_z)}{R}} \tag{8.2}$$

$\gamma = 1$ accounts for left-handed chirality and $\gamma = -1$ for right-handed chirality.

Figs. 8.11 (a) and (b) show the intensities for both neutron polarizations along crystals OFZ47 and OFZ48. The x-axis shows the distance Δz to the initial joining point of compositional difference. As mentioned above, the scattering intensities are proportional to the square of the spin moments. However, since we optimized the integrated areas (yellow squares in Fig. 8.10) at each position Δz in order to account for the changing length of the wave vector and the changing mosaic spread, the intensities may not be used as a quantitative measure of the spin moments.

For crystal OFZ47 (Fig. 8.11 (a)) no scattering intensities were measured for the "down" polarization (red dots). The intensities that appear are solely due to the not spin flipped neutrons. For the "up" polarization (black dots) large scattering intensities are found at the beginning of the crystal. Consistent with the onset of the steep compositional transition the scattering intensities first increase up to a maximum around $\Delta z = 2\,\mathrm{mm}$ and then decrease strongly. This behavior illustrates the evolution of the size of the magnetic moments of $Fe_{1-x}Co_xSi$ as a function of the Co concentration. It is consistent with the literature [176]. For better statistics the measurement time for $\Delta z = 17\,\mathrm{mm}$ (surrounded by the green ellipse) was increased by a factor of four. Following Eq. (8.2) we determined the helix chirality γ of crystal OFZ47 as displayed in Fig. 8.11 (c) by the black data. Within the error bars, that strongly increase with decreasing intensities, a constant $\gamma \approx +1$ was obtained for crystal OFZ47, which clearly determines the helix to be left-handed along the entire crystal.

The scattering intensities for crystal OFZ48 are shown in Fig. 8.11 (b). Prior to $\Delta z = 0\,\mathrm{mm}$ very low scattering intensities are observed for both neutron polarizations. For a short distance, -3 mm $< \Delta z < 0$ mm, the scattering signal even disappeared completely. Only after the onset of the steep compositional transition the scattering intensity for the "up" polarization started to increase. This leads to a helix chirality as shown in Fig. 8.11 (c) by the red dots. For $\Delta z > 0\,\mathrm{mm}$ $\gamma \approx +1$ and the magnetic helix is clearly left-handed. However, for $\Delta z < 0\,\mathrm{mm}$, i.e., in pure $Fe_{0.9}Co_{0.1}Si$, a clear classification of the chirality is not possible. Starting at $\gamma \approx 0$ at the beginning of the crystal, γ seems to head towards a negative value before the scattering intensities disappear. The observation of $\gamma \approx 0$ might be explained by the observation of a second grain in crystal OFZ48 (see Table 8.1), that may have a helical order of opposite chirality. However, the volume fraction of the second grain was measured to be only around 5%. In addition, we do not have an explanation for the complete disappearance of the scattering intensity. Further studies are necessary to clarify the unusual properties of OFZ48.

As mentioned above, the length of the scattering vector $\mathbf{q}_z$ is a measure of the wave vector of the helix $|\mathbf{Q}|$. Figs. 8.12 (a) and (b) show the evolution of the scattering vector

along crystals OFZ47 and OFZ48, respectively. Comparison of the spatial dependence of $\mathbf{q}_z$ measured at MIRA with the spatial dependence of the Co-content obtained from the EDX analysis (see Fig. 8.8) allowed us to determine the composition dependence of $|\mathbf{Q}|$ as shown in Fig. 8.12 (c). With increasing Co content the wave vector increases strongly to a maximum $|\mathbf{Q}| = 0.02\,\text{Å}^{-1}$ at $x \approx 0.15$. Further increase of the Co composition leads to a gradual decrease of the wave vector. The composition dependence of $|\mathbf{Q}|$ we obtained for the gradient crystals OFZ47 and OFZ48 is qualitatively in good agreement with the data reported for single crystals with various compositions, reported in [100]. However, the maximum of the wave vector was reported to be around $x = 0.2$.

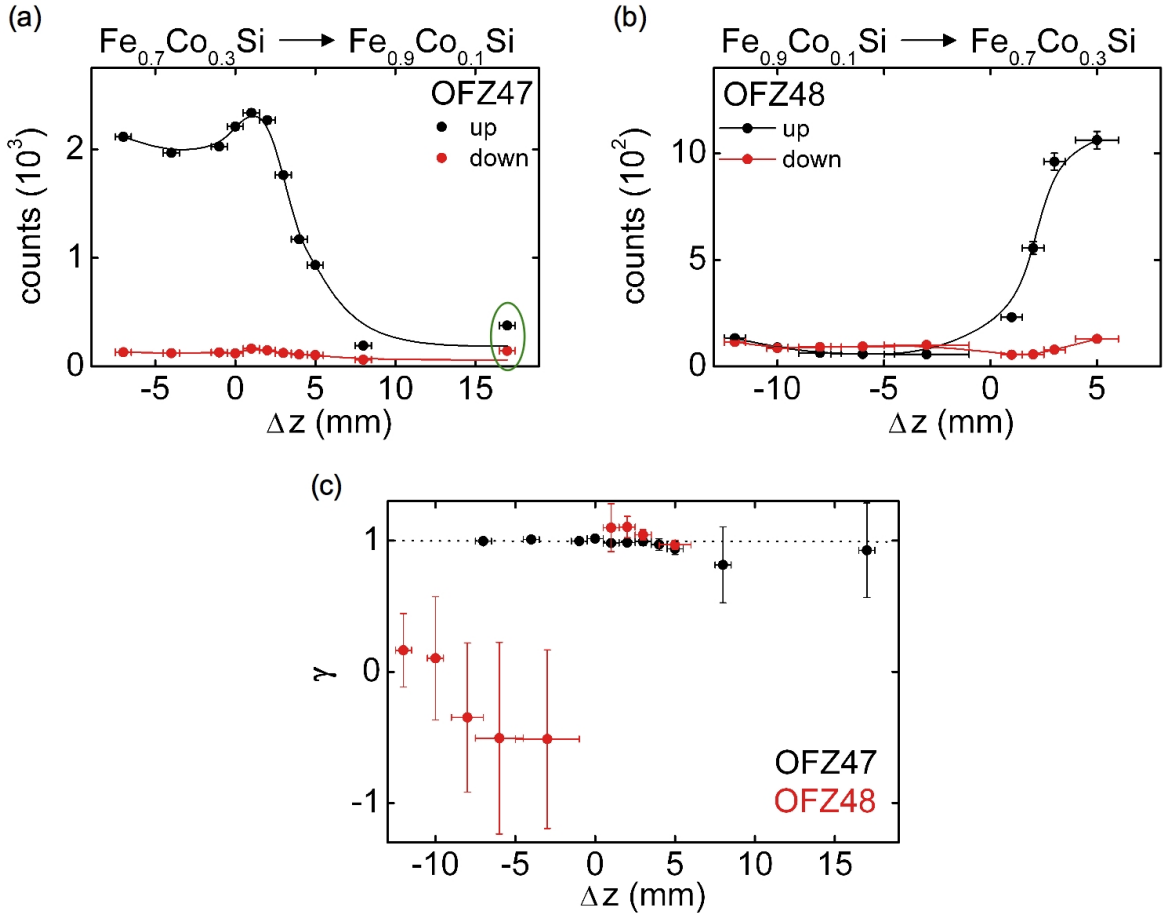

Figure 8.11: (a, b) Scattering intensities for "up" (black) and "down" (red) polarized neutrons measured at positive scattering vectors $+\mathbf{q}_z$ along OFZ47 and OFZ48. The x-axis shows the distance Δz to the initial joining point of compositional difference. The solid lines serve as a guide to the eye. (c) Helix chirality γ as de-termined with Eq. (8.2) from the scattering intensities shown in (a) and (b). For crystal OFZ47 (black data) $\gamma \approx +1$, determining the helix to be left-handed along the entire crystal. For crystal OFZ48 (red) the helix chirality is also left-handed for $\Delta z > 0\,\text{mm}$. However, for $\Delta z < 0\,\text{mm}$, i.e., in $Fe_{0.9}Co_{0.1}Si$, no clear identification of the chirality of OFZ48 is possible.

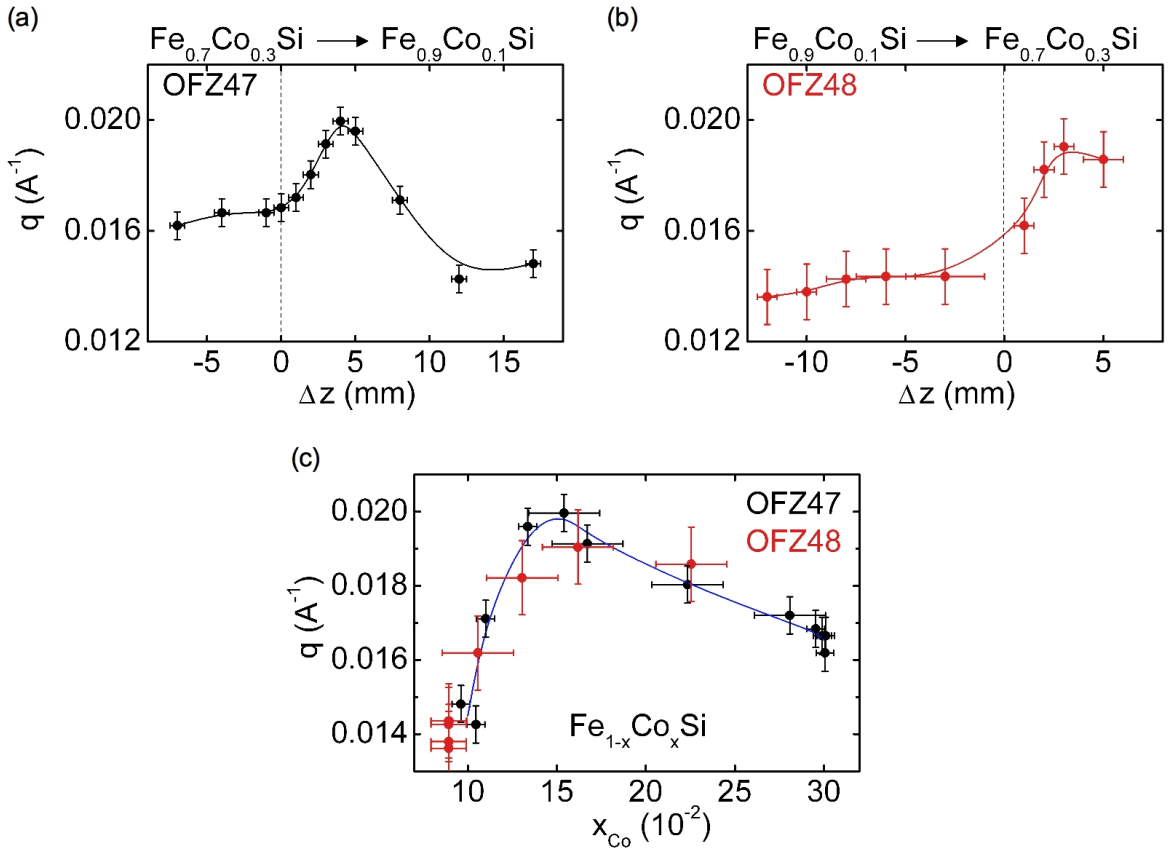

Figure 8.12: (a, b) Scattering vector as a function of the crystal position for gradient crystals OFZ47 and OFZ48. The x-axis shows the distance Δz to the initial joining point of compositional difference. (c) Scattering vector as a function of the Co-content derived from EDX analysis. With increasing Co content the scattering vector increases steeply. After the maximum around $x = 0.15$ a gradual decrease is observed. The solid lines serve as a guide to the eye.

8.2.3.3 $Mn_{1-x}Fe_xSi$ gradient crystals

The $Mn_{1-x}Fe_xSi$ gradient crystals were also investigated in the conical magnetic state. OFZ45 and OFZ46 were measured at a temperature of 450 mK and in external fields of 110 mT and 180 mT, respectively. For details on the phase diagrams of $Mn_{1-x}Fe_xSi$ see Ref. [78]. The measurements were carried out at very low temperatures, since the magnetic transition temperature in $Mn_{1-x}Fe_xSi$ decreases strongly with increasing Fe content as shown in Fig. 1.13. However, even at these low temperatures we did not detect scattering intensities for $x > 0.1$. The experimental parameters are summarized in Table 8.2.

The neutron scattering investigation of the $Mn_{1-x}Fe_xSi$ gradient crystals was carried out similar to the examination of the $Fe_{1-x}Co_xSi$ crystals as described above. Fig. 8.13 shows the sum of all scattering intensities measured along crystal OFZ45 with unpolarized neutrons. From this image it becomes clear that the scattering vectors change considerably, $0.035\,\text{Å}^{-1} < |\mathbf{q}_z| < 0.075\,\text{Å}^{-1}$, in the investigated range of composition. In addition, it shows that the scattering intensities decrease for large scattering vectors.

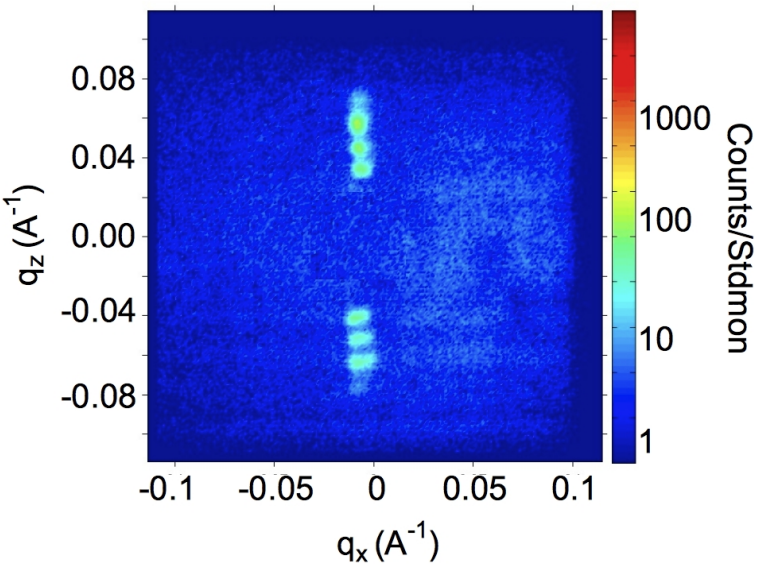

Figure 8.13: Sum of all scattering intensities measured along crystal OFZ45 with unpolarized neutrons. The increasing scattering vector $\mathbf{q}_z$ arises from a strong variation of the wave vector of the helix as a function of the composition. For large $\mathbf{q}_z$ the scattering intensities decrease.

Figs. 8.14 (a) and (b) show the scattering intensities for neutron polarization "up" (black) and "down" (red) measured along crystals OFZ45 and OFZ46, respectively. For crystal OFZ45 pronounced scattering intensities are found for polarization "up", while no intensities appear for polarization "down". In contrast, for crystal OFZ46 scattering intensities are measured for neutrons with polarization "down", while no intensities appear for polarization "up". Along crystal OFZ45 the scattering intensities decrease and disappear around $\Delta z = 7\,\mathrm{mm}$, as indicated by the dashed green line. As shown in Fig 8.15 (c), this corresponds to a Fe-doping of $x = 0.1$. This is consistent with crystal OFZ46, where scattering intensities appear at $\Delta z = 2.5\,\mathrm{mm}$, which also corresponds to a Fe-content close to $x = 0.1$. The scattering intensities illustrate the evolution of the size of the magnetic moments in $Mn_{1-x}Fe_xSi$ as a function of Fe composition as reported in Ref. [78]. The scattering intensities in Fig. 8.14 (a) that are surrounded by the green line indicate two intensities at different $\mathbf{q}_z$ that appeared simultaneously. Each diffraction spot was analyzed individually, which results in the reduced intensity for each spot taken by itself. The origin of the reduced scattering intensity at position $\Delta z = 8.5\,\mathrm{mm}$ in crystal OFZ46 (see Fig. 8.14 (b), green circle) is unclear.

Following Eq. (8.2), we determined the helix chirality γ for both OFZ45 and OFZ46, as shown in Fig. 8.14 (c) by the black and red data, respectively. For crystal OFZ45 $\gamma \approx 1$, which refers to a left-handed magnetic helix, while for crystal OFZ46 $\gamma \approx -1$, which refers to a right-handed helix. This indicates that the chirality of the magnetic helix of the starting compound, i.e., in our case left-handed for MnSi and right-handed for $Mn_{0.85}Fe_{0.15}Si$, is preserved along the compositional gradient and does not change at a critical composition. Hence, the chirality of MnSi at the beginning of OFZ45 is left-handed, while the chirality of MnSi at the end of OFZ46 is right-handed.

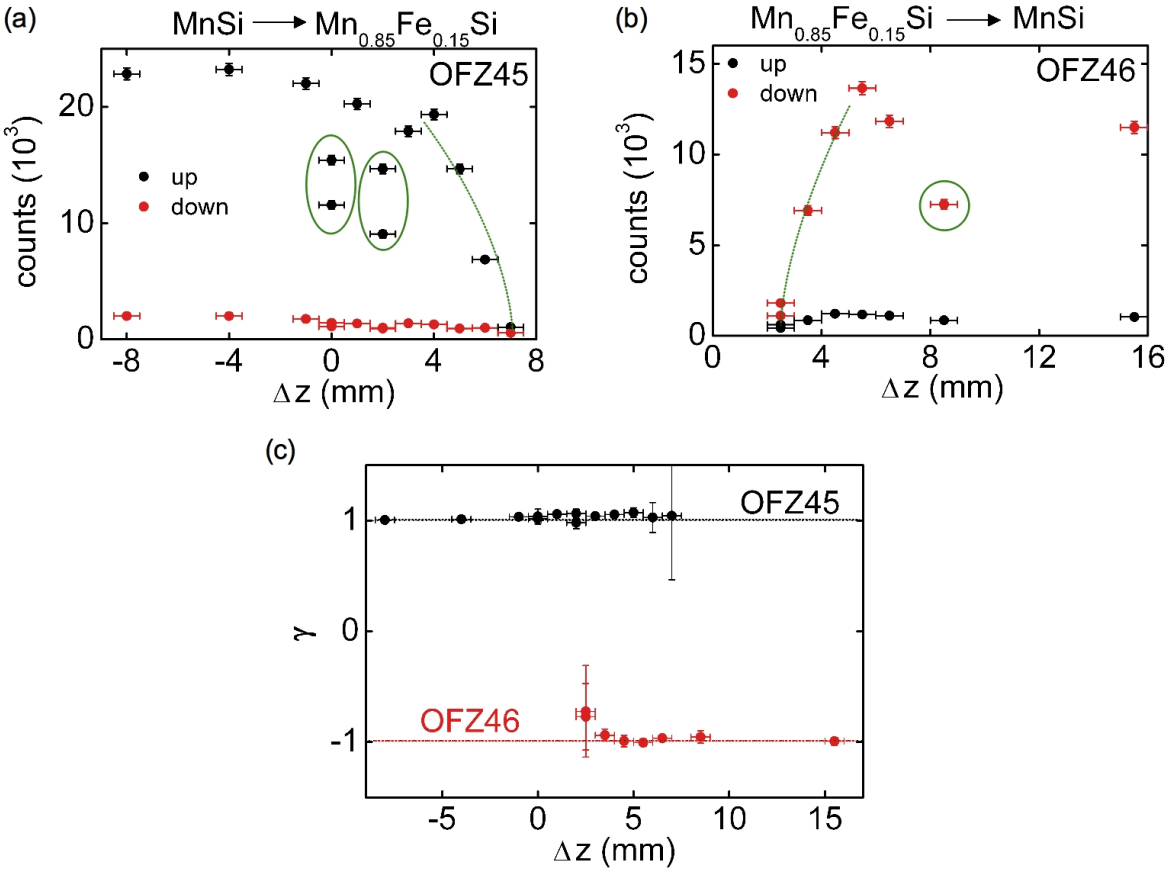

Figure 8.14: (a, b) Scattering intensities for "up" (black) and "down" (red) polarized neutrons measured at positive scattering vectors $+\mathbf{q}_z$ along the $Mn_{1-x}Fe_xSi$ gradient crystals OFZ45 and OFZ46. The x-axis shows the distance Δz to the initial joining point of compositional difference. The dashed green lines serve as a guide to the eye. The reduced scattering intensities surrounded by the green ellipse in (a) result from a simultaneous appearance of two intensities at different $\mathbf{q}_z$ that were analyzed individually. The origin of the reduced scattering intensity surrounded by the green line in (b) is unclear. (c) Helix chirality γ as determined, following Eq. (8.2), from the scattering intensities shown in (a) and (b). For crystal OFZ45 $\gamma \approx +1$, identifying the helix to be left-handed. For crystal OFZ46 $\gamma \approx -1$, identifying the helix to be right-handed.

The evolution of the scattering vector in OFZ45 and OFZ46 is shown in Figs. 8.15 (a) and (b), respectively. For crystal OFZ45 the spatial $\mathbf{q}_z$-dependence corresponds very well with the spatial composition dependence measured with EDX (see Fig. 8.7 (a)). Also for crystal OFZ46 the onset of magnetic scattering with two different scattering vectors $\mathbf{q}_z$ at $\Delta z = 2.5\,\mathrm{mm}$ corresponds very well with the step in the Fe content seen in EDX (see Fig. 8.7 (b)). We were hence able to combine both measurements and derive the composition dependence of the wave vector in $Mn_{1-x}Fe_xSi$ as shown in Fig. 8.15 (c). The black and red data correspond to OFZ45 and OFZ46, respectively. The scattering vector increases linearly with increasing Fe-content. This linear behavior is consistent with data for single crystals as indicated by the blue line [96]. In this study three $Mn_{1-x}Fe_xSi$ single crystals with nominal composition $x = 0.04, 0.08, 0.12$ were investigated.

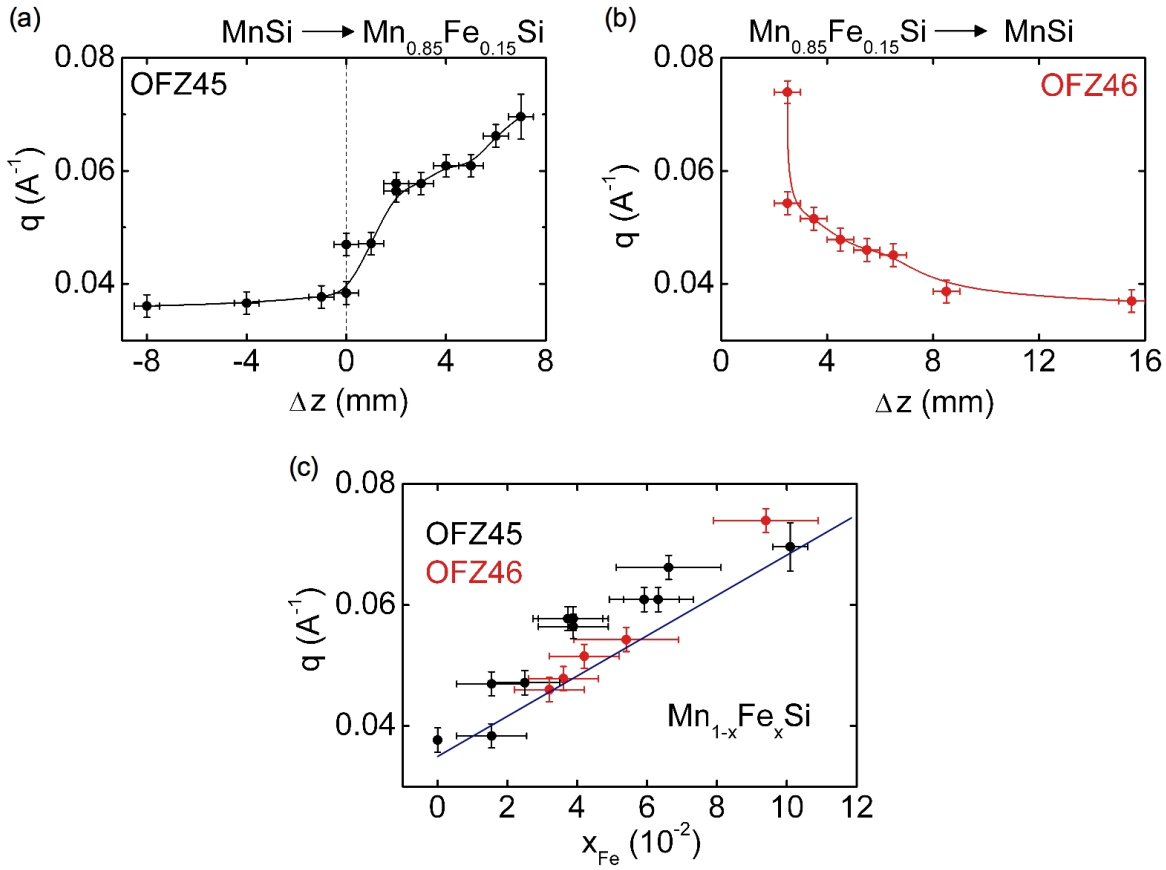

Figure 8.15: (a, b) Scattering vector $\mathbf{q}_z$ as a function of the crystal position for OFZ45 and OFZ46. The x-axis shows the distance Δz to the initial joining point of compositional difference. The solid lines serve as a guide to the eye. (c) Scattering vector $\mathbf{q}_z$ as a function of the Fe-content as derived from EDX analysis. With increasing Fe content the wave vector of the helix increases linearly. It is consistent with data for single crystals as indicated by the blue line [96].

8.3 Discussion

The investigation of the chirality of the helical order in $Mn_{1-x}Fe_xSi$ and $Fe_{1-x}Co_xSi$ was motivated by two papers published by Grigoriev *et al.* [100, 101]. In these publications they report that the chirality of the magnetic helix in $Mn_{1-x}Fe_xSi$ and $Fe_{1-x}Co_xSi$ depends on the composition. The observation of such a symmetry breaking would be of great general importance for many disciplines in the natural sciences, since two enantiomers should generally always exist with equal probability. Up to now no spontaneous symmetry breaking is established that would account for the observation of homochirality in inorganic chemistry. Therefore we wanted to reexamine the observation reported by Grigoriev *et al.*. Furthermore we note that, from statistical considerations, the total number of $Mn_{1-x}Fe_xSi$ and $Fe_{1-x}Co_xSi$ crystals whose chirality was investigated [100, 101, 104, 107] is too low to support any conclusive statements about the handedness of the chirality. In the case of pure MnSi, the most intensively studied compound, the total number of crystals investigated is, to the best of our knowledge, no more than 10.

Irrespective of the statistical argument, there are a number of possibilities known so far that may affect the chirality of the B20 compounds. Examples are: (i) The crystal structure of the B20 compounds is not entirely understood. The existence of superstructures, cf. complex metallic alloys, may have a strong influence on the handedness of the helical order. (ii) Interactions of the crystal structure with the environment during crystal growth, e.g., direction of rotation, temperature gradients, or contact to crucible, may cause a preferred handedness of the chirality. These interactions would be independent of spontaneous crystallization. Only from those two examples it is obviously difficult to clearly assign the origin of possible symmetry breaking in the B20 compounds to intrinsic or extrinsic reasons. Since from theory no intrinsic spontaneous symmetry breaking is expected, we believe that the origin of the observation of a preferred composition dependent handedness in $Mn_{1-x}Fe_xSi$ and $Fe_{1-x}Co_xSi$ is subtle and extrinsic.

In our investigation we attempted to minimize any extrinsic interactions that may arise from crystal growth. We used the vertical floating zone technique as a crucible free method and applied similar growth parameters, e.g., direction of rotation and growth velocity, for all crystals. The nucleation of different grains at the steep compositional gradient was avoided by starting the growth with a seed and feed with the same composition.

For $Mn_{1-x}Fe_xSi$ we observed only one chirality of the magnetic helix in each gradient crystal OFZ45 and OFZ46. Due to the decreasing scattering intensity with increasing Fe content we could not measure the chirality when crossing the critical composition $x = 0.12$ [101]. Nevertheless, from the observation of a left- and right-handed chirality for OFZ45 and OFZ46, respectively, we speculate that no spontaneous symmetry breaking occurred when crossing the critical concentration. From the existence of both left- and right-handed chirality in pure MnSi we hence conclude that the handedness of the chiral magnetic order in $Mn_{1-x}Fe_xSi$ does not intrinsically depend on the composition.

However, starting with MnSi in OFZ45 and $Mn_{0.85}Fe_{0.15}Si$ in OFZ46 we found a left-handed and, respectively, right-handed chirality for each crystal. This is consistent with the composition dependent trend in favor of a specific chirality as reported by Grigoriev *et al.* [101]. This observation might be pure coincidence. Nevertheless, we can not exclude that there exists a subtle extrinsic effect that promotes, depending on the composition, a specific handedness of the magnetic helix at the beginning of the growth. Assuming such an extrinsic effect, the floating zone growth of gradient crystals would allow us to grow $Mn_{1-x}Fe_xSi$ crystals with a predefined chirality.

In the case of $Fe_{1-x}Co_xSi$ we observed a left-handed chirality for crystal OFZ47, that did not switch handedness when the critical composition $x = 0.2$ was crossed. We hence observed the same chirality for $Fe_{0.7}Co_{0.3}Si$ and $Fe_{0.9}Co_{0.1}Si$. This is in stark contrast to the claim of only left-handed ($x < 0.2$) and only right-handed ($x > 0.2$) helices in $Fe_{1-x}Co_xSi$ reported by Grigoriev *et al.* [100]. In addition, we note that the left-handed chirality of crystal OFZ47, for which the crystal growth was started from $Fe_{0.7}Co_{0.3}Si$, is inconsistent with the right-handed chirality reported for $Fe_{1-x}Co_xSi$ with $x > 0.2$ [100, 104].

For crystal OFZ48 the situation is more complicated. Examining γ as a function of Δz (see Fig. 8.11 (c)), it seems that the chirality switches its handedness. This change of

handedness does not coincide with the critical composition, though. Taking into account that the scattering intensity disappeared prior to the jump of γ and that it was extremely weak in the beginning of the crystal, we note that OFZ48 displays unusual behavior. The properties of OFZ48 are especially strange in comparison to its counterpart OFZ47, where clear scattering intensities were obtained along the entire crystal. Hence, further studies on OFZ48 are needed to clarify this issue.

8.4 Summary and Outlook

Vertical float-zoning with an image furnace is an excellent method for the crystal growth of silicon based B20 compounds, as confirmed by the large number of high quality MnSi, $Mn_{1-x}Fe_xSi$, $Mn_{1-x}Co_xSi$, and $Fe_{1-x}Co_xSi$ single crystals that were grown as part of this thesis and as part of the diploma theses of Wolfgang Münzer [95] and Andreas Bauer [98].

As part of this thesis we extended our crystal growth expertise through the growth of four crystals with a given gradient of the composition, that was implemented during crystal growth with the image furnace:

- $MnSi \rightarrow Mn_{0.85}Fe_{0.15}Si$ (OFZ45)
- $Mn_{0.85}Fe_{0.15}Si \rightarrow MnSi$ (OFZ46)
- $Fe_{0.7}Co_{0.3}Si \rightarrow Fe_{0.9}Co_{0.1}Si$ (OFZ47)
- $Fe_{0.9}Co_{0.1}Si \rightarrow Fe_{0.7}Co_{0.3}Si$ (OFZ48)

Single-crystallinity of the four gradient crystals was confirmed by means of X-ray Laue diffraction and single crystal neutron diffraction at RESI at FRM II. EDX analysis showed that for all crystals the strongest compositional variation took place within less than 8 mm, a distance comparable to the height of the zone.

Small angle neutron scattering with polarized neutrons identified a left-handed chirality of the magnetic order along OFZ45 and OFZ47, while a right-handed chirality was found for OFZ46. The handedness of the chirality did not change with changing composition. From these observations we conclude that the handedness of the chiral magnetic order in $Mn_{1-x}Fe_xSi$ and $Fe_{1-x}Co_xSi$ does not depend on the composition and no spontaneous symmetry breaking occurs. Nevertheless, we speculate that there exists a subtle extrinsic effect that promotes a composition dependent handedness of the magnetic helix in $Mn_{1-x}Fe_xSi$ crystals at the beginning of the growth. Assuming such an extrinsic effect, the float-zoning growth of gradient crystals allows us to prepare $Mn_{1-x}Fe_xSi$ crystals with a predefined chirality in the future.

To confirm the relationship between the atomic and magnetic chirality in our gradient crystals assumed in the interpretation an investigation of the crystalline chirality with synchrotron X-ray radiation is necessary. Finally, a detailed examination of the crystal structure of OFZ48 is needed in order to investigate the origin of the unusual low scattering intensities as well as its disappearance prior to the compositional gradient.

Chapter 9

Conclusions

This thesis concerned the development of optical float-zoning under ultrahigh vacuum (UHV) compatible conditions of intermetallic compounds, followed by single crystal growth of selected systems as well as in-depth studies of the physical properties. For the preparation of the starting rods for the float-zoning growth an induction heated rod casting furnace (RCF) was constructed and set up employing cold crucibles. Both the OFZ and the RCF were optimized in the pursuit of highest purity. The optimization towards high purity was found to promote stable growth conditions and, hence, allowed to grow a number of large single crystals of highest purity.

Single crystal growth of twelve intermetallic compounds with different equilibrium phase diagrams was attempted, comprising congruently and incongruently melting systems with narrow and wide homogeneity ranges. For seven of the twelve systems large single crystals were grown. The properties of the Heusler compounds Cu_2MnAl, Mn_3Si, and Fe_2TiSn, the C14 Laves phase $NbFe_2$, and gradient crystals of the B20 compounds $Mn_{1-x}Fe_xSi$ and $Fe_{1-x}Co_xSi$, were investigated in detail. The main results may be summarized as follows.

Cu_2MnAl

Large single crystals were grown of Cu_2MnAl, a compound used for polarizing neutron monochromators. These single crystals showed an isotropic structural mosaic spread, as determined by neutron diffraction of the $\langle 400 \rangle$ and $\langle 111 \rangle$ Bragg intensities. Thus crystal growth with the image furnace avoids the main drawback of Bridgman grown Cu_2MnAl crystals, where the mosaic spread depends strongly on the growth direction [23]. The high purity static inert gas environment in the OFZ was thereby found to be indispensable to reduce oxide forming on the molten zone. This resulted in stable crystal growth.

A study of the polarizing properties in neutron scattering established a low polarization efficiency around 80% for our float-zoned Cu_2MnAl single crystals. However, this low value was found to be due to the small sample dimensions and could be raised to 91% in an assembly of four crystals. For float-zoned single crystals with larger sample dimensions we expect a polarization efficiency around 97%, similar to the polarization efficiency of

the best Bridgman grown crystals. Hence growth of Cu_2MnAl single crystals by vertical float-zoning may be used for a very efficient production of high quality monochromators of polarized neutrons.

Mn_3Si

The Heusler compound Mn_3Si displays itinerant antiferromagnetism below $T_N = 23.5\,K$. Three large single crystals of Mn_3Si were grown by means of "self-flux" vertical traveling solvent zone crystal growth, since Mn_3Si is incongruently melting. The crystals showed excellent single-crystalline properties as inferred from a very narrow structural mosaic spread of $\sim 0.3°$ measured, e.g., for crystal OFZ7. No secondary phases were detected by means of EDX-analysis in single-crystalline samples.

A study of the low temperature properties confirmed the unusual stability of the antiferromagnetic order under large magnetic fields, reported previously for polycrystals [15, 31–33]. Preliminary neutron scattering experiments using neutron focussing guides confirmed the antiferromagnetic order below T_N with $\mathbf{Q} = 0.425 \cdot \mathbf{G}_{111}$. In addition, a tiny additional signal in the magnetization for temperatures below 60 K was observed that shows antiferromagnetic features with a metamagnetic transition at small fields. The nature of this tiny, sample dependent contribution could not be attributed unambiguously to either an intrinsic form of magnetic order or to a small volume fraction of a secondary phase.

Fe_2TiSn

Polycrystals of the Heusler compound Fe_2TiSn have attracted interest as a paramagnetic compound that displays weak ferromagnetism and Kondo correlations due to atomic site disorder [34–37, 40]. As part of this thesis large single crystals of the Heusler compound Fe_2TiSn were grown for the first time. In contrast to previous work [34], the phase-pure float-zoned single crystals do not show a ferromagnetic transition at 250 K. In fact, this ferromagnetic transition may be attributed to the presence of a $Fe_{67}Ti_{25}Sn_8$ impurity phase that primarily forms at grain boundaries.

Moreover, phase-pure Fe_2TiSn single crystals display a number of remarkable features. (i) The vicinity to a putative quantum critical point without need for tuning by an external control parameter. The quantum critical behavior at the border to magnetism observed in the inverse AC - susceptibility, the magnetization, and the specific heat suggests an analogy of Fe_2TiSn with other weak itinerant-electron ferromagnets in the vicinity of a quantum critical point. The resistivity of Fe_2TiSn, however, contrasts this observation and shows a semiconductor-like increase at low temperatures. (ii) An unusual sample dependence of the physical properties of phase-pure single crystal Fe_2TiSn. As the origin of this sample dependence we ruled out impurity phases and proposed structural disorder instead. This would be consistent with split-site disorder of the Fe and Ti atoms as inferred from refinement of synchrotron X-ray powder diffraction data. (iii) The anomaly in the Hall effect under pressure accompanied by an increase of the longitudinal resistivity, which suggest that Fe_2TiSn is a marginal topological insulator.

$NbFe_2$

The C14 Laves phase $Nb_{1-y}Fe_{2+y}$ attracts great interest as a compound that displays ferromagnetic quantum criticality masked by a spin density wave order (SDW) and accompanied by marginal Fermi liquid behavior. Large high quality single crystals of $Nb_{1-y}Fe_{2+y}$ with various compositions were grown for the first time, allowing the investigation of the quantum critical behavior in single crystals. The main results are:

(i) The composition dependent magnetic phase diagram of single crystals seems to follow that obtained for poly-crystalline samples. The ferromagnetic phase shows a quadratic composition dependence (cf. Fig. 7.11), in contrast to the linear dependence reported previously (cf. Fig. 7.2) [60].

(ii) At low temperatures a logarithmic temperature dependence of the specific heat (C/T) as well as a $\rho \propto T^{1.5}$ dependence of the resistivity was observed for OFZ11-2, a crystal close to stoichiometry.

(iii) The strongly anisotropic behavior of the magnetically ordered state observed in $Nb_{1-y}Fe_{2+y}$ single crystals allowed to expand the schematic magnetic phase diagram from 2D to 3D (cf. Fig. 7.22). For B parallel c, the easy axis, the transition changes from first to second order with increasing temperature. The absence of a first order transition for B parallel a suggests the existence of a critical angle of the suppression of the first order transition, i.e., an angle dependent quantum critical point.

(iv) No signs of magnetic order of the SDW state were observed in preliminary neutron diffraction experiments on single crystal OFZ11-2.

Gradient crystals of the B20 compounds $Mn_{1-x}Fe_xSi$ and $Fe_{1-x}Co_xSi$

Recent studies have claimed the absence of crystalline stereoisomers in the B20 compounds $Mn_{1-x}Fe_xSi$ and $Fe_{1-x}Co_xSi$, depending on the composition x [100, 101]. Several single crystals of these compounds were grown with steep compositional gradients as part of this thesis. Based on the chirality of the magnetic helix in these gradient crystals (OFZ45 - OFZ47) both a left- or right-handed crystalline chirality could be stabilized along each crystal. That is, the handedness of the chiral magnetic order did not change with change of composition. A composition dependent spontaneous symmetry breaking of the structural chirality proposed by Grigoriev *et al.* [100, 101] seems therefore extremely unlikely. However, there may be subtle extrinsic effects that promote a composition dependent handedness of the magnetic helix in $Mn_{1-x}Fe_xSi$ crystals at the beginning of the growth. Assuming such extrinsic effects, the float-zoning growth of single crystals with a gradient of the composition implemented during crystal growth would allow to prepare $Mn_{1-x}Fe_xSi$ crystals with a predefined chirality.

Chapter 10

Acknowledgements

This work would certainly not have been possible without the assistance of a number of colleagues and friends. I am deeply grateful for the time and effort these people spent in order to support the progress of this thesis in one way or another. In particular I want to thank:

Prof. Christian Pfleiderer for giving me the opportunity to work on this interesting topic in his group and for supervising this thesis. Thank you very much for all the fruitful discussions, your motivation and guidance, as well as your great support in all fields during the last years. To keep it short, it was great to work together with you.

Prof. Peter Böni for the interesting discussions about neutron scattering, in particular with respect to the polarization analysis of Cu_2MnAl and the gradient crystals. Thanks for the Cu_2MnAl crystals you provided that permitted an early start with the crystal growth experiments.

Barbara Russ for her assistance in setting up the crystal laboratory and getting started with crystal growth. Thank you for all the nice discussions we had beyond physics, for the food delivery that kept me from starving in front of the image furnace and, of course, for your car.

The late **Dr. Günter Behr** for the hands-on introduction to crystal growth with an image furnace at the IFW in Dresden and for the support in setting up the rod casting furnace. For all questions in respect of crystal growth he and his group, in particular **Dr. Nadja Wizent** and **Dr. Anke Köhler**, always had a good advice. Further, I am grateful for the detailed EDX analyses that were carried out at the IFW.

Dr. Andreas Erb for sharing his experience in crystal growth and for proofreading the "Basics of crystal growth" section of this thesis. Further I want to thank **Susanne Meyr**, **Katarzyna Danielewicz**, **Claudia Schweiger**, **Michael Stanger** from the crystal laboratory for the precise and fast preparation of the crystals as well as our nice discussions.

Wolfgang Münzer for the great job he did improving the RCF as part of his diploma thesis. Thank you not only for your support in casting rods and growing crystals, but also

for the nice atmosphere you always managed to create. Sticking to the crystal growers, I also want to thank **Andreas Bauer** for his enormous support in the crystal laboratory, for the late nights in front of the image furnace, and for proofreading of this manuscript. It is good to know that our crystal lab is in good hands.

William Duncan for the successful collaboration on the $NbFe_2$ project and for providing all your data. Besides, it was very interesting to see a Scotsman perform at the Oktoberfest. I am also very grateful to **Dr. Malte Grosche** and **Dr. Manuel Brando** for the very helpful discussions about $NbFe_2$. Further, thanks to William and Manuel for proof-reading the $NbFe_2$ chapter of this thesis.

Dr. Anatoliy Senyshyn for performing the powder diffraction experiments on Fe_2TiSn as well as the Rietveld refinement. I am deeply grateful for the detailed analysis of the disorder phenomena and for the fruitful discussions we had about it. In addition, I want to thank **Dr. Klaudia Hradil** for performing the X-ray single crystal diffraction experiments on Fe_2TiSn as well as our discussions about crystallography.

Dr. Michael Schulz for the long hours we spent at the ANTARES beamline carrying out NDR experiments. I really appreciated the nice discussions about neutron scattering and everything. This way even weekend shifts can be enjoyable. Further I am grateful to **Phillipp Schmakat** who continued the NDR studies of $NbFe_2$ down to lowest temperatures.

Dr. Sergey Masalovich and the whole HELIOS group at FRM II for providing polarized ^3He for my experiments, even at weekends.

Tim Adams and **Florian Jonietz** for their support in the neutron scattering experiments on the gradient crystals and Cu_2MnAl at MIRA. Without your help I would still search for the neutrons.

Dr. Martin Meven, the instrument responsible of HEIDI, **Dr. Björn Pedersen**, the instrument responsible of RESI, and **Dr. Robert Georgii**, the instrument responsible of MIRA, for their support during my neutron scattering experiments and for the detailed discussion of the data.

Rainer Jungwirth for the hours he spent in front of the SEM at the institute for radio chemistry trying to record the best images and EDX data. And you managed!

Robert Ritz, **Christian Franz**, and **Alexander Regnat** for sharing their expertise on Bridgman pressure cells and their support with the *Sweet 16* system. Robert and Chris, I very much appreciated the online support from Rio.

Felicitas Birkelbach and **Max Hirschberger** for their support with the torque magnetization measurements, as well as **Martin Heimgreiter** for the installation of the electric spindle drive.

Andreas Mantwill as well as all the people from the **workshop** of the Physics department for their fast and accurate work. There was always a way to quickly build a part if it was urgently needed.

Stefan Giemsa for helping me out with complex Solid Works constructions and for his advice in any kind of technical problems.

Michael Wagner for quickly carrying out the latest resistivity and magnetization measurements on Fe_2TiSn.

The group of **Elisa Baggio-Saitovitch** at the CBPF in Rio de Janeiro for the warm welcome and the hospitality at their institute. The financial support from the PROBRAL program of the DAAD is gratefully acknowledged.

Dr. Stefan Legl, **Dr. Sebastian Mühlbauer**, and **Dr. Marc Janoschek**, quasi the old generation, for all the discussions, the good atmosphere, and the good time we had together at E21. In this respect I want to expand this appreciation to **all colleagues at E21**. I very much appreciated the friendly and helpful atmosphere in our group.

My family for supporting me during my whole life and for giving me the possibility to realize and follow my own ideas and dreams.

Sophia, who has always been there for me, especially during the last hard months of this work. Thanks for your love and understanding, for the motivation and for cheering me up, for everything - or just for being yourself!

Chapter 11

List of publications

1. Ultra-high vacuum compatible image furnace.
   A. Neubauer, J. Bœuf, A. Bauer, B. Russ, H. v. Löhneysen, and C. Pfleiderer.
   Reviews of Scientific Instruments, accepted for publication, 2010

2. Spin Transfer Torques at Ultralow Current Denities.
   F. Jonietz, S. Mühlbauer, C. Pfleiderer, A. Neubauer, W. Münzer, A. Bauer, T. Adams, R. Georgii, P. Böni, R. A. Duine, K. Everschor, M. Garst, and A. Rosch.
   Science, accepted subject to minor revisions, 2010.

3. Search for Electronic Phase Separation at Quantum Phase Transitions.
   C. Pfleiderer, P. Böni, C. Franz, T. Keller, A. Neubauer, P. Niklowitz, P. Schmakat, M. Schulz, Y.-K. Huang, J. Mydosh, M. Vojta, W. Duncan, F. M. Grosche, M. Brando, M. Deppe, C. Geibel, F. Steglich, A. Krimmel, and A. Loidl.
   Journal of Low Temperature Physics, **161**, 167, 2010.

4. Quantum Phase Transitions in Single-Crystal $Mn_{1-x}Fe_xSi$ and $Mn_{1-x}Co_xSi$: Crystal Growth, Magnetization, AC Susceptibility and Specific Heat.
   A. Bauer, A. Neubauer, C. Franz, W. Münzer, M. Garst, and C. Pfleiderer.
   Physical Review B, **82** (6), 064404, 2010.

5. Towards a Tomographic Reconstruction of Neutron Depolarization Data
   M. Schulz, A. Neubauer, S. Masalovich, M. Mühlbauer, E. Calzada, B. Schillinger, C. Pfleiderer, and P. Böni.
   Journal of Physics: Conference Series, **211**, 012025, 2010

6. Skyrmion lattices in metallic and semiconducting B20 transition metal compounds.
   C. Pfleiderer, T. Adams, A. Bauer, W. Biberacher, B. Binz, F. Birkelbach, P. Böni, C. Franz, R. Georgii, M. Janoschek, F. Jonietz, T. Keller, R. Ritz, S. Mühlbauer, W. Münzer, A. Neubauer, B. Pedersen, and A. Rosch.
   Journal of Physics-Condensed Matter, **22** (16), 164207, 2010.

7. Quantum phase transitions in $NbFe_2$ and $Ca_3Ru_2O_7$.
W. J. Duncan, O. P. Welzel, D. Moroni-Klementowicz, C. Albrecht, P. G. Niklowitz, D. Grner, M. Brando, A. Neubauer, C. Pfleiderer, N. Kikugawa, A. P. Mackenzie, and F. M. Grosche.
physica status solidi b, **247**, 544, 2010.

8. Magnetization of $Pd_{1-x}Ni_x$ near quantum criticality.
C. Franz, C. Pfleiderer, A. Neubauer, M. Schulz, B. Pedersen, and P. Bni.
Journal of Physics: Conference Series, **200**, 012036, 2010

9. Skyrmion Lattice Domains in $Fe_{1-x}Co_xSi$.
T. Adams, S. Mühlbauer, A. Neubauer, W. Münzer, F. Jonietz, R. Georgii, B. Pedersen, P. Böni, A. Rosch, and C Pfleiderer.
Journal of Physics: Conference Series, **200**(3), 032001, 2010.

10. Polarized neutron radiography with a periscope.
M. Schulz, A. Neubauer, M. Mühlbauer, E. Calzada, B. Schillinger, C. Pfleiderer, and P. Böni.
Journal of Physics: Conference Series, **200** (11), 112009, 2010.

11. Skyrmion lattice in the doped semiconductor $Fe_{1-x}Co_xSi$.
W. Münzer, A. Neubauer, T. Adams, S. Mühlbauer, C. Franz, F. Jonietz, R. Georgii, P. Böni, B. Pedersen, M. Schmidt, A. Rosch, and C. Pfleiderer.
Physical Review B, **81** (4), 041203, 2010.

12. Pressure dependence of the magnetization in Pr_5Si_3.
S. Legl, C. Franz, A. Neubauer, C. Pfleiderer, D. Souptel, and G. Behr.
PHYSICA B-CONDENSED MATTER, **404** (19), 2887, 2009.

13. Hall effect and magnetoresistance in MnSi.
A. Neubauer, C. Pfleiderer, R. Ritz, P. G. Niklowitz, and P. Böni.
PHYSICA B-CONDENSED MATTER, **404** (19), 3163, 2009.

14. Quantum order in the chiral magnet MnSi.
C. Pfleiderer, A. Neubauer, S. Mühlbauer, F. Jonietz, M. Janoschek, S. Legl, R. Ritz, W. Münzer, C. Franz, P. G. Niklowitz, T. Keller, R. Georgii, P. Böni, B. Binz, and A. Rosch.
Journal of Physics-Condensed Matter, **21** (27), 164215, 2009.

15. Topological Hall Effect in the A Phase of MnSi.
A. Neubauer, C. Pfleiderer, B. Binz, A. Rosch, R. Ritz, P. G. Niklowitz, and P. Böni.
Physical Review Letters, **102** (18), 186602, 2009.

16. Skyrmion Lattice in a Chiral Magnet.
S. Mühlbauer, B. Binz, F. Jonietz, C. Pfleiderer, A. Rosch, A. Neubauer, R. Georgii, and P. Boni.
Science, **323** (5916), 915, 2009.

17. A polarizing neutron periscope for neutron imaging.
M. Schulz, P. Böni, E. Calzada, M. Mühlbauer, A. Neubauer, and B. Schillinger.
Nuclear Instruments and Methods in Physics Research Section A: Accelerators, Spectrometers, Detectors and Associated Equipment, **605** (1-2), 43, 2009.

Bibliography

[1] C. Pfleiderer. Superconducting phases of f - electron compounds. *Reviews of Modern Physics*, **81** (4), 1551, 2009.

[2] S. Mühlbauer, B. Binz, F. Jonietz, C. Pfleiderer, A. Rosch, A. Neubauer, R. Georgii, and P. Böni. Skyrmion lattice in a chiral magnet. *Science*, **323** (5916), 915, 2009.

[3] S. A. Grigera, P. Gegenwart, R. A. Borzi, F. Weickert, A. J. Schofield, R. S. Perry, T. Tayama, T. Sakakibara, Y. Maeno, A. G. Green, and A. P. Mackenzie. Disorder-sensitive phase formation linked to metamagnetic quantum criticality. *Science*, **306** (5699), 1154, 2004.

[4] H. v. Löhneysen, A. Rosch, M. Vojta, and P. Wölfle. Fermi-liquid instabilities at magnetic quantum phase transitions. *Reviews of Modern Physics*, **79** (3), 1015, 2007.

[5] F. Heusler. *Verhandlungen der Deutschen Physikalischen Gesellschaft* , **5**, 1903.

[6] Claudia Felser, personal communication, 2009.

[7] E. Şaşioglu. First-principle study of the exchange interactions and Curie temperature in Heusler alloys. Ph.D. thesis, Martin-Luther-Universität Halle-Wittenberg, 2005.

[8] C. Felser, G. Fecher, and B. Balke. Spintronics: A Challenge for Materials Science and Solid-State Chemistry. *Angewandte Chemie International Edition*, **46** (5), 668, 2007.

[9] A. N. Vasil'ev, V. D. Buchel'nikov, T. Takagi, V. V. Khovailo, and E. I. Estrin. Shape memory ferromagnets. *Physics-Uspekhi*, **46** (6), 559, 2003.

[10] C. Felser and B. Hillebrands. EDITORIAL: High spin polarization of Heusler alloys. *Journal of Physics D: Applied Physics*, **39**, 2006.

[11] C. Felser and B. Hillebrands. EDITORIAL: New materials with high spin polarization: half-metallic Heusler compounds. *Journal of Physics D: Applied Physics*, **40**, 2007.

[12] C. Felser and B. Hillebrands. EDITORIAL: Cluster issue on Heusler compounds and devices Cluster issue on Heusler compounds and devices. *Journal of Physics D Applied Physics*, **42** (8), 080301, 2009.

[13] L. Castelliz. *Zeitschrift für Metallkunde*, **46**, 198, 1955.

[14] T. Kanomata, K. Shirakawa, and T. Kaneko. Effect of hydrostatic pressure on the Curie temperature of the Heusler alloys Ni_2MnZ (Z = Al, Ga, In, Sn and Sb). *Journal of Magnetism and Magnetic Materials*, **65** (1), 76, 1987.

[15] J. Bœuf. Untersuchungen an den antiferromagnetischen Übergangsmetallverbindungen MnSi, CuMnSb und PdMnTe. Ph.D. thesis, Universität Karlsruhe, 2003.

[16] J. Bœuf, C. Pfleiderer, and A. Faißt. Low-temperature properties of the semi-Heusler compound CuMnSb. *Physical Review B*, **2**, 024428, 2006.

[17] C. Pfleiderer. Are Mn_3Si and CuMnSb antiferromagnetic half-metals? *Physica B: Condensed Matter*, **329-333**, 1085, 2003.

[18] W. Köster and T. Gödecke. Das Dreistoffsystem Kupfer-Mangan-Aluminium. *Zeitschrift für Metallkunde*, **57**, 889, 1966.

[19] B. Michelutti. Magnetization, magnetocrystalline anisotropy, magnetostriction and elastic constants of the Heusler alloy: Cu_2MnAl. *Solid State Communications*, **25**, 163, 1978.

[20] B. Dubois and D. Cheverau. Decomposition of the Heusler alloy Cu_2MnAl at 360°C. *Journal of Materials Science*, **14** (10), 2296, 1979.

[21] Y. Sakka and M. Nakamura. Mechanical and magnetic properties of the rapidly quenched Cu_2MnAl. *Journal of Materials Science*, **25**, 2549, 1990.

[22] R. Kainuma, N. Satoh, X. J. Liu, I. Ohnuma, and K. Ishida. Phase equilibria and Heusler phase stability in the Cu-rich portion of the Cu-Al-Mn system. *Journal of Alloys and Compounds*, **266** (1-2), 191, 1998.

[23] P. Courtois. Characterization of Heusler crystals for polarized neutrons monochromators. *Physica B: Condensed Matter*, **267-268**, 363, 1999.

[24] A. Freund, R. Pynn, W. Stirling, and C. Zeyen. Vertically focussing Heusler alloy monochromators for polarised Neutrons. *Physica B&C*, **120** (1-3), 86, 1983.

[25] P. Courtois, B. Hamelin, and K. H. Andersen. Production of copper and Heusler alloy Cu_2MnAl mosaic single crystals for neutron monochromators. *Nuclear Instruments and Methods in Physics Research Section A: Accelerators, Spectrometers, Detectors and Associated Equipment*, **529**, 157, 2004.

[26] A. Delapalme, J. Schweizer, G. Couderchon, and R. P. de la Bathie. Étude de l'alliage de Heusler (Cu_2MnAl) comme monochromateur de neutrons polarisés. *Nuclear Instruments and Methods*, **95** (3), 589, 1971.

[27] H. Okamoto. Mn - Si (manganese - silicon). *Journal of Phase Equilibria*, **12** (4), 505, 1991.

[28] S. Tomiyoshi, Y. Yamaguchi, M. Ohashi, E. R. Cowley, and G. Shirane. Magnetic

excitations in the itinerant antiferromagnets Mn_3Si and Fe-doped Mn_3Si. *Physical Review B*, **36** (4), 2181, 1987.

[29] S. Tomiyoshi, E. R. Cowley, and H. Onodera. Anomalous behavior of higher-harmonic spin density waves in Mn_3 Si. *Physical Review B*, **73** (2), 024416, 2006.

[30] S. Tomiyoshi, S. Funahashi, and Y. Yamaguchi. Magnetic excitations in Mn_3Si. *Physica B&C*, **120** (1-3), 143, 1983.

[31] M. Dörr, J. Bœuf, C. Pfleiderer, M. Rotter, N. Kozlova, D. Eckert, P. Kerschl, K.-H. Müller, and M. Löwenhaupt. Search for half-metallic antiferromagnetism using pulsed magnetic fields: experimental investigation of Mn_3Si, CuMnSb and PdMnTe. *Physica B: Condensed Matter*, **346-347**, 137, 2004.

[32] C. Pfleiderer, J. Bœuf, and H. v. Löhneysen. Stability of antiferromagnetism at high magnetic fields in Mn_3Si. *Physical Review B*, **65** (17), 172404, 2002.

[33] C. Pfleiderer. Are Mn_3Si and CuMnSb antiferromagnetic half-metals? *Physica B: Condensed Matter*, **329-333**, 1085, 2003.

[34] A. Ślebarski, M. B. Maple, E. J. Freeman, C. Sirvent, D. Tworuszka, M. Orzechowska, A. Wrona, A. Jezierski, S. Chiuzbaian, and M. Neumann. Weak ferromagnetism induced by atomic disorder in Fe_2TiSn. *Physical Review B*, **62** (5), 3296, 2000.

[35] A. Ślebarski, M. B. Maple, A. Wrona, and A. Winiarska. Kondo-type behavior in $Fe_{2-x}M_xTiSn$ (M=Co, Ni). *Physical Review B*, **63** (21), 214416, 2001.

[36] S. V. Dordevic, D. N. Basov, A. Ślebarski, M. B. Maple, and L. Degiorgi. Electronic structure and charge dynamics of the Heusler alloy Fe_2TiSn probed by infrared and optical spectroscopy. *Physical Review B*, **66** (7), 075122, 2002.

[37] A. Ślebarski. Electron-correlation effects in a disordered Fe_2TiSn Heusler alloy. *Journal of Physics D: Applied Physics*, **39** (5), 856, 2006.

[38] A. Jezierski and A. Ślebarski. Atomic disorder and magnetism in Fe_2TiSn alloy. *Journal of Magnetism and Magnetic Materials*, **223** (1), 33, 2001.

[39] Y. Fujita, K. Endo, M. Terada, and R. Kimura. Magnetic properties of Heusler type alloys M_2XSn (M = Fe, Co or Ni, X = Ti or V). *Journal of Physics and Chemistry of Solids*, **33** (7-9), 1443, 1972.

[40] J. Frackowiak, K. Brzakalik, and J. Deniszczyk. ^{57}Fe and ^{119}Sn Mössbauer studies of hyperfine structure in $Fe_{3-x}Ti_xSn$ ($0 \leq x \leq 1$) alloys. *Journal of Alloys and Compounds*, **442**, 242, 2007.

[41] M. Nakabayashi, K. Fukuda, H. Kitagawa, Y. Yamada, S. Kubo, and A. Matsushita. Magnetic and transport properties in Heusler-type Fe_2TiSn compound. *Physica B: Condensed Matter*, **329-333**, 1134, 2003.

[42] H. J. Goldschmitt. *Journal of the Iron and Steel Institute*, **198**, 169, 1960.

[43] A. Raman. *Zeitschrift für Metallkunde*, **57**, 301, 1966.

[44] H. Okamoto. Fe - Nb (iron - niobium). *Journal of Phase Equilibria*, **14** (5), 650, 1993.

[45] E. Paul and L. J. Swartzendruber. The Fe-Nb (Iron-Niobium) system. *Journal of Phase Equilibria*, **7** (3), 248, 1986.

[46] J. Bejarano, S. Gama, C. Ribeiro, and G. Effenberg. *Zeitschrift für Metallkunde*, **84** (3), 169, 1993.

[47] J. H. Zhu, L. M. Pike, C. T. Liu, and P. K. Liaw. Point defects in binary Laves phase alloys. *Acta Materialia*, **47** (7), 2003, 1999.

[48] D. A. Read, G. C. Hallam, M. S. Sahota, and A. Mustaffa. The magnetic properties of Fe-Nb alloys. *Physica B&C*, **86-88** (Part 1), 66, 1977.

[49] Y. Yamada and K. Ôhira. NMR study of $(Zr_{1-x}Nb_x)Fe_2$. *Journal of the Physical Society of Japan*, **52**, 3646, 1983.

[50] S. Ishida, S. Asano, and J. Ishida. Electronic structures and magnetic properties of the C14 Laves phase compounds $ZrMn_2$, $TiFe_2$ and $NbFe_2$. *Journal of the Physical Society of Japan*, **54**, 3925, 1985.

[51] M. Shiga and Y. Nakamura. Magnetic properties of stoichiometric and off-stoichiometric $NbFe_2$. *Journal of the Physical Society of Japan*, **56**, 4040, 1987.

[52] Y. Yamada and A. Sakata. Weak antiferromagnetism in $NbFe_2$. *Journal of the Physical Society of Japan*, **57**, 46, 1988.

[53] H. Wada, M. Hada, M. Shiga, and Y. Nakamura. Low temperature specific heat of Laves phase AFe_2 compounds (A=Nb, Ta and Ti). *Journal of the Physical Society of Japan*, **59**, 701, 1990.

[54] Y. Yamada, H. Nakamura, Y. Kitaoka, K. Asayama, K. Koga, A. Sakata, and T. Murakami. NMR study of weak antiferromagnetism in $NbFe_2$. *Journal of the Physical Society of Japan*, **59**, 2976, 1990.

[55] M. Crook and R. Cywinski. Magnetic transition in $Nb_{1-y}Fe_{2+y}$. *Journal of Magnetism and Magnetic Materials*, **140-144**, 71, 1995.

[56] M. Kurisu, Y. Andoh, and Y. Yamada. Magnetic properties of $NbFe_2$ single crystal. *Physica B: Condensed Matter*, **237-238**, 493, 1997.

[57] M. Brando, D. Moroni-Klementowicz, C. Albrecht, and F. M. Grosche. Quantum criticality in $NbFe_2$. *Physica B: Condensed Matter*, **378-380**, 111, 2006.

[58] R. S. Turtelli, J. Sinnecker, R. Grossinger, A. Penton-Madrigal, and E. Estevez-Rams. Magnetic orderings and temperature dependence of the hysteresis loops of $Nb_{1-x}Fe_{2+x}$. *Journal of Magnetism and Magnetic Materials*, **316**, e492, 2007.

[59] J. Inoue and M. Shimizu. Electronic structure and magnetic properties of off-stoichiometric $NbFe_2$. *Journal of Magnetism and Magnetic Materials*, **79** (2), 265, 1989.

[60] D. Moroni-Klementowicz, M. Brando, C. Albrecht, W. J. Duncan, F. M. Grosche, D. Grüner, and G. Kreiner. Magnetism in $Nb_{1-y}Fe_{2+y}$: Composition and magnetic field dependence. *Physical Review B*, **79** (22), 224410, 2009.

[61] M. Brando, W. J. Duncan, D. Moroni-Klementowicz, C. Albrecht, D. Grüner, R. Ballou, and F. M. Grosche. Logarithmic Fermi-liquid breakdown in $NbFe_2$. *Physical Review Letters*, **101** (2), 026401, 2008.

[62] M. Brando, D. Moroni-Klementowicz, C. Albrecht, W. Duncan, D. Grüner, R. Ballou, B. Fák, and F. M. Grosche. Logarithmic Fermi-liquid breakdown in $Nb_{1.02}Fe_{1.98}$. *Journal of Magnetism and Magnetic Materials*, **310**, 852, 2007.

[63] A. Subedi and D. J. Singh. Band structure and itinerant magnetism in quantum critical $NbFe_2$. *Physical Review B*, **81** (2), 024422, 2010.

[64] D. Shinoda and S. Asanabe. Magnetic properties of silicides of iron group transition elements. *Journal of the Physical Society of Japan*, **21** (3), 555, 1966.

[65] J. Wernick, G. Wertheim, and R. Sherwood. Magnetic behavior of the monosilicides of the 3d-transition elements. *Materials Research Bulletin*, **7** (12), 1431 , 1972.

[66] Y. Ishikawa, G. Shirane, J. A. Tarvin, and M. Kohgi. Magnetic excitations in the weak itinerant ferromagnet MnSi. *Physical Review B*, **16** (11), 4956, 1977.

[67] V. Jaccarino, G. K. Wertheim, J. H. Wernick, L. R. Walker, and S. Arajs. Paramagnetic Excited State of FeSi. *Physical Review*, **160** (3), 476, 1967.

[68] G. Aeppli and F. Z. Kondo insulators. *Comments on Condensed Matter Physics*, **16**, 155, 1992.

[69] N. Manyala, Y. Sidis, J. F. DiTusa, G. Aeppli, D. P. Young, and Z. Fisk. Large Anomalous Hall effect in a silicon-based magnetic semiconductor. *Nature Materials*, **3**, 255, 2004.

[70] H. J. Williams, J. H. Wernick, R. C. Sherwood, and G. K. Wertheim. Magnetic properties of the monosilicides of some 3d transition elements. *Journal of Applied Physics*, **37** (3), 1256, 1966.

[71] L. M. Levinson, G. H. Lander, and M. O. Steinitz. Anomalous Magnetic Behavior of MnSi. *AIP Conference Proceedings*, **10** (1), 1138, 1973.

[72] D. Bloch, J. Voiron, V. Jaccarino, and J. H. Wernick. The high field - high pressure magnetic properties of MnSi. *Physics Letters A*, **51** (5), 259 , 1975.

[73] G. G. Lonzarich. Band structure and magnetic fluctuations in ferromagnetic or nearly ferromagnetic metals. *Journal of Magnetism and Magnetic Materials*, **45** (1), 43, 1984.

[74] G. G. Lonzarich and L. Taillefer. Effect of spin fluctuations on the magnetic equation of state of ferromagnetic or nearly ferromagnetic metals. *Journal of Physics C: Solid State Physics*, **18** (22), 4339, 1985.

[75] T. Moriya. *Spin fluctuations in itinerant electron magnetism*. Springer, Berlin, 1985.

[76] Y. Ishikawa, Y. Noda, Y. J. Uemura, C. F. Majkrzak, and G. Shirane. Paramagnetic spin fluctuations in the weak itinerant-electron ferromagnet MnSi. *Physical Review B*, **31** (9), 5884, 1985.

[77] C. Thessieu, C. Pfleiderer, A. N. Stepanov, and J. Flouquet. Field dependence of the magnetic quantum phase transition in MnSi. *Journal of Physics: Condensed Matter*, **9** (31), 6677, 1997.

[78] A. Bauer. Quantenphasenübergänge und Skyrmion-Gitter in $Mn_{1-x}Fe_xSi$ und $Mn_{1-x}Co_xSi$. Diploma thesis, Technische Universität München, 2009.

[79] K. Motoya, H. Yasuoka, Y. Nakamura, and J. H. Wernick. Helical spin structure in MnSi - NMR studies. *Solid State Communications*, **19** (6), 529, 1976.

[80] Y. Ishikawa, K. Tajima, D. Bloch, and M. Roth. Helical spin structure in manganese silicide MnSi. *Solid State Communications*, **19** (6), 525, 1976.

[81] S. Kusaka, K. Yamamoto, T. Komatsubara, and Y. Ishikawa. Ultrasonic study of magnetic phase diagram of MnSi. *Solid State Communications*, **20** (9), 925, 1976.

[82] P. Bak and M. H. Jensen. Theory of helical magnetic structures and phase transitions in MnSi and FeGe. *Journal of Physics C: Solid State Physics*, **13** (31), L881, 1980.

[83] O. Nakanishi, A. Yanase, A. Hasegawa, and M. Kataoka. The origin of the helical spin density wave in MnSi. *Solid State Communications*, **35** (12), 995, 1980.

[84] I. Dzyaloshinsky. A thermodynamic theory of weak ferromagnetism of antiferromagnetics. *Journal of Physics and Chemistry of Solids*, **4** (4), 241, 1958.

[85] T. Moriya. Anisotropic Superexchange Interaction and Weak Ferromagnetism. *Physical Review*, **120** (1), 91, 1960.

[86] C. Pfleiderer, P. Böni, T. Keller, U. K. Rossler, and A. Rosch. Non-Fermi liquid metal without quantum criticality. *Science*, **316** (5833), 1871, 2007.

[87] C. Pfleiderer, G. J. McMullan, S. R. Julian, and G. G. Lonzarich. Magnetic quantum phase transition in MnSi under hydrostatic pressure . *Physical Review B*, **55** (13), 8330, 1997.

[88] C. Pfleiderer, S. Julian, and G. G. Lonzarich. Non-Fermi-liquid nature of the normal state of itinerant-electron ferromagnets. *Nature*, **414**, 427, 2001.

[89] C. Pfleiderer, D. Reznik, L. Pintschovius, H. v. Löhneysen, M. Garst, and A. Rosch. Partial order in the non-Fermi-liquid phase of MnSi. *Nature*, **427**, 227, 2004.

[90] U. K. Rössler, A. N. Bogdanov, and C. Pfleiderer. Spontaneous magnetic ground states in magnetic metals. *Nature*, **442**, 797, 2006.

[91] A. Neubauer, C. Pfleiderer, B. Binz, A. Rosch, R. Ritz, P. G. Niklowitz, and P. Böni. Topological Hall effect in the A Phase of MnSi. *Physical Review Letters*, **102** (18), 186602, 2009.

[92] C. Pfleiderer, T. Adams, A. Bauer, W. Biberacher, B. Binz, F. Birkelbach, P. Böni, C. Franz, R. Georgii, M. Janoschek, F. Jonietz, T. Keller, R. Ritz, S. Mühlbauer, W. Münzer, A. Neubauer, B. Pedersen, and A. Rosch. Skyrmion lattices in metallic and semiconducting B20 transition metal compounds. *Journal of Physics-Condensed Matter*, **22** (16), 164207, 2010.

[93] A. Neubauer. Hall-Effekt und Magnetwiderstand in schwach-magnetischen Metallen. Diploma thesis, Technische Universität München, 2006.

[94] F. Jonietz, S. Mühlbauer, C. Pfleiderer, A. Neubauer, W. Münzer, A. Bauer, T. Adams, R. Georgii, P. Böni, R. A. Duine, K. Everschor, M. Garst, and A. Rosch. Spin Transfer Torques at Ultralow Current Denities. Accepted subject to minor revisions, 2010.

[95] W. Münzer. Einkristallzüchtung und magnetische Eigenschaften von MnSi und $Fe_{1-x}Co_xSi$. Diploma thesis, Technische Universität München, 2009.

[96] T. Adams. Skyrmiongitter und partielle Ordnung in B20 Übergangsmetallverbindungen. Diploma thesis, Technische Universität München, 2010.

[97] W. Münzer, A. Neubauer, T. Adams, S. Mühlbauer, C. Franz, F. Jonietz, R. Georgii, P. Böni, B. Pedersen, M. Schmidt, A. Rosch, and C. Pfleiderer. Skyrmion lattice in the doped semiconductor $Fe_{1-x}Co_x$ Si. *Physical Review B*, **81** (4), 041203, 2010.

[98] A. Bauer, A. Neubauer, C. Franz, W. Münzer, M. Garst, and C. Pfleiderer. Quantum Phase Transitions in Single-Crystal $Mn_{1-x}Fe_xSi$ and $Mn_{1-x}Co_xSi$: Crystal Growth, Magnetization, AC Susceptibility and Specific Heat. *Physical Review B*, **82** (6), 064404, 2010.

[99] T. Adams, S. Mühlbauer, A. Neubauer, W. Münzer, F. Jonietz, R. Georgii, B. Pedersen, P. Böni, A. Rosch, and C. Pfleiderer. Skyrmion Lattice Domains in $Fe_{1-x}Co_xSi$. *Journal of Physics: Conference Series*, **200** (3), 032001, 2010.

[100] S. V. Grigoriev, D. Chernyshov, V. A. Dyadkin, V. Dmitriev, S. V. Maleyev, E. V. Moskvin, D. Menzel, J. Schönes, and H. Eckerlebe. Crystal handedness and spin helix chirality in $Fe_{1-x}Co_xSi$. *Physical Review Letters*, **102** (3), 037204, 2009.

[101] S. V. Grigoriev, D. Chernyshov, V. A. Dyadkin, V. Dmitriev, E. V. Moskvin, D. Lamago, T. Wolf, D. Menzel, J. Schönes, S. V. Maleyev, and H. Eckerlebe. Interplay between crystalline chirality and magnetic structure in $Mn_{1-x}Fe_xSi$. *Physical Review B*, **81** (1), 012408, 2010.

[102] X. Z. Yu, Y. Onose, N. Kanazana, J. H. Park, J. Han, Y. Matsui, N. Nagaosa, and

Y. Tokura. Real-space observation of a two-dimensional skyrmion crystal. *Nature*, **465**, 901, 2010.

[103] C. Pfleiderer and A. Rosch. Condensed-matter physics: Single skyrmions spotted. *Nature*, **465**, 880, 2010.

[104] M. Ishida, Y. Endoh, S. Mitsuda, Y. Ishikawa, and M. Tanaka. Crystal chirality and helicity of the helical spin density wave in MnSi. II. Polarized neutron diffraction. *Journal of the Physical Society of Japan*, **54** (8), 2975, 1985.

[105] Martin Meven, personal communication, 2010.

[106] M. Blume. Polarization Effects in the Magnetic Elastic Scattering of Slow Neutrons. *Physical Review*, **130** (5), 1670, 1963.

[107] M. Tanaka, H. Takayoshi, M. Ishida, and Y. Endoh. Crystal chirality and helicity of the helical spin density wave in MnSi. I. Convergent-beam electron diffraction. *Journal of the Physical Society of Japan*, **54** (8), 2970, 1985.

[108] K.-T. Wilke and J. Bohm. *Kristallzüchtung*. VEB Deutscher Verlag der Wissenschaften, Berlin, 1988.

[109] F. Rosenberger. *Fundamentals of Crystal Growth 1*. Sringer Verlag, Berlin/Heidelberg, 1979.

[110] P. Haasen. *Physikalische Metallkunde*. Springer, Berlin, 1994.

[111] P. Gille. *Basics of thermodynamics and phase transitions in complex intermetallics, Chapter 3: Solidification*. World Scientific, Singapore, 2008.

[112] J. Burton, R. Prim, and W. Slichter. The Distribution of Solute in Crystals Grown from the Melt. *Journal of Chemical Physics*, **21** (11), 1987, 1953.

[113] W. Tiller, K. Jackson, J. Rutter, and B. Chalmers. The redistribution of solute atoms during the solidification of metals. *Acta Metallurgica*, **1** (4), 428, 1953.

[114] W. G. Pfann. *Zone melting*. Wiley, New York, 1966.

[115] J. Shah. *Crystal Growth, Chapter 4*. Pergamon Press, Oxford, New York, 1975.

[116] P. Keck and M. Golay. Crystallization of silicon from a floating liquid zone. *Physical Review*, **89**, 1297, 1953.

[117] N. Wizent. Hochdruckkristallzüchtung ausgewählter Oxidverbindungen. Ph.D. thesis, IFW Dresden, 2009.

[118] G. Behr and W. Löser. Floating zone crystal growth of multi-component rare earth transition metal intermetallic compounds. *Recent Research and Development in Crystal Growth*, **4**, 129, 2005.

[119] N. Kobayashi. Power required to form a floating zone and the zone shape. *Journal of Crystal Growth*, **43** (4), 417, 1978.

[120] D. A. Hukin, UK Patent F4B-51-A13A3-C10B, 1970.

[121] http://www.horst.de, 2010.

[122] http://www.frm2.tum.de/wissenschaftliche-nutzung/diffraktion/resi, 2010.

[123] http://www.frm2.tum.de/wissenschaftliche-nutzung/diffraktion/heidi, 2010.

[124] William Duncan, personal communication, 2010.

[125] http://www.frm2.tum.de/en/science/radiography/antares, 2010.

[126] http://www.frm2.tum.de/en/science/diffraction/mira, 2010.

[127] http://www.qdusa.com, 2010.

[128] R. Ritz. Phasenübergänge schwach-magnetischer Metalle unter extremen Bedingungen. Diploma thesis, Technische Universität München, 2007.

[129] C. Franz. Experimentelle Untersuchung von ferromagnetischen Quantenphasenübergaängen. Diploma thesis, Technische Universität München, 2008.

[130] http://www.wissel-instruments.de, 2010.

[131] T. F. Smith and C. W. Chu. Will pressure destroy superconductivity? *Physical Review*, **159** (2), 353, 1967.

[132] F. Birkelbach. Aufbau eines Drehmomentmagnetometers. Zulassungsarbeit für das Staatsexamen, Technische Universität München, 2009.

[133] M. Schulz. Radiography with Polarized Neutrons. Ph.D. thesis, Technische Universität München, 2010.

[134] M. Schulz, P. Böni, E. Calzada, M. Mühlbauer, A. Neubauer, and B. Schillinger. A polarizing neutron periscope for neutron imaging. *Nuclear Instruments and Methods in Physics Research Section A: Accelerators, Spectrometers, Detectors and Associated Equipment*, **605** (1-2), 43, 2009.

[135] M. Schulz, A. Neubauer, M. Mühlbauer, E. Calzada, B. Schillinger, C. Pfleiderer, and P. Böni. Polarized neutron radiography with a periscope. *Journal of Physics: Conference Series*, **200** (11), 112009, 2010.

[136] http://www.frm2.tum.de/en/science/service-groups/neutrons-optics/3he-polarizer-helios, 2010.

[137] G. E. Bacon and K. Lonsdale. Neutron diffraction. *Reports on Progress in Physics*, **16** (1), 1, 1953.

[138] P. J. Webster. Heusler alloys. *Contemporary Physics*, **10**, 559, 1969.

[139] E. Babcock, A. Petoukhov, J. Chastagnier, D. Jullien, E. Leliévre-Berna, K. Andersen, R. Georgii, S. Masalovich, S. Boag, C. Frost, and S. Parnell. AFP flipper devices: Polarized ^{3}He spin flipper and shorter wavelength neutron flipper. *Physica B: Condensed Matter*, **397** (1-2), 172, 2007.

[140] Sergey Masalovitch, personal communication, 2010.

[141] Peter Böni, personal communication, 2010.

[142] Christian Pfleiderer, personal communication, 2010.

[143] G. H. Lander, P. J. Brown, and J. B. Forsyth. The antiferromagnetic structure of Mn_5Si_3. *Proceedings of the Physical Society*, **91** (2), 332, 1967.

[144] S. Songlin, W. Dagula, O. Tegus, E. Brück, J. Klaasse, F. d. Boer, and K. Buschow. Magnetic phase transition and magnetocaloric effect in $Mn_{5-x}Fe_xSi_3$. *Journal of Alloys and Compounds*, **334**, 249, 2002.

[145] Tim Adams, personal communication, 2010.

[146] Anatoliy Senyshyn, personal communication, 2010.

[147] Klaudia Hradil, personal communication, 2010.

[148] J. A. Hertz. Quantum critical phenomena. *Physical Review B*, **14** (3), 1165, 1976.

[149] A. J. Millis. Effect of a nonzero temperature on quantum critical points in itinerant fermion systems. *Physical Review B*, **48** (10), 7183, 1993.

[150] G. G. Lonzarich. in *Electron*. Cambridge University Press, Cambridge, England, 1996.

[151] P. G. Niklowitz, F. Beckers, G. G. Lonzarich, G. Knebel, B. Salce, J. Thomasson, N. Bernhoeft, D. Braithwaite, and J. Flouquet. Spin-fluctuation-dominated electrical transport of Ni_3Al at high pressure. *Physical Review B*, **72** (2), 024424, 2005.

[152] E. A. Yelland, S. J. C. Yates, O. Taylor, A. Griffiths, S. M. Hayden, and A. Carrington. Ferromagnetic properties of $ZrZn_2$. *Physical Review B*, **72** (18), 184436, 2005.

[153] M. Uhlarz. Magnetisierung von $ZrZn_2$ unter hohem Druck. Ph.D. thesis, Physikalisches Institut, Universität Karlsruhe, 2004.

[154] D.-X. Qu, Y. S. Hor, J. Xiong, R. J. Cava, and N. P. Ong. Quantum oscillations and Hall anomaly of surface states in the topological insulator Bi_2Te_3. *Science*, **329** (5993), 821, 2010.

[155] Jürgen Kübler, personal communication, 2010.

[156] S.-C. Zhang. Topological states of quantum matter. *Physics*, **1**, 6, 2008.

[157] J. Moore. Topological insulators: The next generation. *Nature Physics*, **5**, 378, 2009.

[158] M. Z. Hasan, H. Lin, and A. Bansil. Warping the cone on a topological insulator. *Physics*, **2**, 108, 2009.

[159] X.-L. Qi and S.-C. Zhang. The quantum spin Hall effect and topological insulators. *Physics Today*, **63** (1), 33, 2010.

[160] K. v. Klitzing, G. Dorda, and M. Pepper. New method for high-accuracy determination of the fine-structure constant based on quantized Hall resistance. *Physical Review Letters*, **45** (6), 494, 1980.

[161] B. A. Bernevig, T. L. Hughes, and S.-C. Zhang. Quantum spin Hall effect and topological phase transition in HgTe quantum wells. *Science*, **314** (5806), 1757, 2006.

[162] M. Konig, S. Wiedmann, C. Brune, A. Roth, H. Buhmann, L. W. Molenkamp, X.-L. Qi, and S.-C. Zhang. Quantum spin Hall insulator state in HgTe quantum wells. *Science*, **318** (5851), 766, 2007.

[163] L. Fu and C. L. Kane. Topological insulators with inversion symmetry. *Physical Review B*, **76** (4), 045302, 2007.

[164] D. Hsieh, D. Qian, L. Wray, Y. Xia, Y. S. Hor, R. J. Cava, and M. Z. Hasan. A topological Dirac insulator in a quantum spin Hall phase. *Nature*, **452**, 970, 2008.

[165] H. Zhang, C.-X. Liu, X.-L. Qi, X. Dai, Z. Fang, and S.-C. Zhang. Topological insulators in Be_2Se_3, Bi_2Te_3 and Sb_2Te_3 with a single Dirac cone on the surface. *Nature Physics*, **5**, 438, 2009.

[166] Y. L. Chen, J. G. Analytis, J.-H. Chu, Z. K. Liu, S.-K. Mo, X. L. Qi, H. J. Zhang, D. H. Lu, X. Dai, Z. Fang, S.-C. Zhang, I. R. Fisher, Z. Hussain, and Z.-X. Shen. Experimental realization of a three-dimensional topological insulator, Bi_2Te_3. *Science*, **325** (5937), 178, 2009.

[167] S. Chadov, X. Qi, J. Kübler, G. H. Fecher, C. Felser, and S.-C. Zhang. Tunable multifunctional topological insulators in ternary Heusler compounds. *Nature Materials*, **9**, 541, 2010.

[168] H. Zhang, S. Chadov, L. Müchler, B. Yan, X. Qi, J. Kübler, S.-C. Zhang, and C. Felser. Topological insulators in ternary compounds with a honeycomb lattice. *arXiv:1010.2195*, 2010.

[169] X.-L. Qi, T. L. Hughes, and S.-C. Zhang. Topological field theory of time-reversal invariant insulators. *Physical Review B*, **78** (19), 195424, 2008.

[170] W. J. Duncan, O. P. Welzel, D. Moroni-Klementowicz, C. Albrecht, P. G. Niklowitz, D. Grüner, M. Brando, A. Neubauer, C. Pfleiderer, N. Kikugawa, A. P. Mackenzie, and F. M. Grosche. Quantum phase transitions in $NbFe_2$ and $Ca_3Ru_2O_7$. *physica status solidi b*, **247**, 544, 2010.

[171] D. Belitz, T. R. Kirkpatrick, and T. Vojta. First order transitions and multicritical points in weak itinerant ferromagnets. *Physical Review Letters*, **82** (23), 4707, 1999.

[172] W. J. Duncan. Quantum Phase Transitions in $NbFe_2$ and $BaFe_2As_2$. Ph.D. thesis, Royal Holloway, University of London, 2010. A draft version of this thesis was available.

[173] Manuel Brando, personal communication, 2010.

[174] D. Lamago, R. Georgii, and P. Böni. Magnetic susceptibility and specific heat of the itinerant ferromagnet MnSi. *Physica B: Condensed Matter*, **359-361**, 1171, 2005.

[175] S. M. Stishov, A. E. Petrova, S. Khasanov, G. K. Panova, A. A. Shikov, J. C. Lashley, D. Wu, and T. A. Lograsso. Heat capacity and thermal expansion of the itinerant helimagnet MnSi. *Journal of Physics: Condensed Matter*, **20** (23), 235222, 2008.

[176] M. P. J. Punkkinen, K. Kokko, M. Ropo, I. J. Väyrynen, L. Vitos, B. Johansson, and J. Kollar. Magnetism of (FeCo)Si alloys: Extreme sensitivity on crystal structure. *Physical Review B*, **73** (2), 024426, 2006.